

UNCLASSIFIED

NAVAL AIR WARFARE CENTER AIRCRAFT DIVISION  
PATUXENT RIVER, MARYLAND



## TECHNICAL REPORT

REPORT NO: NAWCADPAX--97-257-TR

COPY NO. \_\_\_\_\_

### COMPUTATIONAL FLUID DYNAMICS TOOLS FOR ESCAPE SYSTEMS AERODYNAMIC ANALYSIS

Volume 2 of 2

9 February 1998

1998092106  
690

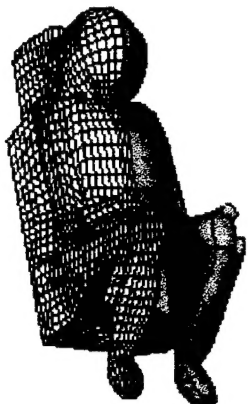
Approved for public release; distribution is unlimited.

UNCLASSIFIED

REPORT DOCUMENTATION PAGE			Form Approved OMB No. 0704-0188
<p>Public reporting burden for this collection of information is estimated to average 1 hour per response, including the time for reviewing instructions, searching existing data sources, gathering and maintaining the data needed, and completing and reviewing the collection of information. Send comments regarding this burden estimate only, other aspect of this collection of information, including suggestions for reducing this burden, to Washington Headquarters Services, Directorate for Information Operations and Reports, 1215 Jefferson Davis Highway, Suite 1204, Arlington, VA 22202-4302, and to the Office of Management and Budget, Paperwork Reduction Project (0704-0188), Washington, DC 20503.</p>			
1. AGENCY USE ONLY (LEAVE BLANK)	2. REPORT DATE 9 February 1998	3. REPORT TYPE AND DATES COVERED	
4. TITLE AND SUBTITLE  Computational Fluid Dynamics Tools for Escape Systems Aerodynamic Analysis (Volume 2 of 2)		5. FUNDING NUMBERS	
6. AUTHOR(S) S. D. Habchi      V. J. Parsatharsay S. G. Rock      A. J. Przekwas G. S. Hufford      Contract No. N62269-92-C-0248		8. PERFORMING ORGANIZATION REPORT NUMBER  NAWCADPAX--97-257-TR CFDRC Report 4128/17	
7. PERFORMING ORGANIZATION NAME(S) AND ADDRESS(ES)  CFD Research Corporation 3325 Triana Blvd. Huntsville, Alabama 35805			
9. SPONSORING/MONITORING AGENCY NAME(S) AND ADDRESS(ES)  Naval Air Warfare Center Aircraft Division 22347 Cedar Point Road Unit #6 Patuxent River, Maryland 20670-1161		10. SPONSORING/MONITORING AGENCY REPORT NUMBER	
11. SUPPLEMENTARY NOTES Project Coordinator: Thomas J. Marquette (Code 4.6.2.1) Naval Air Warfare Center Aircraft Division Patuxent River, Maryland 20670			
12a. DISTRIBUTION/AVAILABILITY STATEMENT  Approved for public release; distribution is unlimited.		12b. DISTRIBUTION CODE	
13. ABSTRACT (Maximum 200 words)  This report documents the findings of a SBIR Phase II study entitled "CFD Analysis of Drag Reduction on an Ejection Seat During High Speed Ejection". The main objectives of this study were to develop and validate Computational Fluid Dynamics (CFD) methodologies for comprehensive aerodynamic analysis of ejection seat and occupant in free flight, and develop and adapt existing CFD technologies for analysis of ejection seat in proximity of aircraft for both steady-state and unsteady seat and aircraft separation using prescribed trajectory.			
14. SUBJECT TERMS Computational Fluid Dynamics (CFD)			15. NUMBER OF PAGES 166
			16. PRICE CODE
17. SECURITY CLASSIFICATION OF REPORT Unclassified	18. SECURITY CLASSIFICATION OF THIS PAGE Unclassified	19. SECURITY CLASSIFICATION OF ABSTRACT Unclassified	20. LIMITATION OF ABSTRACT SAR

## COMPUTATIONAL FLUID DYNAMICS TOOLS

### FOR ESCAPE SYSTEMS AERODYNAMIC ANALYSIS



Final Report

Volume 2 of 2



by

**S.D. Habchi, S.G. Rock, G.S. Hufford, V.J. Parsatharsay and A.J. Przekwas**



CLEARED FOR  
OPEN PUBLICATION

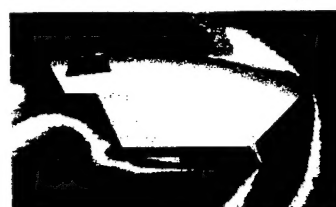
FFB 9 1998

PUBLIC AFFAIRS OFFICE  
NAVAL AIR SYSTEMS COMMAND

*Helen Howard*

for

Naval Air Warfare Center - Aircraft Division  
Patuxent River NAS  
Lexington Park, MD 20670  
Contract No.: N62269-92-C-0248  
Project Coordinator: Thomas J. Marquette



# CFD Research Corporation

3325 Triana Blvd. • Huntsville, Alabama 35805 • Tel.: (205) 536-6576 • FAX: (205) 536-6590 • info@cfdr.com



## COMPUTATIONAL FLUID DYNAMICS TOOLS FOR ESCAPE SYSTEMS AERODYNAMIC ANALYSIS Final Report

Volume 2 of 2

by

S.D. Habchi, S.G. Rock, G.S. Hufford, V.J. Parsatharsay and A.J. Przekwas

December 1996

CFDRC Report 4128/17

for  
Naval Air Warfare Center (NAWC)  
Patuxent River NAS  
Lexington Park, MD 20670

Under Contract No.: N62269-92-C-0248  
Project Coordinator: Thomas J. Marquette, Code 6032

## FORWARD

This is Volume 2 of the final report for an SBIR Phase II study entitled "CFD Drag Reduction on an Ejection Seat During High Speed Ejection". This project was sponsored by the U.S. Navy, Naval Air Warfare Center, Aircraft Division (NAWC-A/D), under contract number N62269-92-C-0204, and conducted by CFD Research Corporation (CFDRC) under project number 4128. The principal investigator of this work was Mr. Sami D. Habchi of CFDRC and the Navy technical monitor was Mr. Thomas J. Marquette of NAWC-A/D. This contract started in April 1992. The original completion date was April 1994, however, in the spring of 1994 the contract was extended (with additional tasks and cost) until June 1996. This final report present results of the 4 year effort including the extension.

This report is divided into two volumes:

- Volume 1: Section 1 through Section 5, describing all seat and occupant methodology development CFD tools adaptations, demonstrations and validations; and
- Volume 2: Section 6 through Section 9, describing methodology selection and development for seat aircraft analysis, along with demonstration and validation results. Volume 2 also includes the conclusion and recommendations for this study. Volume 2 also includes Appendix A which includes all the technical papers documenting the work performed under this contract.

The authors of this report would like to thank the following individuals for their contributions to the overall success of this project:

- Dr. Simon Ho for his help in the NACES geometric modeling and flow analysis process.
- Mr. Mark Ostrander for his help in the OVERFLOW code simulations.
- Dr. Curtis Mitchell of CFDRC for his help in the Overset-Hybrid gridding methodology development and implementation and other CFD-FASTRAN code support and development.
- Dr. Z.J. Wang of CFDRC for his support and advice in the traditional Chimera development and implementation into CFD-FASTRAN, and for CFD-FASTRAN code support.
- Dr. Ken Wintzler of WL/FIMC for providing geometry and surface models for B-1A capsule.

- Dr. Ashok K. Singhal of CFDRC for his overall guidance and direction throughout this effort.
- Mr. Thomas J. Marquette of NAWC-A/D for his active participation in all phases of this work and his suggestions and contributions especially in the validation and design concept assessment tasks.
- Mr. Peter Ayoub of NAWC-A/D for his active participation in this project and his overall guidance and advice throughout this effort.
- Ms. Jennifer Swann of CFDRC for her careful preparation of all reports, presentation material and other documents for this project.

## SUMMARY

This report documents the findings of a SBIR Phase II study entitled "CFD Analysis of Drag Reduction on an Ejection Seat During High Speed Ejection". The main objectives of this study were twofold:

- develop and validate Computational Fluid Dynamics (CFD) methodologies for comprehensive aerodynamic analysis of ejection seat and occupant in free flight; and
- develop and adapt existing CFD technologies for analysis of ejection seat in proximity of aircraft for both steady-state and unsteady seat and aircraft separation using prescribed trajectory.

Mechanical Computer Aided Engineering tools were developed for geometry modeling and algebraic grid generation of ejection seat and occupant and relevant aircraft components. Also an elliptic grid generator was developed for the smoothing of the escape systems grids and for grid clustering and orthogonality control. The grid generator includes a model for adjustment of seat and occupant grids for various pitch and yaw attitudes. Several geometry models and computational grids were created for the NACES seat and occupant, ACES-II seat and occupant, F-16 aircraft including cockpit and F-18 aircraft including cockpit. These computational grids were used for several computational analysis to validate and demonstrate the developed CFD technologies.

The CFD-ACE code was adapted for ejection seat and occupant aerodynamic analysis. A comprehensive assessment of differencing schemes and turbulence modeling was conducted and several guidelines were developed for ejection seat applications. Two high order differencing schemes including Second-Order upwind and Osher-Chakravarthy schemes were implemented in the CFD-ACE code for escape system applications. A force and moment integration module was also developed and implemented into CFD-ACE to calculate the aerodynamic coefficients for the ejection seat and occupant in any orientation and in several body axis systems. Also a seat/occupant attitude control module was implemented into CFD-ACE for unsteady simulation of seat and occupant configurations.

Two new multiple and moving bodies technologies were developed and implemented in the CFD-FASTRAN code for seat and aircraft analysis. The first one features a hybrid-overset gridding technique that utilizes structured and unstructured grids. The second one relies on traditional Chimera overset gridding techniques to model multiple bodies using multiple grid systems. The Chimera technique was adopted for seat and aircraft separation analysis. This Chimera technique features several new techniques, such as Alternating Digital tree, for automatic and efficient handling of hole cutting and tree searching interpolations.

An extensive demonstration and validation study was conducted under this project to

validate the developed and adapted CFD tools. This study was performed in a systematic manner that emphasized validating the basic capabilities of the tools on simple benchmark problems first, and then validating the tools for actual seat and occupant, and seat and aircraft configurations. CFD-ACE was validated for several benchmark blunt body problems including cylinder, half cylinder and sphere problems. CFD ACE was also validate using seat/occupant geometries that included the NACES and ACES-II seat and occupants. An extensive CFD-ACE validation was also conducted using the B-1A escape capsule. CFD predictions were compared to wind tunnel test data for the ACES-II seat and B-1A escape capsule. Excellent agreement was obtained for most of the problems. For the majority of test cases, the CFD predictions were within 5-10 percent of the wind tunnel test data.

CFD-FASTRAN was also validated on an ACES-II and occupant configuration and ACES-II in proximity to F-16 configuration. CFD-FASTRAN predictions compared very well to test data for most of the calculations. Several other demonstration studies including unsteady seat separation from the aircraft were successful as correct and expected flow patterns were predicted.

In summary all the objectives of this SBIR study were accomplished. The CFD tools have already been used in several Phase III efforts for ejection seat design and qualification purposes. Most of the CFD tools have already been delivered to the Navy and are being used by Navy engineers for solving ejection seat and occupant aerodynamics problems.

CFDRC plans to continue various Phase III applications under different non-SBIR contracts from Navy and Industry. Last but not least, the developed tools and experience are also of considerable value in the commercialization of CFDRC software including geometry modelor and grid generator (CFD-GEOM), CFD flow solvers (CFD-ACE and CFD-FASTRAN) and flow visualization software (CFD-VIEW).

## NOMENCLATURE

$a_\infty$	Free-stream speed of sound.
$d$	Model reference length equivalent to the diameter of a circle with area equal to $S$ .
CA	Axial-force coefficient, body axis system, positive downstream, $FA/QS$ .
CN	Normal-force coefficient, body axis system, positive up, $FN/QS$ .
$C_Y$	Side-force coefficient, body axis system, positive nose right, $FY/QS$ .
CML looking	Rolling-moment coefficient, body axis system, positive clockwise upstream, $ML/QS_d$ .
CMM MM/QSd.	Pitching-moment coefficient, body axis system, positive nose up, $MM/QS_d$ .
CMN MN/QSd.	Yawing-moment coefficient, body axis system, positive nose right, $MN/QS_d$ .
CX	$-CA$
CZ	$-CN$
FA	Axial-force, body axis system, positive downstream.
FN	Normal-force, body axis system, positive up.
FX	$-FA$
FY	Side-force, body axis system, positive nose right.
FZ	$-FN$
Mach, $M_\infty$	Free-Stream Mach Number, $U_\infty/a_\infty$ .
ML upstream.	Rolling-moment, body axis system, positive clockwise looking upstream.
MM	Pitching-moment, body axis system, positive nose up.

## NOMENCLATURE (continued)

MN	Yawing-moment, body axis system, positive nose right.
PSA	Static pressure, crewman abdomen.
PSC	Static pressure, crewman chest.
PSH	Static pressure, crewman head.
PSLL	Static pressure, crewman left leg.
PSLR	Static pressure, crewman right leg.
PSSBR	Static pressure, seat back reference.
Q	Free-Stream dynamic pressure.
Re <sub>∞</sub>	Free-stream Reynolds number, $p_{\infty}V_{\infty}d/\mu_{\infty}$ .
S	Model reference area equivalent to the projected frontal area fo the seat and occupant.
α	Angle of attack, $\tan^{-1} w/u$ .
β	Angle of sideslip, $\sin^{-1} v/V_{\infty}$ .
V <sub>∞</sub>	Free-stream velocity, m/s.
μ <sub>∞</sub>	Free-stream viscosity, kg/ms.
p <sub>∞</sub>	Free-stream density, kg/m <sup>3</sup> .

## TABLE OF CONTENTS

	<u>Page</u>
FORWARD	i
SUMMARY	iii
NOMENCLATURE	v
1. INTRODUCTION	1
1.1 Background	1
1.2 Objectives of Phase I Study	2
1.3 Accomplishments of Phase I Study	2
1.4 Objectives of Phase II Study	3
1.5 Accomplishments of Phase II Study	4
1.6 Outline of Remainder of This Report	6
2. COMPUTATIONAL METHODOLOGY DEVELOPMENT AND ADAPTATION FOR SEAT AND OCCUPANT ANALYSIS	7
2.1 Geometry Modeling	7
2.1.1 Geometry Modeling Tools	7
2.1.2 Overview of CFD-GEOM	10
2.1.3 Geometry Modeling Procedure for NACES	11
2.2 Grid Generation	12
2.2.1 Grid Generation Procedure	16
2.2.2 Elliptic Grid Generation	16
2.3 CFD-ACE Flow Solver Adaptations	21
2.3.1 CFD-ACE Overview	21
2.3.2 Numerical Schemes Assessment for Blunt Body Flows	22
2.3.3 Turbulence Modeling Assessment for Blunt Body Flows	23
2.3.4 Grid Adaptation for Moving Seat Analysis	27
2.3.5 Force and Moment Integration Module	27
2.4 Flow Visualization	31
3. CFD TOOLS ASSESSMENT AND VALIDATION FOR SEAT/ OCCUPANT USING SIMPLE GEOMETRIES	32
3.1 Flow Over a Cylinder	33
3.2 M=0.177 Results	36
3.3 M=0.74 Results	44
3.5 M=2.0 Results	48
3.2 Flow Over a Half Cylinder	53
3.3 Flow Over a Sphere	57
3.4 Conclusions from Assessment/Validation Study	60

## TABLE OF CONTENTS (continued)

	<u>Page</u>
4. CFD TOOLS VALIDATION AND DEMONSTRATION FOR ESCAPE SYSTEMS	62
4.1 Ejection Seat and Occupant Validations	62
4.1.1 NACES Seat	62
4.1.2 ACES-II Seat	63
4.2 B-1A Escape Capsule Demonstration and Validation	78
4.3 ACES-II with Mounted Propulsion System Demonstration	92
4.3.1 Geometry and Grid	92
5. UNSTEADY SEAT/OCCUPANT FLOW ASSESSMENT AND SIMULATIONS	102
5.1 Cylinder Simulations	102
5.2 2-D Ejection Seat Simulations	106
5.2.1 Steady State Calculation	107
5.2.2 Unsteady Calculations/Fixed Seat	108
5.2.3 Unsteady Calculations/Rotating Seat	110
5.3 3-D Ejection Seat	113
5.4 Conclusions from Unsteady Simulations	116
6. SEAT/AIRCRAFT TECHNOLOGY EVALUATION AND SELECTION	117
6.1 Overview of Seat/Aircraft Modeling Issues	117
6.2 Summary and Outcome of CFD code Selection Process	118
6.3 CFD Codes Evaluation	120
6.3.1 Flow Over a Cube	120
6.3.2 Flow Over a Cylinder	124
6.3.3 ACES-II Simulations	132
7. CFD-FASTRAN DEVELOPMENT AND ADAPTATION FOR MULTIPLE AND MOVING BODIES	138
7.1 Overset-Hybrid Methodology	138
7.2 Traditional Chimera Methodology	146
7.2.1 Chimera Adaptation for Moving Body Problems	151
8. CFD-FASTRAN DEMONSTRATION AND VALIDATION FOR SEAT/AIRCRAFT CALCULATIONS	159
8.1 Discussion of F-16 and ACES-II Wind Tunnel Test	159
8.2 OVERFLOW Demonstration Calculations	162
8.2.1 OVERFLOW Grids	162
8.2.2 OVERFLOW Simulations	166
8.3 Steady-State CFD-FASTRAN Analysis	169
8.3.1 Geometric Modeling and Grid Generation	169
8.3.2 Steady-State CFD-FASTRAN Simulations	173

## TABLE OF CONTENTS (continued)

	<u>Page</u>
8.3.3 Comparisons to Wind Tunnel Data	177
8.4 Transient CFD-FASTRAN Analysis	181
8.4.1 Application of Chimera to Moving Bodies	181
8.4.2 Seat and Aircraft Simulations	181
9. CONCLUSIONS AND RECOMMENDATIONS	186
9.1 Conclusions from Phase I and Phase II Studies	186
9.2 Commercialization Status and Phase III Potential	187
10. REFERENCES	189
Appendix A. Project Related Technical Conference Publications	A-1
Appendix B. Selected Brochures of CFD Tools	B-1

# COMPUTATIONAL AERODYNAMIC ANALYSIS OF THE NAVY AIRCREW COMMON EJECTION SEAT

by

S.D. Habchi\*, S.Y. Ho\*\*, and G.S. Hufford\*\*

CFD Research Corporation

Huntsville, AL 35805

and

T. Marquette† and P. Ayoub†

Naval Air Warfare Center - Aircraft Division

Warminster, PA 18974

## ABSTRACT

A numerical investigation using CFD techniques was conducted to study the aerodynamic characteristics of the Navy Aircrew Common Ejection Seat and occupant. In addition to the aerodynamic characteristics, a seat stabilization fins concept and Pitot sensing system were analyzed. This paper presents results of the investigation which was conducted for Mach numbers of 0.75, 1.2, 1.5, and 2.0, at angles of attack from 0 to 45 degrees and angle of sideslip from 0 to 30 degrees. A 3D Reynolds-averaged Navier-Stokes code with k- $\epsilon$  turbulence model was used to solve the turbulent compressible flow field around the seat and occupant. CAD and elliptic grid generation tools were used to generate the surface mesh and baseline grid while algebraic adjustment functions were used to orient the grid for other pitch and yaw orientations. The results are presented in the form of force and moment coefficients and are compared to wind tunnel test data of other seats. Surface contours and vector plots are presented to highlight the details of the flowfield.

## INTRODUCTION

For many years, wind tunnel testing and sled experiments have been used to study the aerodynamic characteristics of the fighter aircraft ejection seat.<sup>1-3</sup> Wind tunnel tests have been used for static analysis to analyze various

design concepts to improve the performance envelope of the ejection seat and to develop ways to protect the ejecting pilot.<sup>4-6</sup> Sled experiments have been used for dynamic testing to achieve the same goal. Even though these methods have limitations that are usually associated with high speed flow testing, they have been reliable. However, these methods can be very expensive and limit the number of concepts and conditions to be analyzed. Due to the unexpected nature of the ejection process, the trajectory and orientation of the seat after clearing the aircraft are unpredictable. Previous wind tunnel tests show that the forces exerted on the pilot are highly dependent on the orientation of the seat. Therefore, during the seat analysis process, many seat orientations must be simulated which is very costly using the traditional experimental methods.

During the last few years, numerical methods have been used to study the ejection seat problem. Caruso and Mendenhall<sup>7</sup> conducted a two-dimensional analysis using thin-layer Navier-Stokes methods to demonstrate the use of CFD techniques for the ejection seat problem. Wurtzler<sup>8</sup> used steady state Euler methods to simulate the B-1A escape capsule flow. Baum and Lohner<sup>9</sup> coupled a rigid body motion solver to an unsteady Euler method to study transient effects of pilot ejection. Habchi *et al*<sup>10</sup> conducted a preliminary three-dimensional analysis using

\*Group Leader/Research, Member AIAA

\*\*Project Engineer, Member AIAA

†Member AIAA

Navier-Stokes methods of ejection seat escape systems. Caruso and Mendenhall compared their 2D computations to 3D experimental results and obtained a reasonable comparison at one pitch and yaw orientation. However, the 2D to 3D correction is questionable at best and cannot be applied when the seat is yawed. Wurtzler compared his 3D results to experiment and found discrepancies that he concluded were due to viscous effects that were not modeled. Baum and Lohner did not calculate aerodynamic coefficients and made no comparison to wind tunnel data. Habchi *et al* studied only two seat orientations and used a simplified seat geometry.

This paper presents the results of a three-dimensional computational analysis of the Navy Aircrew Common Ejection Seat (NACES) using a full Navier-Stokes flow solver with  $k-\epsilon$  turbulence model. The complicated 3D geometry modeling and grid generation were accomplished using state-of-the-art CAD tools and standard elliptic grid generation methods. The aerodynamic characteristics of the Navy seat were investigated at Mach numbers ranging from 0.75 to 2.0 at angles of attack from 0 to 45 degrees and angles of sideslip from 0 to 30 degrees. In addition, the effectiveness of a seat stabilization concept that utilizes deployable fins is assessed and a generic ejection seat Pitot sensing system has been investigated. The results presented in this paper were obtained on a workstation (IBM/R6000) with reasonable amount of human effort and modest computational requirements.

This paper briefly discusses the numerical method and explains the geometric modeling and grid generation process. The results are presented and discussed and wherever possible compared to wind tunnel data.

#### Geometry Modeling and Grid Generation

For a complex geometry such as the ejection seat and occupant, surface definition and grid generation issues are very important for the overall success of the CFD analysis. Under this study, efforts were made to preserve the geometric integrity of the seat and occupant using CAD tools. Custom grid generation tools were

developed to produce an economical method to conduct a parametric study of this magnitude.

The CAD based grid generation package, ICEM-CFD<sup>11</sup>, was used to model the surface of the seat and occupant and to create a structured surface mesh. The surface was defined based on CAD definition of the Navy seat and occupant that was ported to ICEM-CFD through an IGES formatted file. Therefore, the modeled surface is based on the actual design of the seat and a CAD defined occupant. Figures 1 and 2 show the CAD wireframe, the shaded surface and mesh surface used for the present calculations. The full scale seat and occupant surface grid used for the parametric analysis has, on average, a resolution along the surface of 1.25 inches and a total of approximately 4000 cells (cells on modeled surface).

An H-type baseline (zero degree sideslip, zero degree pitch) computational grid was created using a three-dimensional elliptic grid generator, developed for this analysis. The elliptic grid generator uses line and orthogonal attraction through Poisson forcing functions near the boundaries and near the seat surface. The line and orthogonal attraction functions are used to cluster the grid and ensure orthogonality near the surface. For this analysis a total of 440,000 cells were used most of which are located in the immediate surrounding of the seat and occupant. The computational domain extended 2 body lengths above, 2 below, 3.75 behind, 2 in front of, and 1.6 to the side of the seat.

Algebraic geometric functions that use Transfinite Interpolation (TFI) methods were used to manipulate the baseline orientation grid for different pitch and yaw orientations. These functions adapt the elliptic grid for the new orientation while preserving its smoothness and orthogonality. Figure 3 shows 3 different pitch and yaw orientation grids created using the algebraic functions. The reason for using the algebraic functions rather than solving the grid elliptically for each new orientation is strictly economical. The CPU time needed to generate the elliptic baseline grid is on the order of 3000 seconds on the IBM/R6000 machine while the time involved in adapting the baseline grid for

different orientations is on the order of few seconds.

## NUMERICAL APPROACH

The blunt body shape of the ejection seat and occupant at high Reynolds number results in highly turbulent flows around the seat and in the wake behind the seat. To accurately predict the flow field and especially in the wake region, the full Navier-Stokes equation has to be solved. Further, at transonic and supersonic speeds, multiple shocks will form around and on the seat surface changing the flow field characteristics. To accurately predict the locality of these shocks and their effect on its aerodynamic behavior, a high order numerical shock capturing scheme that possesses good shock capturing capabilities has to be utilized.

The CFD code used for the present analysis (CFD-ACE<sup>12</sup>) solves the full Navier-Stokes equations in general curvilinear coordinate system. The code employs structured grid techniques and is based on a finite volume pressure-based approach that uses a colocated grid arrangement of flow variables. The code is based on a strongly conservative formulation<sup>13</sup> for the N-S equations which preserve free stream properties and possesses good shock capturing capability. The flow variables are solved sequentially using a modified version of Stone's solver.<sup>14</sup> The code also employs high order differencing schemes including central differencing, Osher-Chakravarthy, second-order upwind in addition to the first-order upwind scheme. For the present calculations the second order upwind scheme was used for most of the subsonic free stream cases while the third order Osher-Chakravarthy scheme was used for most of the supersonic free stream cases.

A standard k- $\epsilon$  turbulence model was used for this analysis to model and capture the viscous effects associated with the wake and the surface of the seat and occupant. The k- $\epsilon$  turbulence model has been proven to capture the correct pressure fields for separated and recirculating type flows.<sup>15</sup> The grid resolution in front and to the side of the seat will probably not allow accurate shear force calculations. However for blunt bodied flows of

this type at high Reynolds numbers the majority of the force is from the pressure loads. Also flow separation will occur due to the sharp edges of the seat and not due to any boundary layer generation. Thus, the primary purpose of the k- $\epsilon$  model is to accurately predict the base pressures behind the seat and the correct flow field inside the wake and in the seat surroundings.

## COMPUTATIONAL RESULTS

To understand the aerodynamic behavior of an ejection seat configuration at all ejection conditions, computations were performed for all flow regimes (subsonic, transonic, and supersonic) at angles of attack from 0 to 60 degrees and angles of sideslip from 0 to 30 degrees. The free stream conditions used for the calculations are:

1. Speed = 408 KEAS,  $M = 0.75$ , 9,600 feet;
2. Speed = 700 KEAS,  $M = 1.2$ , 6,000 feet;
3. Speed = 730 KEAS,  $M = 1.5$ , 15,000 feet;
4. Speed = 640 KEAS,  $M = 2.0$ , 35,000 feet;

where KEAS is Knots Equivalent Air Speed.

The size of the computational grid for these analyses is 220,000 nodes for the symmetric (zero degree sideslip) cases and 440,000 nodes for the full geometry.

### Data Reduction

The standardized body axis systems shown in Figure 4 was used for the calculations of the aerodynamic coefficient. This coordinate system origin is at the Seat Reference Point (SRP) of the ejection seat about which the moment coefficients are calculated. The seat reference point lies in the plane of aerodynamic symmetry at the intersection of the seat back and lower seating area.

The force and moment coefficients computed below are non-dimensional using the seat reference area,  $S$ , and the seat reference length,  $D$ . The seat reference area is defined as the projected frontal area of the seat and occupant at zero degree sideslip and pitch and was calculated to be  $7.4 \text{ ft}^2$  for the NACES seat. The seat reference length,  $D$ , is defined as the diameter of

a circle whose area is equal to the seat reference area ( $D = \sqrt{\pi S}$ ) and was calculated to be 36 inches.

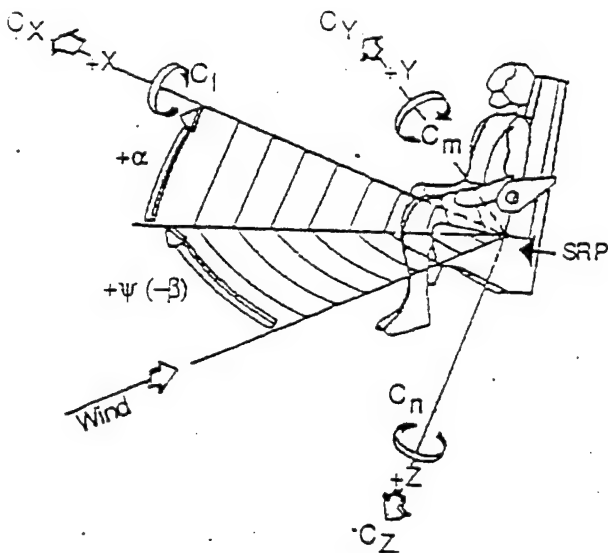


Figure 4. Standard Body-Axis System

The force coefficient in a specific direction ( $i = x, y, z$ ) and the moment coefficient about the seat reference point were calculated as follows:

$$C_{F_i} = \frac{F_i}{QS} \quad (1)$$

where  $F_i$  is the total force in the  $i$  direction

$$C_{M_i} = \frac{M_i}{QSD} \quad (2)$$

where  $Q$  is the free stream dynamic pressure ( $1/2 \rho_\infty U_\infty^2$ ) and  $S$  and  $D$  are the reference area and length, and  $M_i$  is the moment in the  $i$  direction.

The total force in the  $x$ ,  $y$ , and  $z$  direction on a surface cell is integrated as follows:

$$f_i = \int_{cell} P \cdot \hat{n}_i dA + \int_{cell} \tau_s \hat{t}_i dA \quad (3)$$

where  $\hat{n}_i$  is the component of the unit normal in the  $i$  direction,  $\hat{t}_i$  is the component of the unit

tangential in the  $i$  direction, and  $\tau_s$  is the shear stress contributing to skin friction.

The total force on the body is the summation of the forces on each surface cell.

$$F_i = \sum_{j=1}^n (f_i)_j \quad (4)$$

where  $i$  denotes the ( $x$ ,  $y$  or  $z$ ) direction and  $n$  denotes the total number of computational cells on the modeled surface of the seat and occupant.

The pitching moment ( $M_m$ ), yawing moment ( $M_n$ ) and rolling moment ( $M_l$ ) are calculated as follows:

$$M_m = \sum_{k=1}^n (M_{m_i})_k \quad \text{where} \quad M_{m_i} = \int_{cell} F_x dz + F_z dx \quad (5a)$$

$$M_n = \sum_{k=1}^n (M_{n_i})_k \quad \text{where} \quad M_{n_i} = \int_{cell} F_x dy + F_y dx \quad (5b)$$

$$M_l = \sum_{k=1}^n (M_{l_i})_k \quad \text{where} \quad M_{l_i} = \int_{cell} F_z dy + F_y dz \quad (5c)$$

where  $dx$ ,  $dy$ , and  $dz$  are the distances from the SRP, and  $n$  is the total number of surface cells.

The above force and moment coefficients are calculated in a fixed coordinate system in space (corresponding to 0 degree pitch and 0 degree sideslip). To get these coefficients in the standardized body-axis system, which rotates with the seat, shown in Figure 4, two rotation matrices were used, one for pitch and one for sideslip.

#### Seat Aerodynamic Characteristics

The aerodynamic coefficients of the NACES seat were calculated for each orientation as described above. These coefficients are presented in Figures 5 and 6 and compared to wind tunnel test data of three other seats (F-106<sup>1</sup>, ACES-II<sup>2</sup>, and CREST seat<sup>3</sup>). Some of the experimental data for the other seats were interpolated for direct comparison to the computations at the given Mach numbers and seat orientations. Note that

there are no wind tunnel aerodynamic coefficient data available for the NACES seat for direct comparison. However, efforts are presently underway to model the ACES-II seat for direct validation of the CFD model.

Figure 5 presents the longitudinal aerodynamic characteristics of the seats where the axial force coefficient ( $C_x$ ), the normal coefficient ( $C_z$ ), and the pitching moment coefficient ( $C_m$ ) are plotted versus angle of attack at  $M = 0.75$  and  $1.2$  free stream conditions. This figure shows that the trends of the computed NACES results are very similar to the other three seats experimental results, especially the ACES-II and F-106 results.  $C_x$  and  $C_z$  compare very well with the other seats results at all pitch orientations. The magnitude and trends of  $C_m$  are also similar between the NACES computed results and the ACES-II and F-106 results. However, the CREST pitching moment coefficients seem to be much higher than the other three seats. Figure 6 presents the side force coefficient ( $C_y$ ) along with the yawing moment coefficient ( $C_n$ ) and the rolling moment coefficient ( $C_l$ ) versus angle of sideslip ( $\psi$  and  $-\beta$ ) for the same flow conditions. Once again, the trends are very similar between the computed NACES results and the experimental results.  $C_y$  compares very well with the other two seats, while  $C_z$  of the NACES seat seems to be increasing at a faster rate as the sideslip angle increases.

Exact comparisons between all the seats can not be made due to the different geometry and characteristics of each seat. The differences can be attributed to the occupant size, SRP location, and projected frontal area. However, these results show that the CFD model predicts results that have the same trends and similar magnitude of other seats experimental results. In fact, most of the coefficients compare very well between NACES and other seats considering the differences cited above. In addition, the differences between the NACES computed coefficients and the wind tunnel coefficients of the other seats do not seem to be higher than the difference between the other seats' coefficients.

Figure 7 shows the static pressure loads on the surface of the seat and occupant at different pitch and sideslip angles. At the baseline ( $\alpha = 0$ ,  $\beta = 0$ ) orientation, the high pressure zones are located on the neck, abdomen, and knees of the occupant. At this orientation, the projected frontal area is the maximum, therefore resulting in the maximum axial force coefficients (Figure 5). As the pitch angle increases, the high pressure zones shift toward the lower part of the occupant and the seat bottom. The increase causes the projected frontal area to decrease resulting in a monotonic decrease of  $C_x$  as shown in Figure 5.

As the sideslip angle increases, the high pressure zones shift toward the front side of the seat resulting in an increase of the side force and yawing moment coefficients. At high speed ejections, the occupant is most vulnerable to these side loads as he can withstand approximately 35 "g" loads along his front and only 15 "g" loads along his sides.<sup>16</sup>

The pressure loads distribution is very similar for the other 3 high Mach number flow conditions considered. However, the static pressure on the surface of the seat increases at the transonic and supersonic speeds as a result of the bow shock formed in front of the seat at those conditions. Figure 9 shows the free stream Mach number effects on the flow around the seat. At  $M = 0.75$ , the pressure increases gradually as the flow approaches the seat with decreasing velocities and resulting in a decrease of the Mach number. The flow then accelerates past the seat and separates creating a wake and low pressure zones behind the seat. At the higher Mach numbers ( $M = 1.2$ ,  $1.5$ , and  $2.0$ ) a bow shock is located in front of the seat. The bow shock gets closer to the seat as the Mach number increases (as expected). As a result of this shock the pressure sharply increases resulting in higher pressure loads on the occupant front surface. After the shock, the flow decelerates becoming subsonic and then accelerates past the seat becoming supersonic and creating expansion fans near the front and reflected shocks near the back. As the flow separates a large wake is formed behind the seat.

### Pitot Sensing System Analysis

The flow behavior in the region of a generic Navy ejection seat Pitot sensing system was analyzed for transonic and supersonic conditions. A generic seat employs dual Pitot pressure sensors that are deployed upon ejection to supply total pressure readings. These readings are supplied to an electronic microprocessor for altitude and airspeed measurements.

Computations were performed for the Navy ejection seat with the generic Pitot tubes at various pitch and yaw orientations for Mach numbers of 0.75, 1.2, 1.5 and 2.0. The Pitot tubes were not geometrically modeled to conserve computational requirements. The intent of this study is to observe and analyze the flow in the region surrounding the Pitots rather than analyzing the effects the Pitots have on the flowfield.

Figure 8 shows the total pressure in the physical plane of the Pitot tubes for  $M = 0.75$  at various pitch orientations. The small white rectangles designate the location of the Pitot tubes. This figure shows that the Pitots are located far enough from the seat to read undisturbed free stream data (as designated by the magenta color). Figure 9 shows the Mach number contours in the axial physical plane of the Pitot tubes at various free stream Mach numbers. At  $M = 0.75$ , the flow around the Pitot tubes is subsonic, however, at higher Mach numbers ( $M = 1.2, 1.5$ , and  $2.0$ ), the flow near the Pitot tubes is supersonic. Calculations at other pitch and yaw orientations showed that the Pitots remain in a supersonic region as the seat is pitched from  $0$  to  $60$  degrees. However, as the seat is yawed, the right Pitot moves closer to the subsonic zone in front of the seat (subsonic zone after bow/normal shock in front of the seat) while the left Pitot moves closer to the subsonic zone inside the wake and behind the seat.

### Stabilization Fins Analysis

Computational aerodynamic analyses have also been performed on the NACES seat with a pitch/yaw stabilization fin design. The fins are deployed upon ejection for pitch and yaw

stability. Previous wind tunnel<sup>5</sup> and CFD studies<sup>17,18</sup> on the yaw stabilization fins showed that the yaw fins improve the seat yaw stability by 30 to 50 percent. However, the same studies showed that the yaw fins produce an increase of the pitching moment. To improve the fins performance with respect to the pitching moment, a pitch fin has been attached to the yaw fin for pitching stability. This study is conducted to analyze the effect of this design on both pitching and yawing stability. The shaded modeled surface of the NACES seat with the stabilization fins deployed is shown in Figure 10.

Computations were performed for free stream Mach numbers of 0.75 and 1.2 for pitch angles of 15 to 75 degrees and sideslip angles of 0 and 15 degrees. Figures 11 through 13 show the pitching and yawing moment coefficients versus angle of pitch for both free stream conditions. Each one of these figures has four curves. The "no fin" curve represents the seat without the fins deployed. The "P+Y" curve represents the seat with the fins (yaw and pitch fins) deployed. The "P fin only" curve represents the seat with only the pitch fin deployed. The "Y fin only" represents the seat with only the yaw fin deployed. Note that the last 2 curves were obtained by ignoring the forces on the yaw and pitch fins, respectively in the moment coefficient calculations. The flowfields might be slightly different if the fins were not blocked during calculations but computer time cost dictated a comparison in this manner.

For the zero degree sideslip orientations, Figures 11 and 12, show that in general, the stabilization fins (including both pitch and yaw surfaces) result in a slight increase of the pitching moment coefficient for pitch angles less than 30 degrees. As the pitch angle increases beyond 30 degrees, the pitching moment starts decreasing quickly and the positive effects of the fins on pitching stability is accomplished. It is also observed that the increase in the pitching moment at pitch angles less than 30 degrees seem to originate from the yaw surface of the fins. The "P fin only" curve shows that the pitching moment coefficient either stays unchanged or decreases for all orientations, while the "Y fin only" shows an increase in the pitching moment coefficient for pitch angles less than 45 degrees. The reason for

the yaw surface increasing the pitching moment is due to the axial forces exerted on the fin and the fact that the fins are located above the SRP. However, at pitch angles of 45 degrees or higher, part of the fins (outer part) moves below the SRP creating a negative pitching moment for this part, which reduces the overall pitching moment of the seat.

The positive effects of the pitch surface of the fin increases as the pitch angle increases. At higher pitching angles, the pitch fins are subjected to higher pressures (due to more direct contact with incoming flow) on the lower side (see Figure 10) which creates negative pitching moment reducing the overall pitching moment coefficient. Figure 10 presents a bottom view of the seat, and shows that the static pressure on the pitch fin surface drastically increases as the pitch angle increases.

For the 15 degree sideslip orientations, the stabilization fins have similar effects on the pitching moment coefficients. However, the decrease in the pitching moment at the 30 degree or higher pitch angles does not seem to be as strong as that of the zero degree sideslip orientations discussed above. In fact, there is almost no decrease at 45 degree pitch.

Figure 12 shows that the yaw fins always result in an increase of the pitching moment at 15 degrees sideslip; while the pitch fins result in a decrease at 30 degrees pitch or higher. The overall effects of the pitch fins is also reduced at the 15 degree yaw. At 15 degree sideslip, one fin is located outside the wake encountering no upward flow; while the other is located inside the wake encountering more upward flow than a zero degree sideslip (both fins located at edge of wake).

The yawing moment coefficient decreases when the fins are deployed for all yaw orientations (see Figure 13). The decrease varies between 20 and 50 percent. The yaw fin has consistent and positive effects at all orientations as the yawing moment is reduced when the yaw fin is deployed. The pitch fin has small mixed effects. At pitch angles below 30 degrees, the yawing moment increases as a result of the pitch surfaces for  $M = 0.75$  conditions. At pitch angles of 45 degrees and

higher, the yawing moment slightly decreases as a result of the pitch fins. However, the overall effect is negligible (less than 5 percent). The yaw fins have consistent and positive effects on the yaw stability for all orientations at both speeds as seen in Figure 13. The results show that at non-zero sideslip orientation, one of the yaw fins encounters high surface pressure loads. These pressure loads result in a decrease of the yawing moment due to their location behind the SRP.

Figures 11 through 13 show that the stabilization fins have very similar effects on the seat stability at both the  $M = 0.75$  and  $M = 1.2$  speeds considered under this study. However, in general, the fins have slightly more positive effects under the  $M = 0.75$  test conditions.

## SUMMARY AND CONCLUSIONS

Numerical investigations using advanced CAD and grid generation tools with 3D Navier Stokes code have been conducted to study the aerodynamic characteristics of a Navy ejection seat. An ejection seat Pitot sensing system and a stabilization fin design have been analyzed. This paper presented the results of the computations for different flow speeds at various seat pitch and yaw orientations.

The computed aerodynamic coefficients of the NACES seat were compared to experimental coefficients of other seats. The computed NACES results agree favorably with the other seats where similar trends were observed at various flow conditions and seat orientations.

The results of the Pitot sensing system analysis showed that at subsonic free stream conditions, the Pitot tubes are located in a subsonic zone far enough from the seat to read undisturbed airflow data. At transonic and supersonic free stream conditions, the flow around the Pitots is supersonic at most seat analyzed orientations. The stabilization fin results showed that the fins enhance yaw stability for all orientations considered and improve pitching stability at angles of pitch of 30 degrees or higher.

The results of this computational analysis, including comparison to wind tunnel test data,

demonstrate the feasibility and effectiveness of using CFD techniques for ejection seat analysis.

#### ACKNOWLEDGEMENTS

This research has been funded by the Naval Air Warfare Center, Aircraft Division, Warminster under the sponsorship of Mr. F. Terry Thomasson, Naval Air Systems Command AIR-531. The authors would like to thank Dr. Andrzej Przekwas and Dr. Ashok Singhal of CFD Research Corporation for their technical suggestions and support throughout this work, and Ms. J. Swann for her preparation of the manuscript.

#### REFERENCES

1. White, B.J., "Aeromechanical Properties of Ejection Seat Escape Systems," AFFDL-TR-74-57 (AD787194, April 1974).
2. Reichenau, D.E., "Aerodynamic Characteristics of a Full Scale ACES-II Ejection Seat with a Small Female or Large Male Manikan at Mach Numbers from 0.2 to 1.4," AEDC-TR-87-16, 1987.
3. Reichenau, D.E., "Aerodynamic Characteristics of a Half-Scale CREST Seat at Mach Numbers from 0.6 to 3.0," AEDC-TR-88-6, 1988.
4. Lundy, T.E., and Braddock, W.F., "Wind Tunnel Tests of the Flow Stagnation Protective Concept and Ejection Seat Stability Devices," AAMRL-TR-85-053, 1987.
5. Ayoub, P., and Yost, P., "Wind Tunnel Tests of a 0.65 Scale Ejection Seat with and without Yaw Stabilizers," NADC-84093-60, April 1984.
6. Hawkins, K.F., "Boeing Wind Tunnel Tests of the NACES Pitot-Static Sensors and Sequencers Unit," Contract No. N00019-85-C-0143, CDRL Item A003, Feb. 1987.
7. Caruso, S.C., and Mendenhall, M.R., "Computational Analysis of High Speed Ejection Seats," AIAA-90-0403, Jan. 1990.
8. Wurtzler, K., "Application of an Euler Code to the B-1A Escape Capsule," AIAA-90-0431, Jan. 1990.
9. Baum, J.D., and Lohner, R., "Numerical Simulation of Pilot/Seat Ejection from an F-16," AIAA-93-0783, 1993.
10. Habchi, S.D., *et al*, "CFD Analysis of Ejection Seat Escape Systems," SAE paper 921924, Aerotech 92 Meeting, 1992.
11. Bertin, D., Lordon, J., and Morcaux, V., "A New Automatic Grid Generation Environment for CFD Applications," Aerospatiale, 1992.
12. CFD Research Corporation, "CFD-ACE: Theory Manual," Version 1.0, CFDRC Report GR-93-1, September 1993.
13. Yang, H.Q., Habchi, S.D., and Przekwas, A.J., "A General Strong Conservation Formulation of Navier-Stokes Equations in Non-Orthogonal Curvilinear Coordinates," AIAA-92-0187, Jan. 1992.
14. Stone, H.L., "Iterative Solution of Implicit Approximation of Multi-Dimensional Partial Differential Equations," *SIAM J. Num. Annual*, vol. 5, 1968.
15. Rubesin, M.W., "Turbulence Modeling for Aerodynamic Flow," AIAA-89-0606, Jan. 1989.
16. Reichenau, D.E. and White, B.J., "Aerodynamic Characteristics of the ACES-II Ejection Seat at Transonic Mach Numbers," *SAFE Journal*, 1987.
17. Habchi, S.D. and Przekwas, A.J., "CFD Analysis of NACES Seat With Yaw Fins," Final Report for NADC, CFDRC Report 4127/1, December 1991.
18. Habchi, S.D., Hufford, G.S., and Przekwas, A.J., "CFD Analysis of NACES Seat with Yaw Fins Deployed at 60° Sweepback Angle," CFDRC Report 4129/1 for NAWC-A/D, August 1992.

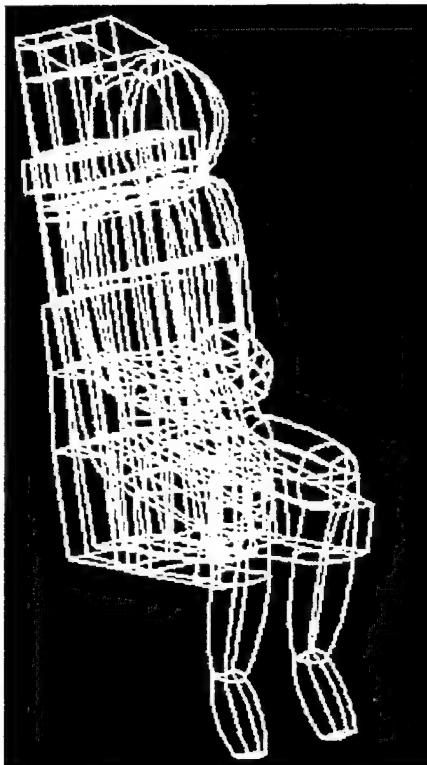


Figure 1. Wireframe of CAD model.

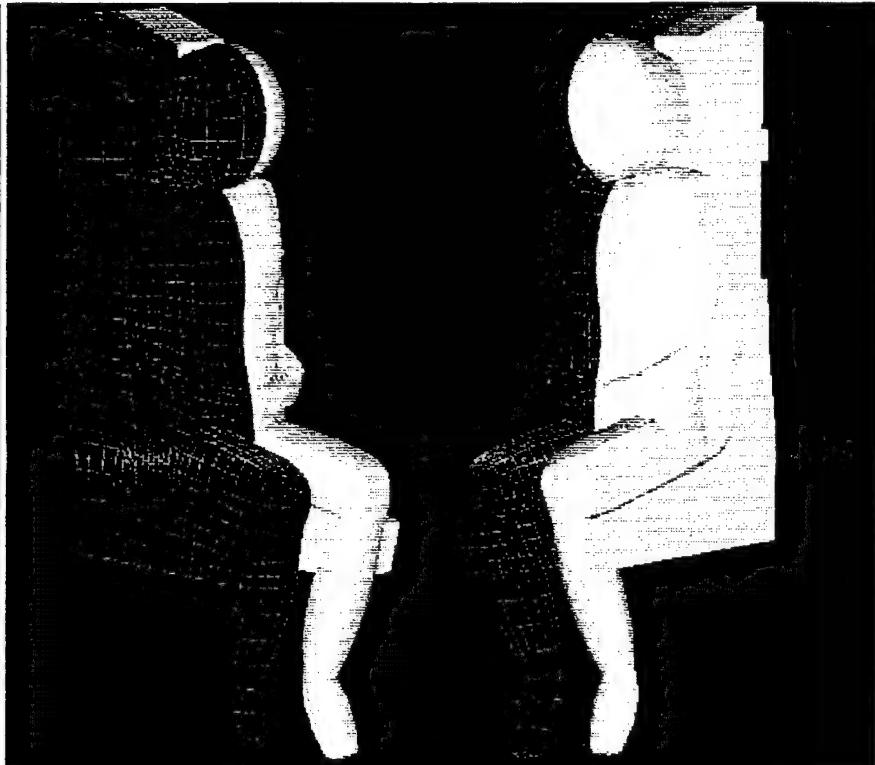


Figure 2. Surface mesh and shaded surface of CFD model.

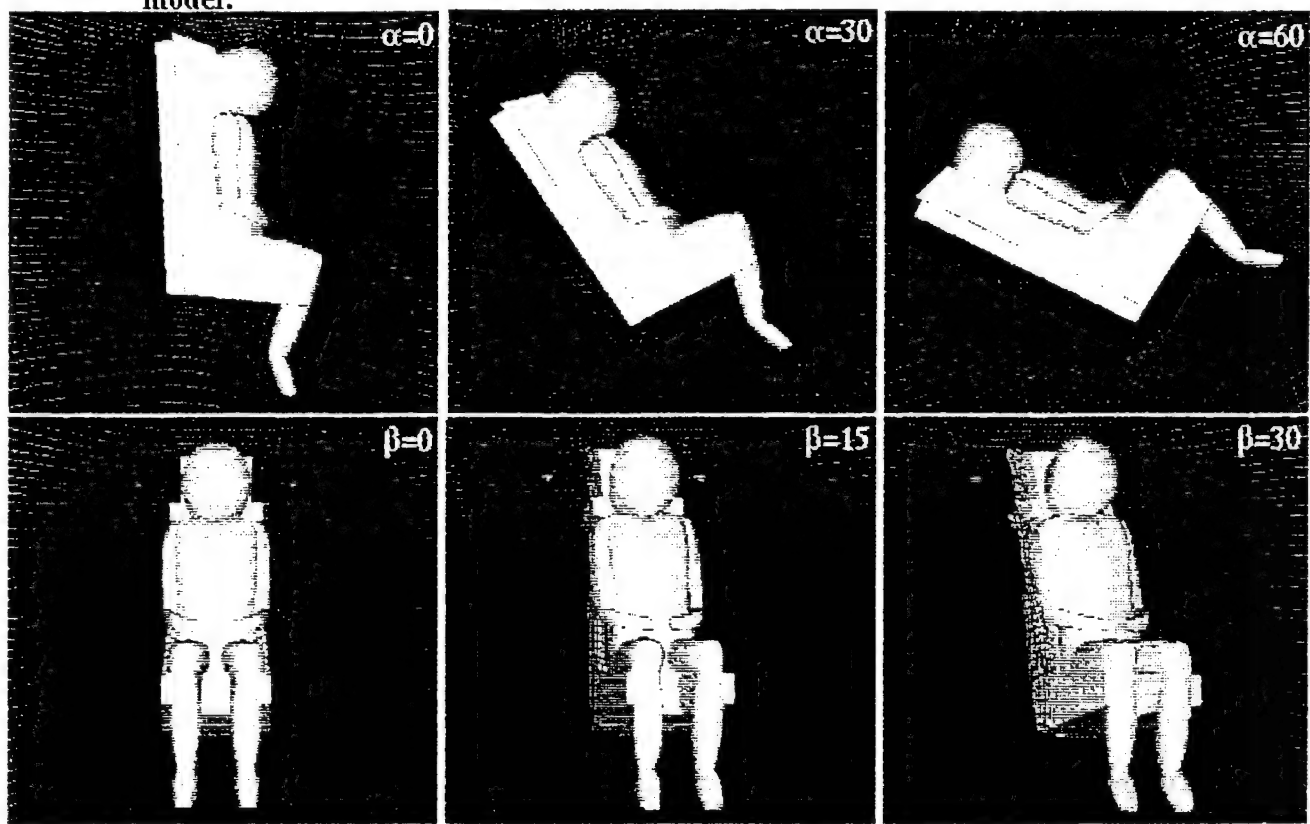
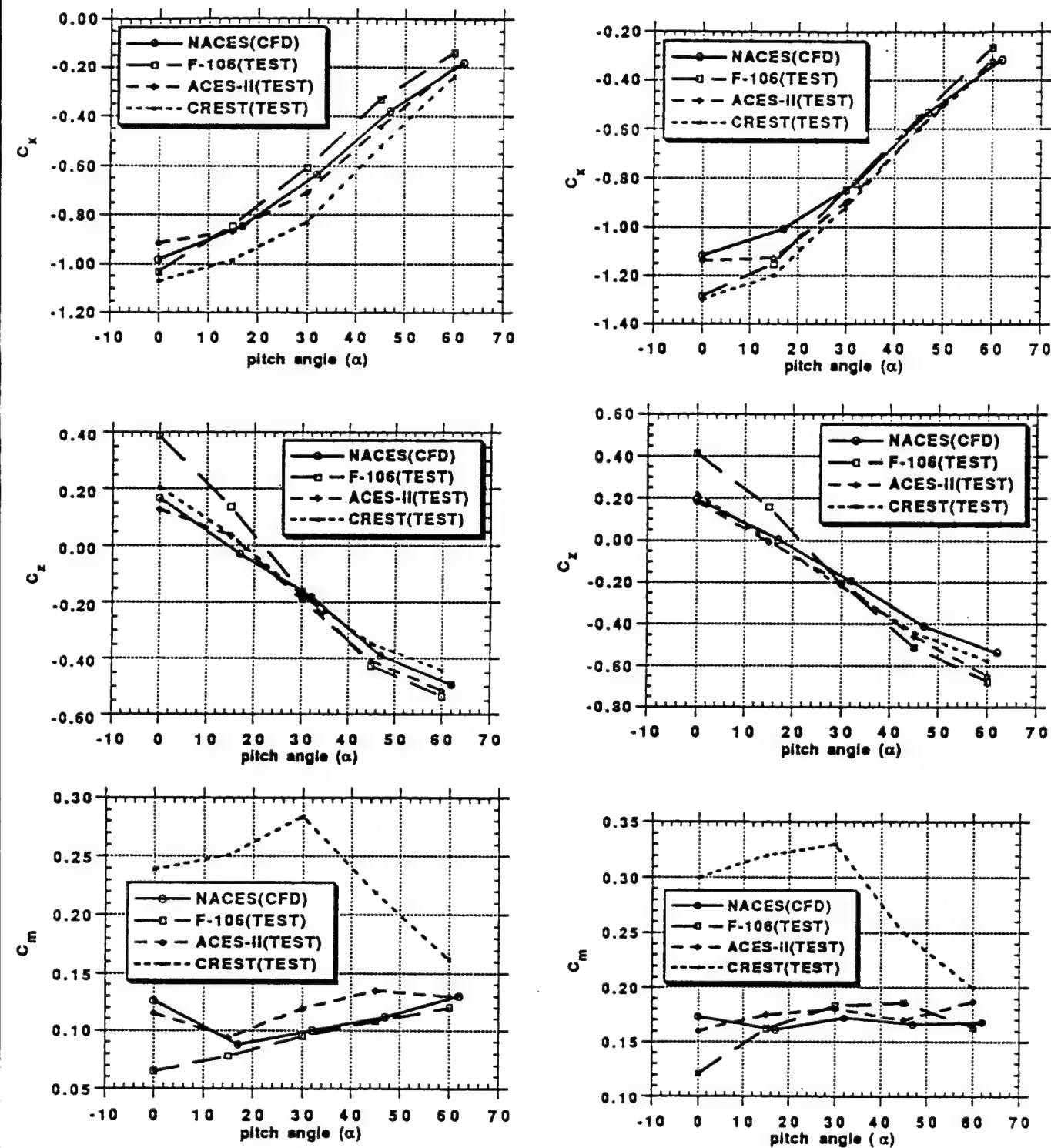


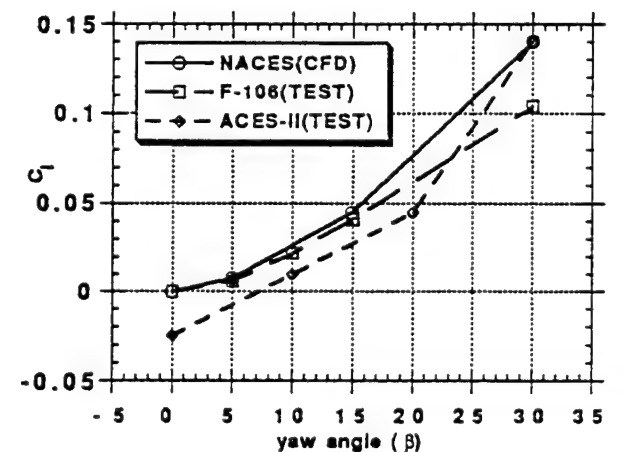
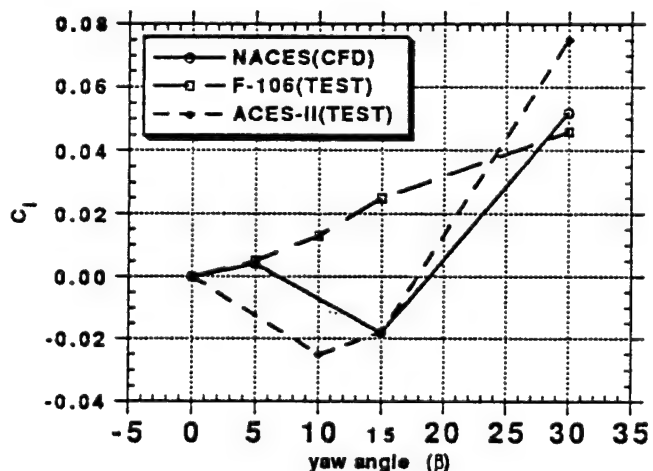
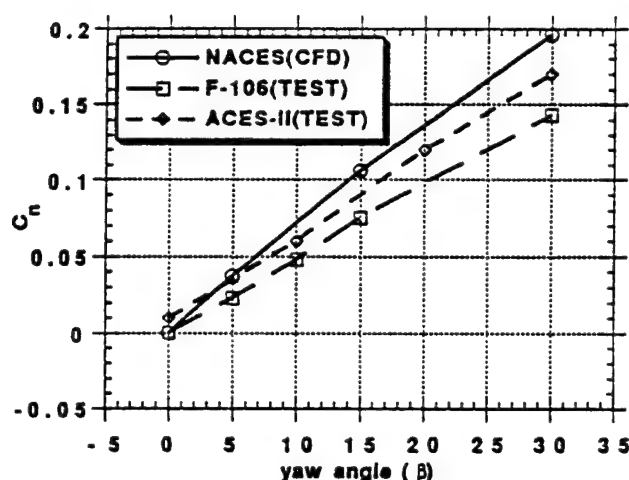
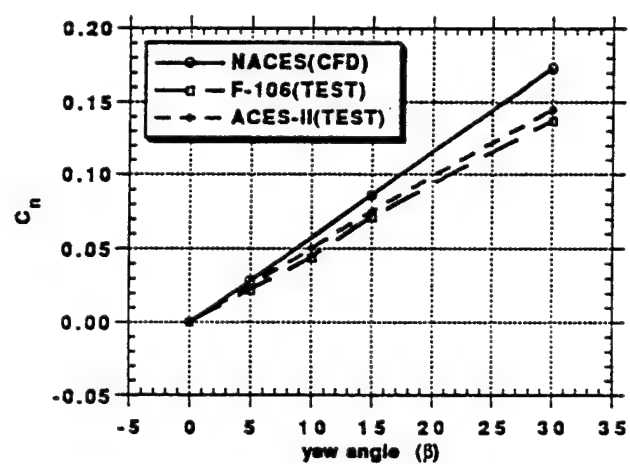
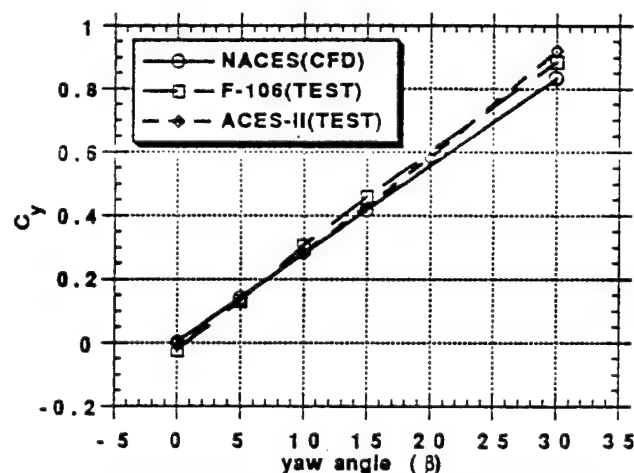
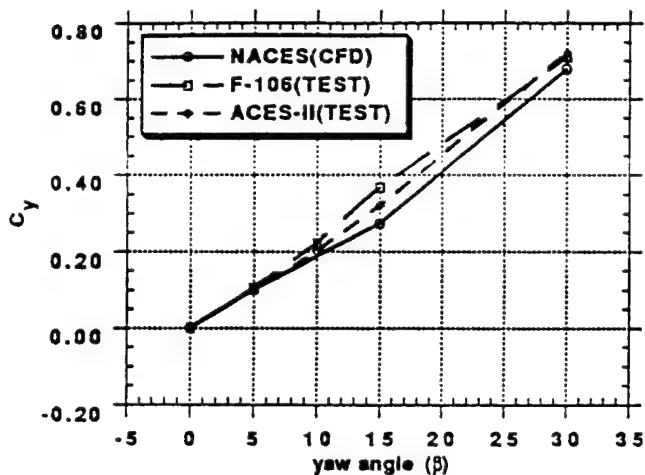
Figure 3. Computational grid adjusted for different pitch ( $\alpha$ ) and sideslip ( $\beta$ ) orientations.



$M = 0.75$

$M = 1.2$

Figure 5. Predicted and Experimental Aerodynamic Coefficients Versus Pitch Angle for Various Ejection Seats;  $\beta = 0$



$M = 0.75$

$M = 1.2$

Figure 6. Predicted and Experimental Aerodynamic Coefficients Versus Sideslip Angle for Various Ejection Seats;  $\alpha = 17$

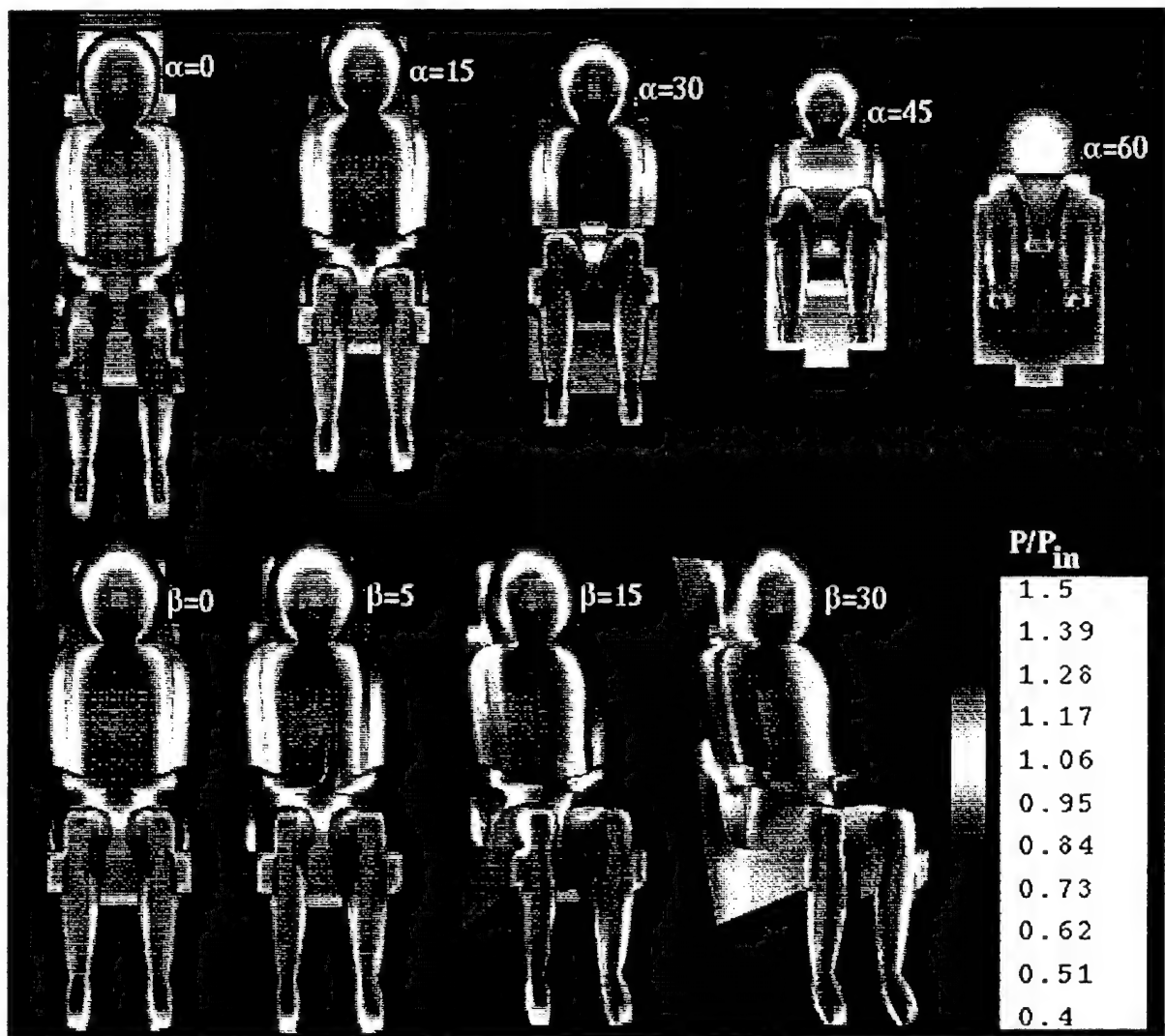


Figure 7. Seat/Occupant surface static pressure for various pitch and yaw orientations;  $M=.75$

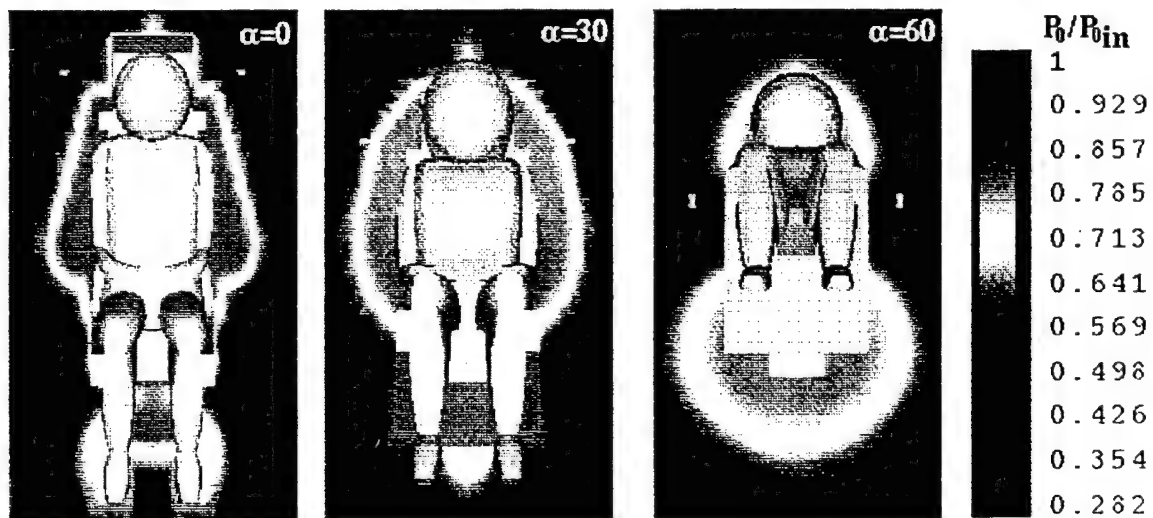


Figure 8. Total pressure in physical plane of Pitot tubes for various pitch angles;  $M=.75$

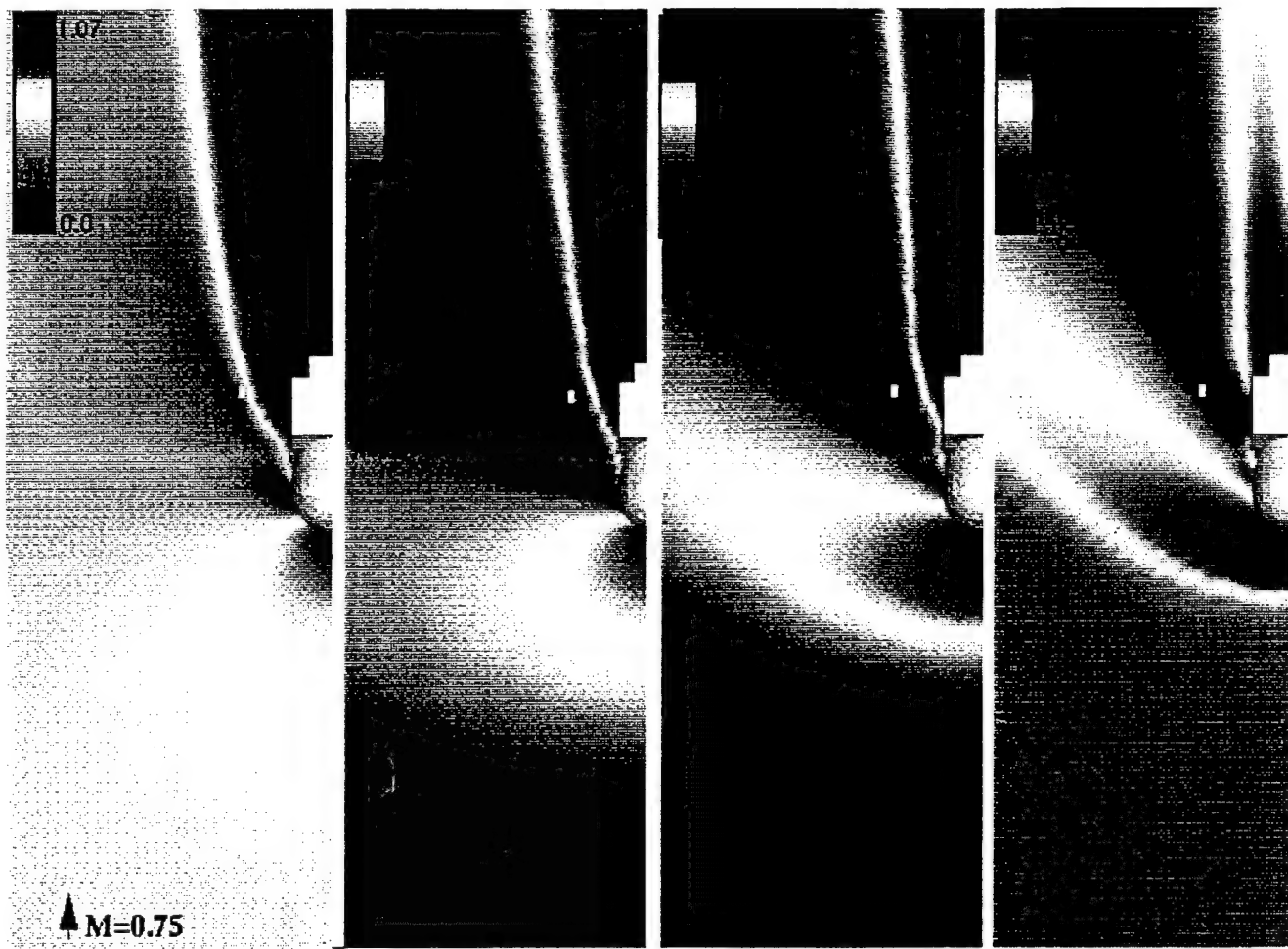


Figure 9. Mach number contours in the physical plane of the Pitots for different inlet conditions.

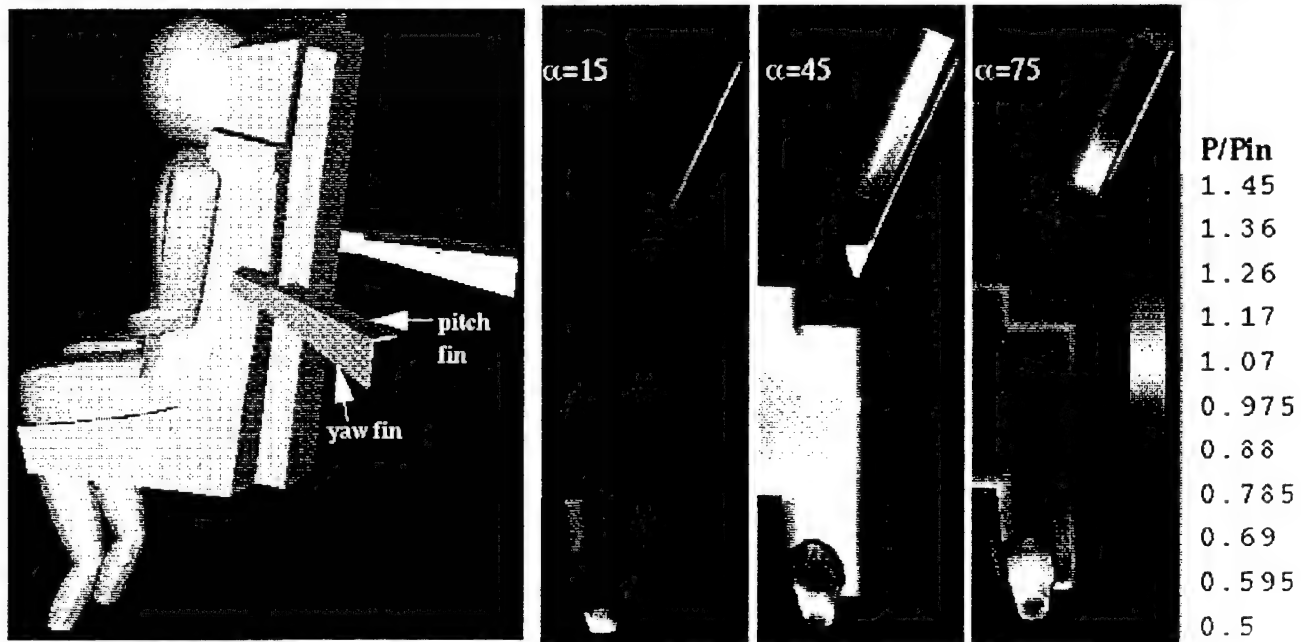


Figure 10. Shaded surface of seat and fins and bottom view of surface static pressure contours.

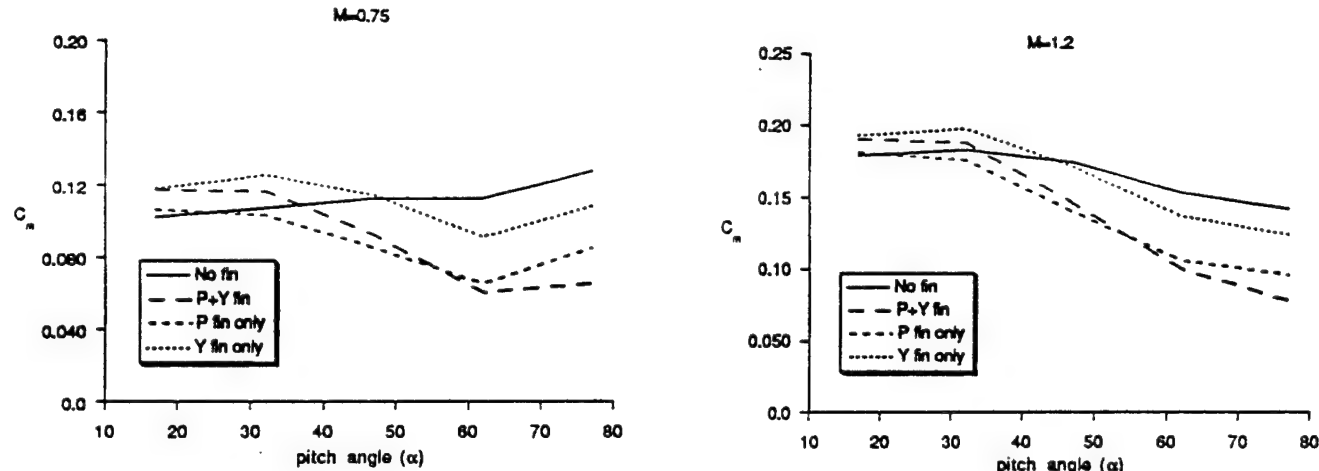


Figure 11. The Pitching Moment Coefficient Versus Pitch Angle for the Seat With and Without Fins;  $\beta = 0$

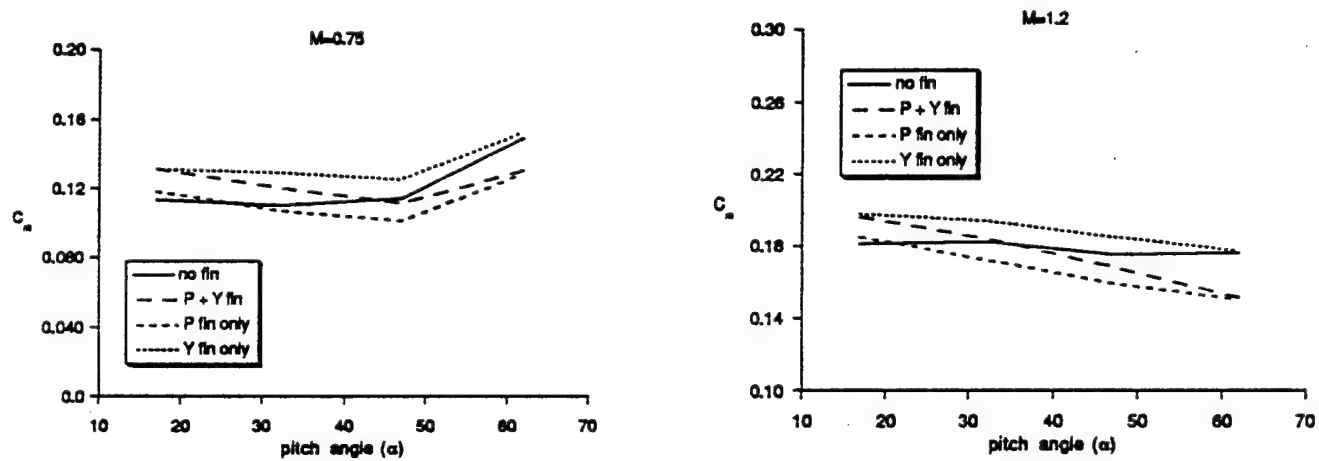


Figure 12. The Pitching Moment Coefficient Versus Pitch Angle for the Seat With and Without Fins;  $\beta = 15$

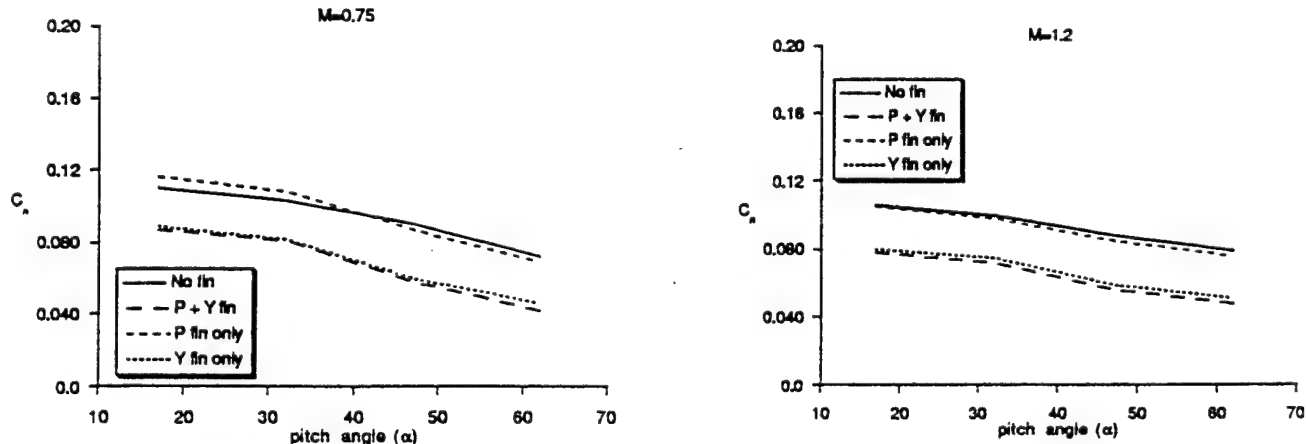


Figure 13. The Yawing Moment Coefficients Versus Pitch Angle for the Seat With and Without Fins;  $\beta = 15$



**AIAA-94-0751**

**Validation of CFD Methodology  
for Ejection Seat Applications**

**G.S. Hufford and S.D. Habchi  
CFD Research Corporation  
Huntsville, AL**

**32nd Aerospace Sciences  
Meeting & Exhibit  
January 10-13, 1994 / Reno, NV**

# VALIDATION OF CFD METHODOLOGY FOR EJECTION SEAT APPLICATIONS

by  
G.S. Hufford\* and S.D. Habchi\*\*  
CFD Research Corporation  
3325 Triana Blvd.  
Huntsville, AL 35805

## ABSTRACT

Three dimensional numerical simulations of a seat/occupant ejection seat system are presented using a pressure based Navier-Stokes code with turbulence modeling. Numerical simulations for benchmark blunt body problems of flow over a cylinder, a half cylinder, and a sphere are analyzed to determine the effects of grid refinement, differencing scheme, and turbulence modeling for the typical high Reynolds number blunt body problem. These results are applied to the ejection seat simulation. Comparisons between various CFD methodologies and experiment are given for both the simple geometries and the ejection seat. Results show that discrepancies between numerical methodologies are minor at supersonic speeds, but are significant at subsonic or transonic speeds. These discrepancies depend greatly on the grid refinement, differencing scheme and turbulence model used in the simulation. Comparisons between computational and experimental force and moment coefficients as well as pressure distributions are given in selected cases where experimental data exists.

## INTRODUCTION

An accurate numerical simulation of a pilot ejection from a high speed aircraft is a very difficult task. Pilot ejections are inherently three dimensional unsteady turbulent flowfields with complicated shock interaction at transonic and supersonic speeds. The complicated geometric configurations of pilot ejection seat systems cause added difficulties in obtaining a

proper geometric model as well as a suitable computational grid. Important issues in the numerical simulation of pilot ejections are:

1. The proper geometric modeling of the pilot ejection system. The use of state-of-the-art CAD tools are necessary for proper surface modeling.
2. The generation of suitable computational grids. The complex geometry causes complications in the generation of grids whether structured or unstructured methods are used.
3. The proper modeling of turbulence. The blunt bodied ejection seat causes highly turbulent flow fields behind the seat which may affect force and moment coefficient data.
4. The accuracy of the numerical scheme in resolving shock and near wall viscous effects becomes important.
5. The cost of a numerical simulation can become prohibitively expensive in terms of computational resources and simulation turn around time.
6. The unsteady nature of the store separation problem of pilot ejection requires time accurate numerical simulations.

Blunt bodied ejection seat type problems have recently been studied by several authors using

\*Project Engineer, Member AIAA

\*\*Group Leader/Research, Member AIAA

various assumptions and simplifications. For example, Wurtzler<sup>1</sup> used steady state Euler equations to simulate the B-1A Escape Capsule, Caruso and Mendenhall<sup>2</sup> used laminar thin shear layer equations to model 2-D ejection seat flow, Baum and Lohner<sup>3</sup> coupled rigid body motion equations to an Euler flow solver to simulate unsteady 3-D ejection from an aircraft, and Habchi *et. al.*<sup>4</sup> conducted preliminary 3-D Navier-Stokes ejection seat calculations that led to the present study. By necessity each of the above authors made assumptions about either the flow field, the geometrical model or both. These assumptions may seriously effect the quality of the results obtained for a given simulation. For example, Wurtzler attributes his differences with experiment to the lack of viscous effects in his numerical model.

The emphasis of this paper is to analyze the effects of the differencing scheme, the turbulence model, and grid resolution for a blunt bodied ejection seat problem at subsonic, transonic, and supersonic speeds. Since a limited amount of experimental data exists on the particular ejection seat studied in this paper, and the fact that refined ejection seat computations are very expensive, simpler blunt bodies (cylinder, half cylinder, and sphere) are studied to establish trends in the CFD methods used for typical blunt bodied problems. When applicable, the computational results are compared to experimental results to determine the quality of a given simulation.

The results presented in this paper address issues one through five above. In particular these issues are addressed in conjunction with obtaining the quality of numerically predicted force and moment coefficients for free flight ejection. The focus of this paper is to quantify the differences in results obtained using different differencing schemes, turbulence models, and grid refinement levels for the ejection seat blunt body problem. In addition issues regarding computational and human cost are addressed throughout the paper. The unsteady effects of the pilot ejecting from an aircraft and the aircraft proximity effects are being addressed but will be neglected in the present paper.

After a brief discussion of the numerical approach and physical models used in this study, results are presented for the simple blunt body cases of a cylinder, half cylinder, and sphere. Conclusions from these results are applied to the ejection seat case. The ejection seat surface creation and grid generation are discussed and results from selected ejection seat runs are presented.

## NUMERICAL APPROACH AND PHYSICAL MODELS

The CFD code used in this study is CFD-ACE.<sup>5</sup> This code solves the full Navier-Stokes equations in a general curvilinear coordinate system using a structured, collocated finite volume approach. The code employs a pressure based method and sequentially solves the flow variables using a modified version of Stone's<sup>6</sup> solver. Features of the code include four different types of differencing schemes (Upwind, Second Order Upwind, Central and Osher-Chakravarthy) and three different turbulence models (Baldwin-Lomax, standard k- $\epsilon$ , and a low Reynolds number k- $\epsilon$  model).

## SIMPLE BLUNT BODY RESULTS

Since a limited amount of experimental data exists on the particular ejection seat studied in this paper and refined ejection seat computations are expensive, an analysis of simpler blunt bodied geometries is conducted under this study. The blunt body analysis is used to evaluate the different differencing schemes, turbulence models and grid refinement levels for subsonic, supersonic and transonic simulations. The emphasis of this analysis is to determine specific trends for the different CFD methodologies and evaluate their usefulness for the complicated three dimensional ejection seat geometry. The specific geometries studied are a cylinder, a half cylinder and a sphere.

### Cylinder

The first simple geometry chosen is a 2-D cylinder. Although the cylinder is a simple geometrical entity, which allows easy creation of a computational grid, the flow over a cylinder is

an unsteady turbulent flow with separation. Since the ejection seat simulations are steady state simulations, the steady state Navier-Stokes equations with turbulence modeling are solved. This solution is in essence a time averaged solution which is comparable to time averaged experimental data presented in Jones<sup>7</sup> and Roshko.<sup>8</sup> The purpose of these simulations is to see if a given CFD methodology is capable of predicting the point of separation and the base pressure (surface pressure in the separated flow region) if the grid is sufficiently refined. The ejection seat has massive flow separation behind the seat due to sharp corners which induce flow separation. Since the majority of the ejection seat flow separation is determined from sharp corner locations, the cylinder is in fact a more difficult test case since separation is induced from an adverse pressure gradient as opposed to sharp corners.

A high Reynolds number simulation ( $Re = 8.27 \times 10^6$ ), which has been found to be fully turbulent during wind tunnel tests, was chosen as a test case since the ejection seat has been assumed to experience fully turbulent flow. For this Reynolds number, simulations at  $M = 0.177$ ,  $M = 0.74$ , and  $M = 2.0$  were conducted using the Upwind, Second Order Upwind, and Central differencing schemes, the standard  $k-\epsilon$  model<sup>9</sup>, and a slightly modified version of the standard  $k-\epsilon$  model with six different grid resolution levels. In addition selected runs were completed using the Osher-Chakravarthy differencing scheme and the low Reynolds number turbulence model of Chien.<sup>10</sup>

The data presented in Jones and Roshko is for low speed flow only. Specifically, a simulation in Jones is at  $M = 0.177$  with  $Re = 8.27 \times 10^6$  while Roshko simulated low speed flow ( $M < 0.3$ ) at  $Re = 8.4 \times 10^6$ . Both of these experiments have surface pressure data and drag data for comparison. At the higher Mach numbers similar experimental data has not been published. Therefore, the high Mach number simulations will be used only to compare the different CFD methodologies to one another.

Parameters for the six different grids used in

these simulations are given in Table 1 and depicted in Figure 1.  $D_2$  is 2.097 cylinder diameters for each of the grids. The grid distribution is determined using a hyperbolic tangent function. In each case the grid is polar with the outer boundary diameter equal to 55 times the simulated cylinder diameter. In each case, only half of the cylinder was modeled since the geometry is symmetric although a full cylinder case was completed and compared exactly to the half cylinder result. Figure 1b shows a grid close-up near the cylinder surface from the coarsest grid used, labeled GRID in Table 1.

Table 1. Grid Parameters for the Cylinder Cases

Name	Size	D1
GRID	59x88	$2.621 \times 10^{-3}$
GRID_f	59x88	$2.621 \times 10^{-4}$
GRID_f2	59x88	$2.621 \times 10^{-5}$
GRID_f3	149x88	$2.621 \times 10^{-5}$
GRID_f8	199x132	$2.621 \times 10^{-5}$
GRID_f10	199x132	$2.621 \times 10^{-6}$

PA-93-2111

Figures 2a and 2b show surface pressure coefficients for the Grid\_f2 and Grid\_f10 grids for the various differencing schemes using the standard  $k-\epsilon$  turbulence model plotted against the cylinder angle  $\beta$  defined in Figure 1a. In addition a solution for a laminar case (i.e., without using a turbulence model) was obtained using Upwind differencing to show the importance of turbulence modeling in these simulations. In the coarser grid case (Figure 2a) the minimum pressure point is overpredicted and the separation point (point where pressure becomes constant) is located about 15 degrees downstream of the experimental values. Both the Second Order Upwind and Central schemes give very similar results while the Upwind scheme predicts separation much further downstream. The downstream shift in separation is due to the added numerical viscosity in the First Order Upwind scheme as opposed to the Second Order Upwind scheme. All cases predict a higher base pressure than the two experiments although the difference between the simulation and the Jones experiment is comparable to the

difference between the two experiments. The finer grid results in Figure 2b more accurately predict the minimum pressure point (note that the 85 degree point of Roshko is an errant data point and is not physical<sup>8</sup>), however, the base pressure value is still overpredicted and the separation is still downstream of experiment. It is interesting to note that a comparison of the two experimental results shows that separation occurred in a similar location (~105 degrees), however, the base pressure values were different.

In an attempt to determine if the separation location was affecting the base pressure the standard turbulence model was modified such that the proportionality factor of turbulent viscosity to  $k$  and  $\epsilon$  was reduced. In the standard model  $\nu_t = C_\mu k^2 / \epsilon$  where  $C_\mu = 0.9$ . For the modified version of the  $k$ - $\epsilon$  model,  $C_\mu$  was modified to 0.05. In Launder and Spalding's original paper<sup>9</sup> a variable  $C_\mu$  was used for a low Reynolds number model which essentially sets its value to .09 in fully turbulent regions and from .009 to .09 in laminar regions such as the laminar sub-layer of a boundary layer. Figure 2c shows Central differencing results for each grid using the lower  $C_\mu$ . Note that separation was moved forward and the minimum pressure was slightly reduced, but the base pressure was not affected. Also from this figure note that Grid and Grid\_f are similar as well as Grid\_f2, Grid\_f8 and Grid\_f10. For the first two cases the value of  $y^+$ , at the first cell off the cylinder boundary, was greater than 11.5 and hence the turbulent law of the wall function was used to determine wall shear stress, while for the latter three cases the  $y^+$  value was less than 11.5 and the shear stress at the wall was determined directly from the radial velocity gradients.

As a final attempt at a better comparison to experiment, the Low Reynolds number turbulence model of Chien<sup>10</sup> was used for the finest grid. The finest grid had at least 10 points in the laminar sublayer justifying an attempt with a low Reynolds number turbulence model. Figure 2d shows the resulting surface pressure curve and its comparison to the standard  $k$ - $\epsilon$  model. Unfortunately the Low Reynolds number model predicted separation further downstream than

the standard model resulting in a detrimental effect. Since convergence for this model was more difficult than the standard model and no improvements were observed no further experimentation was continued with the Low Reynolds number model.

Although the pressure distributions are somewhat similar between experiment and computation, the differences that exist in separation location and base pressure value produce differences in predicted drag. Table 2 shows the predicted drag coefficients for the Upwind, SOU, and Central schemes using the standard  $k$ - $\epsilon$  model and also shows the results of a case utilizing the central scheme and  $C_\mu = 0.05$ . Note that the differences between the two experimental results are due to differences in the final base pressure. In all cases the computational drag underpredicts the experimental drag. Ironically the Upwind differencing drag is closer to experiment than the Central differencing cases due to the shift of the pressure curve between 80 and 130 degrees.

Table 2. Drag Coefficients for the Cylinder at  $M = 0.177$ ,  $Re = 8.27 \times 10^6$

Case	$C_D$ (upwind)	$C_D$ (SOU)	$C_D$ (central)	$C_D$ (central $C_\mu = 0.05$ )
GRID	.373	.274	.255	.281
GRID_f	.392	.226	.236	.296
GRID_f2	.440	.288	.301	.351
GRID_f8	.324	.255	.273	.297
GRID_f10	.318	.257	.296	.326

Experiment: Jones  $C_D = .532$ ; Roshko  $C_D = .709$  PA-03-21 12

The surface pressure curves for transonic flow over a cylinder ( $M=0.74$ ) for Grid\_f2 and Grid\_f10 are given in Figure 3a-b. As in the previous  $M=0.177$  case, the results for Central, SOU and Osher differencing produce very similar results while the Upwind differencing predicts separation further downstream. In this case separation occurs just downstream of the transonic shock in all cases. Thus, correct prediction of the shock location is crucial for proper separation location. Also note that the laminar case that was obtained is inadequate as was the case at  $M=0.177$ . Lowering the value of  $C_\mu$  predicts an earlier shock location and hence separation,

however, the final value of base pressure in the separation region is essentially the same for different grid resolution levels as well as for different values of  $C_\mu$ . Table 3 shows drag coefficient values for three different grids. In terms of a percentage basis the difference in predicted drag for the various differencing schemes, turbulence models, and grids is much smaller than at  $M=0.177$ .

Table 3. Drag Coefficients for the Cylinder at  $M = 0.74$ ,  $Re = 8.27 \times 10^6$

Case	$C_D$ (upwind)	$C_D$ (SOU)	$C_D$ (central)	$C_D$ (central $C_\mu = 0.05$ )
GRID	1.140	.964	.916	.862
GRID_f2	1.174	.952	.937	.893
GRID_f10	1.084	.883	.944	.889

PA-93-2113

Figure 4 shows surface pressure curves for supersonic ( $M=2.0$ ) flow over a cylinder for two different grids. In this case the differences in surface pressure between grids and differencing schemes is minimal. As was the case for the  $M=0.177$  and  $M=0.74$  cases, the converged laminar case predicts earlier separation, however, in this case the result is much closer to the turbulence results. Also note that lowering  $C_\mu$  had no effect on the surface pressure curves. Table 4 shows drag coefficient values for the various cases. Note that very little difference is observed for any of the cases.

Table 4. Drag Coefficients for the Cylinder at  $M = 2.0$ ,  $Re = 8.27 \times 10^6$

Case	$C_D$ (upwind)	$C_D$ (SOU)	$C_D$ (central)	$C_D$ (central $C_\mu = 0.05$ )
GRID	1.403	1.433	1.395	1.387
GRID_f2	1.401	1.432	1.403	1.398
GRID_f3	1.403	1.371	1.423	1.418

PA-93-2114

### Half Cylinder

In each of the cylinder cases the proper location of the separation point was a determining factor in predicted drag, however, the separation point did not greatly effect the final base pressure value in the separated region. Since most of the separation in the ejection seat problem is due to

separation from a sharp corner, a study of a half cylinder geometry was undertaken. Note that the definition for  $\beta$  is identical to the cylinder from 0 to 90 degrees, however, from 90 to 180  $\beta$  is defined as:

$$\beta_i = 90^\circ \left( \frac{r_i}{r_{max}} \right) + 90^\circ$$

where  $r_{max}$  is the maximum cylinder radius and  $r_i$  is the distance from the  $r_{max}$  point at the  $i$  grid location. These variables are depicted in Figure 5a. Table 5 gives the grid parameters for the half cylinder cases with a sample grid, Grid\_f6 in Figure 5b. Note that  $D_2$  equals 2.099 cylinder diameters and the outer boundary was 55 times the cylinder diameter. In both cases grid cells were clustered near the sharp corner of the half cylinder.

Table 5. Grid Parameters for the Half Cylinder Cases

Name	Size	D1
GRID_f6	88x131	$2.621 \times 10^{-5}$
GRID_f8	198x131	$2.621 \times 10^{-5}$

PA-93-2115

Figures 6 through 8 show results for  $M=0.177$ ,  $M=0.74$  and  $M=2.0$  for two different grids and varying differencing schemes using the standard  $k-\epsilon$  turbulence model. For the subsonic case the coarser grid (Figure 6a) shows strong oscillations in surface pressure at the corner ( $\beta=90$ ) even though the results are well converged. The finer grid (Figure 6b) shows reduced oscillations however, they are still present. In each case, Central differencing produces the smallest oscillations. As in the previous cylinder cases the SOU and Central results are quite similar showing almost identical values of base pressure in the separated flow region. Even though separation is forced at 90 degrees the predicted base pressure value using the Upwind scheme is significantly less than the Central and SOU scheme predictions. A laminar (no turbulence model used) solution was also obtained for the coarser grid. Separation for the laminar case occurred before the sharp corner. A constant value of base pressure was not obtained in the

separated region for the laminar case. The effect of modifying the  $k-\epsilon$  turbulence model by reducing  $C_\mu$  was minimal in terms of base pressure prediction for the half cylinder.

Figure 7 shows transonic surface pressures for the half cylinder. As was the case in the full cylinder the shock location and hence separation occurred before  $\beta = 90$  degrees. Thus, these results are quite similar to the full cylinder results. Lowering the value of  $C_\mu$  had similar effects as in the full cylinder cases.

Figure 8 shows supersonic surface pressures for the half cylinder. At this Mach number separation is again forced at 90 degrees. Note that as was the case in the full cylinder, using various differencing schemes had very minor effects on predicting the surface pressures. In addition the laminar results were almost identical to the turbulent results since separation location was not an issue.

Tables 6-8 show drag coefficients for each Mach number for various differencing schemes and grids. At  $M = 0.177$ , the finer grid always predicts lower drag due to a slightly larger base pressure behind the cylinder. As witnessed by Figure 6, these differences are quite small however, due to the larger surface area behind the half cylinder they have a somewhat large impact on drag. At  $M = 0.74$ , a similar trend holds for the Upwind and SOU differencing results, however, the Central differencing results are much less grid sensitive. At  $M = 2.0$ , the differences in drag are very insensitive to changes in differencing scheme, grid, and turbulence model, as was the case in the full cylinder.

Table 6. Drag Coefficients for the Half Cylinder at  $M = 0.177$ ,  $Re = 8.27 \times 10^6$

Case	$C_D$ (upwind)	$C_D$ (SOU)	$C_D$ (central)	$C_D$ (central $C_\mu = 0.05$ )
GRID_f6	.861	.678	.646	.604
GRID_f8	.761	.599	.602	.562

PA-93-21 16

Table 7. Drag Coefficients for the Half Cylinder at  $M = 0.74$ ,  $Re = 8.27 \times 10^6$

Case	$C_D$ (upwind)	$C_D$ (SOU)	$C_D$ (central)	$C_D$ (central $C_\mu = 0.05$ )
GRID_f6	1.192	.974	.962	.902
GRID_f8	1.104	.904	.965	.908

PA-93-21 17

Table 8. Drag Coefficients for the Half Cylinder at  $M = 2.0$ ,  $Re = 8.27 \times 10^6$

Case	$C_D$ (upwind)	$C_D$ (SOU)	$C_D$ (central)	$C_D$ (central $C_\mu = 0.05$ )
GRID_f6	1.408	1.418	1.399	1.387
GRID_f8	1.409	1.392	1.418	1.410

PA-93-21 18

### Sphere

All of the previous results and established trends have been for two dimensional simulations. Since the ejection seat is a three dimensional body, verification of these trends is necessary in 3-D. Thus, results for flow over a sphere at subsonic ( $M=0.1$ ), transonic ( $M=0.955$ ) and supersonic ( $M=2.0$ ) Mach numbers were obtained. The subsonic Mach number value was changed for comparison to the experimental surface pressure and drag results of Achenbach<sup>11</sup> and the transonic Mach number was changed to compare to experimental results of Bailey *et. al.*<sup>12,13</sup> Experimental drag results for the supersonic case also exist in Bailey *et. al.*<sup>12,13</sup> The Reynolds numbers based on sphere diameter for the subsonic, transonic, and supersonic cases were  $5 \times 10^6$ ,  $1 \times 10^6$ , and  $7 \times 10^5$ , respectively. Table 9 shows the various grid sizes used for the sphere simulation.  $D_1$  and  $D_2$  are spacing parameters defined earlier for the cylinder. For the first four grids the ratio of outer boundary to cylinder diameter is 10:1 while for grid sphere\_f5 the ratio is 100:1.  $\beta$  is also defined the same as for the cylinder. For economic reasons, an axisymmetric version of the CFD-ACE code was used for these simulations.

Table 9. Grid Parameters for the Sphere Case

Name	Size	D1	D2
sphere	50x45	$2.621 \times 10^{-3}$	.5242
sphere_f	50x45	$2.621 \times 10^{-4}$	.5242
sphere_f2	50x45	$2.621 \times 10^{-5}$	.5242
sphere_f4	150x90	$2.621 \times 10^{-5}$	.5242
sphere_f5	150x90	$2.621 \times 10^{-5}$	2.621

PA-83-21 10

Figure 9 shows surface pressure results for the  $M=0.1$  case for each grid using Central differencing and for each differencing scheme using the *sphere\_f4* grid. Note that the coarser grids (sphere, *sphere\_f*) with values of  $y^+$  of the first cell greater than 11.5 show similar results while the finer grids show earlier separation. This is the same trend noticed for the cylinder. However, the base pressure in the separated region is not constant as it was for the cylinder. The experimental results also do not show constant base pressure values, however, the variations are much less than in the computation. As in the cylinder case, the predicted base pressure values are always larger than those of the experiment. Also note that SOU and Central differencing results are quite similar while the Upwind differencing results show separation further downstream. However, none of the cases predicts separation as early as experiment. In an attempt to predict earlier separation and obtain better comparisons to experiment the value of  $C_\mu$  was lowered to 0.05 as in the cylinder simulations. Note in Figure 9b that indeed the separation was predicted earlier, however, the oscillations in base pressure were greater for this case than the standard  $k-\epsilon$  cases. In the cylinder cases this detrimental effect in the fully separated region was not observed.

Figure 10 shows transonic surface pressures for each grid using Central differencing and for each differencing scheme using the *sphere\_f4* grid. As was the case for the cylinder, the shock location determines separation. Figure 10a shows the sensitivity of shock location to streamwise grid refinement and the relative insensitivity to radial grid refinement. Figure 10b shows the sensitivity of shock location to differencing scheme. Note that the shock location for the

sphere is more sensitive to differencing scheme than for the cylinder.

Figure 11 shows supersonic surface pressures for each grid using Central differencing and for each differencing scheme using the *sphere\_f4* grid. As was the case for the cylinder the differences between the various grids and differencing schemes were much smaller than the other Mach numbers.

Tables 10-12 show predicted drag values from the computations and the experiments reported by Achenbach<sup>11</sup> and Bailey.<sup>12,13</sup> For the subsonic case note again that the Upwind results show better correlation to experiment even though the surface pressure comparisons are worse. On a percentage basis the differences between the computation and experiment for the sphere test cases are quite similar to the cylinder. The transonic comparison to experiment are better on a percentage basis than subsonic. Note that the Upwind cases predict higher drag than experiment while the higher order schemes predict lower drag than experiment. The supersonic comparison to experiment is quite good for all test cases.

Table 10. Drag Coefficients for the Sphere at  $M = 0.1$ ,  $Re = 5 \times 10^6$

Case	$C_D$ (upwind)	$C_D$ (SOU)	$C_D$ (central)	$C_D$ (Osher)
sphere	.220	.084	.089	.077
sphere_f	.239	.070	.091	.072
sphere_f2	.272	.096	.132	.108
sphere_f4	.153	.064	.086	.070
sphere_f5	.159	.061	.094	.074

Experiment (Achenbach):  $C_D = .242$

PA-83-21 110

Table 11. Drag Coefficients for the Sphere at  $M = 0.955$ ,  $Re = 1 \times 10^6$

Case	$C_D$ (upwind)	$C_D$ (SOU)	$C_D$ (central)	$C_D$ (Osher)
sphere	.956	.725	.711	.690
sphere_f	.975	.671	.714	.668
sphere_f2	.995	.634	.727	.663
sphere_f4	.878	.586	.677	.620

Experiment (Bailey):  $C_D = .845$

PA-83-21 111

Table 12. Drag Coefficients for the Sphere at  $M = 2.0$ ,  $Re = 7 \times 10^5$

Case	$C_D$ (upwind)	$C_D$ (SOU)	$C_D$ (central)	$C_D$ (Osher)
sphere	1.047	1.044	1.032	1.023
sphere_f	1.037	1.019	1.029	1.012
sphere_f2	1.029	.998	1.025	1.004
sphere_f4	1.038	.986	1.027	1.004

Experiment (Bailey):  $C_D = 1.0$

PA-00-21 112

### CONCLUSIONS BASED ON SIMPLE GEOMETRY TEST CASES

1. The supersonic test cases were much less dependent on turbulence modeling and differencing scheme for all cases. The comparison of predicted and experimental drag for the sphere shows all differencing schemes produce good drag prediction.
2. The subsonic cases were quite dependent on turbulence modeling and differencing scheme. For the cylinder and sphere, good pressure predictions were obtained before separation, however, near separation and in the separated region the pressures showed discrepancies with experiment. Due to extra numerical diffusion in the Upwind scheme, separation was always predicted further downstream than the SOU, Central, and Osher differencing schemes.
3. At transonic speeds the shock location determines separation. Hence turbulence modeling and differencing scheme choice affect the results. However, the resulting differences in drag coefficient are smaller in terms of percentages than the subsonic cases.
4. For the sharp corner separation of the half cylinder test case, the Upwind differencing scheme predicts lower base pressures than the higher order schemes, causing higher drag predictions.

### EJECTION SEAT ANALYSIS

Using the results of the simple geometry cases as a guide, ejection seat validation cases were run at subsonic, transonic, and supersonic Mach numbers.

The geometric modeling and grid generation for the ejection seat is first described with a discussion of the results to follow.

### Geometric Modeling and Grid Generation

A successful evaluation and validation of CFD technology for ejection seat applications must have a sufficient geometric model that preserves the actual geometry to correctly capture the flow physics. Geometrical issues become very important when force and moment coefficients as well as flow details near the seat surface are desired. A significant portion of the human cost involved in ejection seat simulations is in creating a suitable geometrical model and a surface grid.

The ejection seat model and surface grid used in this study, were created using the CAD based grid generation package ICEM-CFD.<sup>14</sup> ICEM-CFD is a CAD package capable of reading IGES data and is coupled to an algebraic grid generator which creates structured CFD grids. Its use for the ejection seat simulations included obtaining a preliminary CAD description of the seat, the creation and modification of the preliminary model to obtain the final ejection seat surface model, and the subsequent surface grid generation.

Figure 12 shows the wireframe diagram of the CAD model and Figure 13 shows the subsequent surface mesh created for the baseline ejection seat computations. Note that special care was taken to preserve the contours of the occupant and the integrity of the model to correctly capture the flow compressions and expansions around the model. Once the surface grid and preliminary proximity grid to the seat were created, the full computational grid was obtained using elliptic grid generation techniques.

An elliptic grid generator, patterned after Shieh<sup>15</sup>, with line and orthogonality functions implemented through Poisson forcing functions, has been developed to generate ejection seat grids. Figure 14 shows a sample computational plane for the baseline ejection seat grid.

### Results

Based on the results for the simpler geometries,

ejection seat results were obtained for a low and high order differencing scheme for three different grid resolutions using only the standard  $k-\epsilon$  turbulence model. The experimentation with different turbulence models shows that improvements over the standard  $k-\epsilon$  model are possible, especially for predicting separation point location, however, since the major region of separated flow for the ejection seat is determined by the corners of the seat in the rear, the cost of additional simulations does not warrant such experimentation with the seat. Results from the simpler geometries also showed that improvements are possible as the grid is refined, especially for the subsonic cases. However, to properly obtain grid resolution for the ejection seat similar to the simpler geometries would take several million cells. A simulation of this size is prohibitively expensive. Computer resources were not available under this study for computations of this size. Instead, three levels of grid resolution, the finest of which is 406,000 cells, will be considered to observe the effects of grid refinement and compare the trends to the simpler geometries.

Tables 13-15 show the force and moment coefficients at  $M = 0.3$ ,  $0.74$ , and  $2.0$  in the body axis coordinate system defined in Figure 15. The force and moment coefficients are non-dimensionalized using the projected frontal area of the ejection seat,  $7.4 \text{ ft}^2$ , and a reference length equal to  $\sqrt{4S/\pi} = 3.07 \text{ ft}$ . The reference point about which moments were taken is at the seat SRP, located in the plane of symmetry where the seat back and seat sitting surface meet. All of the results reported in Tables 13-15 are at  $17^\circ$  pitch and zero yaw. The  $17^\circ$  pitch location is the orientation at ejection. Note that the zero pitch plane is for a vertical seat back position. For each Mach number, three different grids were used. The baseline grid has a total of 1803 surface cells and 199,584 computational cells. The fine\_1 grid has 3,781 surface cells and 318,318 computational cells and the fine\_2 grid has 3,781 surface cells and 406,000 computational cells. Only half of the geometry was simulated due to the symmetric geometry. The computational domain extended 2 body lengths above, 2 below, 3.75 behind, 2 in front of, and 1.6 to the side of the seat, respectively. A body length is defined as

the vertical distance from the top of the head to the tip of the toe. For each grid results were obtained using the Upwind and either SOU or Osher differencing schemes with the  $k-\epsilon$  turbulence model. An inviscid result was obtained using Upwind differencing for the baseline grid.

Table 13. Ejection Seat Force and Moment Coefficients at  $M = 0.3$

grid	turbulence	scheme	$C_x$	$C_z$	$C_m$
baseline	$k-\epsilon$	upwind	-.773	.0132	.0726
fine_1	$k-\epsilon$	upwind	-.762	.0133	.0571
fine_2	$k-\epsilon$	upwind	-.750	.0282	.0597
baseline	$k-\epsilon$	SOU	-.732	.0533	.0670
fine_1	$k-\epsilon$	Osher	-.690	.0353	.0480
fine_2	$k-\epsilon$	Osher	-.696	.0394	.0546
baseline		inviscid	-.771	.0181	.0771

PA-93-21114

Table 14. Ejection Seat Force and Moment Coefficients at  $M = 0.74$

grid	turbulence	scheme	$C_x$	$C_z$	$C_m$
baseline	$k-\epsilon$	upwind	-.919	.0054	.1023
fine_1	$k-\epsilon$	upwind	-.920	.0103	.0908
fine_2	$k-\epsilon$	upwind	-.910	.0237	.0891
baseline	$k-\epsilon$	SOU	-.843	.0030	.0880
fine_1	$k-\epsilon$	SOU	-.864	.0286	.0759
fine_2	$k-\epsilon$	SOU	-.858	.0405	.0787
baseline		inviscid	-.905	.0027	.1088

PA-93-21114

Table 15. Ejection Seat Force and Moment Coefficients at  $M = 2.0$

grid	turbulence	scheme	$C_x$	$C_z$	$C_m$
baseline	$k-\epsilon$	upwind	-1.065	-.0402	.254
fine_1	$k-\epsilon$	upwind	-1.067	-.0413	.262
fine_2	$k-\epsilon$	upwind	-1.075	-.0375	.257
baseline	$k-\epsilon$	Osher	-1.068	-.0338	.249
fine_2	$k-\epsilon$	Osher	-1.084	-.0265	.253
baseline		inviscid	-1.056	-.0395	.249

PA-93-21115

A persistent trend from the simplified geometry results is the decrease in axial force ( $C_x$ ) for the SOU or Osher scheme versus the Upwind scheme at the subsonic Mach numbers. In addition, very little difference was obtained between SOU and Upwind results at the supersonic Mach number which was also observed for the simple geometry cases. Additionally, only minor changes in the coefficients were observed as the grids were refined.

The force coefficients for the inviscid cases at each Mach number for the baseline grid are very similar to the  $k-\epsilon$  results. This indicates that either the grid is too coarse to properly capture turbulence or that turbulence effects are unimportant in the surface pressure predictions. The very fine grid results for the simplified blunt body geometries indicate turbulence effects are important on the base pressure and hence force coefficients. Although little difference in force coefficients was obtained, differences in the flow patterns behind the seat were observed for the  $k-\epsilon$  versus inviscid results. These differences, however, did not translate into differences in predicted force coefficients.

Inviscid cases were attempted for the higher order differencing schemes. These cases had poor convergence properties. The use of the  $k-\epsilon$  turbulence model improved the convergence properties for the high order differencing schemes. The importance of obtaining higher order accurate solutions was established in the simple geometry section and is also apparent in Tables 13-15. Therefore, the  $k-\epsilon$  model, at the least helps in stabilizing convergence and obtaining results using higher order differencing schemes. The effect of turbulence modeling on the force coefficients with refined ejection seat grids is a topic of ongoing study.

Table 16 shows experimental results<sup>16,17,18</sup> for several different ejection seats at the Mach numbers and orientations simulated computationally. In some cases, the experimental results were interpolated to match the orientations simulated in the computations. The ejection seat simulated in the computations and shown in Figure 13 is the Navy Aircrew Common Ejection Seat (NACES) for which no experimental results are available for comparison. However, the size and shape of the ACES II, F-106 and F-101 seat are similar to the NACES seat. The CREST seat represents the furthest deviation from NACES. A comparison of Tables 13-15 with Table 16 shows that for the subsonic test cases the SOU and Osher results compare somewhat better to experiment than the Upwind results, especially for the axial ( $C_x$ ) coefficient. At  $M = 2.0$ , the only experimental data is for the CREST seat. At  $M = 0.74$ , the

CREST seat has a higher axial force than the other seats and the computations. Not surprisingly, this trend persists at  $M = 2.0$ . In general, the computational predictions using the higher order schemes at subsonic speeds and either scheme at supersonic speed yield adequate comparisons to experiment.

Table 16. Experimental Force and Moment Coefficients for Several Ejection Seats at 17 Degrees Pitch

Seat	Mach No.	$C_x$	$C_z$	$C_m$
ACES II	0.3	-.692	-.037	.062
F-101	0.3	-.590	-.023	.025
ACES II	0.74	-.845	.004	.097
F-106	0.74	-.812	.096	.080
F-101	0.74	-.758	-.003	.069
CREST	0.74	-.966	.001	.255
CREST	2.0	-1.2	0	.35

PA-83-21116

Numerous computations for different seat pitch and yaw orientations have been completed by the authors. Some of these results are presented in Reference 19 and compared to experiment. Generally good comparisons to experiment were obtained at the different orientations.

## CONCLUSIONS

The present paper establishes the ability to use CFD methodology to adequately predict force and moment coefficients for a complicated three dimensional body at subsonic, transonic or supersonic Mach numbers. Simple geometries, such as cylinders, half cylinders, and spheres, as well as complex ejection seat configurations have been used to assess the importance of grid resolution, turbulence modeling, and differencing schemes.

The importance of using higher order differencing schemes at subsonic and transonic Mach numbers was established both for the simple geometry and ejection seat cases. At supersonic Mach numbers little difference in predicted force coefficients was noticed between low order and high order differencing schemes for the simple geometries or the ejection seat.

The effect of turbulence modeling on the force

coefficient results was noticeable for the simple geometries at subsonic and transonic Mach numbers. However, at supersonic Mach numbers the effect of turbulence on force coefficients was negligible. For the ejection seat cases, turbulence modeling had much less of an effect on force coefficient results than the simpler geometry cases.

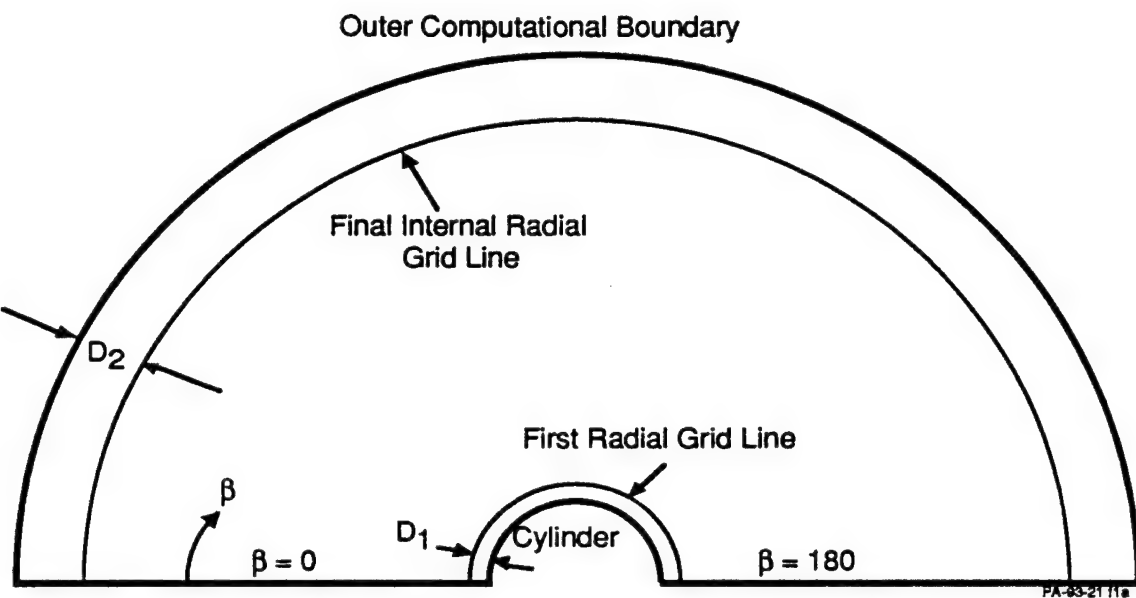
Grid refinement issues were important for the simple geometry test cases at subsonic and transonic speeds with respect to resolution of the boundary layers and location of transonic shocks. At the supersonic speed grid refinement was essentially unimportant for surface pressure prediction. The ejection seat results showed minor differences as the grids were refined from 200,000 to 400,000 grid cells.

#### ACKNOWLEDGEMENTS

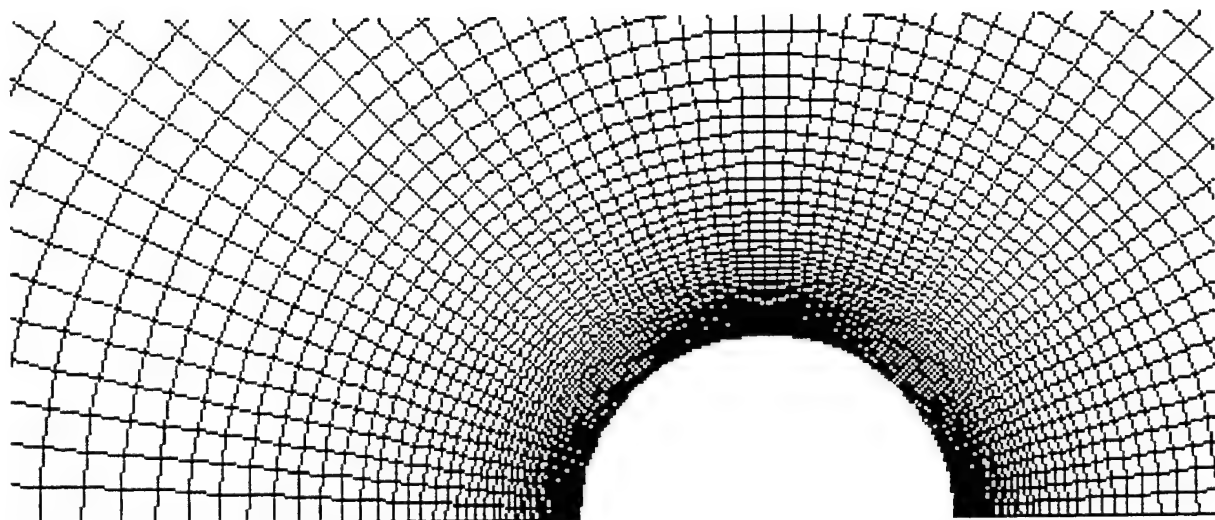
This research has been funded by the Naval Air Warfare Center, Aircraft Division, Warminster under the sponsorship of Mr. F. Terry Thomasson, Naval Air Systems Command AIR-531. The technical monitor for this project is Mr. Thomas J. Marquette. The authors would like to acknowledge the technical support of Dr. Andrzej Przekwas of CFDRC and the preparation of this manuscript by Ms. J. Swann.

#### REFERENCES

1. Wurtzler, K., "Application of an Euler Code to the B-1A Escape Capsule," AIAA-90-0431, Jan. 1990.
2. Caruso, S.C., and Mendenhall, M.R., "Computational Analysis of High Speed Ejection Seats," AIAA-90-0403, Jan. 1990.
3. Baum, J.D., and Lohner, R., "Numerical Simulation of Pilot/Seat Ejection from an F-16," AIAA-93-0783, 1993.
4. Habchi, S.D., Przekwas, A.J., Marquette, T. and Ayoub, P., "CFD Analysis of Ejection Seat Escape Systems," SAE-921924, Oct. 1992.
5. CFD Research Corporation, "CFD-ACE: Theory Manual," Version 1.0, CFDRC Report GR-93-1, September 1993.
6. Stone, H.L., "Iterative Solution of Implicit Approximations of Multidimensional Partial Differential Equations," *SIAM J. Num. Anal.*, vol. 5, No. 3, Sept. 1968.
7. Jones, G.W., Cincotta, J.J., and Walker, P.W., "Aerodynamic Forces on a Stationary and Oscillating Circular Cylinder at High Reynolds Numbers," NASA-TR-R-300, 1969.
8. Roshko, A., "Experiments on the Flow Past a Circular Cylinder," *JFM* 10, 345-356, 1961.
9. Launder, B.E., and Spalding, D.B., "The Numerical Computation of Turbulent Flows," *Computer Methods in Applied Mechanics and Engineering*, vol. 3, 269-289, 1974.
10. Chien, K-Y, "Predictions of Channel and Boundary Layer Flows with a Low Reynolds Number Turbulence Model," *AIAA Journal*, vol. 20, 33-38.
11. Achenbach, E., "Experiments on the Flow Past Spheres at Very High Reynolds Numbers," *JFM* 54, 565-575, 1972.
12. Bailey, A.B., and Hiatt, J., "Sphere Drag Coefficients for a Broad Range of Mach and Reynolds Numbers," *AIAA Journal*, vol. 10, 1436-1440, 1972.
13. Bailey, A.B., and Starr, R.F., "Sphere Drag at Transonic Speeds and High Reynolds Numbers," *AIAA Journal*, vol. 14, 1631, 1976.
14. Bertin, D., Lordon, J., and Morcaux, V., "A New Automatic Grid Generation Environment for CFD Applications," *Aerospatiale*, 1992.
15. Shieh, C.F., "Three-Dimensional Grid Generation Using Elliptic Equations with Direct Grid Distribution Control," AIAA-83-0448, Jan. 1983.
16. Reichenau, D.A., "Aerodynamic Characteristics of a Full-Scale ACES-II Ejection Seat with a Small Female or Large Male Manikin at Mach Numbers from 0.2 to 1.4," Calspan Corporation, AEDC-TR-87-16, Aug. 1978.
17. White, B.J., "Aeromechanical Properties of Ejection Seat Escape Systems," AD-787 194, Air Force Flight Dynamics Laboratory, WPAFB OH, April 1974.
18. Reichenau, D.A., "Aerodynamic Characteristics of a Half-Scale CREST Ejection Seat at Mach Numbers from 0.6 to 3.0," Calspan Corporation/AEDC Division, AED-TR-88-6, July 1988.
19. Habchi, S.D., Ho, S.Y., and Hufford, G.S., "Computational Aerodynamic Analysis of the Navy Aircrew Common Ejection Seat," AIAA-94-0395, 1994.

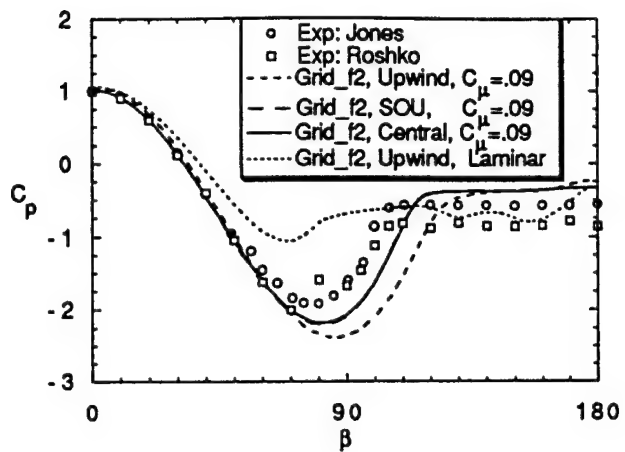


(a) description of cylinder grid parameters

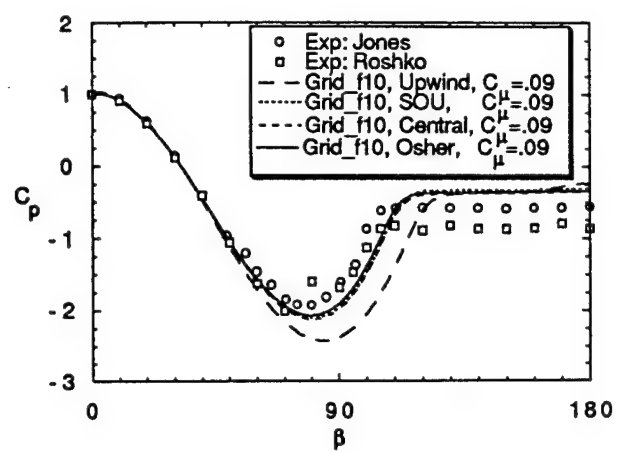


(b) sample grid

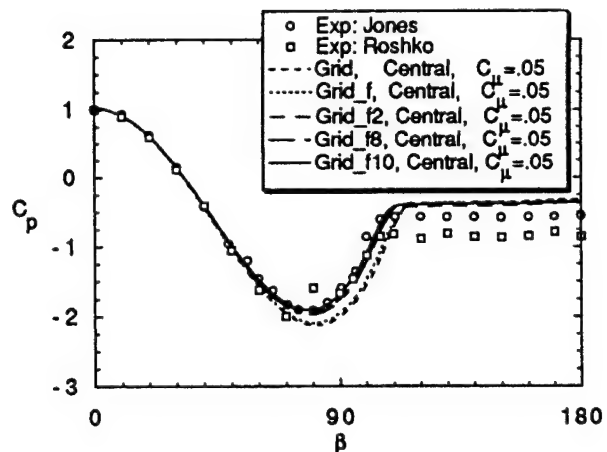
Figure 1. Description of Cylinder Grid Parameters and a Sample Coarse Grid



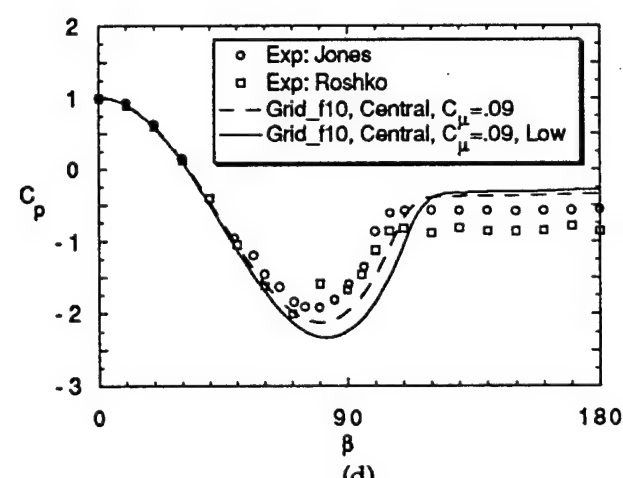
(a)



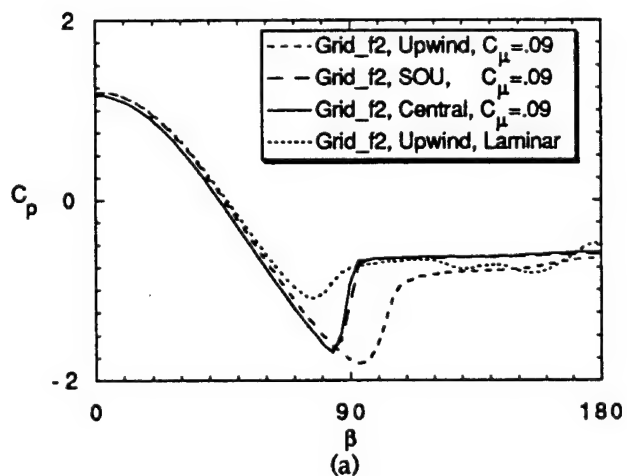
(b)



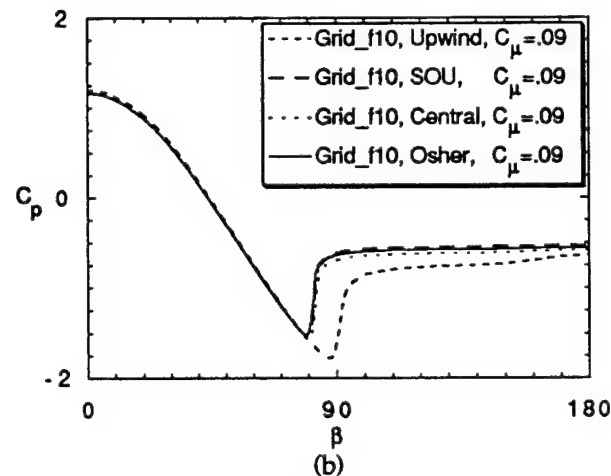
(c)



(d)

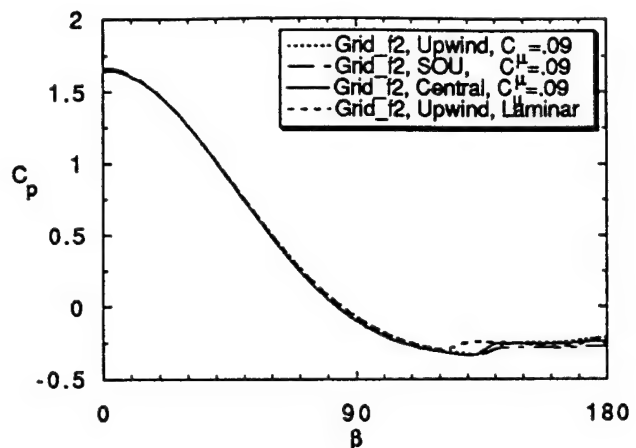
Figure 2. Cylinder Surface Pressures  $M = 0.177, Re = 8.27 \times 10^6$ 

(a)

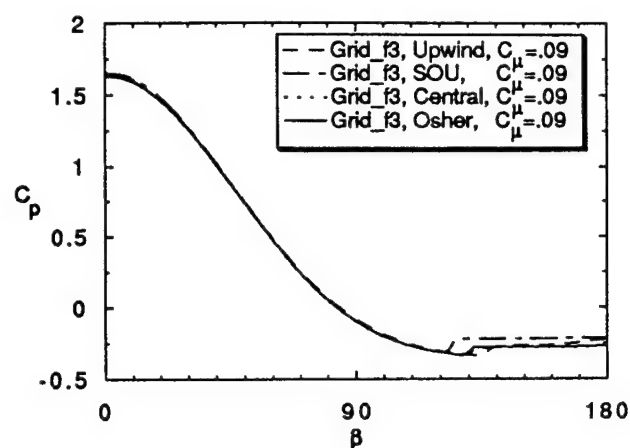


(b)

Figure 3. Cylinder Surface Pressures  $M = 0.74, Re = 8.27 \times 10^6$



(a)



(b)

Figure 4. Cylinder Surface Pressure at  $M = 2.0$ ,  $Re = 8.27 \times 10^6$

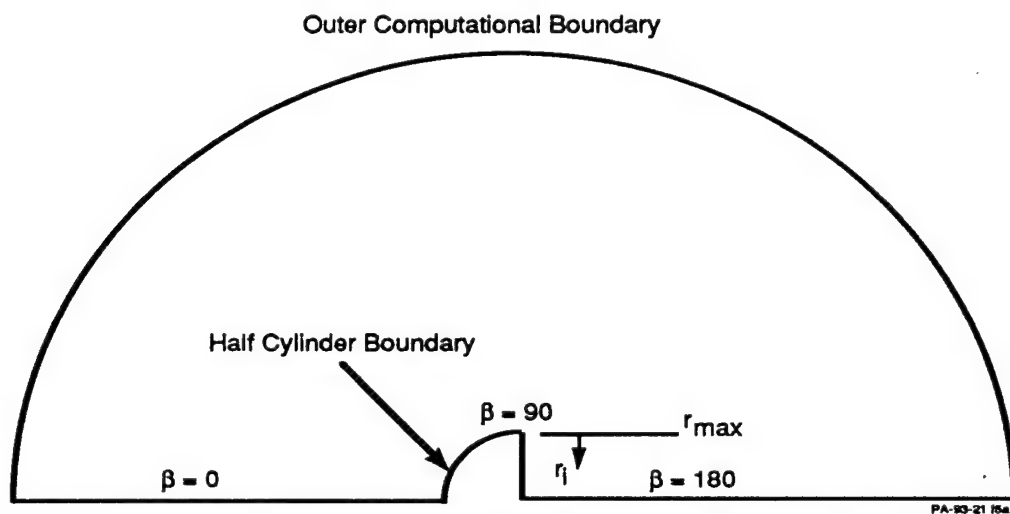


Figure 5a. Definition of the Angle  $\beta$  for the Half Cylinder Cases

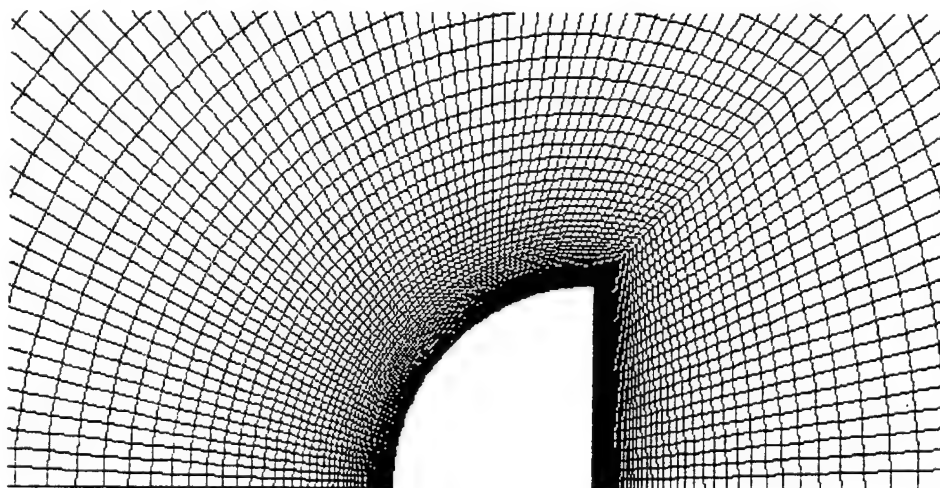


Figure 5b. Sample Half Cylinder Coarse Grid

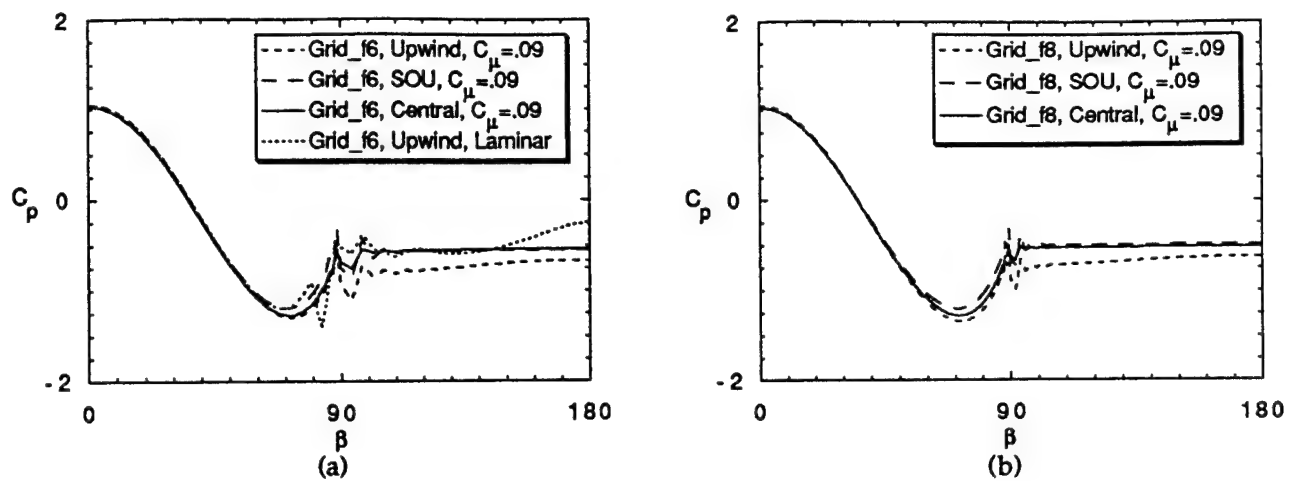


Figure 6. Half Cylinder Surface Pressures  $M = 0.177$ ,  $Re = 8.27 \times 10^6$

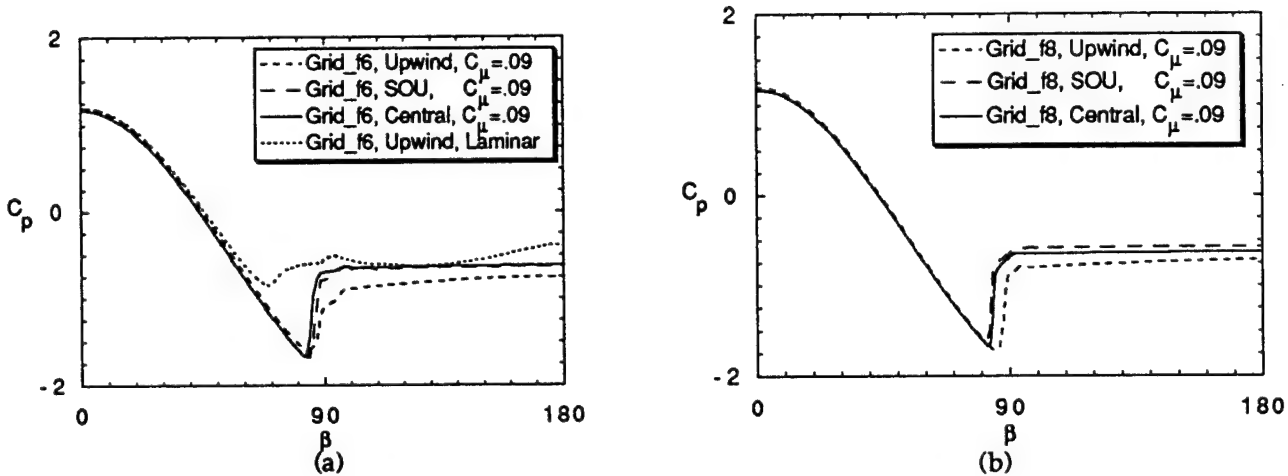


Figure 7. Half Cylinder Surface Pressures  $M = 0.74$ ,  $Re = 8.27 \times 10^6$

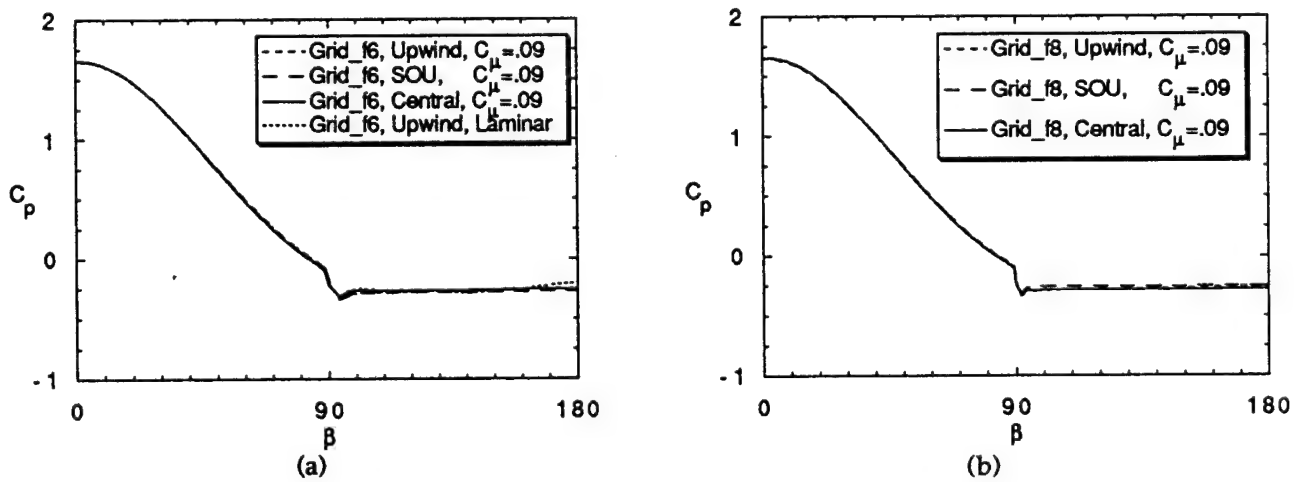


Figure 8. Half Cylinder Surface Pressures  $M = 2.0$ ,  $Re = 8.27 \times 10^6$

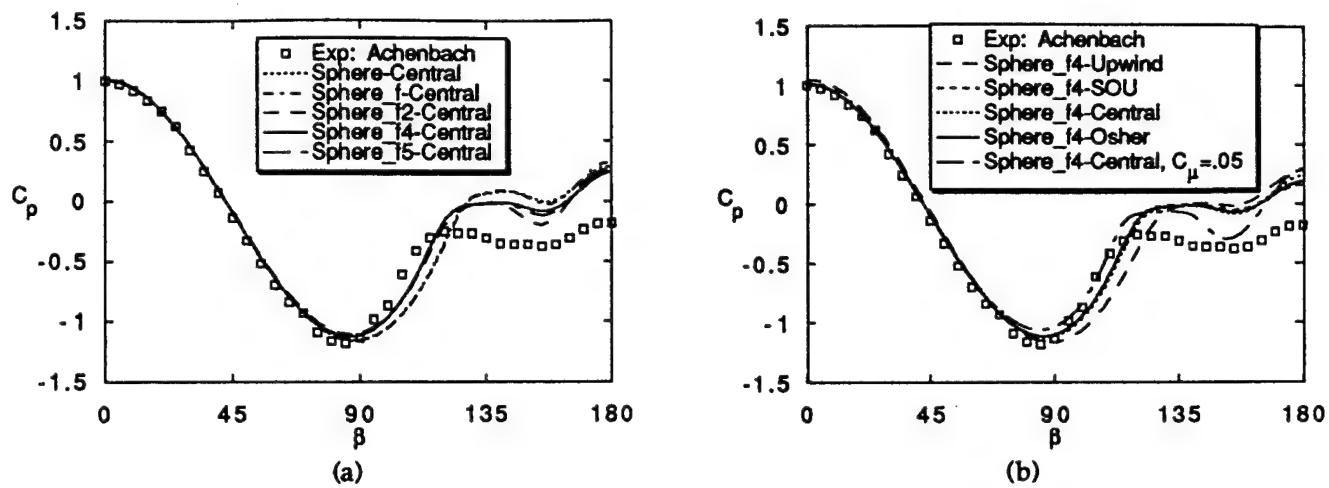


Figure 9. Sphere Surface Pressures at  $M = 0.1$ ,  $Re = 5 \times 10^6$

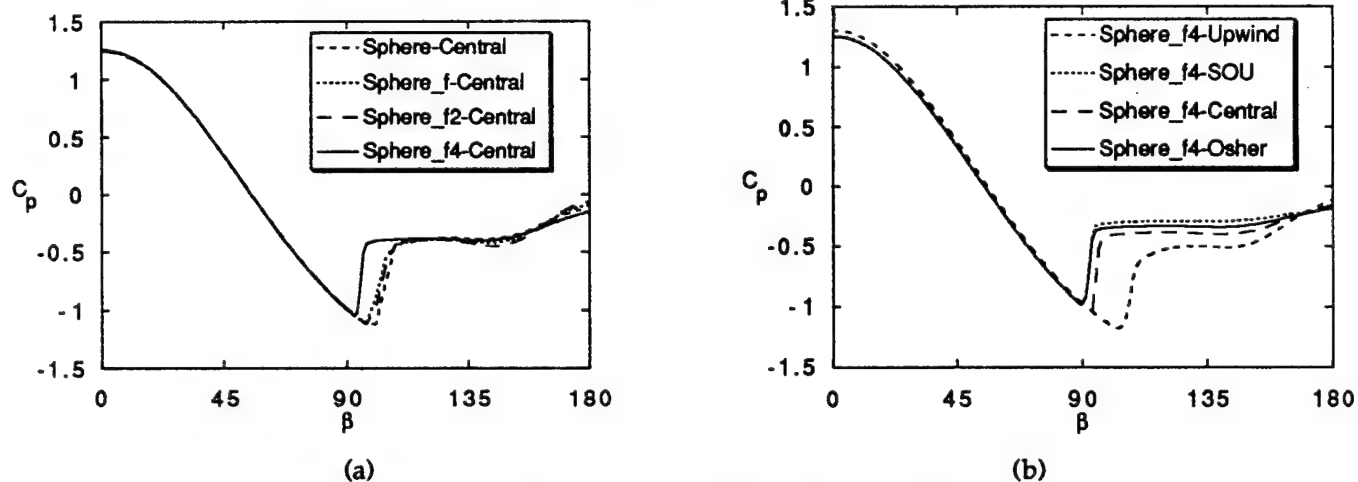


Figure 10. Sphere Surface Pressures at  $M = 0.955$ ,  $Re = 1 \times 10^6$

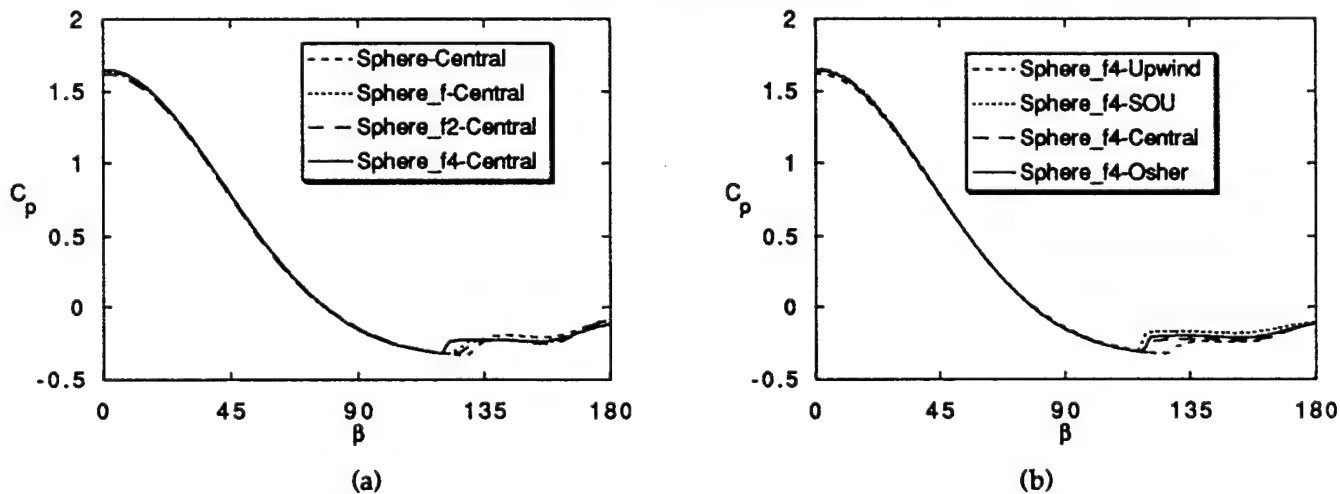


Figure 11. Sphere Surface Pressures at  $M = 2.0$ ,  $Re = 7.0 \times 10^5$

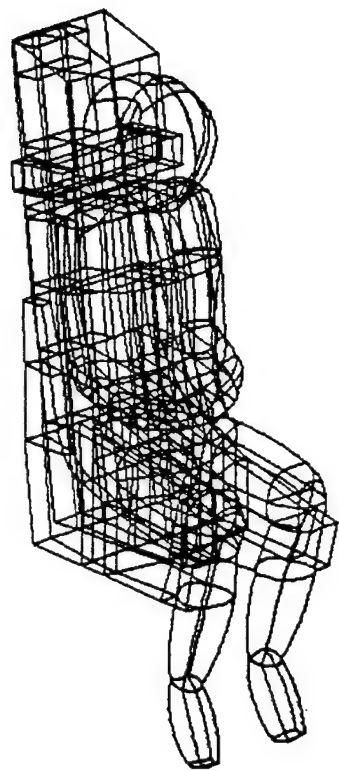


Figure 12. Wireframe CAD Model of the Ejection Seat

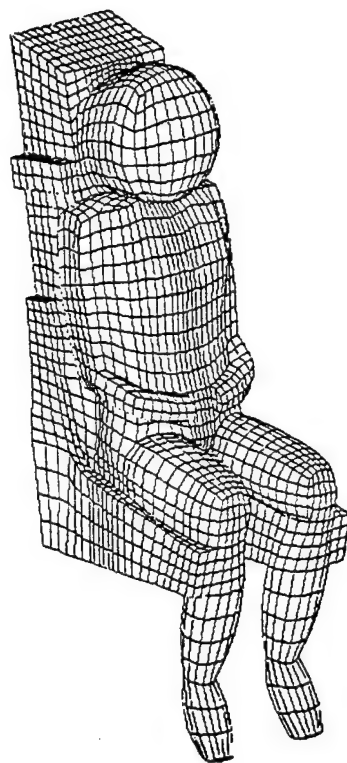


Figure 13. Ejection Seat Surface Mesh

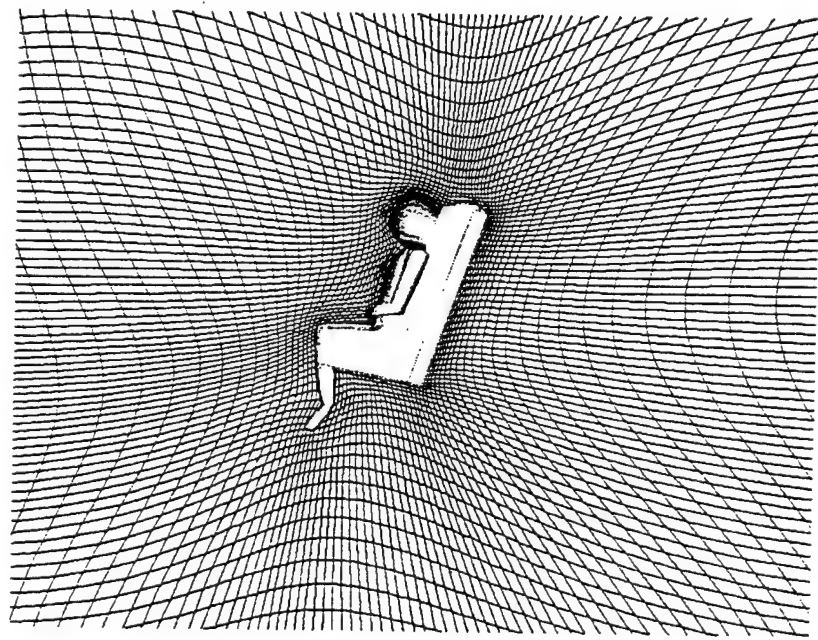


Figure 14. Sample Computational Plane for the Baseline Ejection Seat Grid

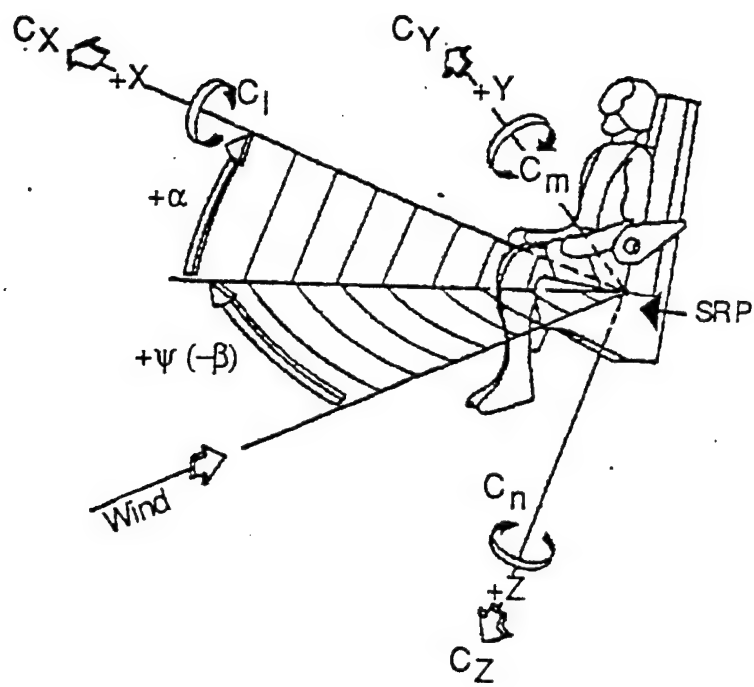


Figure 15. Body Axis Coordinate System for Force and Moment Definition



**AIAA-95-0187**

## **Navier-Stokes Computational Analysis of the B-1A Escape Capsule**

**S.D. Habchi and G.S. Hufford  
CFD Research Corporation  
Huntsville, AL**

**and**

**T. Marquette  
Naval Air Warfare Center - Aircraft Division  
Warminster, PA**

**33rd Aerospace Sciences  
Meeting and Exhibit  
January 9-12, 1995 / Reno, NV**

**For permission to copy or republish, contact the American Institute of Aeronautics and Astronautics  
370 L'Enfant Promenade, S.W., Washington, D.C. 20024**

# NAVIER STOKES COMPUTATIONAL ANALYSIS

## OF THE B-1A ESCAPE CAPSULE

by

S.D. Habchi\* and G.S. Hufford\*\*

CFD Research Corporation

Huntsville, AL 35805

and

T. Marquette\*\*\*

Naval Air Warfare Center - A/D

Warminster, PA 18974

### ABSTRACT

A numerical investigation using a full Navier-Stokes code has been conducted on the B-1A escape capsule. This study is part of an ongoing validation effort of a CFD methodology for escape system analysis. Results were obtained for two similar but slightly different surface models of the escape capsule at Mach numbers of 0.3, 0.95, and 2.2 for pitching angles ranging from -30 to +30 degrees. Results are presented in the form of force, moment, and pressure coefficients and compared to wind tunnel test data at all conditions. Comparisons to previous Euler results are given at  $M = 0.3$  for pitching angles from -15 to +15 degrees. Surface pressure and flow contours are also included to highlight details of the flow field. Analysis of the results shows that a full Navier-Stokes code can accurately obtain coefficient information for this class of blunt body problems. This analysis also showed that proper surface geometry modeling is critical for the success of this type of CFD study.

### INTRODUCTION

Aircrew extrusion from aircraft during distress is mainly done using open ejection seats nowadays due to their lower cost and weight penalties compared to closed escape systems. However, several escape capsules have been developed for use in U.S. tactical aircraft including the USAF F-111 capsule which is currently in operation. Escape capsules are still being considered for use in future aircraft, especially those traveling at

very high altitude approaching hypersonic speeds. The attraction to escape capsules for crew removal is the increase in safety due to protection from high pressure and thermal loads that are usually associated with open ejection seats. The B-1A escape capsule, Figure 1, was developed in the early 1970's but was never selected for use in the final production B-1B aircraft. However, a significant amount of wind tunnel testing was conducted on small scale models including a 0.036 model<sup>1</sup> at several Mach numbers including 0.3, 0.95 and 2.2.

Computational Fluid Dynamic (CFD) methods have been recently evaluated and considered for escape system analysis<sup>2-4</sup>. The most promising and applied code has been developed by the authors of this paper. This code utilizes the full Navier-Stokes method and has been validated against wind tunnel test data of several ejection seats<sup>5-7</sup>. The purpose of this study was a further validation of the CFD technology for escape system application using the B-1A escape capsule due to the availability of its wind tunnel data.

The B-1A escape capsule has a blunt body with a flat bottom and flat rear with vast separation and recirculation zones. It has already been analyzed using panel methods and using the Euler MERCURY code. It was concluded from the Euler analysis that a Navier-Stokes solution is required due to the dominance of the viscous effects.<sup>3</sup>

\*Group Leader/Research, Member AIAA

\*\*Project Engineer, Research, Member AIAA

\*\*\*Member AIAA

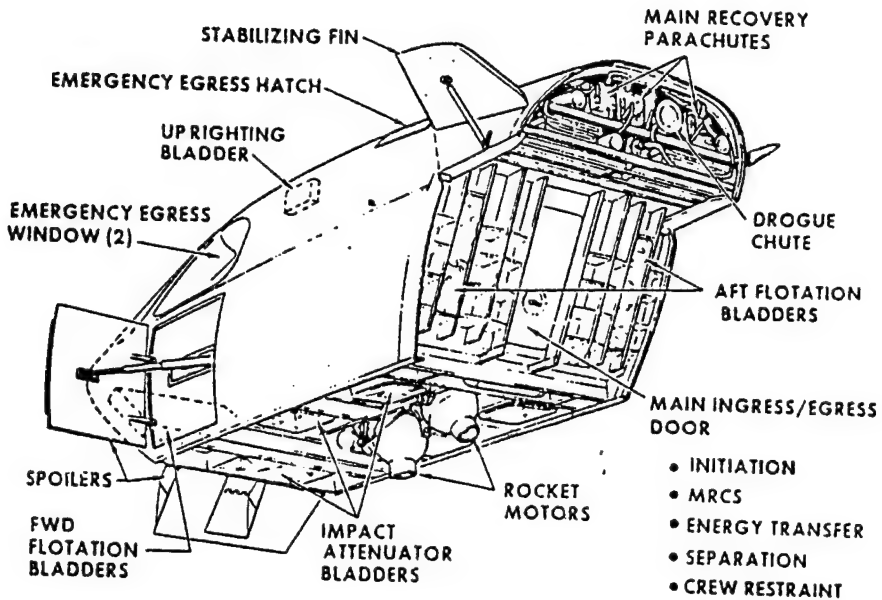


Figure 1. B-1A Escape Capsule

This paper presents the results of a three-dimensional analysis of the B-1A escape capsule using the full Navier-Stokes code developed for ejection seat applications. These simulations were conducted using the  $k-\epsilon$  turbulence model and several high order differencing schemes. Due to questions regarding the upper surface of the escape capsule, two escape capsule models were analyzed. The results are compared to wind tunnel test data and Euler method results that were obtained using the MERCURY code. The geometry and computational grid were created using state-of-the-art CAD tools and elliptic grid generation methods. Computations were performed for several angles of attack at Mach numbers of 0.3, 0.95, and 2.2. The results presented in this paper were performed on an IBM RISC/6000 workstation with reasonable amount of human effort and modest computational requirements.

The remaining sections of this paper briefly discuss the numerical method and explains the geometric modeling and grid generation procedure. The results will be presented and compared to wind tunnel and Euler data followed by the conclusions made from the analysis.

#### Geometry Modeling and Grid Generation

Surface representation and grid generation issues are critically important for the overall success of the escape capsule CFD analysis. Questions regarding the upper surface definition of the B-1A escape capsule required that two separate (but similar) capsule geometries be analyzed. The effects of the differing escape capsule models on the resulting surface pressure and aerodynamic force and moment coefficients are quite interesting. These results are presented and discussed in later sections.

The first escape capsule model analyzed is the same representation used in previous Euler computations<sup>3</sup>. This representation was obtained in the form of IGES curves and a structured Plot-3D surface grid shown in Figure 2. Note that the IGES curves are selected lines in the Plot-3D grid. B-spline surfaces were obtained using the Icem-CFD grid generation environment<sup>8</sup> by interpolating between the IGES curves. With this surface, a computational surface grid of arbitrary resolution can be constructed using the Icem-CFD grid generation environment.

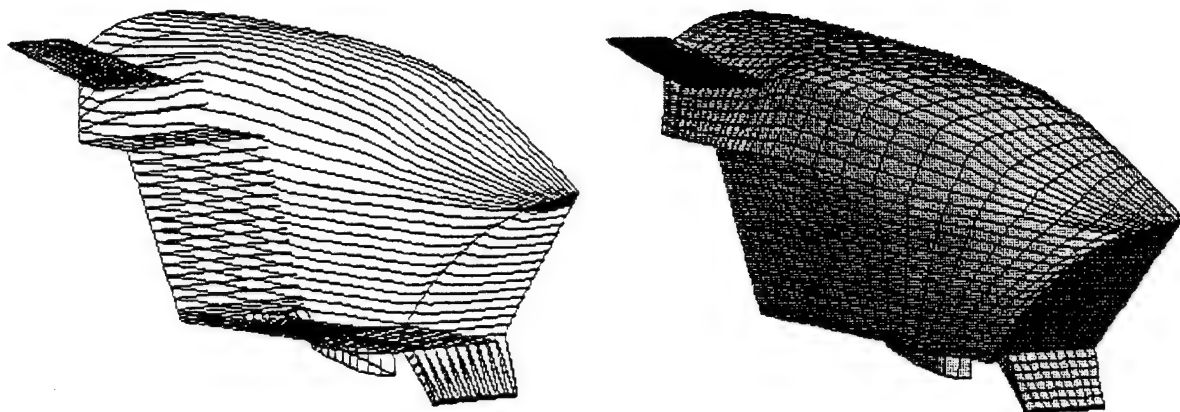


Figure 2: B1-A escape capsule, Model 1; Left: IGES Curves; Right: Plot-3D.

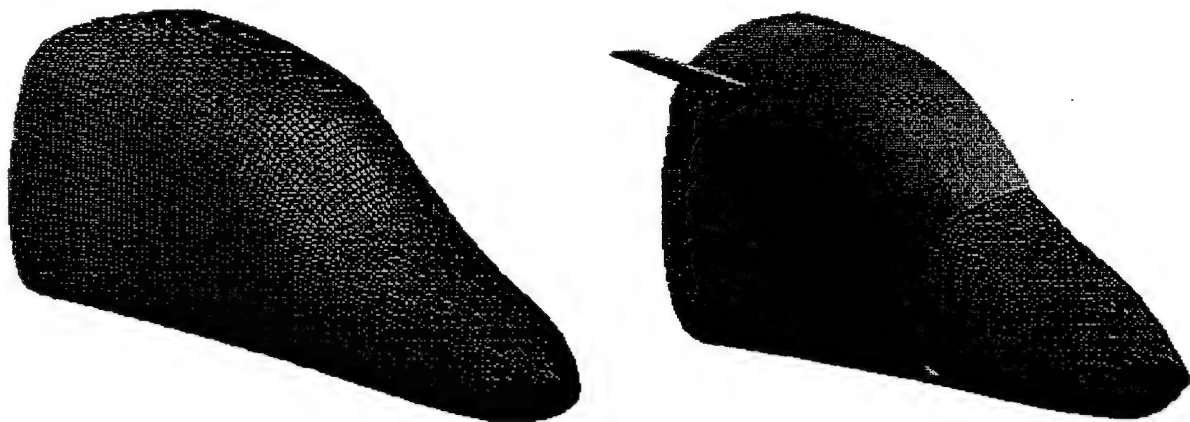


Figure 3: External surface representation of B1-A aircraft nose. Figure 4: Overlay of B1-A aircraft with Model 1 escape capsule.

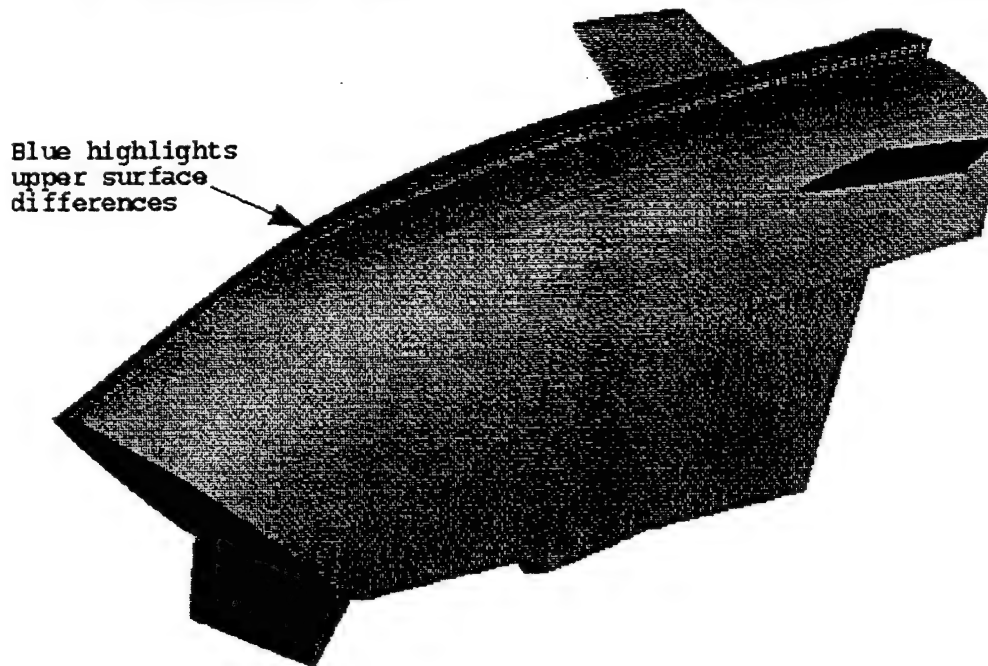


Figure 5: Comparison between the two surface models of the escape capsule. Left: Model 1. Right: Model 2 (from aircraft surface).

Comparisons between the modelled upper surface of the escape capsule with pictures from the experimental results<sup>1</sup> raised questions about the integrity of the CFD surface model. This led to the use of an alternate upper surface representation obtained from a structured Plot-3D grid of the B-1A aircraft shown in Figure 3. The alternate representation was obtained by overlaying the aircraft Plot-3D grid with a Plot-3D grid of the first escape capsule model to locate the relevant portion of the aircraft geometry for the escape capsule as shown in Figure 4. The CFD-GEOM grid generation package<sup>10</sup> was used to extract the aircraft geometry from the Plot-3D grid and merge it with the first escape capsule model. The difference between the two models is limited to the upper surface differences. Figure 5 shows representations of the first and second capsule models together. Note that the second capsule model is slightly below the first capsule model and the surface curvature is different, especially just aft of the nose. The Model 2 surface representation was used for all the results presented in the next section. Selected results from the Model 1 surface (the surface analyzed with the MERCURY code) are presented to illustrate the error introduced by the erroneous surface geometry.

The computational structured grid surrounding the capsule was created using an elliptic grid generator which uses line and orthogonal attraction through Poisson forcing functions. Several grid sizes were used to determine the sensitivity of results to grid resolution and to obtain grid independent results. Figure 6 shows the selected computational grid at the symmetry plane in the immediate surroundings of the capsule using the Model 2 geometry.

#### Numerical Approach

The blunt body shape of the escape capsule at high Reynolds number results in highly turbulent flows around the capsule and in the wake behind it. To accurately predict the forces on the surface and especially in the wake region, the full Navier-Stokes equation has to be solved. Further, at transonic and supersonic speeds, multiple shocks will form around and on the surface changing the flow field characteristics.

To accurately predict the locality of these shocks and their effect on the capsule forces and moment coefficients, a high order numerical shock capturing scheme that possesses good shock capturing capabilities has to be utilized.

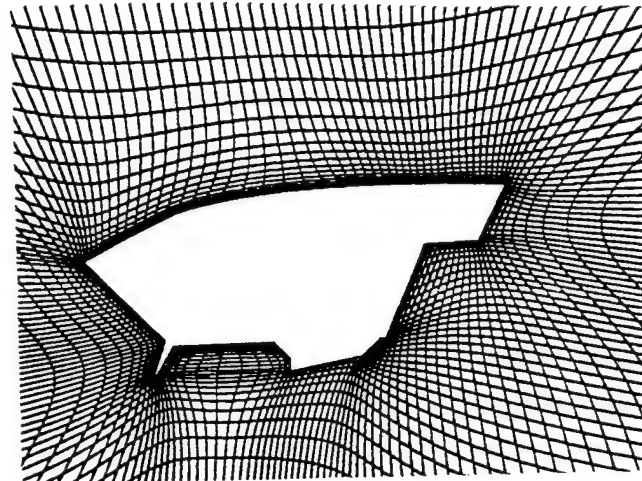


Figure 6. Computational Grid at the Centerline of the Capsule

The CFD code used for the present analysis (CFD-ACE)<sup>10</sup> solves the full Navier-Stokes equation in general curvilinear coordinate systems. The code employs structured grid techniques and is based on a finite volume pressure-based approach that uses a colocated grid arrangement of flow variables. The code is based on a strongly conservative formulation<sup>11</sup> for the N-S equations which preserve free stream properties and possesses good shock capturing capability. The flow variables are solved sequentially using a modified version of Stone's solver<sup>12</sup>. The code also employs high order differencing schemes including central differencing, Osher-Chakravarthy, second-order upwind, in addition to the first-order upwind scheme. For the present calculations, a high order scheme was used for all calculations.

A standard k- $\epsilon$  turbulence model was used for this analysis to model and capture the viscous effects associated with the wake and the surface of the capsule. The k- $\epsilon$  turbulence model has been

proven to capture the correct pressure fields for separated and recirculating type flows<sup>12</sup> and has given good results that compare well with wind tunnel test data for ejection seat<sup>4-5</sup> analysis previously conducted under this study.

## COMPUTATIONAL RESULTS

Computations were performed for free stream Mach numbers of 0.3, 0.95, and 2.2 at wind tunnel conditions<sup>1</sup>. Several angles of attack were considered including  $\alpha = -30, -15, 0, 15$ , and  $30$  degrees. Table 1 below shows the matrix of the test cases for this study.

Results of  $M=0.3$  calculations will be first presented and compared to wind tunnel test data and MERCURY code results. They will be followed by results from  $M=0.95$  and  $M=2.2$  calculations which will also be compared to wind tunnel test data. Note that MERCURY code results were only available at  $M=0.3$ .

Figure 7 presents the force and moment coefficients from the  $M=0.3$  present calculations (using Model 1 and Model 2 geometries) along with the wind tunnel test data and those of the MERCURY code. Overall, the results of the present study compare well with test data, and much better than those of the MERCURY code, especially for zero and positive pitching angles. Note however that the MERCURY code results may have been obtained with the erroneous geometry of Model 1. Results for the Model 1 surface obtained with CFD-ACE are better than the available MERCURY results however, they are worse than the Model 2 results. Both CFD calculations compare better to test data at the

higher pitching angles ( $\alpha > 0$ ) for drag and lift coefficients (CD and CL). The pitching moment from the present calculations using the Model 2 geometry, however, shows excellent agreement with test data at the lower pitching angle ( $\alpha < 0$ ) and some deviations at  $\alpha = 15$  and  $30$  degrees. This behavior is puzzling considering that CD and CL show very good agreement while CM shows the largest deviation from test data. The MERCURY code results for CM show a large discrepancy with test data throughout the whole pitching envelop considered (part of this deviation may be due to the geometry errors of Model 1). The reason for the larger discrepancies of CD and CL between CFD and test results at the negative pitching angles may be explained by the surface pressure coefficients shown below in Figure 8.

Figure 8 compares the surface pressure coefficient to test data at several locations where wind tunnel measurements were taken. Figure 9 shows the location of pressure taps where the measurements were made<sup>1</sup>. Figure 8 (top right) shows that at  $\alpha = -15$ , the predicted pressure coefficient for the Model 2 geometry at the top surface (points 1, 2, 3, 4, and 5 in Figure 9) of the capsule stays constant after the third measurement point while the test data show a monotonic decrease in pressure all the way to the rear of the capsule. This calculated higher pressure at the top contributes to the predicted higher CD and lower CL values shown in Figure 7 for  $\alpha < 0$ . At  $\alpha = 15$  (bottom right) the comparison of  $C_p$  on the top surface is much better especially near the rear of the capsule.

Table 1. Escape Capsule Simulation Cases

$\alpha$	$\beta$	$M = 0.3$	$M = 0.95$	$M = 2.2$
-30	0	X	X	X
-15	0	X	X	X
0	0	X	X	X
15	0	X	X	X
30	0	X	X	X

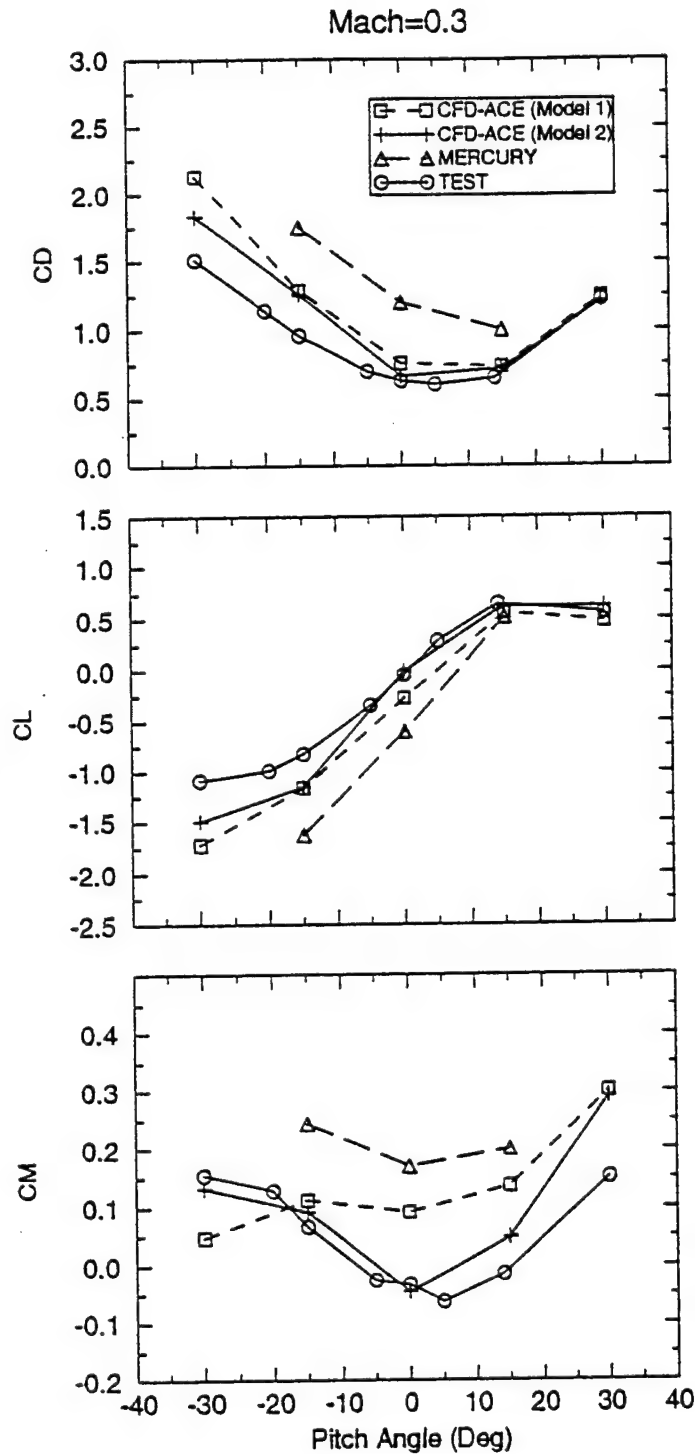


Figure 7. Comparison of Force and Moment Coefficients to Wind Tunnel Test Data and MERCURY Code Results;  $M = 0.3$

The reason for the discrepancy in  $C_p$  values at  $\alpha = -15$  may be due to the lack of capturing a growing boundary layer at this orientation due to not using a fine enough grid resolution in this region. Figure 8 (right) also illustrate the magnitude of the error introduced by the surface geometry. Model 1 predictions show large errors near the nose of the capsule and at the rear especially at  $\alpha = 0$  and 15 degrees. The major part of this error is due to the differences in the top surface geometry shown earlier in Figure 5. Therefore, based on this finding it is believed that better agreement may have been obtained with the MERCURY code if the correct surface geometry was used.

Figure 8 (left) also presents comparisons of  $C_p$  values between the present Model 2 calculations, test data and MERCURY code results at the front and bottom surfaces of the capsule. At  $\alpha = 0$  and 15 degrees the agreement with test data is excellent at the front surface (points 15, 16, and 24). This is due to the front surface being almost perpendicular to the oncoming flow at these orientations (see pressure contours presented in Figure 12). At  $\alpha = -15$ , the spoiler affects the flow on the front face and introduce some perturbations which in turn result in a small discrepancy between predicted and test results. On the bottom surface (points 19, 20 and 21 in Figure 9) the present results compare well to test data especially at  $\alpha = 0$  and -15 degrees. This indicates that the present CFD code captures the viscous effects due to the flow recirculations caused by the presence of the spoiler.

Figure 10 shows comparisons of the pressure coefficient at the rear bottom surface (point 33) and rear upper surface (point 34). The agreement between the present calculations and test data at the upper surface (point 34) is excellent for all orientations and better than the MERCURY predictions as expected. At the lower rear surface (point 33) the agreement is not as good. This may be due to the strong viscous interaction not completely being captured because of lack of grid resolution in that region. This agreement is worst at  $\alpha = -15$  degrees where the recirculation zone is the biggest as shown later in Figures 11 and 12.

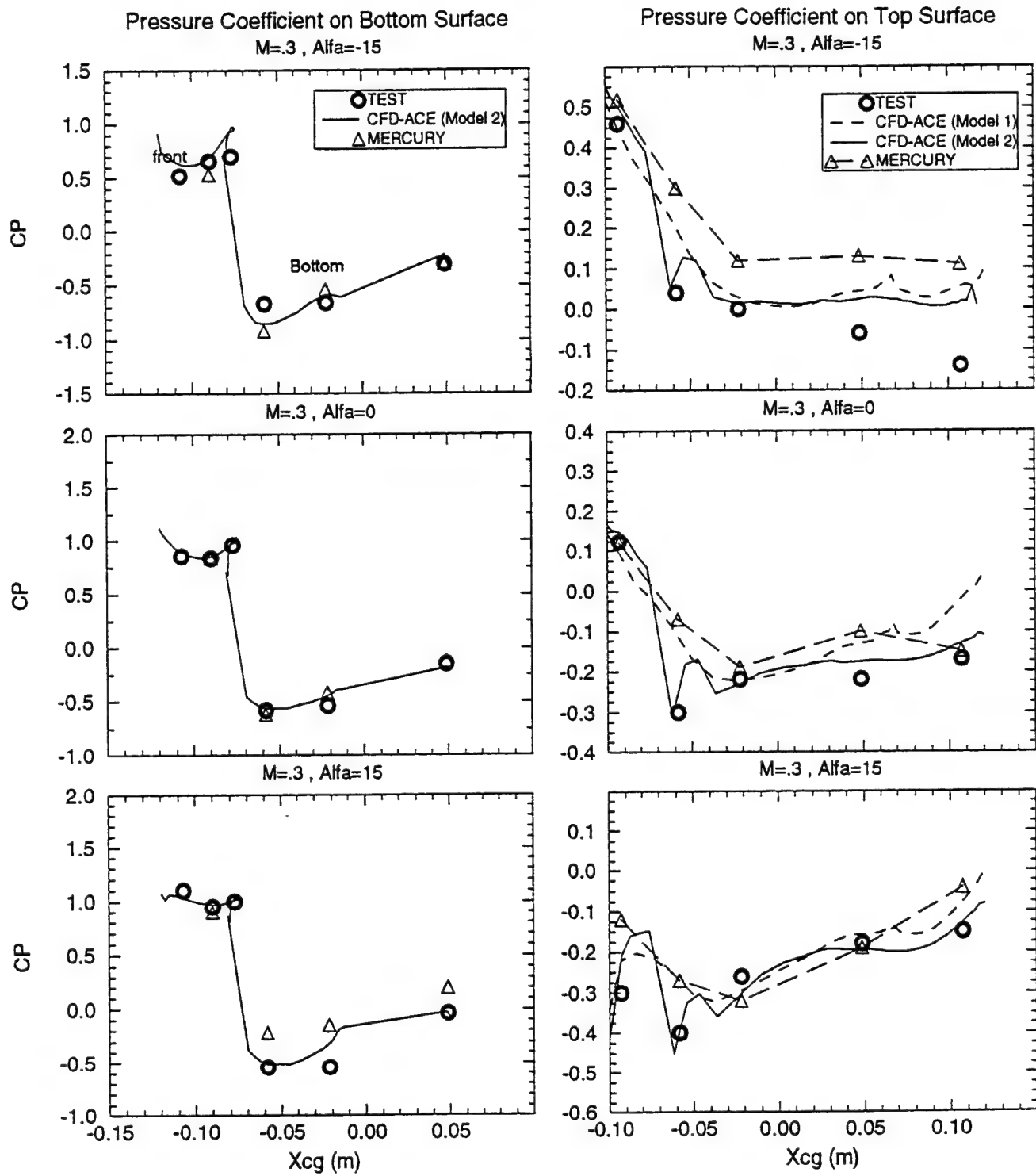
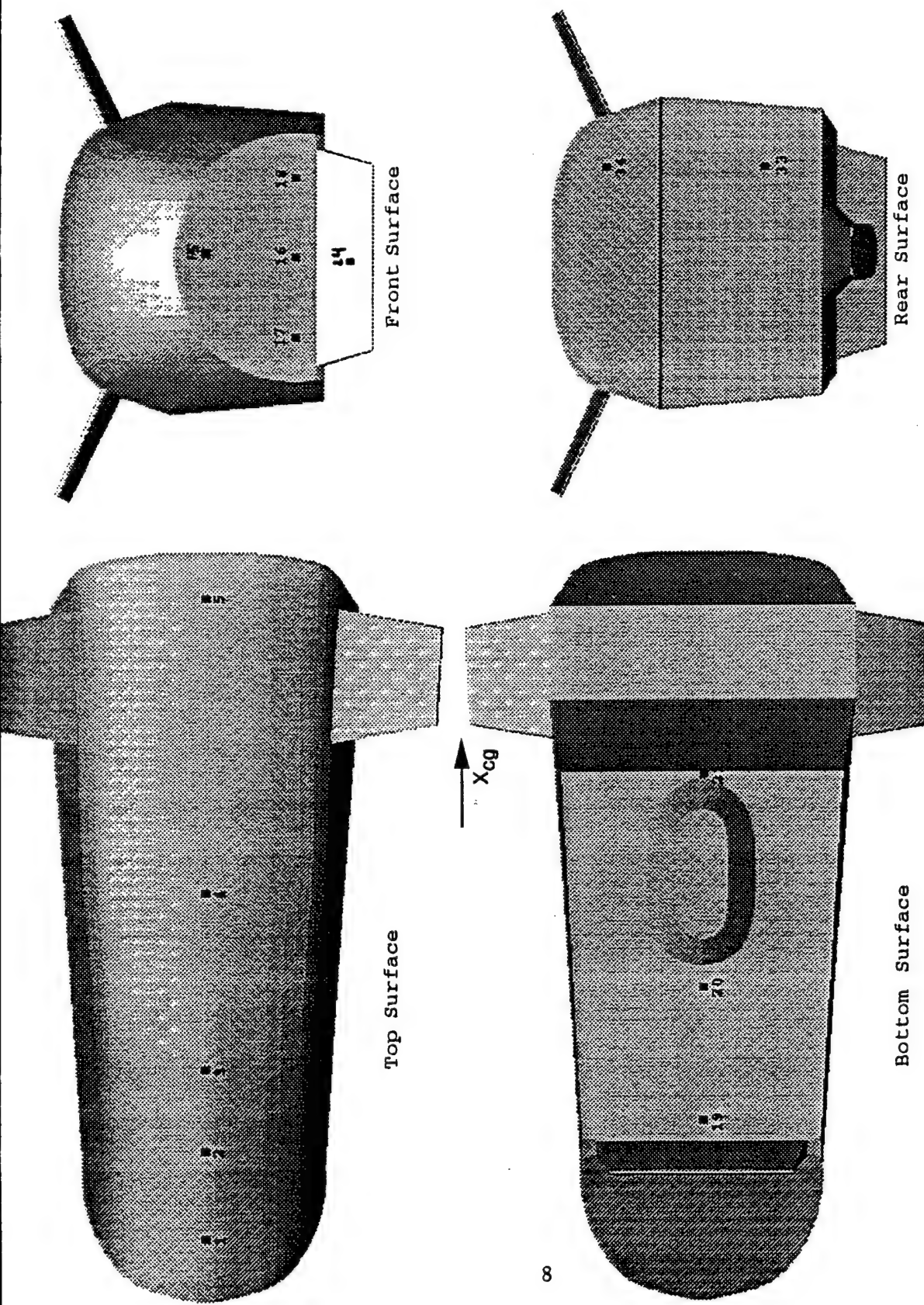


Figure 8. Predicted and Measured Force Coefficients for  $M = 0.3$  for Top, Front and Bottom Surfaces



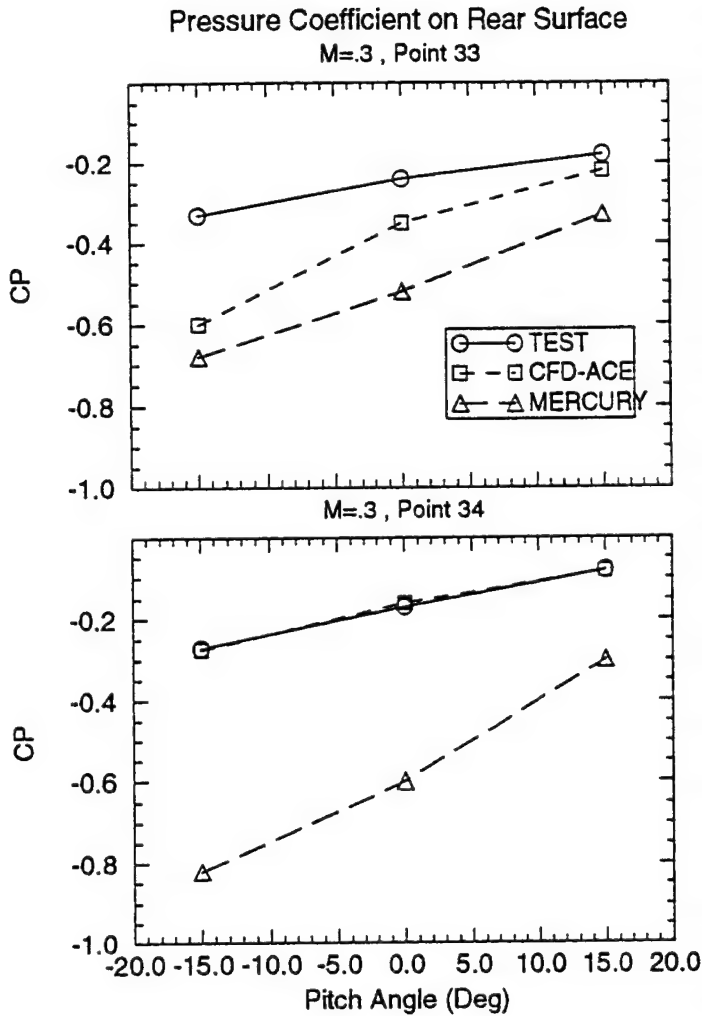


Figure 10. Comparison of the Pressure Coefficient to Wind Tunnel Test Data at (a) the bottom rear of the capsule; and (b) top rear of the capsule

The flow behavior and construction around the capsule may be better understood by the velocity vectors. Figure 11 shows the velocity vectors near the centerline of the capsule for  $\alpha=-15, 0$  and  $15$  degrees at  $M=0.5$ . At  $\alpha=0$  and  $-15$ , the presence of the spoiler dominates the flow as it forces separation away from the bottom of the capsule creating a large recirculation zone behind it and low pressure regions are shown in Figure 12. Figures 12 also shows the high pressure encountered at the front surface of the capsule at

$\alpha=0$  and  $15$  degrees. At the negative pitching angles the recirculation zone gets stronger and bigger as it covers the rocket housing and causes a strong upward motion of the flow that impinges on the bottom back of the capsule. Figure 11 also indicates that two large recirculation zones may take place near the outer surfaces of the capsule due to the strong upward motion that takes place near the symmetry plane separating between the two zones on the sides. To investigate this further the velocity vectors are drawn at several cross planes along the capsule and in the wake to show the progression of the flow and the formation of the recirculation zones as shown in Figure 13. A strong recirculation zone forms below the capsule right after the flow goes past the spoiler (Figure 13a). The recirculation zone gets wider as the flow moves downstream and eventually occupies most of the area below the tail of the capsule (Figure 13d). This large recirculation zone moves upward and gets weaker as the flow moves away from the capsule (Figure 13g and 13h). Figure 13 also shows that a swirling flow forms downstream of the tip of the fins and gets bigger and weaker finally disappearing as the flow moves farther downstream of the capsule (Figure 13h).

Figure 14 presents the force and moment coefficients from the present calculations and compares them to test results at  $M=0.95$  and  $M=2.2$ . Overall the agreement is much better between CFD predictions and test data at the higher Mach numbers than at  $M=0.3$ . This is expected due to the weaker viscous interaction and smaller recirculation zones which makes the results less dependent on turbulence and other numerical and physical modeling. The agreement is within 15 percent throughout except for the pitching moment at  $\alpha=30$  for  $M=0.95$  and  $\alpha=-30$  for  $M=2.2$ . Like the pitching moment for  $M=0.3$  at  $\alpha>15$ , this behavior could not be explained since both CD and CL compare very well at these conditions. Figure 15 and 16 compare the pressure coefficient at the front, bottom and top surfaces to test data at  $M=0.95$  and  $M=2.2$  respectively. At  $M=0.95$  the agreement on the front face is excellent, however at  $M=2.2$  some discrepancies are observed and may be due to the presence of the bow shock located very close to the nose of the capsule as shown later in Figure 17.

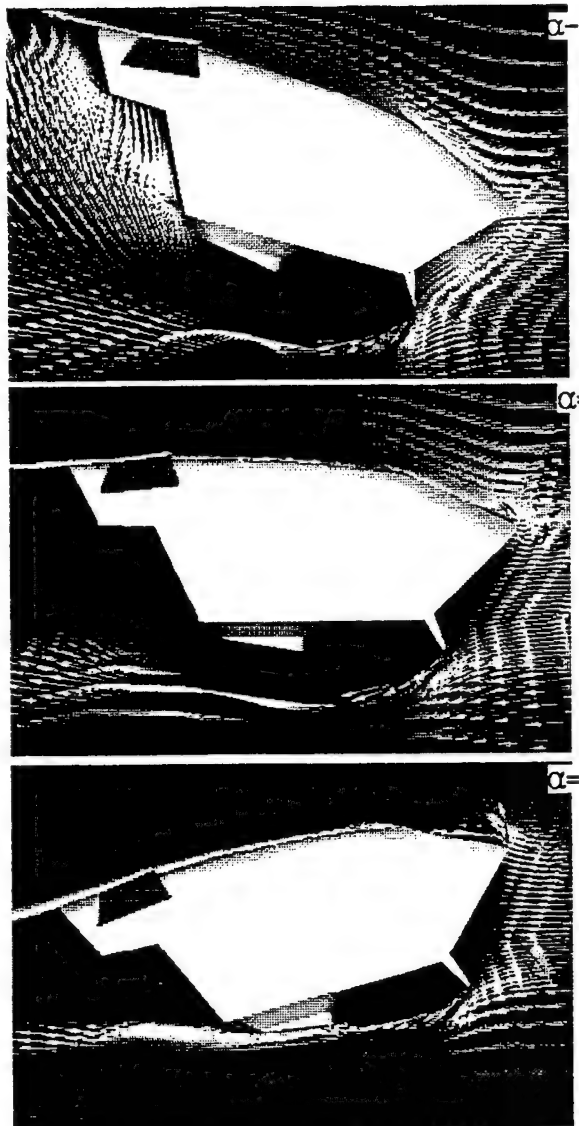


Figure 11: Velocity vectors at the symmetry plane for various pitch orientations ;  $M=0.3$ .

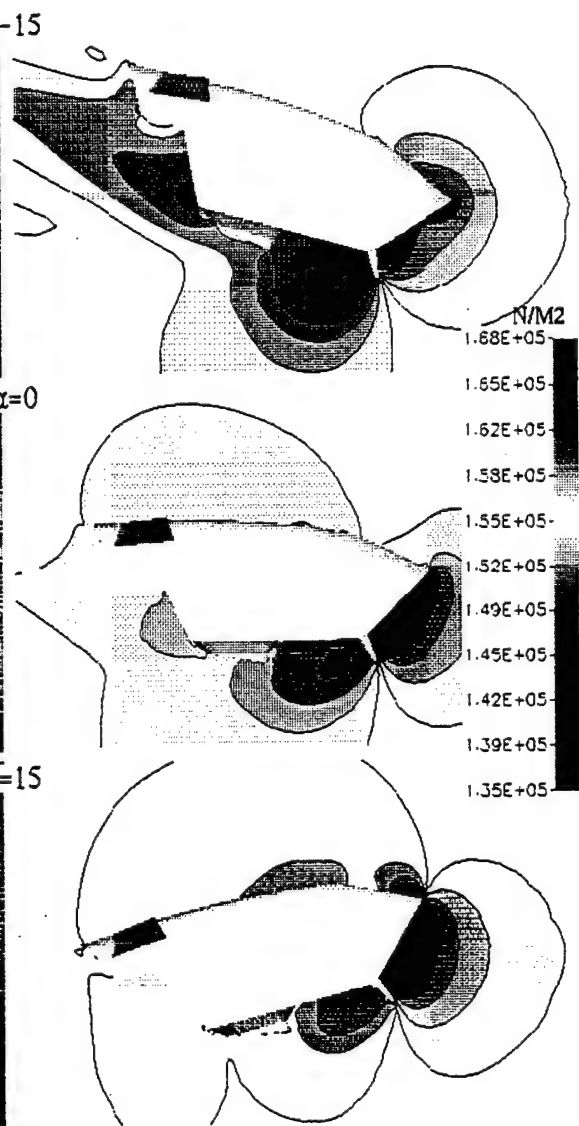


Figure 12: Pressure contours at the symmetry plane for various pitch orientations ;  $M=0.3$ .

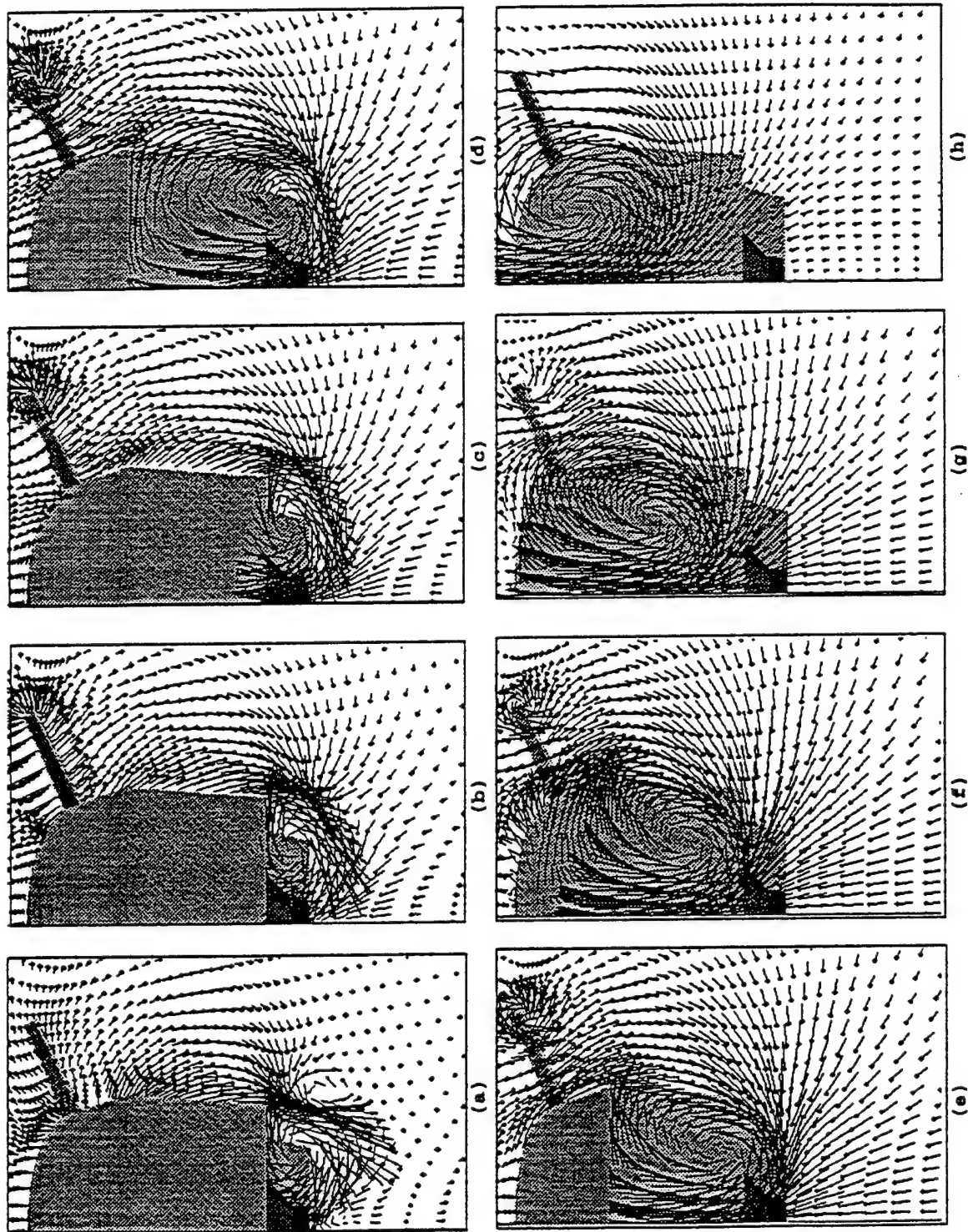


Figure 13. Velocity Vectors at Selected Computational Planes along the B-1A Capsule;  $M = 0.3, \alpha = 0$

(a)-(h): from front to rear of the capsule

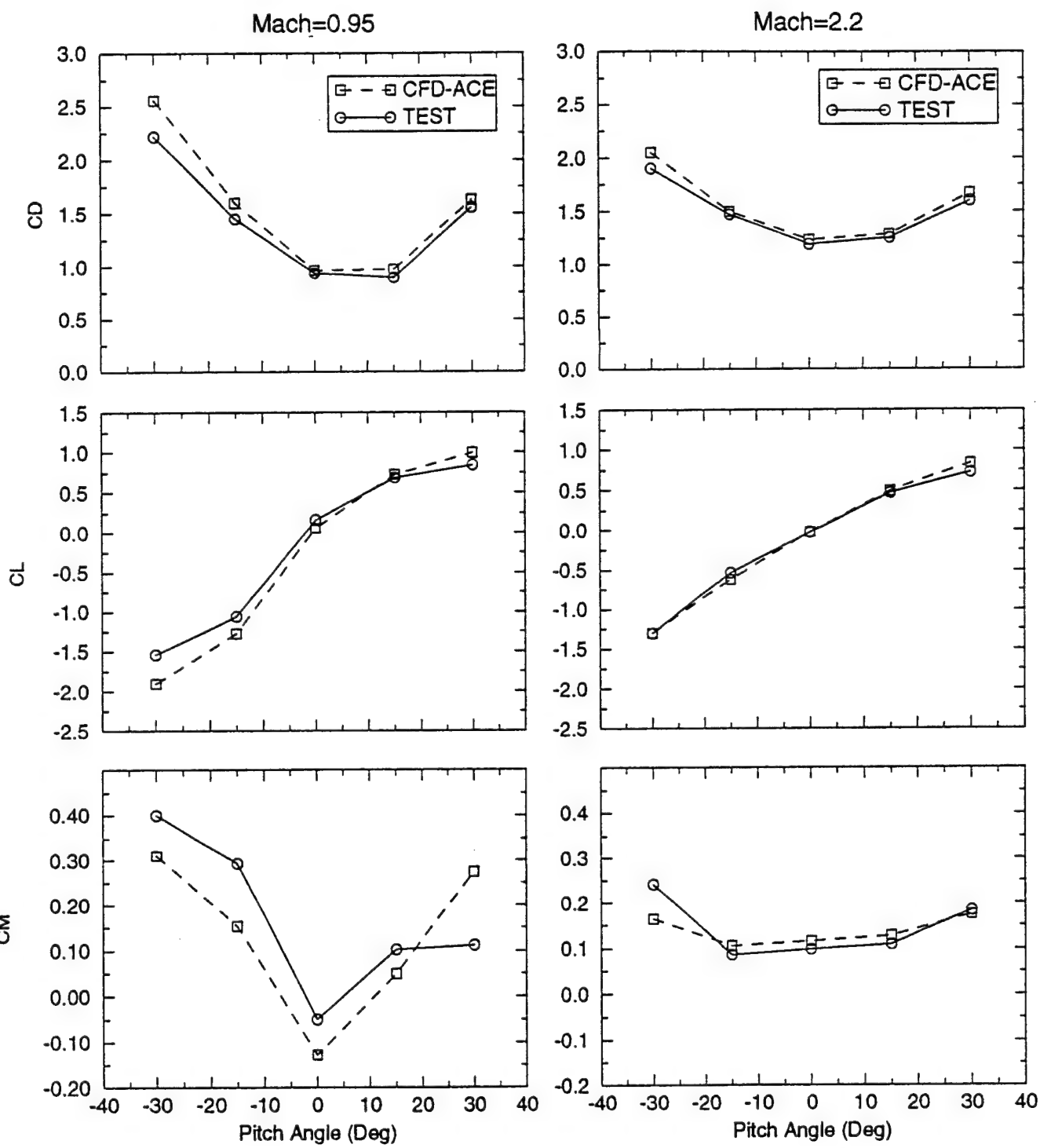


Figure 14. Comparison of Force and Moment Coefficients to Wind Tunnel Test Data

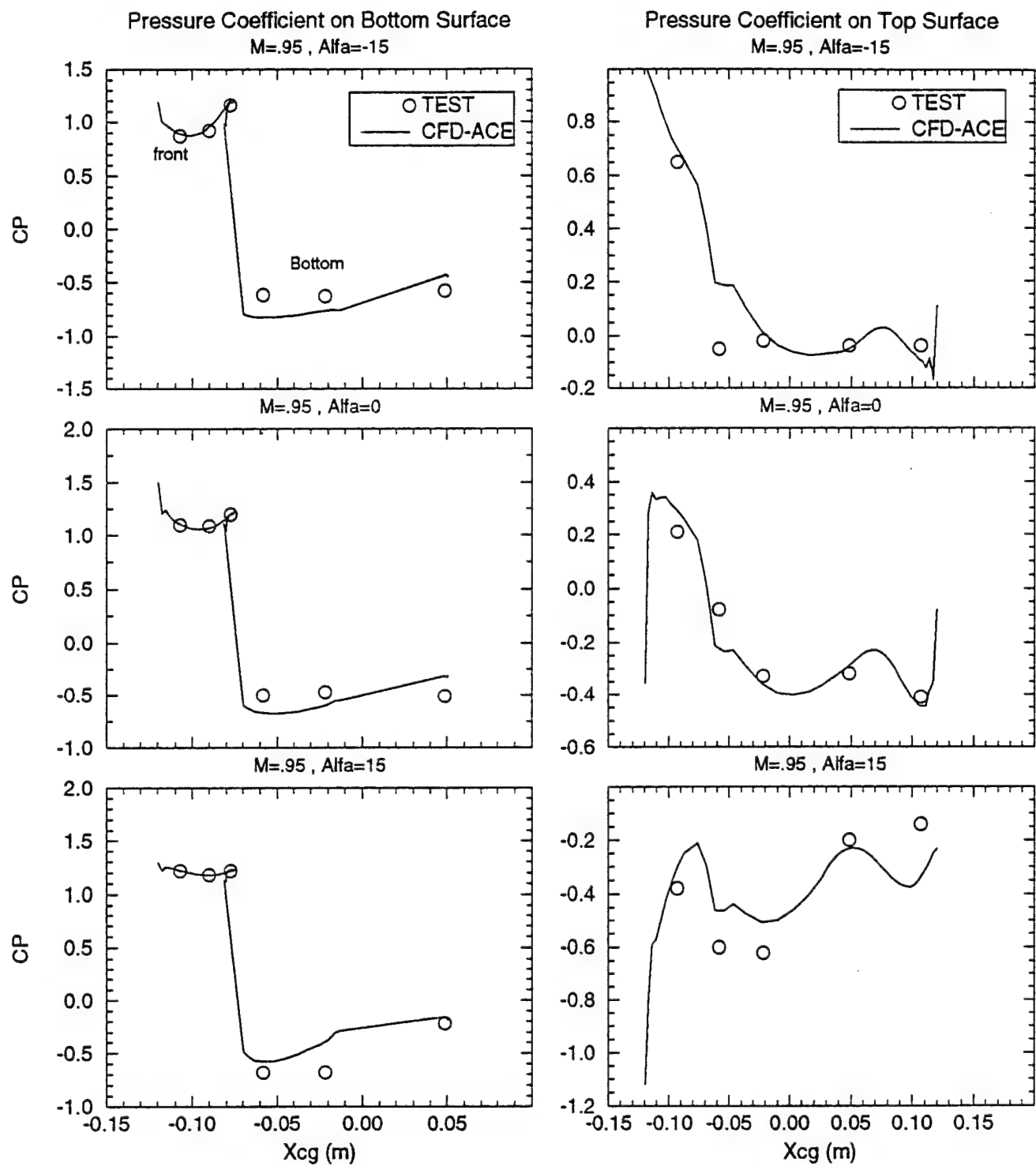
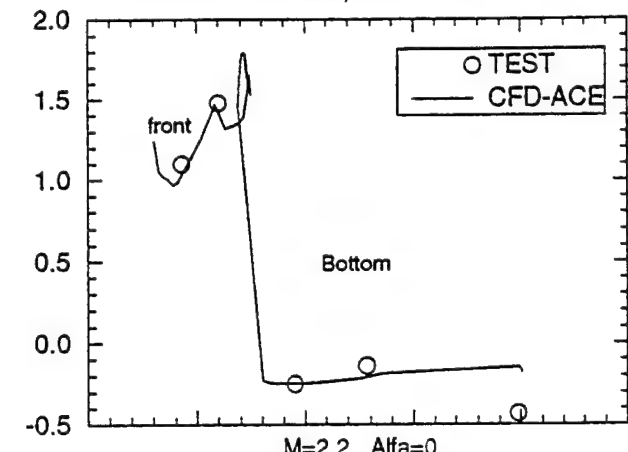


Figure 15. Predicted and Measured Force Coefficients for  $M = 0.95$  for Top, Front and Bottom Surfaces

Pressure Coefficient on Bottom Surface  
 $M=2.2$  ,  $\text{Alfa}=-15$



Pressure Coefficient on Top Surface  
 $M=2.2$  ,  $\text{Alfa}=-15$

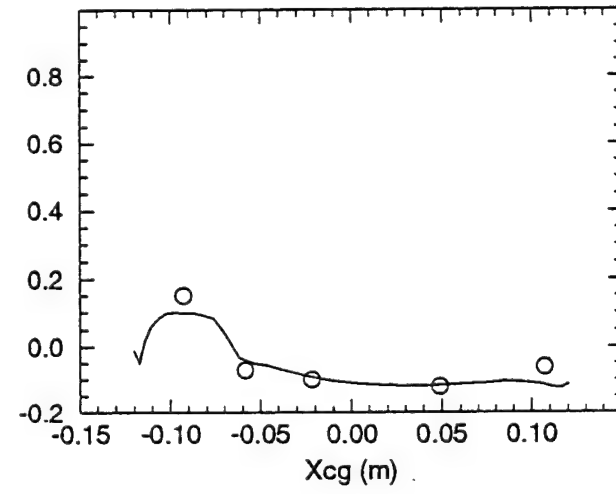
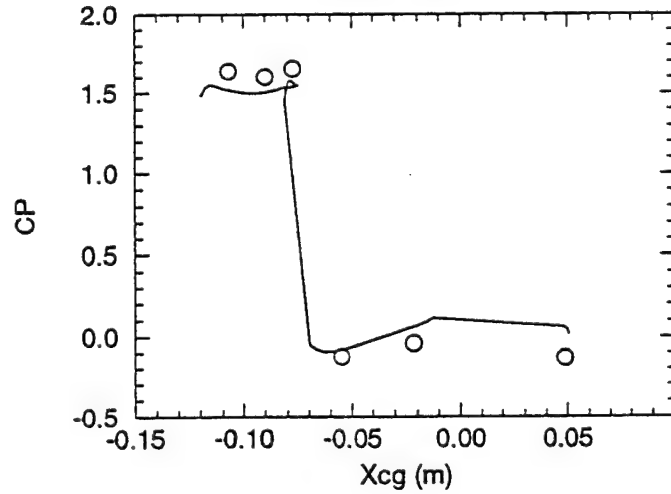
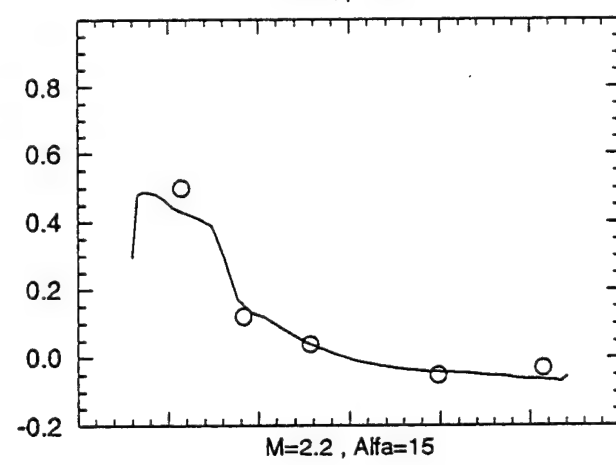
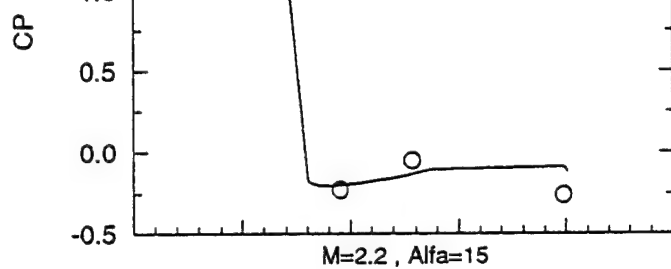
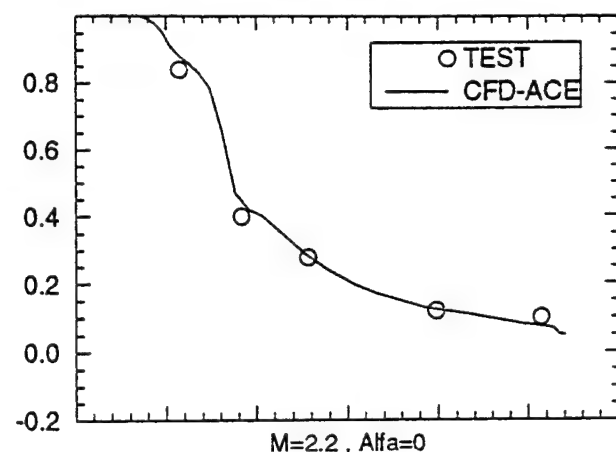


Figure 16. Predicted and Measured Force Coefficients for  $M = 2.2$  for Top, Front and Bottom Surfaces

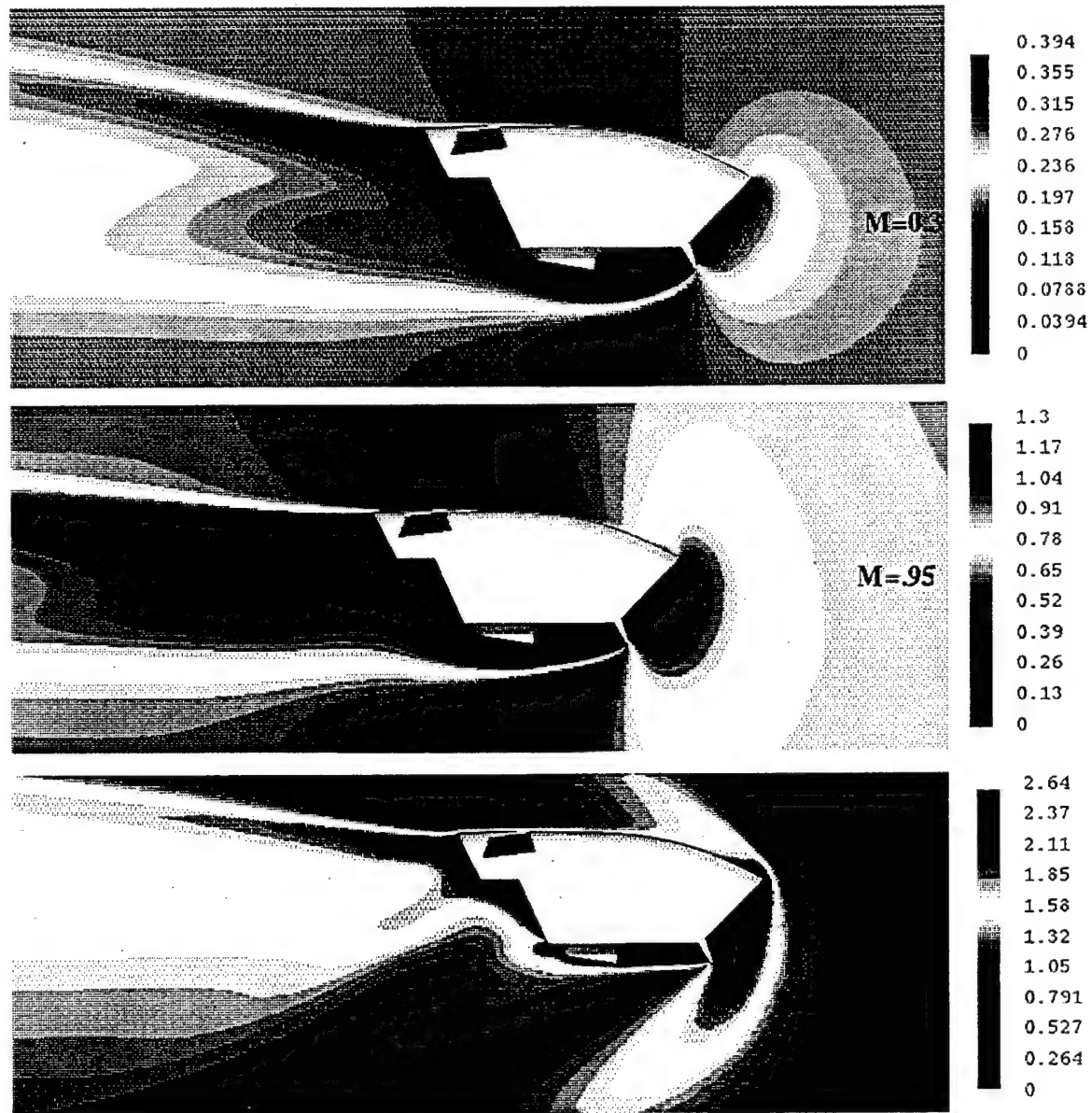


Figure 17: Mach number contours at the symmetry plane for various free stream Mach number conditions

Some numerical noise usually takes place around the shock especially when using a high order differencing scheme like the Osher-Chakravarthy third order scheme used for these cases. At the bottom face agreement is better at  $M=2.2$  due to the narrower and smaller recirculation zones and in turn weaker viscous effects. At the top surface the agreement is good for  $M=2.2$  and some discrepancies are shown for  $M=0.95$  especially at the back of the capsule at  $\alpha=15$  degrees.

Finally, to show the differences in the flow structure and progression for the various free stream Mach numbers, the Mach number contours at the symmetry plane are shown in Figure 17. At the subsonic  $M=0.3$  condition, the flow approaches the capsule with increasing pressures and decreasing Mach numbers. Separation is formed at the bottom of the spoiler and at the rear top of the capsule. At  $M=0.95$  several reflected shocks are observed including one at the spoiler and one on the top surface at the end of the windshield. An expansion fan is also formed at the rear of the top surface. At  $M=2.2$ , the flow is dominated by a strong bow shock located near the front nose of the capsule and the spoiler. Several shocks also take place at the fins surface which is not shown in this figure.

## SUMMARY AND CONCLUSIONS

Numerical calculations using advanced CAD and grid generation tools and 3D full Navier-Stokes code have been conducted on the B-1A escape capsule in free stream conditions. Results were obtained for various Mach numbers and pitch angles. Force, moments and pressure coefficients were calculated and compared to wind tunnel test data and earlier Euler code results.

The present CFD results compared well to test data and much better than the Euler code results, at  $M=0.3$ , as expected since viscous interactions are important due to large recirculation zones that take place below and behind the capsule. At higher Mach numbers of 0.95 and 2.2 the present calculations compared very well to wind tunnel test data and better than at  $M=0.3$ . It was concluded from the present calculations that exact surface geometry modeling is crucial for

obtaining accurate results. It was also concluded that some of the discrepancies reported with the Euler results may be due to errors in the surface geometry representation.

It was also shown that a full Navier Stokes solution is capable of obtaining accurate results for this class of blunt bodied geometries.

## ACKNOWLEDGEMENTS

This research has been funded by the Naval Air Warfare Center, Aircraft Division at Warminster, PA under the sponsorship of Mr. F. Terry Thomasson, Naval Air Systems Command AIR-531. The authors would like to thank Mr. Peter Ayoub of NAWC-AD and Dr. Andrzej Przekwas of CFDRC for their technical guidance and support through this effort and Ms. J. Swann for the preparation of this manuscript.

## REFERENCES

1. Benson, J.M., "High Speed Wind Tunnel Tests of an 0.36 Scale Model of the B-1A Escape Module to Investigate General Stability and Control Characteristics," Rockwell Report NA-71-116, vol. 1-3, 1971.
2. Caruso, S.C. and Mendenhall, M.R., "Computational Analysis of High Speed Ejection Seats," AIAA-90-0403, Jan. 1990.
3. Wurtzler, K., "Application of an Euler Code to the B-1A Escape Capsule," AIAA-90-0431, Jan. 1990.
4. Baum, J.D., and Lohner, R., "Numerical Simulation of Pilot/Ejection Seat from an F-16," AIAA-093-0783, 1993.
5. Habchi, S.D., *et al*, "CFD Analysis of Ejection Seat Escape Systems," SAE Paper 921924, Aerotech, 92 Meeting, 1992.
6. Habchi, S.D., *et al*, "Computational Aerodynamic Analysis of the Navy Aircrew Common Ejection Seat," AIAA-94-0395, Jan. 1994.
7. Habchi, S.D., Hufford, G.S. and Przekwas, A.J., "CFD Analysis of NACES Seat with Yaw Fins Deployed at 60° Sweepback Angle," CFDRC Report 4129/1 for NAWC-A/D, August 1992.
8. Bertin, D., Lordon, J and Morcaux, V., "A New Automatic Grid Generation

Environment for CFD Applications,"  
Aerospatiale, 1992.

- 9. CFD Research Corporation, "CFD-GEOM:  
Users Manual" CFDRC Report GR-94-1,  
1994.
- 10. CFD Research Corporation, "CFD-ACE:  
Theory Manual," Version 1.0, CFDRC  
Report GR-93-1, Sept. 1993.
- 11. Yang, H.Q., Habchi, S.D., and Przekwas,  
A.J., "A General Strong Conservation  
Formulation of Navier-Stokes Equations in  
Non-Orthogonal Curvilinear Coordinates,"  
AIAA-92-0187, Jan. 1992.
- 12. Stone, H.L., "Iterative Solution of Implicit  
Approximation of Multi-Dimensional  
Partial Differential Equations," *SIAM J.  
Num. Annual*, vol. 5, 1968.
- 13. Rubeson, M.W., "Turbulence Modeling for  
Aerodynamic Flow," AIAA-89-0606, Jan.  
1989.

# TRANSIENT SIMULATION OF TURBULENT FLOW OVER BLUNT BODIES

by

S.D. Habchi\* and G.S. Hufford\*\*  
CFD Research Corporation  
Huntsville, AL 35805

## ABSTRACT

This paper focuses on the use of unsteady CFD methods for the turbulent flow over generic blunt bodies with specific interest in Ejection Seat configurations. The unsteady CFD simulations are compared to experiments as well as to steady state CFD results. The unsteady simulations include a fixed geometry with a resulting unsteady flow pattern as well as a rotating geometry. Particular attention is given to comparisons between time averaged CFD results and analogous steady state CFD results. Specific detailed demonstration problems include a cylinder and a generic 2-D ejection seat. A limited demonstration problem on a 3-D ejection seat is also included.

## INTRODUCTION

The analysis of the aerodynamic characteristics of fighter aircraft ejection seat systems has typically been done using wind tunnel and ejection sled experiments. Recently, computational fluid dynamics technology has been used to supplement these expensive testing procedures in the design and analysis of ejection seat systems. The use of computational fluid dynamics in ejection seat aerodynamic analysis provides many challenges to the CFD engineer. The ejection seat is an extremely complicated geometry operating in an unsteady, turbulent environment. For this reason the problem must be simplified to obtain meaningful results in an acceptable period of time. Much of the work to date has focused on using steady state simulations on the free flight ejection seat<sup>1-4</sup>. This work has focused on obtaining force and moment coefficients using the

steady state Navier-Stokes equations with  $k-\epsilon$  turbulence modeling for the NACES and ACES ejection seat systems as well as the B-1A Escape Capsule. Comparisons to experiment (discrepancies range from 5 to 20%) have shown this to be an adequate computational technique for predicting free flight ejection seat aerodynamic characteristics.

Although steady state techniques have proven adequate for engineering purposes, it is realized that unsteady effects can play a prominent role in any high Reynolds number blunt bodied problem such as the ejection seat. In particular the blunt bodied ejection seat configuration may produce unsteady Karman vortex like shedding even when the seat is in a non-rotating position. For seats ejected from an aircraft the unsteady translation and rotation of the seat provides added unsteady dimension. The implications of these unsteady effects on predicted force and moment coefficients as well as their implications in the ejection seat design process is a largely unexplored topic. Caruso and Mendenhall<sup>5</sup> briefly explored this topic for the non-rotating 2-D ejection seat problem using the Navier-Stokes equations without turbulence modeling while Baum and Lohner<sup>6</sup> focused on a full 3-D Euler simulation coupled to rigid body motion algorithm to simulate a pilot ejecting from an aircraft.

The focus of this paper is to assess the unsteady effects on generic blunt bodies using the unsteady Navier-Stokes equations with  $k-\epsilon$  turbulence modeling with specific interest in the ejection seat problem. Particular attention will be given

\*Group Leader / Research AIAA Member

\*\*Project Engineer / Research AIAA Member

to comparisons between time averaged unsteady CFD simulations and steady state CFD simulations and the resulting comparisons to available experimental results. Specific problems analyzed include a fixed cylinder, a fixed 2-D ejection seat and a rotating 2-D ejection seat. Also, limited simulations were performed on an unsteady fixed and rotating 3-D ejection seat. The analysis of these problems focuses on the differences between using time averaged force and moment coefficients from the unsteady simulations as opposed to the steady state simulations in the design process.

### **NUMERICAL APPROACH**

Flows over blunt bodies, such as the ejection seat, at high Reynolds number results in highly turbulent and viscous flow fields. To accurately predict the flow fields, especially in the wake region, the full Navier-Stokes equation must be solved. For unsteady calculations where vortex shedding patterns develop in the wake, accurate viscous and turbulence modeling along with a high order time marching scheme are essential for obtaining accurate results.

The CFD code used for the present analysis (CFD-ACE<sup>7</sup>) solves the full Navier-Stokes equations in a general curvilinear coordinate system. The code employs structured grid techniques and is based on a finite volume pressure-based approach that uses a colocated grid arrangement of flow variables. CFD-ACE has a conservative moving grid capability which was used under this study when the seat is pitched and the grid is adjusted accordingly. The code is based on a strongly conservative formulation<sup>8</sup> for the N-S equations which preserve free stream properties and possesses good shock capturing capability. The flow variables are solved sequentially using a modified version of Stone's solver<sup>9</sup>. The code also employs high order differencing schemes including central differencing, Osher-Chakravarthy, second-order upwind in addition to the first-order upwind scheme. For unsteady calculations the code uses a first order backward Euler and second order Crank-Nicholson time marching scheme. The code employs several methods for time stepping including using a constant time step that was used for the present

calculation. The CFD code also employs several turbulence models including the standard  $k-\epsilon$  and RNG turbulence models which were used for the present calculations. The results presented in this paper were obtained using the central differencing and second order upwind spatial schemes and the Crank-Nicholson time marching scheme.

### **RESULTS**

Calculations were performed in a step-by-step manner that started with flow over a cylinder at different Reynolds numbers. Calculations over a 2D ejection seat geometry were then performed at  $M = 0.6$  and followed by unsteady 3D ejection seat calculations. This section will first present the cylinder results, followed by the 2D and 3D ejection seat results.

#### **Cylinder**

The cylinder is a classic unsteady blunt body problem which results in Karman vortex shedding even when the cylinder is not rotating. Substantial experimental work has been completed on stationary as well as rotating and oscillating cylinders which is summarized in Schlichting<sup>10</sup>. In particular work by Jones<sup>11</sup> and Roshko<sup>12</sup> provides dual experimental results at the turbulent subsonic Reynolds number of  $M = .177$ ,  $Re = 8.27 \times 10^6$ . Additionally a substantial amount of previous steady state numerical work on turbulent subsonic cylinders has been previously presented by the authors<sup>3</sup>. The focus of the steady state numerical work was to determine the effects of grid resolution and turbulence modeling on the predicted drag coefficients and their comparison to the experimental results. The work presented in this section presents analogous unsteady CFD results for the unsteady turbulent cylinder problem and the resulting comparisons to experiment and the previous steady state work. Specifically results were obtained at  $M=0.177$  for Reynolds numbers of  $1.4 \times 10^4$ ,  $1.4 \times 10^5$ ,  $1.4 \times 10^6$ , and  $8.27 \times 10^6$ .

Before presenting the results, the issue of the initial conditions for these simulations and the resulting effect on solution uniqueness must be addressed. In the steady state simulations an

unperturbed free stream condition was used to obtain the familiar steady state two vortex flow pattern shown in Figure 1. If the same initial condition is used in an unsteady simulation, the solution converges to the same steady state two vortex pattern of Figure 1. However, if a perturbed asymmetric initial condition is used with all other parameters unchanged (i.e., same time-step, boundary conditions, differencing schemes and grid) a periodic Karman vortex shedding pattern is realized as shown in Figure 2. Different perturbed initial conditions have been used to obtain the same periodic vortex shedding pattern. Thus, the ability exists to obtain a non-unique numerical solution to the cylinder problem depending on the initial condition used. In nature (or the wind tunnel) the periodic vortex shedding pattern is observed. The ability to obtain a steady state numerical solution (even if a transient simulation is done) suggests that the vortex shedding pattern observed in nature is triggered by the inherent perturbations present in the initial flow field. These observations show that even though steady state numerical solutions may be obtained for the blunt body problem, they may not be unique solutions.

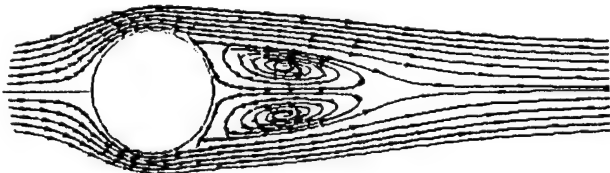


Figure 1. Typical Steady State Flow Field Pattern;  $M=0.177$ ,  $Re = 8.27 \times 10^6$

Even though the flow field pattern for the steady state and periodic solutions are somewhat different, the real question from a design and analysis point of view is: How different are the force and moment coefficients obtained from the unsteady results as opposed to the steady state results?

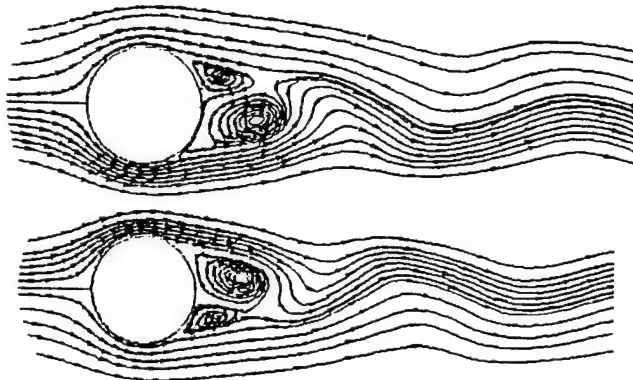


Figure 2. Typical Unsteady Vortex Shedding;  $M = 0.177$ ,  $Re = 8.27 \times 10^6$

Before lift and drag experimental comparisons are made a comparison of the shedding frequency (Strouhal number) to experimental results is useful. An example of the unsteady vortex shedding frequency is observed by plotting the  $u$  and  $v$ -velocities as a function of time at a location of 1 cylinder diameter behind the cylinder as shown in Figure 3. Note that the flow settles to a steady periodic pattern after about 0.7 seconds in this case. The time step used for each of these cases was .001 sec. Table 1 shows the Strouhal number comparisons to experimental values given in Schlichting. The coarse grid results refer to a  $117 \times 87$  polar grid using a non-dimensional first cell spacing of  $2.621 \times 10^{-3}$  while the fine grid results refer to a  $117 \times 175$  polar grid with a non-dimensional first cell spacing of  $2.621 \times 10^{-5}$ . At a  $Re = 8.27 \times 10^6$  the coarse grid corresponds to  $y^+$  of about 500 while the fine grid corresponds to  $y^+ \sim 5$ . Note at the lower Reynolds number (laminar separation) the coarse grid results produce good comparison to experiment.

At the higher Reynolds number (turbulent separation) the coarse grid results are similar to the low Reynolds result and do not compare well to experiment. The fine grid produces results much closer to experiment although the RNG turbulence model results are somewhat better than the  $k-\epsilon$  results. Note that at  $1.4 \times 10^6$  a true periodic solution does not exist in nature due to the laminar/turbulent transition which occurs in this Reynolds number range. The CFD solution, which assumes turbulent flow everywhere, finds a periodic solution.

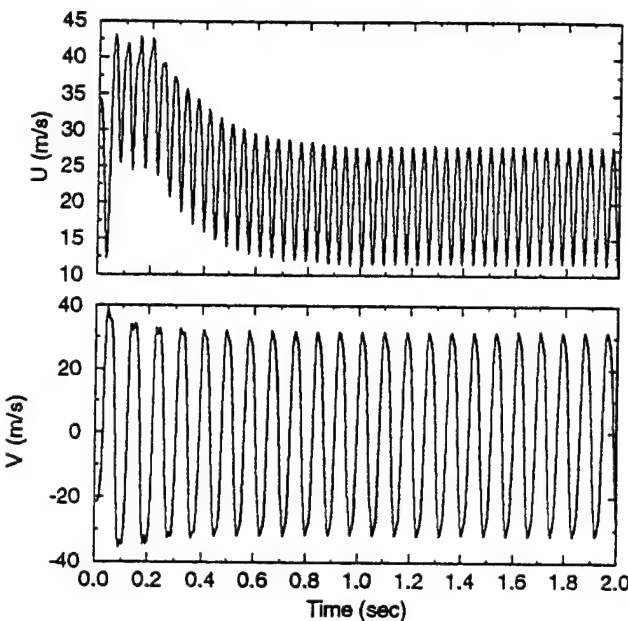


Figure 3. History of  $u$  and  $v$  Velocities at a Location Behind the Cylinder for  $M = 0.177$ ,  $Re = 8.27 \times 10^6$

Experimental steady state results for drag at  $Re = 8.27 \times 10^6$ ,  $M = 0.177$  have separately been obtained by Jones<sup>11</sup> and Roshko<sup>12</sup> to be .532 and .789 respectively. The difference in their results is due to a differing constant back pressure value in the separated region. Table 2 shows drag results at  $M = .177$ ,  $Re = 8.27 \times 10^6$  for the steady and unsteady cases. The unsteady value represents a time averaged value once the periodic vortex pattern was established. Figure 4 shows the drag and lift histories for the coarser grid with  $k-\epsilon$  turbulence model case. The steady state (2 vortex pattern) drag results do not compare very well to experiment. A thorough analysis of numerical factors affecting the steady state drag was presented in Reference 3. In particular the grid resolution and turbulence model constants significantly affect the resulting drag, an observation confirmed by the results in Table 2. The unsteady results in each case produced significant improvement in the drag predictions, especially for the RNG turbulence model. Even

Table 1. Computational Strouhal Numbers for  $M = .177$

Re	Turbulence Model	Grid	S	Experiment (Schlichting)
$1.4 \times 10^4$	$k-\epsilon$	coarse	.185	.198
$1.4 \times 10^5$	$k-\epsilon$	coarse	.179	.196
$1.4 \times 10^6$	$k-\epsilon$	coarse	.179	--
$8.27 \times 10^6$	$k-\epsilon$	coarse	.189	.292
$8.27 \times 10^6$	$k-\epsilon$	fine	.353	.292
$8.27 \times 10^6$	RNG	fine	.311	.292

Table 2. Steady and Unsteady Drag Results for  $Re = 8.27 \times 10^6$ ,  $M = .177$

Case	Grid	$C_D$	Case	Grid	$C_D$
Steady $k-\epsilon$	Coarse	.235	Unsteady $k-\epsilon$	Coarse	.303
Steady $k-\epsilon$	Fine	.19	Unsteady $k-\epsilon$	Fine	.37
Steady RNG	Fine	.28	Unsteady RNG	Fine	.76
CD from Experiment - Jones: .532, Roshko: .789					

the coarse grid case, which did not compare well for Strouhal number, has significant improvement although, less pronounced than the other 2 cases.

The difference in drag results for steady state simulations as opposed to time averaged unsteady simulations was significant. Additionally the magnitude of the difference was dependent on the grid and turbulence model employed. These results underscore the possible differences between steady state and unsteady numerical results for the blunt-bodied vortex shedding case.

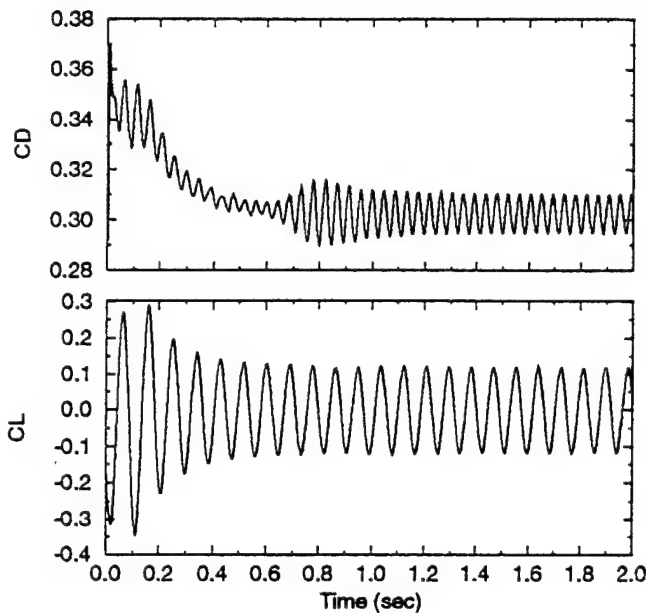


Figure 4. Lift and Drag Coefficients for  $M = 0.177$  and  $Re = 8.27 \times 10^6$

#### 2D Ejection Seat

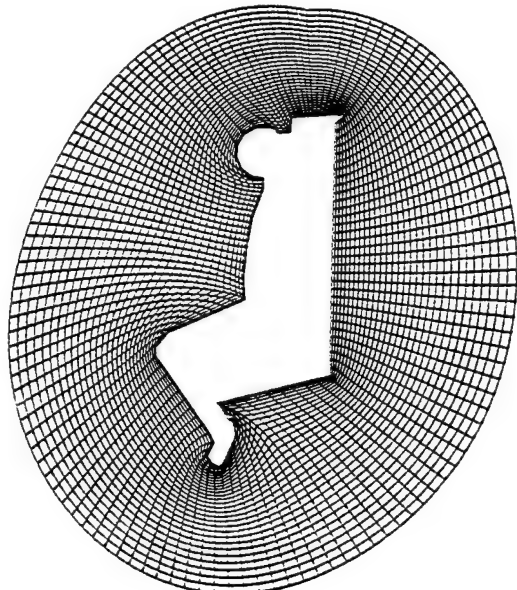
To understand the flow characteristics around a typical ejection seat geometry and to assess the importance and effects of flow unsteadiness on aerodynamic coefficients, several calculations have been performed on a 2D ejection seat geometry. The 2D geometry was chosen for strictly economic purposes, for, to conduct a study of this magnitude on a full 3D ejection seat grid (similar grid resolution) would be economically

very expensive in terms of needed computer resources. It is anticipated, however, that the unsteady effects will be more pronounced with the 2D geometry than the 3D geometry because larger flow separation and increased wake size with the 2D geometry. To assess this effect a limited 3D coarser grid resolution unsteady simulation is performed and the results are presented in the following section.

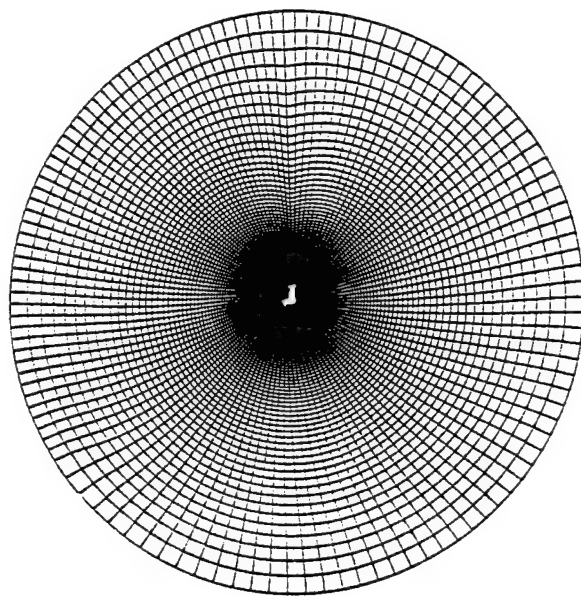
For the 2D ejection seat geometry, several calculations have been performed. The history of the calculations is as follows: first steady state calculations were performed on a typical mid-plane 2D ejection seat geometry and grid and aerodynamic coefficients were calculated. Second, unsteady calculations were performed on the same geometry for 1.5 seconds in steps of .001 seconds starting from a perturbed solution (as discussed in the cylinder section above). Then unsteady calculations were performed on a seat pitched from 0 to 45 degrees and then pitched back from 45 to 0 degrees. A utility was developed to rotate the seat and adjust the grid for the new seat orientation. Several initial conditions, time step and pitching angle increments were used. The results from all the above discussed calculations are presented below.

**Steady State Calculation:** Figure 5 shows the elliptically smoothed computational grid used for the 2D fixed ejection seat geometry. The calculation domain extends about 5 seat heights around the ejection seat. Calculations were performed at  $M = 0.6$  and  $Re = 8 \times 10^6$ . A first order upwind scheme was used to get the results shown in Figure 6. Attempts to use a higher order central differencing scheme failed as convergence was difficult due to oscillations. Figure 6 presents the upwind results where the streamline and pressure contours are shown. The streamline contours indicate the presence of two recirculation eddies in the back of the seat.

The flow separates near the head and feet of the occupant and reattaches about 2.5 seat/occupant heights downstream. The drag and lift coefficients were normalized by the seat/occupant height which is 1.848 m. The calculated  $C_D$  and  $C_L$  were 1.38 and -.257, respectively.

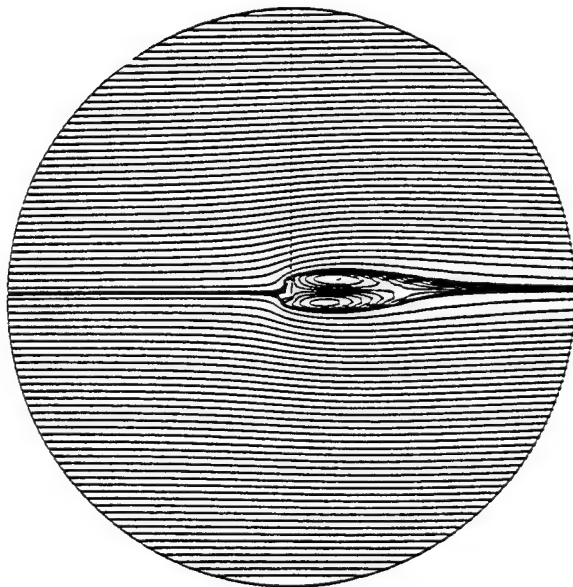


Near Field

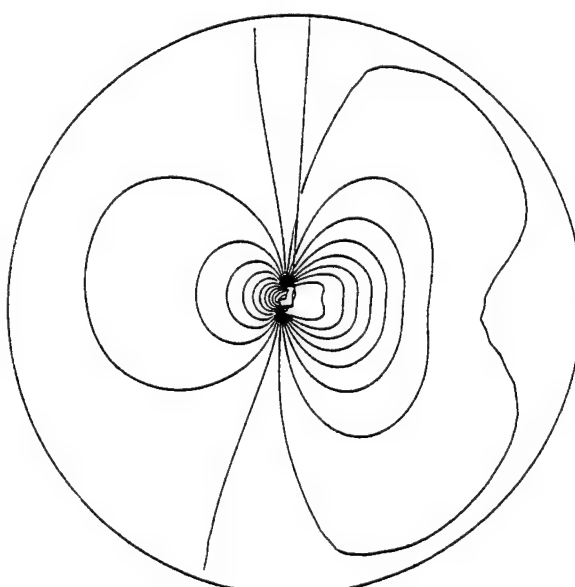


Far Field

Figure 5. Near Field and Far Field Views of 2D Ejection Seat Grid



Streamline Contours



Pressure Contours

Figure 6. Streamline Contours (a) and Pressure Contours (b) from 2D Ejection Seat Steady State Calculations

**Unsteady Calculations/Fixed Seat:** Unsteady calculations were then performed on the same geometry to observe the vortex shedding formation and their effects on the calculated drag

and lift coefficients. When converged steady state results were used for the initial conditions, the solution would converge and settle to that of steady state solution and no perturbations or

oscillations would be formed. To get an unsteady vortex shedding solution, a perturbed initial condition was used. Calculations were performed for 1.5 seconds in time step increments of .001 seconds.

The flow for the first 150 time steps (time = .15 seconds) seems unstable and does not show any cyclical or repetitive patterns. After this initial stage a clear cyclical pattern is observed (as seen in Figure 7) and a typical vortex shedding flow pattern is formed as seen in the streamline contours shown in Figure 8. Figure 7 shows the history of drag and lift coefficients and the perfect oscillations associated with vortex shedding flows. Note that the average values of  $C_D$  and  $C_L$  are about 2.0 and -3.25 respectively and they differ considerably from the steady state results which were calculated to be 1.38 and -2.57 for  $C_D$  and  $C_L$ .

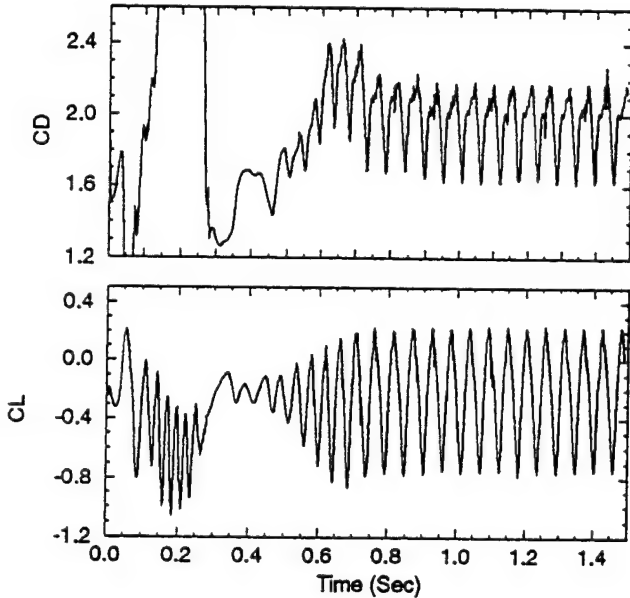


Figure 7. Drag and Lift Coefficients From Unsteady Calculations Over a 2D Fixed Ejection Seat

The discrepancy between the time average and steady state results is about 30 and 20 percent for  $C_D$  and  $C_L$  respectively which is very similar to the discrepancies found for the cylinder geometry. Figures 6 and 8 reveal that the size of the wake is larger for the unsteady calculation. The larger wake results in lower overall back

pressure which in turn results in the higher time average drag and lower lift (due to inclination of bottom surface).

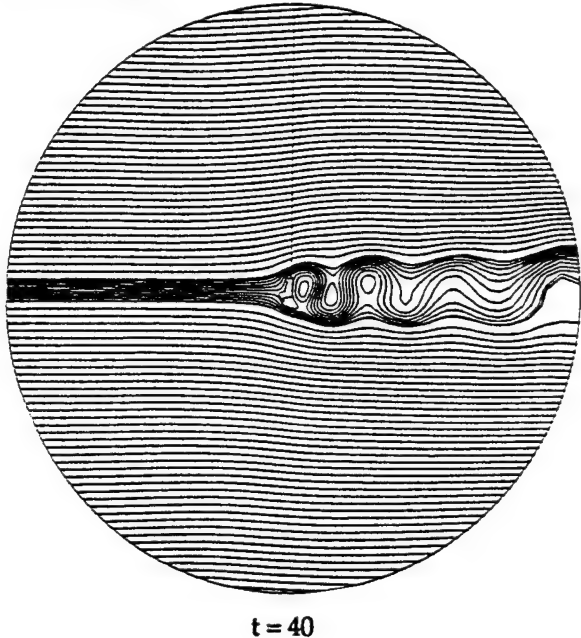


Figure 8. Typical Vortex Shedding Behind 2D Ejection Seat Geometry from Transient Calculation;  $M = 0.6$

**Unsteady Calculations/Rotating Seat:** Several calculations were performed for a pitching (i.e. rotating) seat. The same computational grid used for the fixed orientation was utilized for these calculations. The seat was pitched each time step according to an assigned pitching angle increment and the computational grid was adjusted accordingly. A grid adjustment routine that retains the elliptic smoothness of the original grid was used for this purpose. CFD-ACE moving grid capability was used to retain full conservation as the grid is moved each time step.

Figure 9 presents the lift and drag coefficients for the case using unsteady fixed seat initial conditions and timestep of .0011 seconds and pitching angle increments of .05 degrees. The pitching envelope goes from 0 to 45 degrees and back from 45 to 0 degrees. The drag coefficient decreases as the pitching angle increases as expected due to the lower projected frontal area. The oscillation patterns persist throughout and

the amplitude becomes smaller at the higher pitching angles. As the seat is pitched back from 45 to zero degrees, the same type of oscillations are observed and the lift and drag pattern traceback around an imaginary time averaged line of the 0 to 45 degree results.

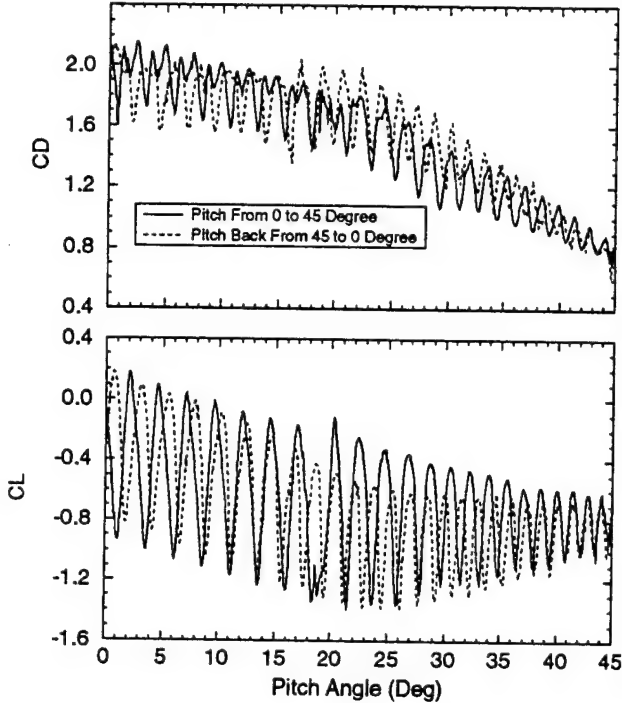


Figure 9. Lift and Drag Coefficient for a Pitching Seat Using Unsteady Initial Conditions

Figure 10 shows the streamline contours at different pitching orientations. The vortex shedding pattern is observed throughout, however, the amplitude becomes smaller and dies down as the pitch angle increases.

Several other calculations were performed using the steady state results as the initial conditions. Pitch angle increments of .05, .1, .2, and .5 were used. The corresponding time steps were .0011, .0022, .0044 and .011, respectively. The purpose of these calculations was to observe the formation of flow oscillations if any and at what time step and pitching angle increments they would form and how the results compare to the above results (starting from unsteady fixed seat results).

Figure 11 presents the drag and lift coefficients for all the calculations performed on the pitching seat including the steady state results. It is observed that a large discrepancy exists between steady state and transient initial conditions, at the lower pitching angles (i.e.  $\alpha=0$ ) as discussed above for the fixed seat. As the pitching angle increases the discrepancies become smaller due to the shrinking size of the wake and therefore the reduction of the vortex shedding effects. At  $dt = .011$  and  $d\alpha = .5$ , the drag and lift coefficients along with the streamline contours (presented in Figure 12) show no oscillations throughout the pitching envelope and no vortex shedding is formed. As smaller time steps are used (and in turn smaller pitching angle increments)

oscillations start to form, and they ultimately appear to follow the same pattern as the unsteady initial condition case especially at  $Dt = .0011$  and  $D\alpha = .05$  degrees. This behavior is different from the unsteady calculations on a fixed seat using steady state converged results for initial conditions where the solution always stayed at that of the steady solution and no oscillations were formed.

It seems like the pitching of the seat introduces the perturbations that ultimately result in the oscillations and vortex shedding mechanism. What is interesting is that these oscillations seem to converge on a unique solution irrespective of the initial conditions as long as the perturbations are introduced.

### 3D Ejection Seat

Steady state calculations have previously been performed on a 3D ejection seat and results have compared well with wind tunnel test data<sup>2</sup>. A state-of-the-art CAD and grid generation procedure have been utilized to generate the grid for this complex geometry. Figure 13 shows the CAD wire frame and surface grid for the ejection seat geometry. Figure 14 shows a sample surface model and computational grid plane for the baseline ( $\alpha = 0$ ,  $\beta = 0$ ) orientation. Figure 15 shows sample steady state results for the force and moment coefficients which compare very well to wind tunnel test data.

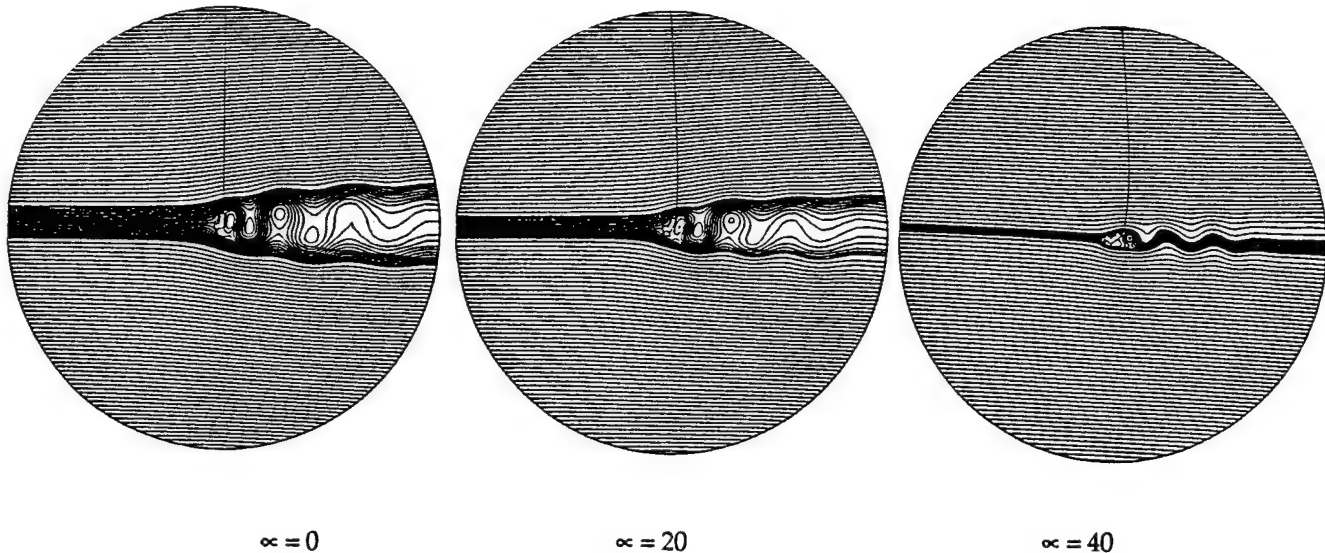


Figure 10. Streamline Contours for 2D Seat at Different Pitch Angles; Unsteady Initial Conditions

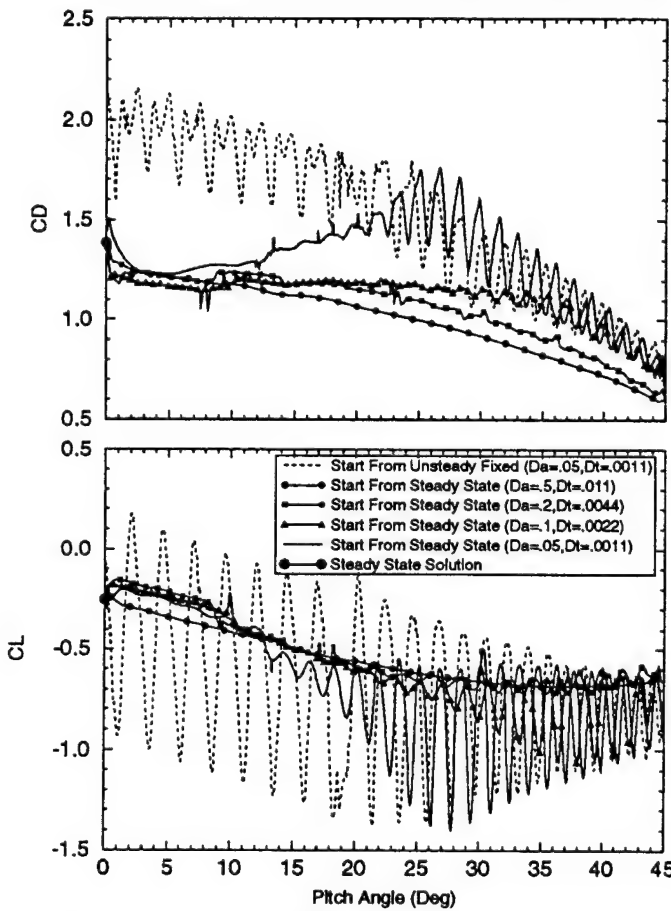


Figure 11. Drag and Lift Coefficients for a 2D Pitching Set

To assess the importance of unsteady effects on the 3D ejection seat results a limited unsteady analysis was conducted on the 3D ejection seat geometry. Note however, that the grid resolution (as seen in Figure 14) is much coarser than the 2D ejection seat grid resolution (shown previously in Figure 5). The grid resolution may be an important factor in predicting flow oscillations and vortex shedding.

Unsteady calculations were performed for a fixed as well as a rotating seat using both steady state and perturbed initial conditions. Results are presented for: unsteady calculation of flow over a full ejection seat geometry starting from perturbed initial conditions, and unsteady calculation of flow over a pitching half ejection seat geometry starting from steady state solutions.

Results from unsteady calculations over a 3D ejection seat geometry starting from steady state solutions showed no oscillations and quickly converged to the steady state solutions as was observed in the 2D ejection seat calculation. The above calculations were repeated with perturbed initial conditions. In this case the steady state solution was run for few iterations only to get a perturbed non-converged solution which was used as the initial condition. Figure 16 presents the axial velocity and pressure vs. time at a

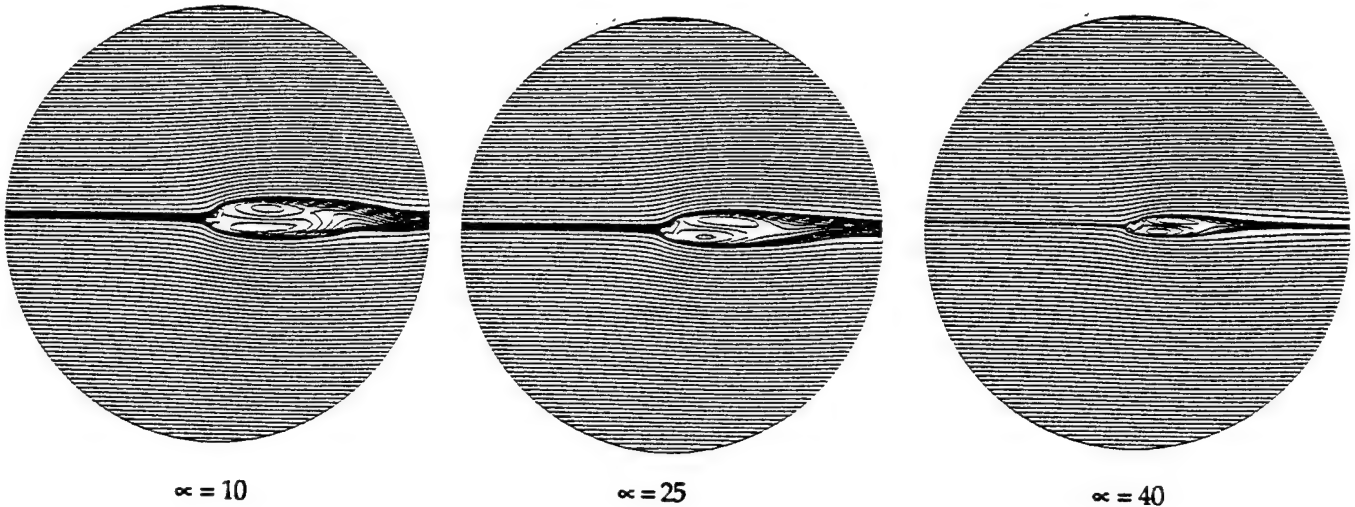


Figure 12. Streamline Contours at Different Pitch Orientations; Steady State Initial Conditions

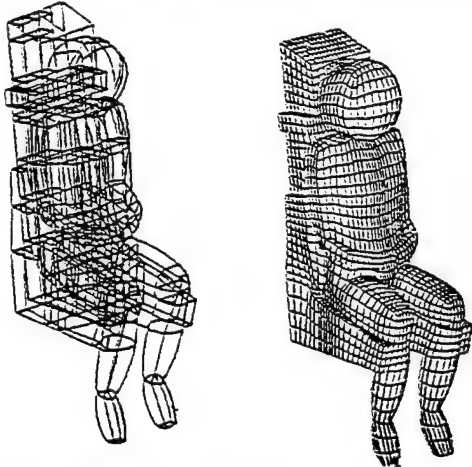


Figure 13. Wireframe CAD Model and Surface Mesh for the Ejection Seat

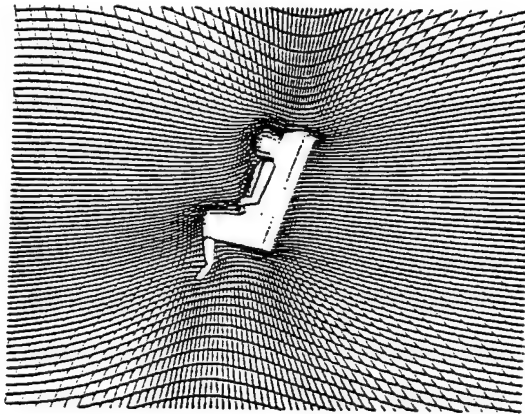


Figure 14. Sample Computational Plane for the Baseline Ejection Seat Grid

monitoring point behind the seat near the symmetry plane. Some perturbations and oscillations are observed initially however, these oscillations die out monotonically as time increases and the solution eventually approaches the steady state solution. These results are indeed different than the 2D results (although same time step was used) when starting from perturbed solutions. The 2D results showed flow fluctuations and oscillations that persisted throughout with constant frequency and amplitude which indicated that the flow was actually unsteady in nature with vortices shedding from the wake.

The force and moment coefficients were also calculated at each time step and presented in Figure 17 along with the steady state results. It is also shown that the coefficients quickly converge to a steady state solution.

3D unsteady calculations were also performed over a half 3D pitching ejection seat geometry. The half geometry was selected due to symmetry conditions and because of economic reasons. Note that calculations were also performed on a fixed half ejection seat geometry and the results were identical to those of the full geometry presented in Figure 16 and 17. For this case the initial

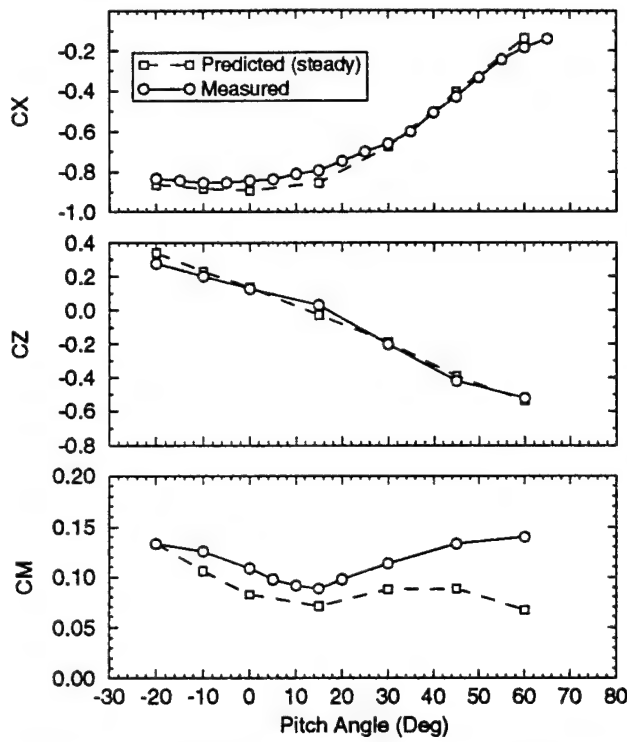


Figure 15. Predicted Steady State and Measured Aerodynamic Coefficients for the ACES-II Ejection Seat

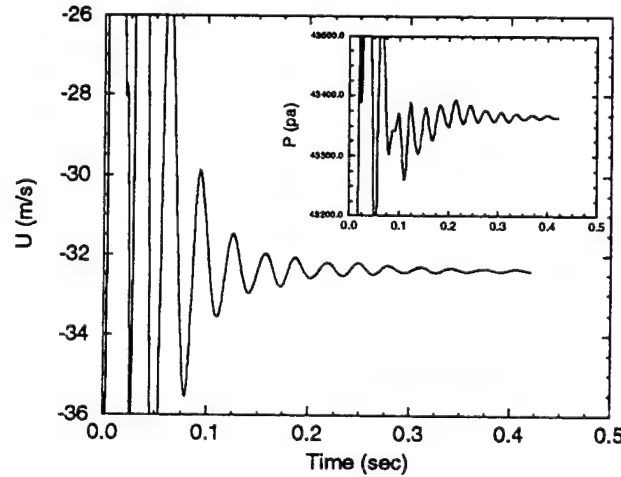


Figure 16. History of Velocity and Pressure at a Location Behind the 3D Full Ejection Seat Geometry

conditions were the steady state converged solution. Two different simulations were performed that correspond to two different time steps and pitching angle increments. In each case the solution was run for 1 second and a pitching envelope from 0 to 45 degrees. In one case the pitching increment was 0.5 degrees while in the other case the increment was 0.1 degrees which correspond to a time step of 0.011 and 0.0022 seconds, respectively. The grid was automatically adjusted after the seat is pitched as was done for the 2D seat calculations. Also, the CFD-ACE moving grid capability was used to retain full conservation of the governing equation.

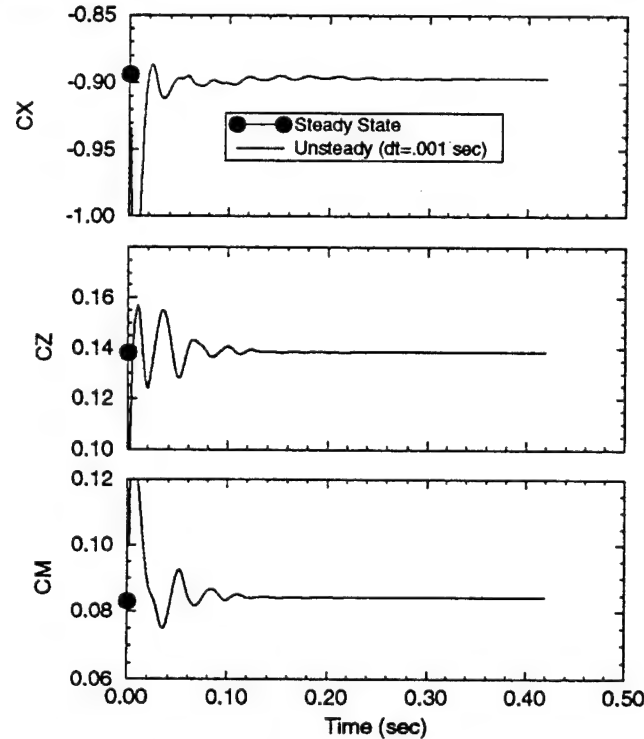


Figure 17. History of Aerodynamic Coefficients from 3D Ejection Seat Calculations

The force and momentum coefficients were calculated at each time step and are presented in Figure 18. The calculated steady state and unsteady results are virtually identical which seems to suggest that flow unsteadiness is negligible for both pitching angle increments. In fact, the solution from both unsteady calculations is exactly the same as shown in Figure 17 which means reducing the time step and pitching angle increment did not contribute to any flow

unsteadiness. It should be mentioned that the 2D calculations on a pitching seat showed vortex shedding and flow oscillation developing after  $\alpha = 25$  degrees for the increment of 0.1 degrees.

All of the 3D calculations so far produced no flow unsteadiness, vortex shedding or any perturbations. In every case the results converge to a steady state solution after a short time. Flow unsteadiness were expected to have much less of an effect on the aerodynamic characteristics of the seat in 3D than the previous 2D calculations showed. However, it is surprising that no flow oscillations or perturbations persisted for all the cases simulated no matter how small the time step used.

Reasons for the lack of flow unsteadiness in the 3D calculations are probably due to the coarseness of the grid used in the 3D calculations as compared to the 2D calculations.

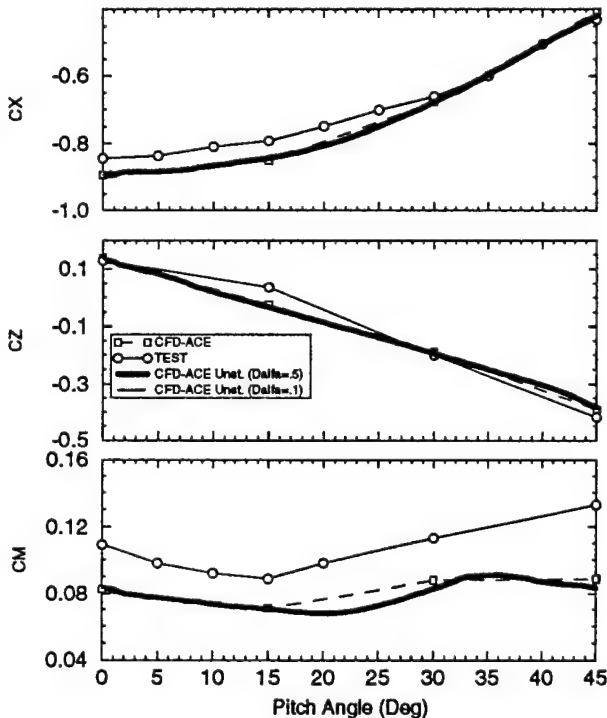


Figure 18. Aerodynamic Coefficients vs Pitching Angle for Steady and Unsteady 3D Ejection Seat Simulations

## CONCLUSION

Steady state and unsteady turbulent CFD simulations were performed on blunt-bodied type geometries with special interest in aircraft ejection seat geometries. The purpose of these simulations was to assess the importance of the unsteady flow effects on the calculated ejection aerodynamics characteristics. Simulations for a 2D cylinder geometry showed several characteristic, some of which persisted with a 2D mid-plane ejection seat geometry. These characteristics include: Selection of initial condition is critical to obtaining asymmetric solution with unsteady oscillations, and drag and lift coefficient values significantly differ between steady and time averaged unsteady solutions. The values of drag and lift coefficients are largely dependent on grid resolution and turbulence model used.

The 2D ejection seat results showed that the discrepancies between steady state and unsteady solution became smaller as the seat pitching angle increases and the wake size shrinks. Also, unsteady results for a rotating seat converge to a unique solution (irrespective of initial condition) if a small enough pitching angle and time step increments are used.

Limited unsteady analysis on a 3D ejection seat geometry showed no flow oscillation and resulted in aerodynamic coefficients similar to those of steady state. These results compared well to experiment (within 20%). To capture unsteady aerodynamic effects a much larger grid must be employed. At this time the anticipated benefit from these results does not justify the additional cost. For engineering purposes the 3D steady state results appear adequate.

## ACKNOWLEDGEMENTS

This research has been funded by the Naval Air Warfare Center, Aircraft Division at Warminster, PA under the SBIR program. The authors would like to thank Mr. Tom Marquette of NAWC-AD for his substantial technical help and support through this effort and Ms. J. Swann for the preparation of this manuscript.

## **REFERENCES**

1. Habchi, S.D., Przewkas, A.J., Marquette, T., and Ayoub, P., "CFD Analysis of Ejection Seat Escape Systems," SAE Aerotech '92 921924, Anaheim, CA, Oct. 1992.
2. Habchi, S.D., Ho, S.Y., Hufford, G.S., Marquette, T., and Ayoub, P., "Computational Aerodynamic Analysis of the Navy Aircrew Common Ejection Seat," AIAA-94-0395, 32nd Aerospace Sciences Mtg., Reno, NV, Jan. 1994.
3. Hufford, G.S. and Habchi, S.D., "Validation of CFD Methodology for Ejection Seat Applications," AIAA-94-0751, 32nd Aerospace Sciences Mtg., Reno, NV, Jan. 1994.
4. Habchi, S.D., Hufford, G.S. and Marquette, T., "Navier-Stokes Computational Analysis of the B-1A Escape Capsule," AIAA-95-0187, 33rd Aerospace Sciences Mtg., Reno, NV, Jan. 1995.
5. Caruso, S.C. and Mendenhall, M.R., "Computational Analysis of High Speed Ejection Seats," AIAA-90-0403, Jan. 1990.
6. Baum, J.D. and Lohner, R., "Numerical Simulation of Pilot/Seat Ejection from an F-16," AIAA-93-0783, 1993.
7. CFD Research Corporation, "CFD-ACE: Theory Manual," Version 1.0, CFDRC Report GR-93-1, Sept. 1993.
8. Yang, H.Q., Habchi, S.D. and Przekwas, A.J., "A General Strong Conservation Formulation of Navier-Stokes Equations in Non-Orthogonal Curvilinear Coordinates," AIAA-92-0187, Jan. 1992.
9. Stone, H.L., "Iterative Solution of Implicit Approximation of Multi-Dimensional Partial Differential Equations," *SIAM J. Num. Annual*, vol. 5, 1968.
10. Schlichting, H., "Boundary Layer Theory," 7th Edition, McGraw-Hill, New York, 1979.
11. Jones, G. W., Cincotta, J. J. and Walker, P.W., "Aerodynamic Forces on a Stationary and Oscillating Circular Cylinder at High Reynolds Number," NASA-TR-R-300, 1969.
12. Roshko, A., "Experiments on the Flow Past a Circular Cylinder," *JFM* 10, 345-356, 1961.

## 6. SEAT/AIRCRAFT TECHNOLOGY EVALUATION AND SELECTION

All the methodologies and results presented and discussed so far in this report were focused on the seat and occupant in free flight without interference from the aircraft. Several studies including wind tunnel tests have shown that the proximity to the aircraft, in the early stages of ejection, have considerable effects on the aerodynamic characteristics of the ejection seat. The purpose of this effort, which constitute a large portion of this project, was to extend the capabilities of the developed CFD tools to handle full analysis of the seat and occupant in proximity to the aircraft. The developed CFD tools shall be capable of handling both steady-state and transient analysis for seat and aircraft flows.

Three different CFD codes and methodologies were selected to be evaluated for the seat and aircraft analysis. These included CFD-ACE, CFD-FASTRAN and OVERFLOW codes.

### 6.1 Overview of Seat/Aircraft Modeling Issues

In order to study the aerodynamic characteristics of the ejection seat near the aircraft and to assess the proximity effects of the aircraft, the CFD tools need to be developed, demonstrated and validated for seat and aircraft analysis of both quasi-steady and transient simulations.

The extensions of CFD tools to include numerical simulation of an ejection seat separating from an aircraft is a very complex and challenging computational problem. The complexity of the problem is the result of many computational and simulation techniques needed to perform a full numerical time dependent simulation. Some of the techniques needed for such a simulation include:

- a. **Geometric Modeling and Surface Definition Techniques.** An interactive user-friendly CAD package that is tailored toward CFD application is needed for accurate representation of the seat and aircraft flow surface. This package needs to be integrated to the grid generation tools used for computational mesh generation.
- b. **Fast and Efficient Grid Generation Techniques.** The grid generation techniques should be automated and able to adjust the computational grid for moving boundaries without interference from the user. The computational requirements of the grid generation should only be a fraction of the total simulation requirement.
- c. **Grid Adaptation Methods.** These methods are categorized as either mesh movement, mesh enrichment or adaptive remeshing. Common to these methods is the principle of improving the flow field resolution by strategically refining and distributing the grid points within the domain.

- d. **Moving Grid Methods.** In order to account for arbitrary body motions in the governing equations during the numerical simulations, a moving grid technique is required which preserves the time accuracy of the flow dynamics.
- e. **Turbulence Effects Modeling Techniques.** The flows associated with seat/ aircraft separation will have vast separation regions with turbulent flows. A turbulence model that is capable of predicting the viscous effects associated with such flows is needed.
- f. **High Order Shock Capturing Differencing Scheme.** Accurate numerical schemes are needed to solve the time dependent flows with strong shocks at supersonic freestream conditions.
- g. **Rigid Body Motion Dynamics.** Techniques are needed to allow transient flow simulation with either prescribed motion of the rigid bodies (prescribed trajectory) or fully coupled body kinematics and fluid dynamics (6 Degree of Freedom (6DOF) model).
- h. **Post-Processing and Visualization Techniques.** Due to the complex flow fields and the amount of data generated from a transient calculation, post-processing and sophisticated visualization tools are needed for the understanding of results. Post-processing tools are required for the calculation of aerodynamic and other performance coefficients while the visualization tools are needed to visualize and comprehend 3D field properties such as pressure, Mach number, turbulence quantities, etc.

Each one of these techniques or issues needs to be evaluated in terms of user friendliness (ease of use), solution accuracy, computational efficiency, upgrade compatibility, and integration/compatibility with the other techniques.

## **6.2 Summary and Outcome of CFD code Selection Process**

Geometry modeling, grid generation and post processing issues were addressed first and quickly satisfied by adapting CFD-GEOM for geometry modeling and grid generation, the elliptic grid generator (CFD-GRID) for grid smoothing and CFD-VIEW for flow visualization. These tools were already adapted for escape systems applications and were adequate for the seat and aircraft analysis.

In light of the modeling issues described above, a study was conducted to select the most suitable CFD code or methodology for the seat and aircraft analysis. This study was conducted in a step by step manner as follow:

- use simple geometries (that has similar flow features to the seat and aircraft) and coarse grids to get familiar with basic functionalities of each code and to assess the difficulties (or ease-of-use) of setting up the problem. A flow over a cube problem was selected for this step.

- use a 2D simple benchmark flow problem to test the prediction accuracy and efficiency of each code. The flow over a 2D cylinder was selected for this step.
- conduct simulation on a seat and occupant geometry and compare predicted aerodynamic coefficients to test data. The purpose of this step was to test the prediction accuracy and efficiency of each code on a representative 3D seat and occupant geometry.

After this basic technology assessment study, the performance of each method was assessed and compared to the other methods. It was decided at this stage to drop CFD-ACE from the running due to its lack of capabilities to handle multiple and moving bodies. This capability was necessary to model the seat separation from the aircraft. The addition of such a capability to CFD-ACE was determined to be beyond the scope of this effort. A major restructuring of the code would have been necessary for such an addition.

Several conclusions were also made about the performance and capabilities of CFD-FASTRAN and OVERFLOW. These will be summarized later in this section. Some of these conclusions were that OVERFLOW requires too much user interference for this type of problem especially dealing with using blockages to represent the seat and occupant geometry. Another conclusion was that OVERFLOW predictions were very good providing very fine grids were used. With reasonable and affordable size grids, OVERFLOW predictions quickly deteriorated. Another problem with selecting OVERFLOW was that the Chimera methodology available in OVERFLOW at that time did not support moving bodies. Also the seat and aircraft modeling for steady state simulation proved cumbersome and slow especially dealing with the PEGSUS code as will be described later in this report. These conclusions necessitated a shift of focus to CFD-FASTRAN.

The hybrid grid capabilities already available in CFD-FASTRAN would allow for the modeling of the seat and aircraft in fixed positions. CFD-FASTRAN did not have the capability to handle moving bodies such as the seat separation from the aircraft. However, the hybrid structure of CFD-FASTRAN would make it somewhat easier (than CFD-ACE) to add such a capability. Several methodologies were investigated to be added to CFD-FASTRAN to model seat and aircraft separation.

Two different techniques were developed and implemented into CFD FASTRAN for the moving body problem. The first one was the Overset Hybrid methodology, which showed great promise in the beginning, for steady state fixed body problems, but proved too slow for the moving body problem. This was due to limitations with unstructured grid technology in general and the Advancing Front technique in particular. The other methodology, that ultimately proved to be successful, was the traditional Chimera Overset methodology. The Overset technique was implemented in CFD-FASTRAN and used successfully for Seat/Aircraft steady state and unsteady Simulations. The traditional problems of Chimera (such as slow gridding and interpolation procedures) were overcome by using different and newer methods as described below in the CFD-FASTRAN adaptations section.

The process of CFD codes evaluation and selection is described below, followed by the description of CFD-FASTRAN code development and adaptation for moving bodies. The results from steady state and transient analyses are then presented and discussed.

### 6.3 CFD Codes Evaluation

The focus of this task was to assess the capabilities of 3 CFD codes, that use three different methodologies, for seat/aircraft simulations. The considered CFD codes included CFD-ACE, OVERFLOW, and CFD-FASTRAN. Note that CFD-ACE has been extensively used for the seat/occupant analysis and therefore was not tested to the same extent as the other two codes. In fact, the focus of the testing is to obtain results from OVERFLOW and CFD-FASTRAN and compare them to those of CFD-ACE and available wind tunnel and experimental data.

The assessment task was conducted in a step-by-step manner. First simple 2D calculations were performed to test the basic capabilities of the codes and to get a feel for how a problem such as seat/occupant and seat/aircraft is setup and handled from both the ease-of-use and efficiency standpoints. Second a benchmark simple geometry (cylinder) problem was used to test the prediction accuracy and efficiency of the CFD codes. Finally a seat/occupant geometry was used to test the prediction accuracy and efficiency of the codes on actual 3D seat and occupant geometry. The results from these three studies are presented below.

#### 6.3.1 Flow Over a Cube

The CFD-ACE computational grid typically used for the solution of flow past an ejection seat is a single-block, H-mesh with interior blanking for the solid portion of the seat and pilot. CFD-FASTRAN handles the geometry and grid topology (i.e. blockages) in the same manner as CFD-ACE. However at the time of the start of this effort, it was unknown how OVERFLOW handles such topology. Therefore a simple 2d problem was selected to evaluate this modeling feature. This problem was also used to get familiar with the code usage and to assess the numerical and physical models as well as convergence characteristics of the code.

The flow past half of a cube was selected. The grid was a single-block, Cartesian mesh with the solid portion of the cube blanked out in manner analogous to the previous CFD-ACE methodology. The problem was run at a freestream Mach number of 0.6, which is the same as some of the previous ACES-II seat simulations.

CFD-ACE has been structured so that portions of the grid can be blanked out or treated as solid by specifying a zero value for the integer iblank array at a particular location. This iblank information is an integral part of the CFD-ACE input grid. Since OVERFLOW was created to take advantage of the chimera grid oversetting methodology, the concept of blanking out portions of the problem is also inherent to the code. With OVERFLOW, the iblank values are not set from reading an blanked grid file, but are read in from the chimera pre-processing file. As the single-block case here does not pass through a pre-processor, the blanking is not set. OVERFLOW allows for this by

the specification of blanked regions entirely with boundary conditions. This is considerably more work for the user than the same type of problem in CFD-ACE, but it is possible. Whereas CFD-ACE automatically identifies a solid area from the change in the *i*blank values, each face of an interior blanked region in OVERFLOW must be called out separately, and then those nodes in the interior of the solid surface have another boundary condition specified to prevent their values from being updated. To add another complexity, the wall specification for the one- and two-equation turbulence models requires additional input of the wall locations and directions normal to the surface. The application of the various boundary conditions is shown schematically in Figure 6-1.

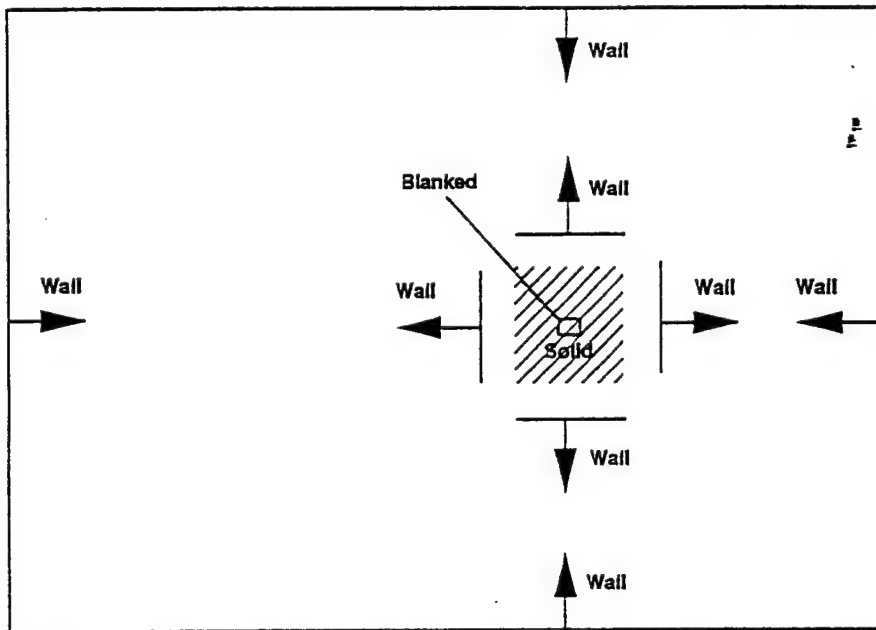


Figure 6-1. Boundary Condition Schematic for Flow with Interior Blockages

As stated before, the grid for this test case was Cartesian, with dimensions of (29x21x11). The physical extent of the problem was 1.0 meter in height, 0.5 meters in width, and 2.0 meters in length. The computational grid and problem outline is shown in Figure 6-2. The grid was clustered somewhat toward the cube surface, but not anywhere close enough to resolve details of the boundary layer.

Another purpose to the running of cases for this simple cube geometry was to build up experience running the OVERFLOW code with different selections for the solution algorithms and their relation to the computer requirements for a converged solution. The main algorithm choices involve selecting the scheme for treatment of the LHS terms, the RHS terms, and the overall dissipation scheme for both sides. OVERFLOW is an amalgamation of the codes F3D and ARC3D, and both types of solution algorithms are available for use by the user, although the ARC3D schemes were found to be preferable based on these results.

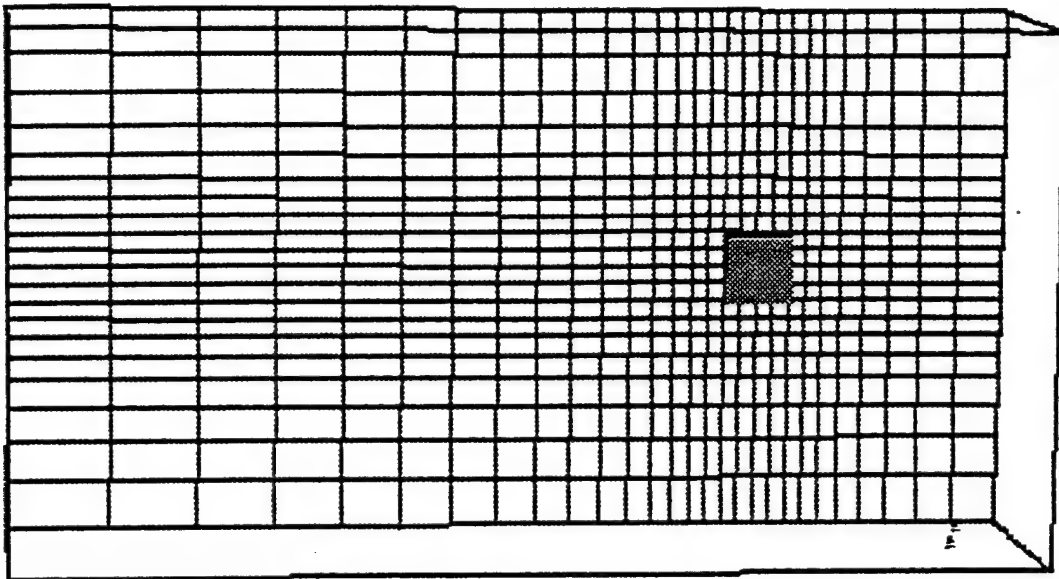


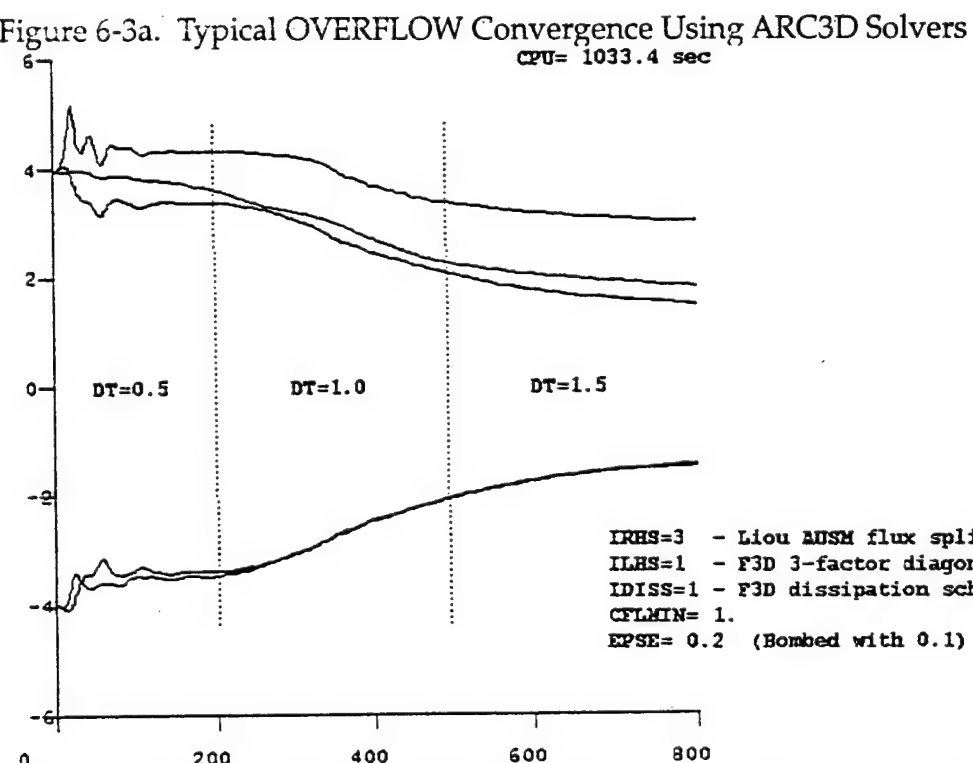
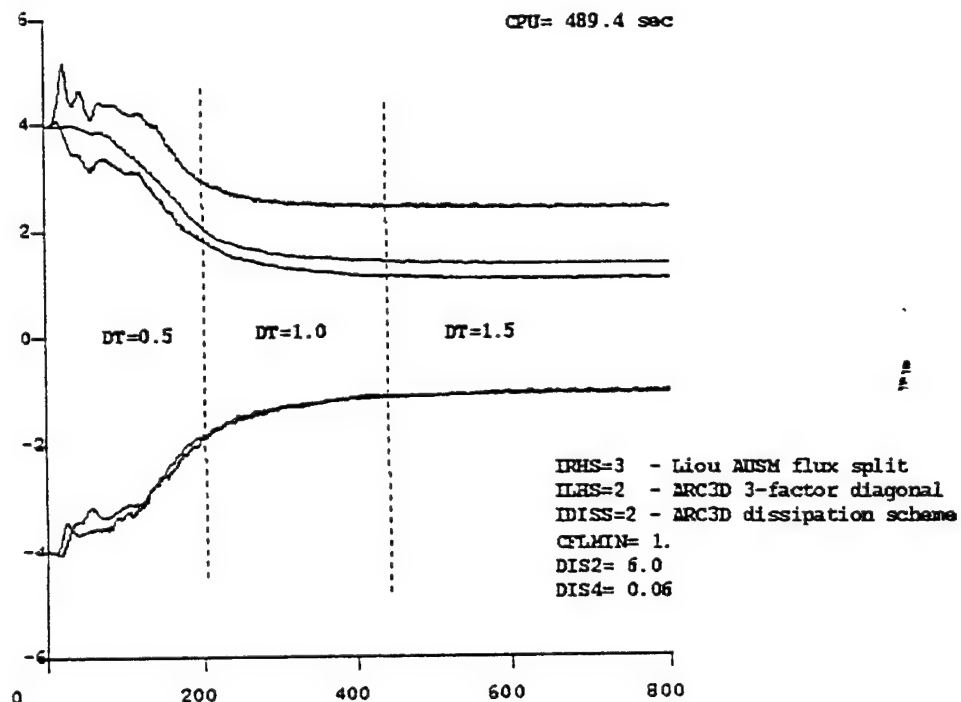
Figure 6-2. Computational Mesh for Problem of Flow Past Cube

In drawing conclusions about the performance, the main criteria was the amount of cpu time related to the number of time steps needed for convergence. To ascertain convergence, the integrated forces on each of the walls was plotted as a function of time step. Two of the most pertinent plots are shown in Figure 6-3a. The convergence plot shown in Figure 6-3a is the result of using the Liou AUSM flux split scheme for the RHS terms, ARC3D 3-factor diagonal scheme for the LHS terms, and ARC3D dissipation schemes throughout. Judging by the slope of the lines, convergence is obtained after approximately 400 time steps. The total cpu time for the entire 800 steps was 489.4 seconds. Using the same Liou scheme for the RHS, but F3D options for LHS and dissipation, the result is seen in Figure 6-3b. The time step ramping in both cases is the same. It takes the full 800, if not more, before the solution settles down, and the cpu time has increased to 1033.4 seconds. Judging by these numbers, the ARC3D choices produce at least a five-fold increase in performance.

Both the Liou AUSM flux splitting and the more traditional central differencing for the RHS terms worked well for this problem. The Liou scheme did tend to produce quite ragged force plots for too high a value for the time step, either by large values for DT or the parameter CFLMIN. Although the Liou scheme worked well for this problem, it did not work well on the larger isolated ACES-II ejection seat case or the later cylinder results.

The code typically is sensitive in the initial transient, requiring either smaller values for the time step (DT<0.5) or higher multipliers on the artificial viscosity (DIS2>2 and DIS4>.02 when using the ARC3D schemes). However, if high values for the artificial

viscosity multipliers are needed initially, they should be lowered later when possible, as the computed forces were observed to change slightly with changes in the coefficients. This implies that the most accurate results would be obtained with the artificial viscosity values as small as practical.



### 6.3.2 Flow Over a Cylinder

As the ejection seat problem involves turbulent flow past a bluff body, it is important to characterize the accuracy of the candidate CFD code and its turbulence models for this class of problems. The flow over a cylinder was selected as a suitable test case for this purpose. One reason for this is that the geometry is topologically simple and accurate grids are easy to generate for this small problem as stated earlier in this report (Section 3). A second reason is the existence of test data for this problem. The cylinder problem was used for CFD-ACE numerical and physical modeling assessment for the seat and occupant configuration (see Section 3.1.1). Computational grids were already available from the CFD-ACE code analysis of this problem.

The three codes were tested to determine the prediction accuracy on this particular problem. Shown in Figure 6-4 are the best solutions obtained with the three primary codes. The results are shown as pressure coefficient versus angle around from the leading stagnation point on the cylinder. In all cases, it was with a fine mesh of 120x120 cells and mesh spacing of .00001 to .00005 meters at the surface. The OVERFLOW code produced the most accurate solution, using the 1-equation Baldwin-Barth turbulence model. Next most accurate was CFD-ACE, employing a modified  $k-\epsilon$  model denoted as RNG in the literature. The results with CFD-FASTRAN were similar to CFD-ACE using the  $k-\epsilon$  turbulence model. The RNG model is not available in CFD-FASTRAN.

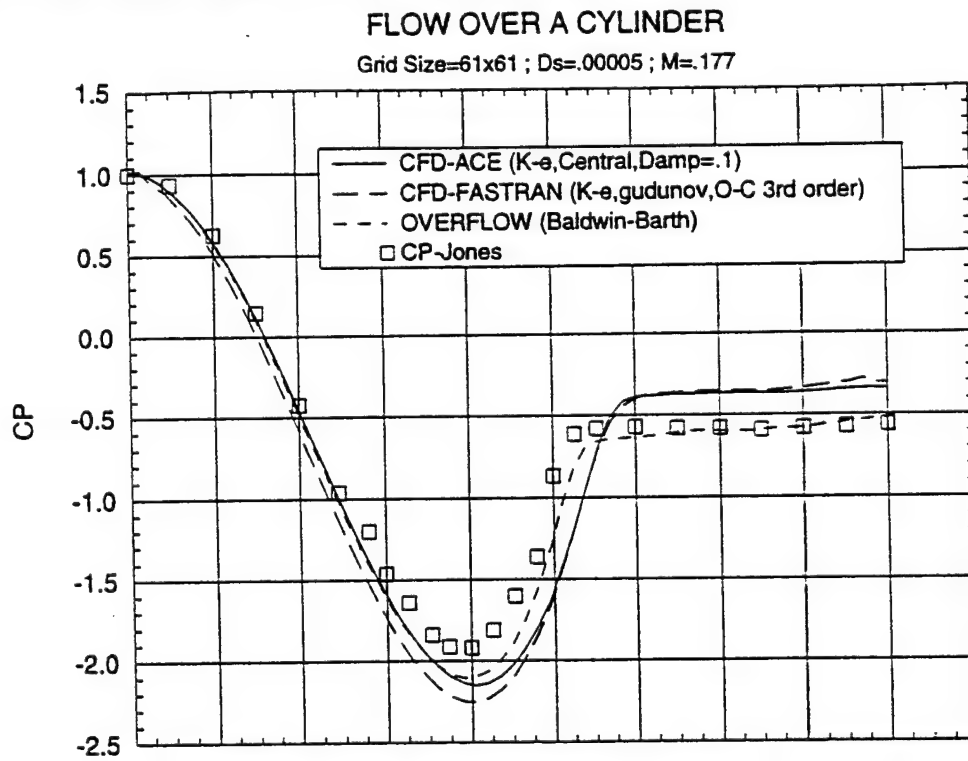


Figure 6-4. Best Comparisons with Data for Cylinder Flow

Several relatively fine-grid solutions with two turbulence models using OVERFLOW are shown in Figure 6-5. For each, the initial cell spacing was 0.00005 meters, and grid dimensions of 61x61 and 121x121 were used. Two curves are shown using the Baldwin-

Barth turbulence model on different size grids, while only one curve is shown for the  $k-\epsilon$  results, that using the small of the two grids. The  $k-\epsilon$  results are observed to miss the data rather badly, both in terms of prediction of the separation point too far aft and the computed base pressure being too high. The Baldwin-Barth model, however comes very close to the data from Jones for the 61x61 mesh, and on the 121x121 mesh the match is even better. The computed pressure coefficient practically passes through every data point.

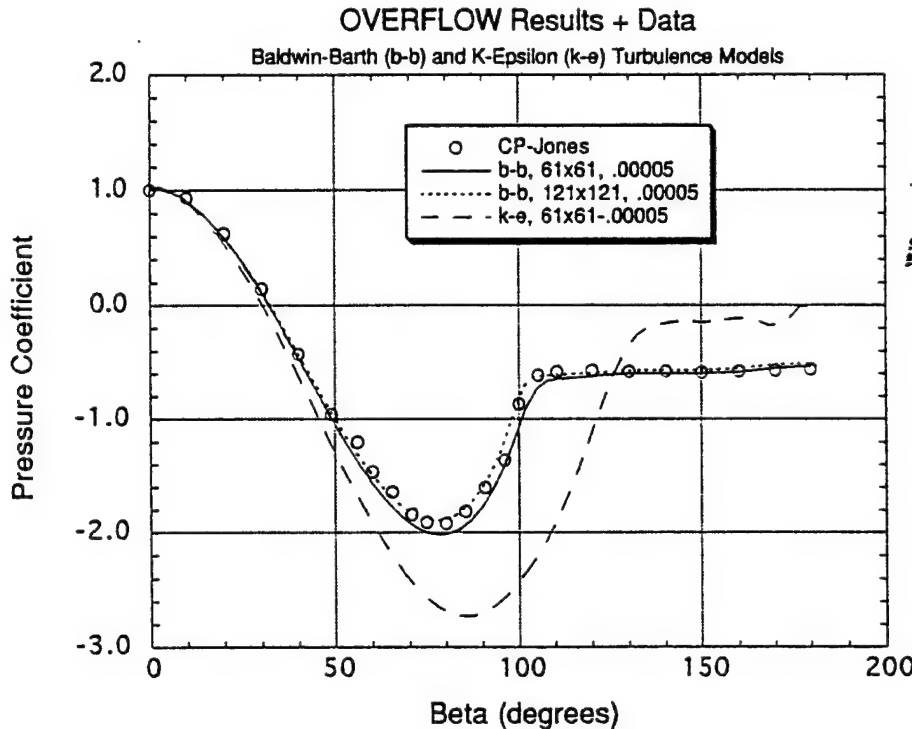


Figure 6-5. Two Grids and Two Turbulence Models Solutions with OVERFLOW

These results were very gratifying, but it was felt that the grid required to achieve those same  $y^+$  values in the boundary layer of a real configuration might prove impractical. A series of three runs using increasingly-coarse mesh resolution at the cylinder surface was performed, the results of which are shown in Figure 6-6. The series of meshes start at the previous value of .00005 meters for the first cell spacing and increase by a factor of 10 thereafter. The coarsest mesh has only 48 points, which gives the grid near the surface the same stretching ratio of approximately 1.2 as used in the original 61x61 mesh. It can be seen that the accuracy of the pressure coefficient predictions drops off dramatically with increasing grid resolution. The pressure in the accelerated-flow region from 60-90 degrees is badly over-predicted, while the base flow pressure level is seen to decrease. The OVERFLOW code is obviously very sensitive to the quality of the grid in the boundary layer.

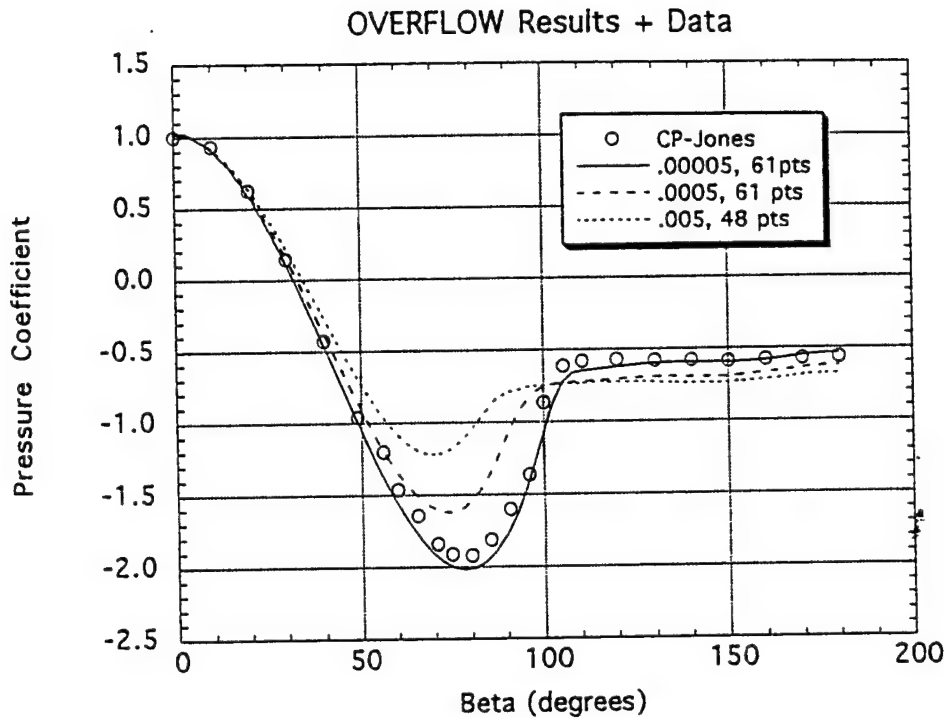


Figure 6-6. Effect of Near-Surface Grid Resolution on Accuracy using OVERFLOW

An element of the learning curve in using OVERFLOW has been in knowing when a solution is converged. This is not so obvious as it is when using a code like CFD-ACE, where one monitors the solution residuals and claims convergence after dropping the residuals by five or six orders of magnitude. OVERFLOW simply reports a global 12-norm, which is not guaranteed to drop by more than one or two orders, even for a converged solution. A useful auxiliary method of checking convergence with OVERFLOW has been monitoring the integrated pressure coefficients as a function of time step. The expected behavior is for the forces to oscillate about some value, with the oscillations damping out as the solution progresses. This can be seen in Figure 6-7, where the time history is shown, with three positions called out, at 700, 1200, and 1600 steps. Initially, it was thought that the solution at point A was converged, since the oscillations have died out, but the flow field at that time was observed to have a strange multiple-cell recirculation pattern, as seen in Figure 6-8a. As the solution converges further, the recirculation pattern continues to change, becoming more reasonable by step 1200 and shown in Figure 6-8b. By step 1600, the flow has settled down to the expected steady-state pattern seen in Figure 6-8c.

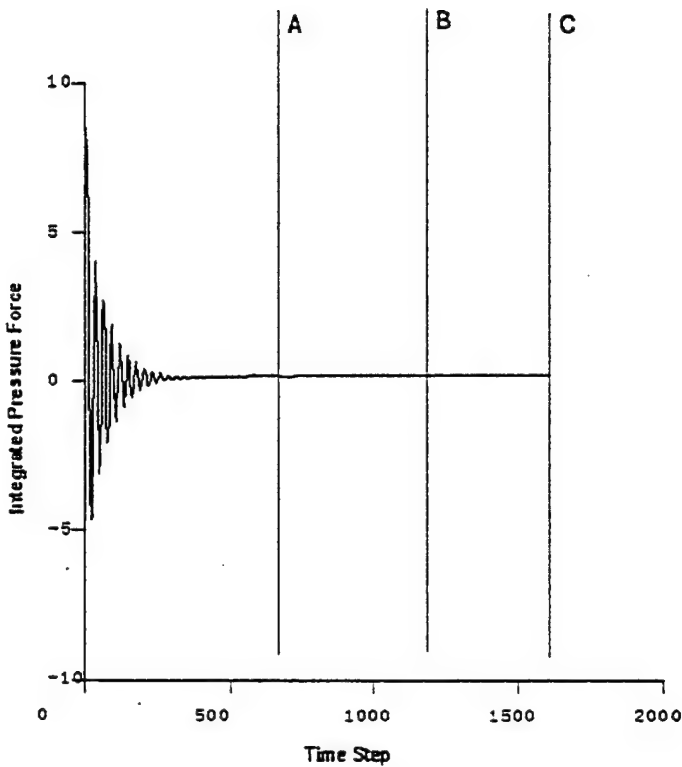


Figure 6-7. Time History of Integrated Forces on Cylinder Using OVERFLOW

Results from CFD-ACE form the primary comparison with OVERFLOW and CFD-FASTRAN, since the previous ejection seat work has been performed using this code. Two turbulence models were used in the CFD-ACE runs, a standard  $k-\epsilon$  turbulence model and a renormalization group (RNG)  $k-\epsilon$  model. The CFD-ACE  $k-\epsilon$  results were presented in Section 3.1.

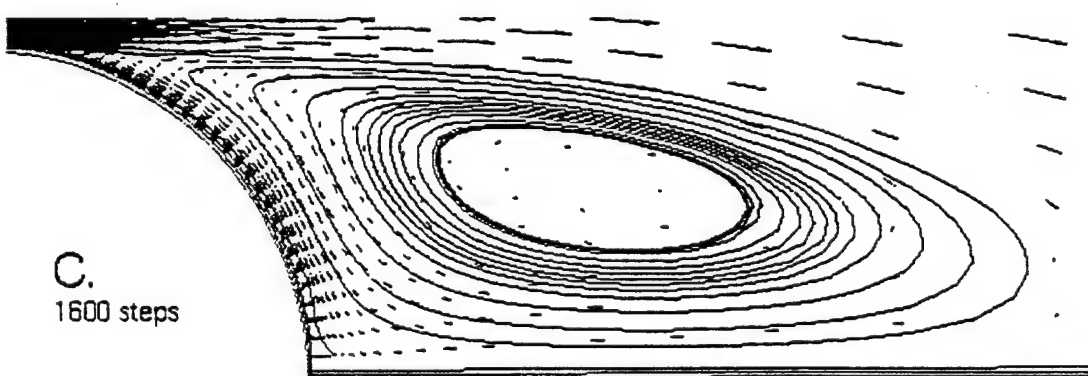
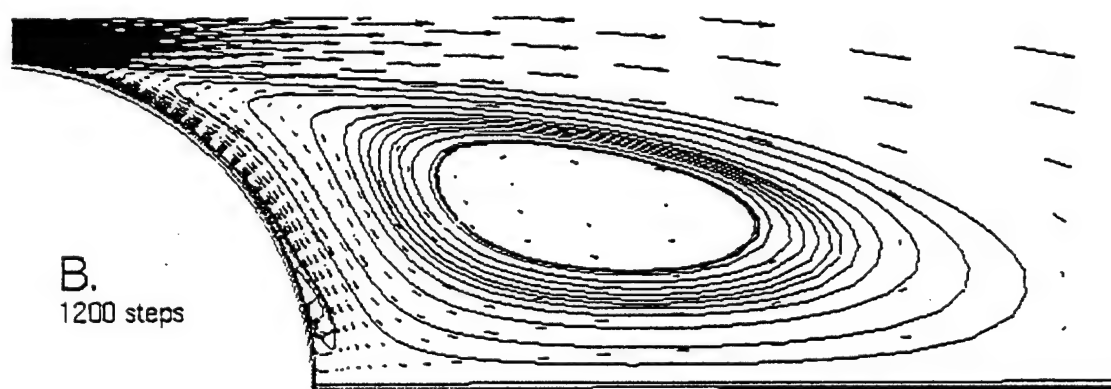
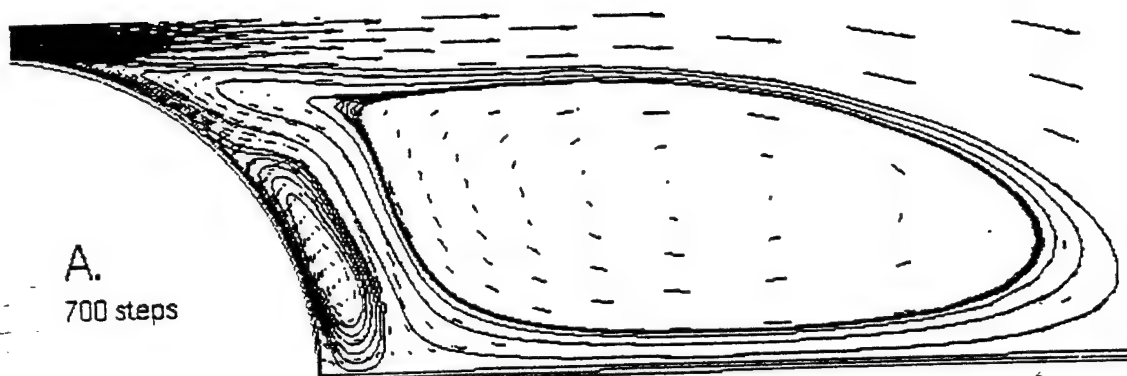


Figure 6-8. Time-Wise Evolution of Base Flow Recirculation in OVERFLOW Solution

The  $k-\epsilon$  results are shown again in Figure 6-9a. The CFD-ACE results are not nearly so grid-dependent as were the OVERFLOW results presented in the first section. The curves track right along with each other across the entire range of cell spacings, from  $y^+$  values of less than 1 up to almost 700. The separation point is predicted similarly in all the runs, as is the base pressure behind the cylinder. Conventional wisdom has it that in using a  $k-\epsilon$  turbulence model with wall functions as in CFD-ACE, it is best to keep the grid near the wall to a  $y^+$  range of 30-80. The medium-density grid having its first cell spacing at 0.0005 meters falls into that category. However, it is observed that the grids that are both finer and coarser than this mesh match the data slightly better. The order of best to worst match goes: .00005, .005, .0005. Two runs were made at the coarsest level (48 points away from cylinder) with different grid distributions in the circumferential direction. There was no discernible difference in the two results, as they can barely be differentiated on the plot.

Figure 6-9 consists of two side-by-side plots. The left plot is titled "ACE Results (k-epsilon) + Data" and the right plot is titled "ACE Results (RNG) + Data". Both plots show the Pressure Coefficient on the y-axis (ranging from -2.5 to 1.5) versus Beta (degrees) on the x-axis (ranging from 0 to 200). The plots include data points for CP-Jones (open circles) and several CFD-ACE results. The legend for the left plot includes: CP-Jones (open circle), 121x121-.00001 (solid line with open triangles), 121x121-.00005 (dashed line with open triangles), 61x61-.0005 (solid line with open squares), 61x48-.005 (dotted line with open squares), and 121x48-.005 (dash-dot line with open squares). The legend for the right plot includes: CP-Jones (open circle), 61x61-.00005 (solid line with open triangles), 61x61-.0005 (dotted line with open triangles), 121x48-.005 (dashed line with open squares), and 61x48-.005 (dash-dot line with open squares). In both plots, the pressure coefficient starts at 1.0 at 0 degrees, drops to a minimum of approximately -2.2 at 80 degrees, and then rises to a peak of approximately -0.5 at 120 degrees before settling back to -0.5 at 200 degrees. The data points for CP-Jones are scattered around these curves, with the CFD-ACE results generally tracking the data points closely.

Figure 6-9. CFD-ACE Results Using the  $k-\epsilon$  and RNG Turbulence Models

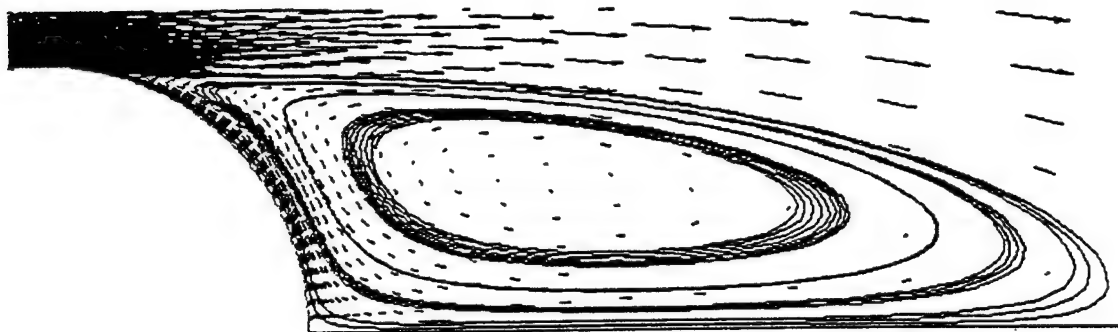
The same trends are reproduced in Figure 6-9b, which shows results using CFD-ACE and the RNG turbulence model. The match to the data is much better for this option than the  $k-\epsilon$  turbulence model. The same trends for matching the data are found for the various grid sizes and grid resolution. There was no difference between the 61x48 and 121x48 mesh results at the first cell spacing of 0.005 meters. As with the  $k-\epsilon$  results, the finest mesh produced the closest match to the data.

The change in the physical features of the flowfields can be seen in Figure 6-10, where velocity vectors and particle traces are shown for the separated region of the cylinder for the OVERFLOW results using Baldwin-Barth and CFD-ACE results using both the  $k-\epsilon$  and RNG turbulence models. The views and particle release points are not identical, but changes in the flow can be seen. The separated area in the OVERFLOW solution starts closer to the top of the cylinder, is initially tangent to the dominant flow direction, but closes out within two cylinder diameters. The separation zone for the ACE solution with RNG model appears to start farther back, being sloped at a negative angle initially. The slope of the zonal boundary then turns more parallel to the x-axis and elongates the cell, finally closing out farther down stream than the OVERFLOW solution. The ACE solution with the  $k-\epsilon$  model produces a separated region considerably shorter than with the RNG model, even though the pressures levels in the base flow region are very close to each other in the two solutions. The higher pressure level in the base flow region correlates with the separation point occurring farther aft on the cylinder surface.

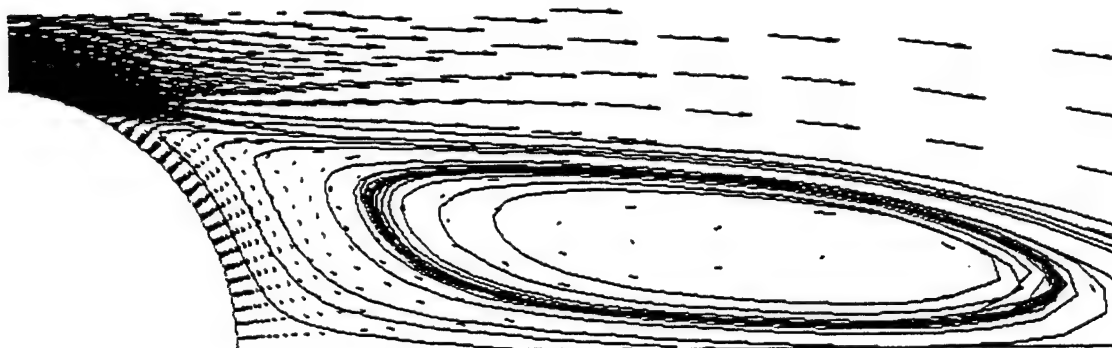
The CFD-FASTRAN code was run using the same fine grids as the previous two codes. Two turbulence models were used, the same  $k-\epsilon$  model as in CFD-ACE and a two-equation,  $k-w$  turbulence model. Pressure coefficient profiles from these runs are shown in Figure 6-11, where two of the finer-grid meshes were used in the analysis. The two different turbulence models did not appreciably change the flow field. CFD-FASTRAN predictions were very similar to CFD-ACE using the same turbulence model. The small difference might be attributed to the difference in solution methodology. CFD-ACE is a pressure based code while CFD-FASTRAN is a density based code. Density based codes do not perform well for low Mach number flows. Since the Mach number for this problem is .177 (near incompressible) and much lower than typical ejection seat flows, it is expected that CFD-FASTRAN will perform better for the ejection seat problem.

In general, CFD-ACE converged in less iterations per run, although for the grids with the 0.00001 meter mesh spacing at the surface, the convergence was slowed somewhat. Due to the lower cpu per time step, the overall resources were comparable for OVERFLOW and CFD-ACE on this problem. The OVERFLOW code however, does take up considerably less memory per node than CFD-ACE, so greater grid densities can be employed in the mesh without paying a high cost. Cases run with CFD-FASTRAN required numbers of steps comparable to that producing convergence with OVERFLOW, however, CFD-FASTRAN needed more CPU time because it employed one of the more intensive computational schemes in the code.

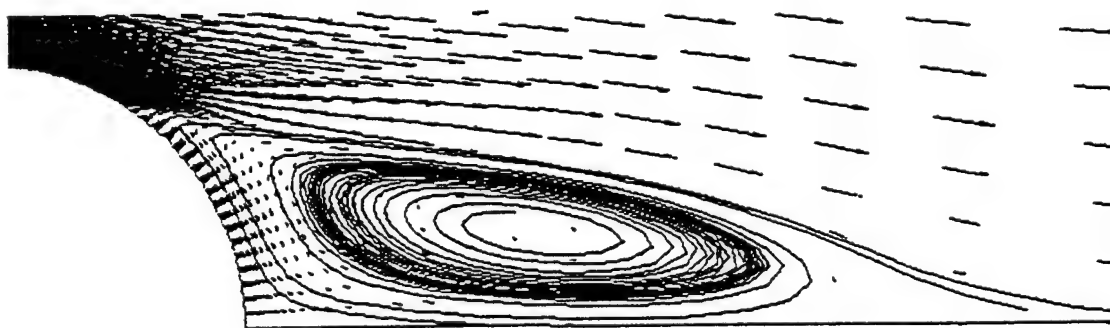
For this problem, the best results computed using CFD-ACE and OVERFLOW were roughly equivalent. OVERFLOW could more accurately predict the flowfield using the Baldwin-Barth turbulence model, but a fine mesh with values of  $y_+$  on the order of five or less was required to achieve these results. The accuracy of the solution fell off faster with the OVERFLOW code when the grid resolution was decreased (increasing cell size). CFD-FASTRAN predictions with the standard  $k-\epsilon$  turbulence model were similar to those of CFD-ACE with the same model.



OVERFLOW : Baldwin-Barth



CFD-ACE : RNG Model



CFD-ACE : k-epsilon Model

Figure 6-10. Comparison of Base Flow Recirculation Pattern Using OVERFLOW and CFD-ACE

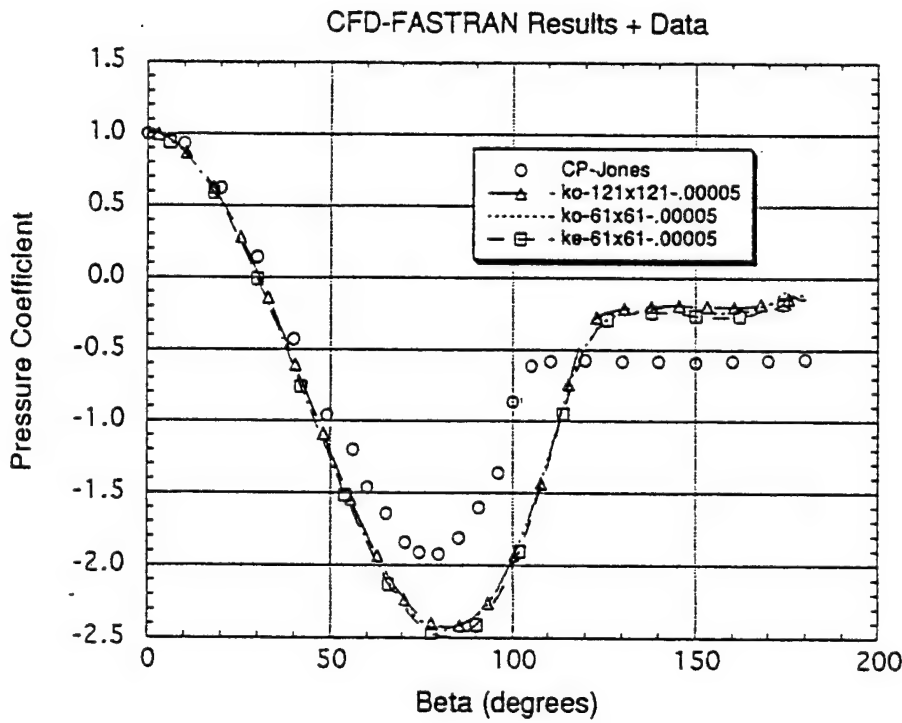


Figure 6-11. CFD-FASTRAN Results Using Two Turbulence Models on Fine Meshes

### 6.3.3 ACES-II Simulations

To further assess the CFD codes prediction accuracy and efficiency, Several calculations were performed on the ACES-II seat and occupant geometry with both CFD-FASTRAN and OVERFLOW codes. A CFD-ACE database for the ACES-II seat was already available from a previous task of this project (see Section 4.1.2). Most of this effort was involved in OVERFLOW calculations due to the lack of experience with the code and due to certain difficulties that were encountered in the process. CFD-FASTRAN input structure is very similar to that of CFD-ACE; therefore performing these calculations using already existing grids and input files from CFD-ACE was a relatively easy process.

The simulations with OVERFLOW started by using some of the parameters recommended by the code developers at NASA Ames and learned from the cube simulations. However, it was fast learned that the set of parameters that worked for the cube and cylinder do not necessarily work as well for the ejection seat. The major reasons may be the size and skewness of the grid. Therefore, the ejection seat simulations started again by trying various turbulence models and solver switches.

After discussions with the code developers and running a test case with ACES-II, it was found that k-e turbulence model as implemented in OVERFLOW would be very difficult to work and get converged solutions. Because the Baldwin-Lomax model is not adequate for flows with big wakes and large recirculation zones (also Baldwin-Lomax

requires very fine grids) the only choice that was left was the Baldwin-Barth model which performed well on the cylinder case using very fine grid resolution.

Different runs were made with various solver switches to choose the optimum parameters (such as CFL number, differencing scheme, time step, etc) to use for ejection seat simulations. Figure 6-12 shows the normalized residuals for all the runs. As can be seen from the figure, the residuals dropped considerably between time steps of 7000 and 10000 with a specific set of parameters. This set was chosen for the simulation and a new run started from scratch. Figure 6-13 shows the history of convergence for the aerodynamic coefficients. This figure clearly shows that the solution has converged after 2500 time steps which require about 51 CPU hours on the IBM workstation. This same run requires about 12 CPU hours using the CFD-ACE code. However, subsequent runs using different seat orientations and restarting from a previous solution require only about 300 time steps or about 6 hours of CPU time which is comparable to CFD-ACE.

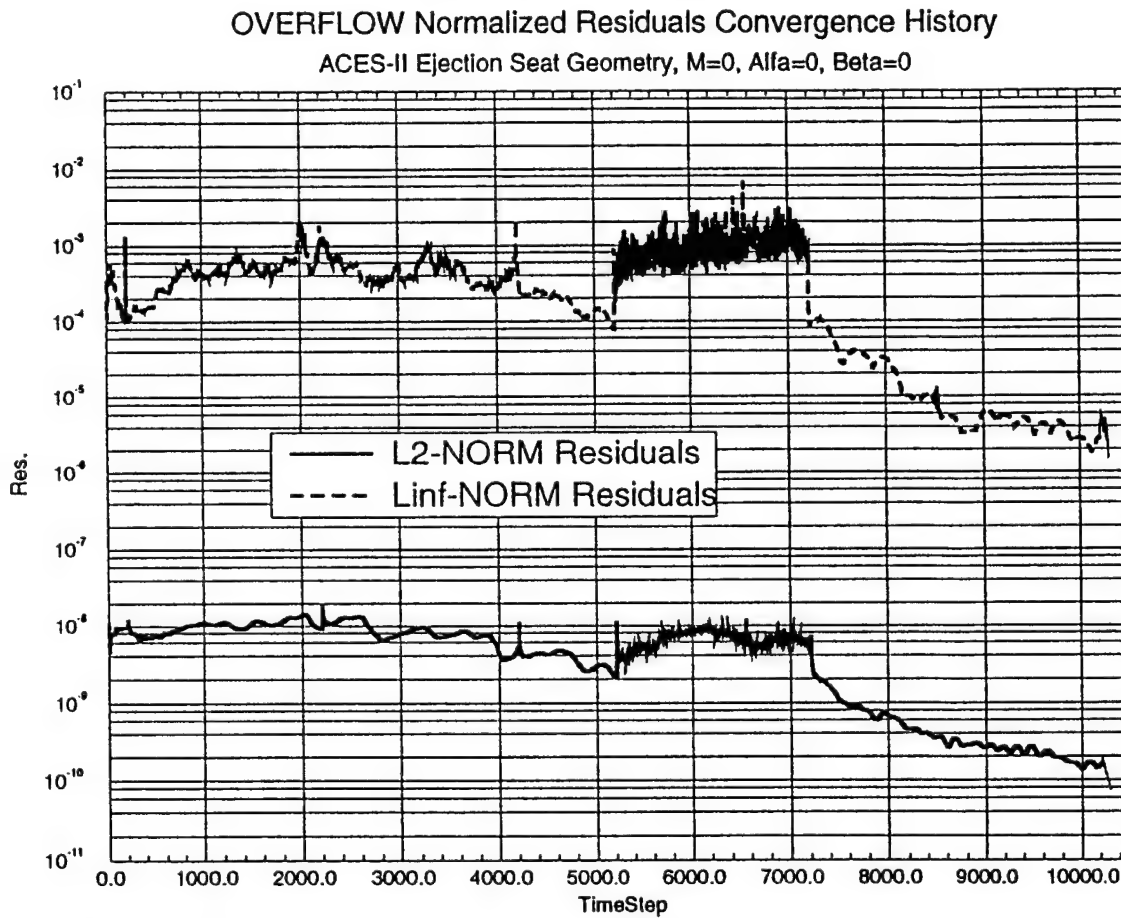


Figure 6-12. OVERFLOW Convergence Characteristics of ACES-II Geometry

OVERFLOW Aerodynamic Coefficients Convergence History for ACES-II Seat  
M=0.6 , Alfa=0 , Beta=0 , Baldwin-Barth Turbulence Model

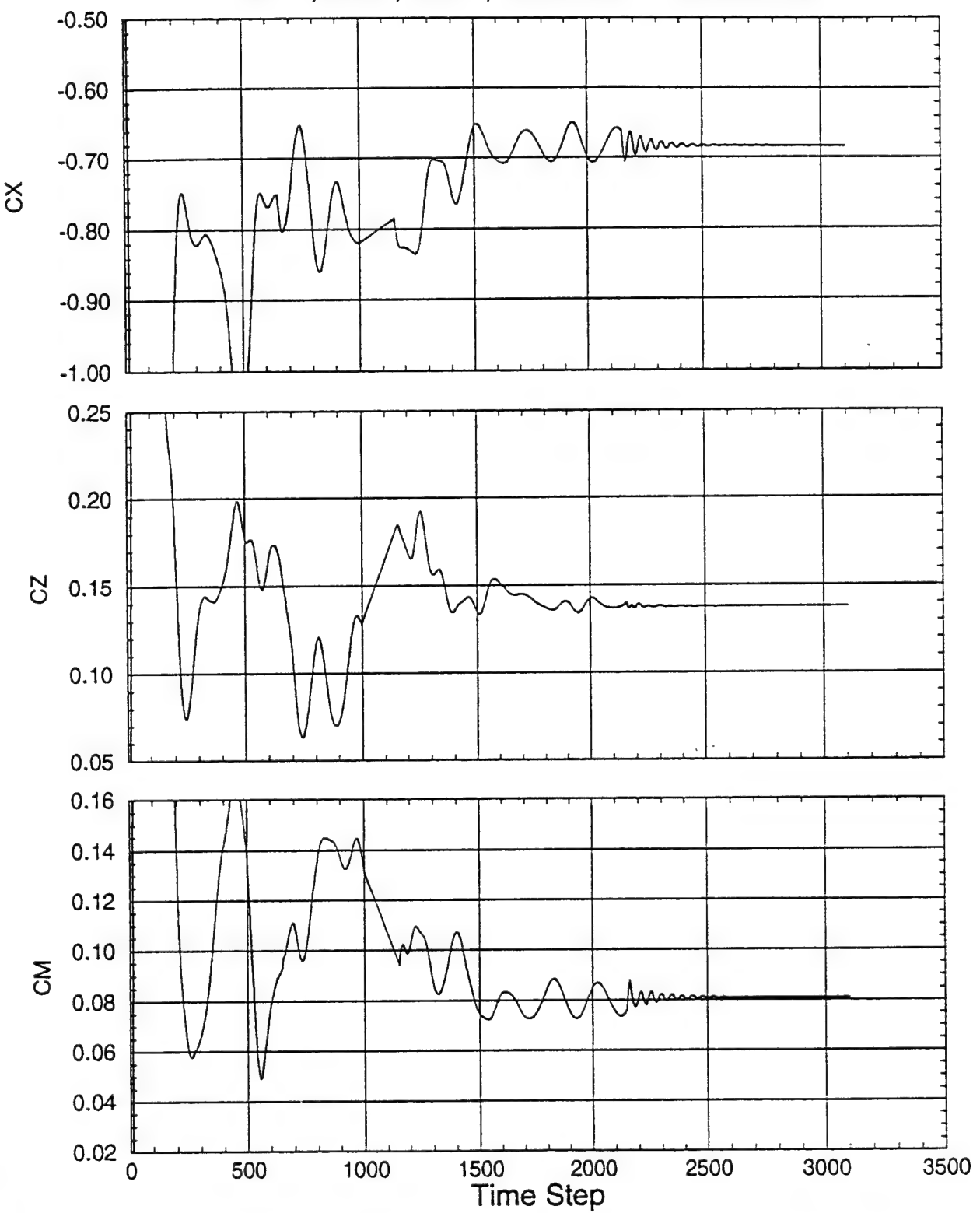


Figure 6-13. OVERFLOW Aerodynamic Coefficients Convergence History with a Chosen Set of Solver Parameters

Based on the results which showed some discrepancy with the force coefficient,  $C_x$ , at zero pitch and yaw orientation, it was decided to get a solution with laminar and inviscid model for benchmarking the turbulence model. However, as Figure 6-14 shows, convergence was very difficult to obtain and the idea was abandoned.

CFD-FASTRAN simulations were also conducted on the ACES-II seat and occupant geometry at various pitch orientations. As stated above, due to existing experience with the CFD-FASTRAN code, these simulations were relatively easy to perform. CFD-FASTRAN support blockages in the same manner as CFD-ACE. These simulations were performed with the  $k-\epsilon$  turbulence model and a second order differencing scheme. Converged results were obtained in reasonable time (slightly longer than CFD-ACE; about 1 hour per case).

Figure 6-15 shows the OVERFLOW results (i.e. aerodynamic coefficients) obtained using the Baldwin-Barth model, compared to CFD-ACE, CFD-FASTRAN and wind tunnel test data for different pitching orientations. Throughout the pitching envelope CFD-ACE is most accurate (CFD-ACE is within 5-10 percent, CFD-FASTRAN is within 10-20 percent while OVERFLOW is within 15-30 percent for force coefficients). It is obvious that OVERFLOW does not perform equally as well on the ejection seat and the cylinder using the Baldwin-Barth model. The main reason for this discrepancy is that Baldwin-Barth requires fine grids near the wall which is available with the cylinder and not with the seat. It would not be economically feasible to use grids with this resolution with the ejection seat geometry.

OVERFLOW Aerodynamic Coefficients Convergence History for ACES-II Seat  
 $M=0.6$ ,  $\text{Alfa}=0$ ,  $\text{Beta}=0$

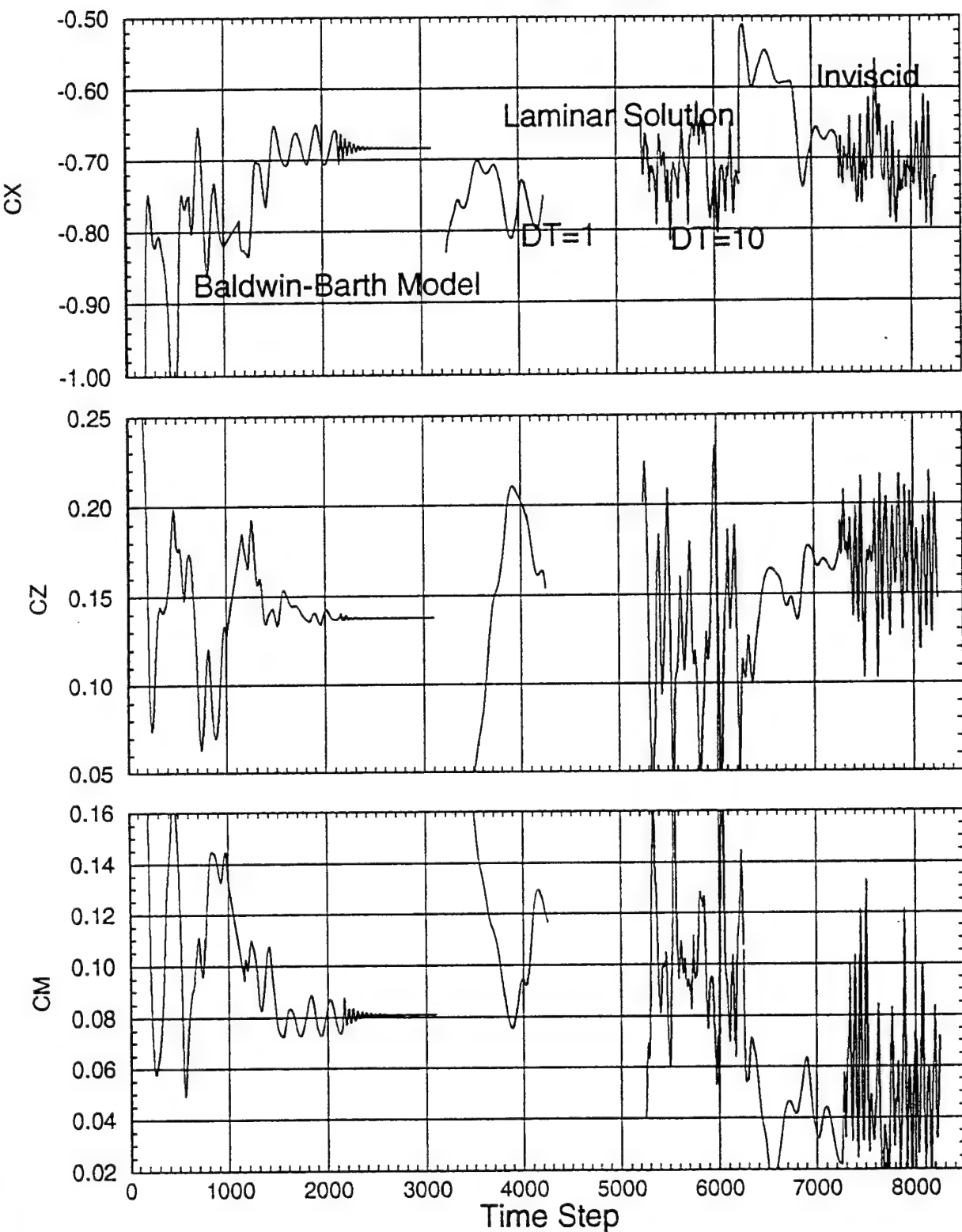


Figure 6-14. OVERFLOW Convergence Characteristics for Laminar and Inviscid Models

## CFD CODES VALIDATION USING ACES-II GEOMETRY

Mach Number = 0.6

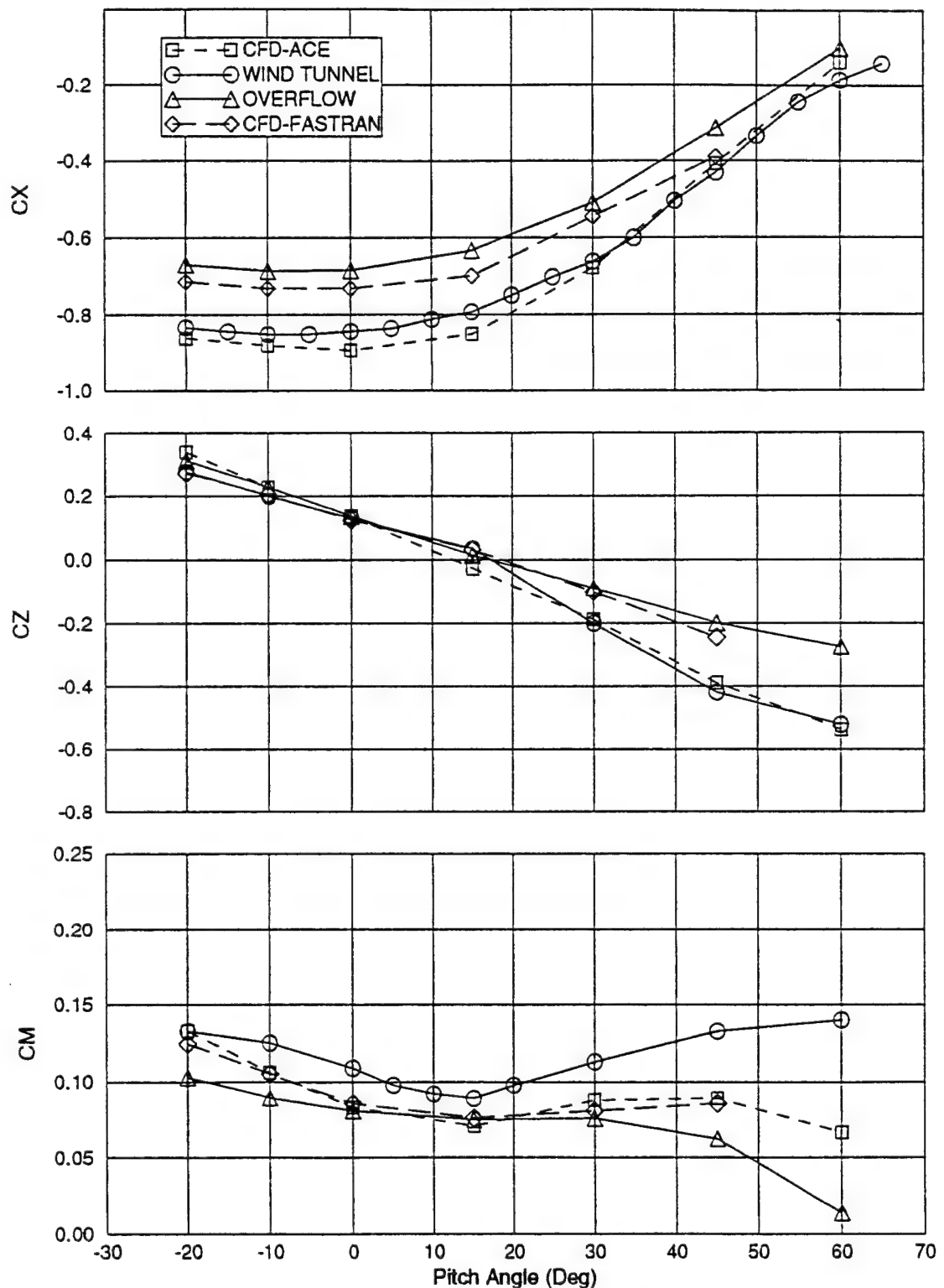


Figure 6-15. Predicted ACES-II Coefficients Compared to Test Data

## 7. CFD-FASTRAN DEVELOPMENT AND ADAPTATION FOR MULTIPLE AND MOVING BODIES

One of the major objectives of this phase II study was the development of a CFD methodology for conducting steady-state and unsteady simulations of seat/occupant separation from an aircraft. The simulation of seat/occupant and aircraft separation using CFD is a challenging task for several reasons. First, the seat/occupant, cockpit, canopy, and aircraft are by themselves complex bodies that make geometric modeling and grid generation difficult. Furthermore, when these bodies are combined for separation analysis, the generation of a single topological grid system becomes impractical. Secondly, when transient separation analysis is required, the complex grid systems around each body must adjust as the bodies move relative to one another. For these reasons, geometric modeling and grid generation methodologies are paramount.

In the past decade, the chimera overset methodology has become the most widely accepted approach for solving moving body problems [32,33]. The chimera methodology uses a series of structured meshes to discretize a complex body or bodies into individual grids reducing the complexity of grid generation. These individual grids are then composited into a set of overset or overlapping grids. During the solution procedure, flow field information is then passed between the individual grids along domain boundaries.

Numerous researchers have used the overset chimera methodology to study a variety of steady state problems involving complex bodies including modern aircraft [34-39]. Recently, investigators have been using the method for moving-body problems. Some examples include Shuttle Solid Rocket Booster separation [40], safe store separation [41,42], and multiple store release [43].

In this study, two chimera methods were investigated and implemented into CFD-FASTRAN. The two methods are similar but rely on different methods for performing the inter-grid communication. The first method to be implemented was the overset-hybrid approach which relies on a "patching" unstructured grid for inter-grid communication. Due to the expense and complexity of generating unstructured patching grids, this method proved to be unfeasible for transient applications. As a result, the more robust traditional-chimera approach which relies on trilinear interpolation for inter-grid communication was implemented into CFD FASTRAN. Although, the overset-hybrid approach was abandoned in favor of the traditional-chimera approach, both of these methods and their adaptation into CFD-FASTRAN are discussed below.

### 7.1 Overset-Hybrid Methodology

An overset-hybrid scheme was first implemented into CFD-FASTRAN to perform seat and aircraft simulations. In standard hybrid-grid methods, a combination of structured and unstructured grids are employed to model a configuration. The structured and unstructured regions are connected along common domain boundaries by conservative

cell interfaces. In the overset-hybrid approach, the hybrid grid methodology and the chimera grid methodology are combined.

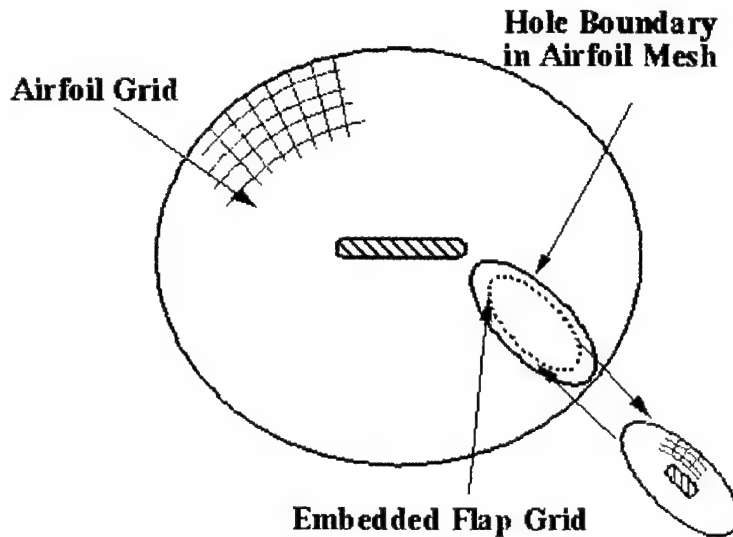


Figure 7-1. Overset-Hybrid Scheme Mesh-to-Mesh Communication

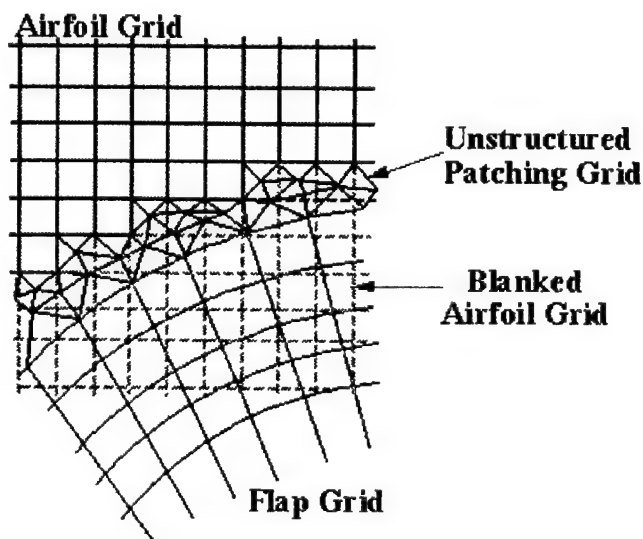


Figure 7-2. Overset-Hybrid Scheme Grid Overlap Region

The overset-hybrid methodology is outlined in Figure 7-1 for a flapped airfoil geometry. As with the traditional chimera methodology, structured grids are employed to grid major configuration components, i.e. the flap and airfoil. The structured grids are then combined in a Chimera fashion, where the minor body grids (flap grid) overset the

major body grids (airfoil grid). As a result of the oversetting, the overlapping grid cells in the major grids are blanked (in the chimera sense). At this point, a distinction between traditional-chimera hole cutting procedures and overset-hybrid hole cutting procedures must be made. In the traditional chimera scheme (Figure 7-10), the flap surface is used as a hole creation boundary for the airfoil grid. However, in the overset-hybrid scheme (Figure 7-2), the outer boundary of the flap grid is employed as the hole creation boundary for the airfoil grid. The result of this type of hole cutting is an open interconnecting region between the flap grid and the interior of the airfoil grid, see Figure 7-2. These interconnecting regions are filled with an unstructured grid to provide inter-grid communication. This unstructured grid replaces the interpolation schemes employed by the traditional chimera scheme. The major advantage to the overset-hybrid scheme is that it is guaranteed to be fully conservative whereas the traditional chimera scheme is not. However, the disadvantage of the overset-hybrid scheme is its increased complexity and computational expense. Experience has shown that the traditional chimera and conservative chimera schemes produce nearly identical results for a wide range of problems of interest.

To demonstrate the grid generation process for the overset-hybrid methodology, a simple three dimensional example is presented. Consider the case of a rectangular grid overset onto a pair of background grids representing an outer flow-field domain and a cavity domain. This grid system is topologically equivalent to an ejection seat grid positioned within an aircraft and cockpit grid system. Figure 7-3a is a centerline cut of the rectangular body grid overset onto the cavity and outer domain grids. The cavity and outer domain grids are connected by a simple blocked interface. In Figure 7-3b, the interconnecting region between the rectangular body and the other grid domains is cut using an analytical shape function. In this case a sphere is used; however, any analytical shape that encloses the rectangular grid could be used. After hole creation is completed, the grids are imported into CFD-GEOM, and an unstructured advancing front grid generator is used to link the cut faces of the cavity and outer grids to the exterior of the rectangular grid, Figure 7-3c. The final three-dimensional overset-hybrid grid system is shown in Figure 7-3d. This overset-hybrid grid system can now be imported into CFD-FASTRAN for flow-field simulations.

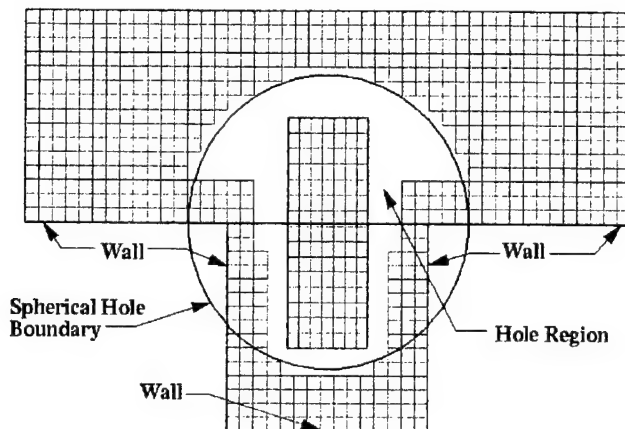


Figure 7-3a. Overset Hybrid Grid System for Rectangular Body in Cavity

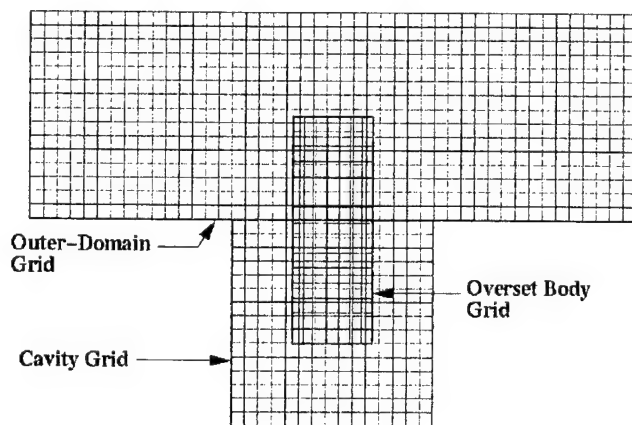


Figure 7-3b. Hole Creation in Cavity and Outer Domain Grids

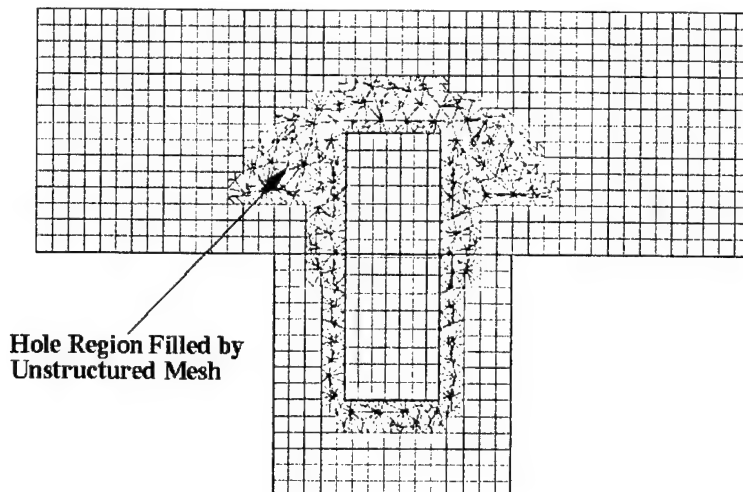


Figure 7-3c. Centerline Cut View of Overset-Hybrid Grid System

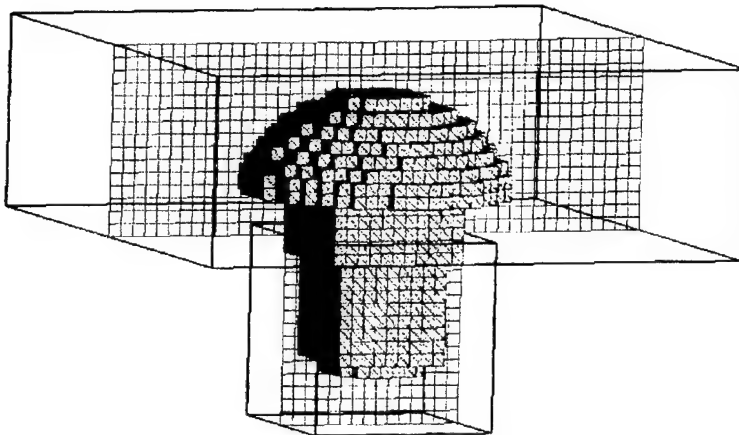


Figure 7-3d. Three-Dimensional View of Grid System with Shaded Hole Boundary

Flow solver demonstrations for the overset-hybrid methodology were conducted for a seat and aircraft configuration. The modeled geometry was a half scale F-16 and ACES-II ejection seat at a 23.8 inches separation distance from the aircraft. In Figure 7-4, the created computational grids at the symmetry plane are shown. A hole was created (see Figure 7-5) in the major grid as a result of the superposition of the minor grid. The blanked space between the minor and major grids was filled using the unstructured advancing front gridding methodology. Also note that the size of the hole is small (see Figure 7-6) therefore making regridding efficient. Flow simulations at a free stream Mach number of 1.2 were performed with the adapted CFD-FASTRAN code, and successful results were obtained as seen in Figures 7-7 through 7-9.

In theory, the overset-hybrid methodology can be employed for moving body simulations by allowing the unstructured grid to deform as the ejection seat is moved. The unstructured grid would use a spring analogy to deform until a distortion threshold was exceeded. At this point, the holes would be automatically re-cut, and the structured grids would be reconnected with a new unstructured grid. The new unstructured grid would then need to be initialized using the flow field solution from the preceding time step. This initialization would require the use of interpolation schemes similar to those employed for traditional chimera.

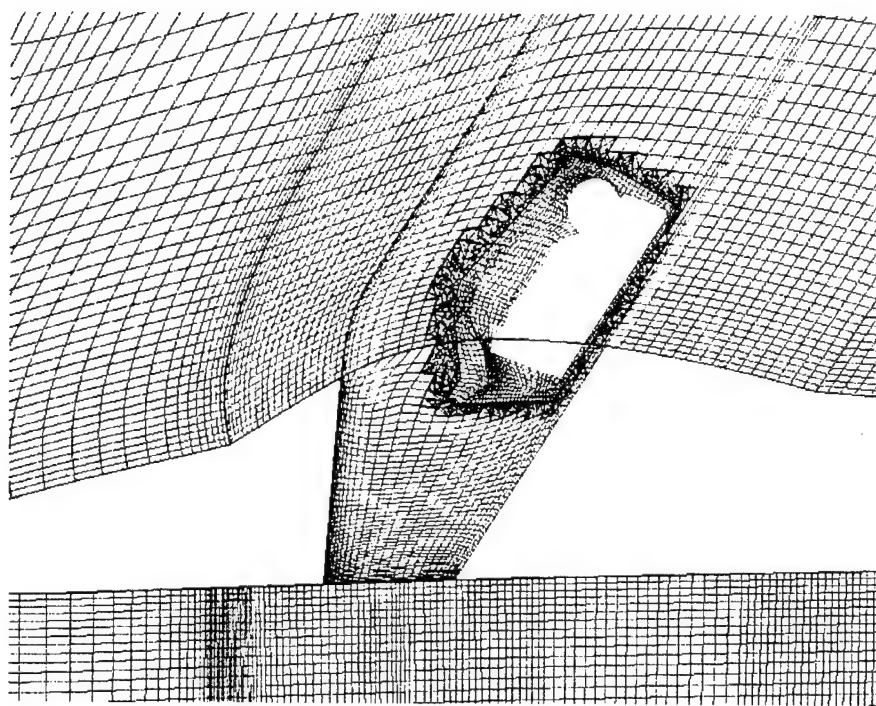


Figure 7-4. Overset-Hybrid Grid at Mid-Computational Plane for 0.5 Scale ACES-II at 23.8 inches Separation Distance from F-16 Aircraft

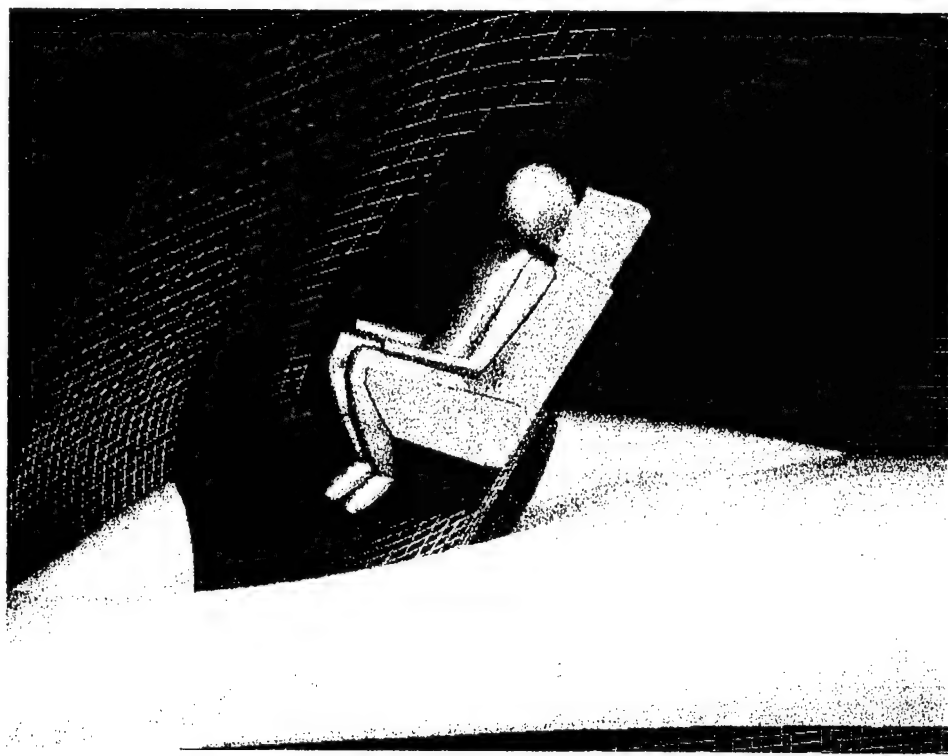


Figure 7-5. Hole in Major Grid Before Created by Oversetting Seat Grid

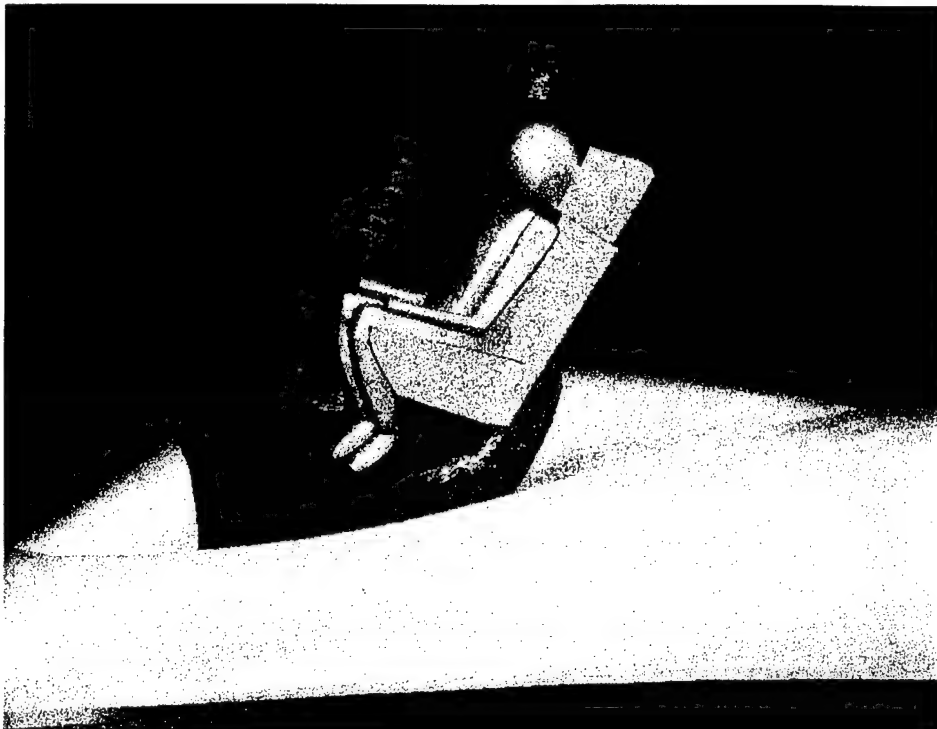


Figure 7-6. Unstructured Grid Generated to Fill Hole and Connect Minor and Major Grid Surfaces

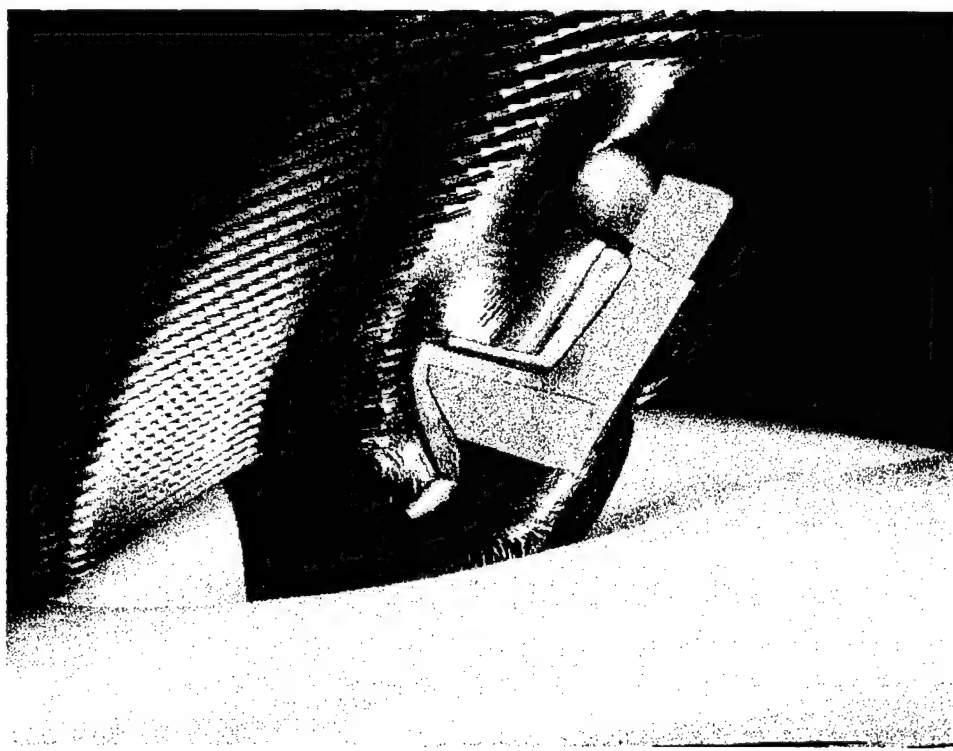


Figure 7-7. Velocity Vectors at Mid-Computational Plane for Free Stream  $M = 1.2$

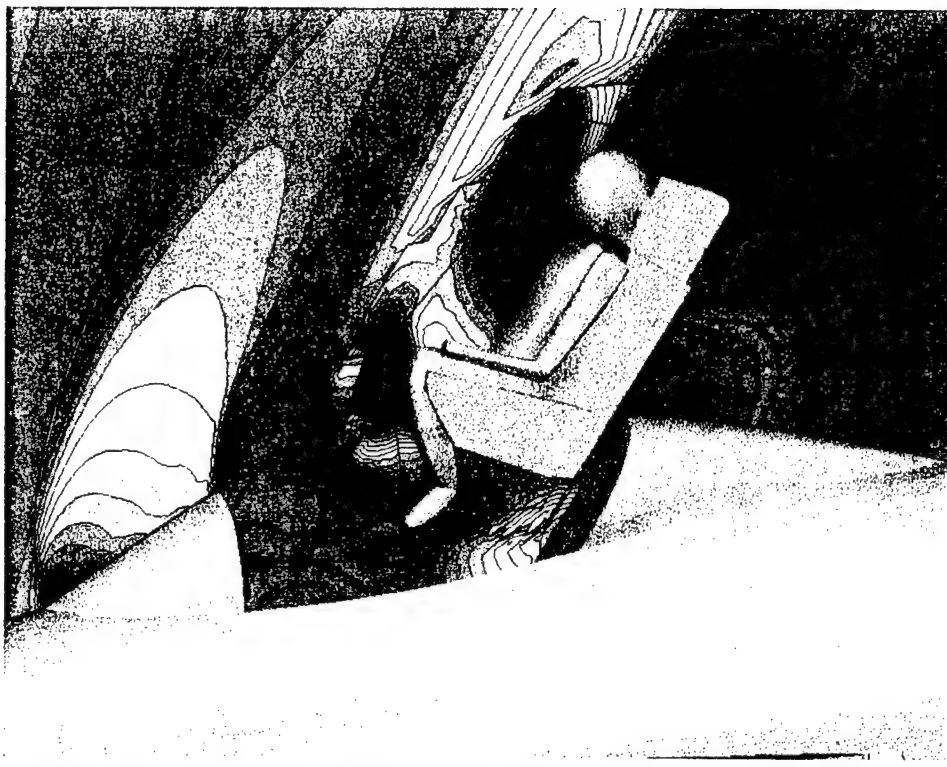


Figure 7-8. Pressure Contours at Mid-Computational Plane for Free Stream  $M = 1.2$



Figure 7-9. Seat and Aircraft Pressure Contours for Free Stream  $M = 1.2$

In practice, the overset-hybrid methodology has proven to be unsuited for moving body simulations. The primary reason for this failure is the inability to stretch the unstructured grids without producing cells with negative volumes. This has proven to be true for even the simplest geometries. Secondly, the fully conservative nature of the overset-hybrid methodology is compromised when the unstructured grid is initialized through interpolation. Therefore, the major advantage of the overset-hybrid method is negated for moving body problems. More practically, the cost of generating unstructured grids is prohibitive for all but the simplest of geometries. For these reasons, the overset-hybrid method was abandoned for moving body problems.

## 7.2 Traditional Chimera Methodology

After the difficulties associated with the overset-hybrid scheme were fully explored, the traditional chimera methodology was implemented into CFD-FASTRAN for the simulation of both steady state and transient ejection seat problems. The original chimera methodology was developed by Steger and Benek [32,33]. The general concept behind Chimera is illustrated in Figure 7-10, which depicts two independently generated meshes representing a flapped airfoil. The flap mesh is embedded (overset) within the airfoil mesh. The hole cutting and interpolation processes are illustrated in Figure 7-11. A hole is created within the airfoil mesh to remove the points within the airfoil mesh that are interior to the flap. The hole boundary points of the airfoil mesh are then updated by interpolation from the flap mesh. The flap mesh outer boundary also receives flow field information interpolated from appropriate mesh points in the airfoil mesh. In this manner, a set of independent grids can be combined to form a single grid system.

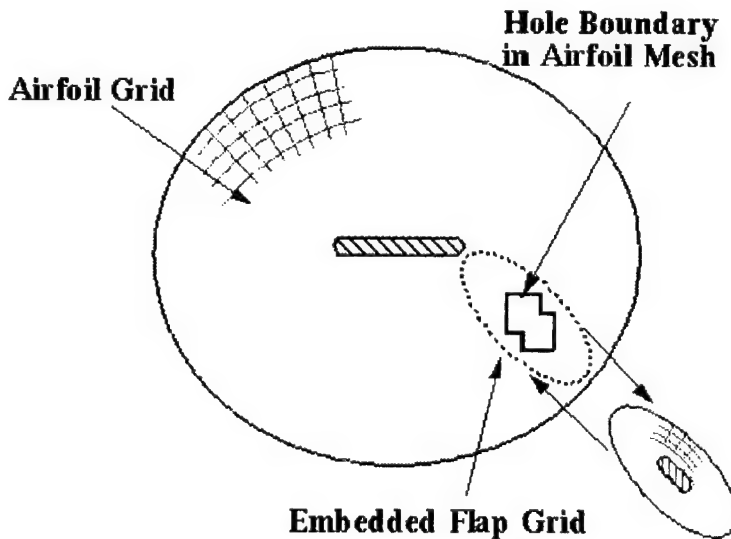


Figure 7-10. Traditional Chimera Scheme Mesh-to-Mesh Communication.

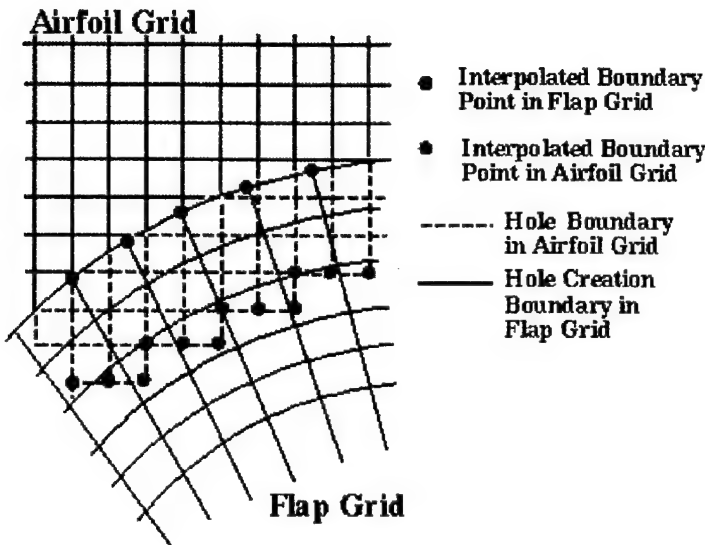


Figure 7-11. Traditional Chimera Scheme Grid Overlap Region.

The most difficult task in implementing chimera is the compositing of the grids. This task requires that all of the chimera outer and hole boundaries be identified and that interpolation stencils be created. This process can be very user intensive because of the input required to define chimera hole cutting regions. The process can also be very CPU intensive because extensive search routines are required to identify appropriate interpolation stencils. The PEGSUS code [34] developed at AEDC and NASA Ames is widely used to perform this task. PEGSUS is a stand-alone code that produces a file consisting of interpolation information that is used by a flow solver to perform inter-grid communication. The PEGSUS code is often difficult to employ because it is not highly automated and is not an integral part of the flow solver. Additional problems develop with PEGSUS when moving bodies are considered. As a grid translates and rotates with a given body, new holes and interpolation coefficients are needed as a grid passes through the surrounding domains. To be time accurate, the interpolation coefficients at the outer boundary of the store grids must be updated at each time step. Updating the interpolation coefficients at each time step is computationally expensive. To illustrate the CPU expense for PEGSUS, the process of hole cutting and interpolating is often 2 to 5 times more expensive than the actual flow solver.

CFD-FASTRAN has been implemented with a recently developed, fast and completely automated grid compositing module [44]. This grid compositing module completely eliminates the use of the PEGSUS code. Furthermore, this module is based on general hole-cutting schemes and efficient tree searching interpolation routines. These new routines reduce the CPU expense of hole cutting and interpolation to a fraction of the flow solver expense. These new routines also greatly simplify the use of chimera and are ideally suited for moving body problems.

An outline of the automated hole cutting algorithm is presented below:

- a. **Grid Relations:** In some grid compositing algorithms, the grids are defined in a hierarchical manner. For example, a grid containing another grid is considered a parent or a major grid. The other grid is the child or the minor grid. The present algorithm is designed for arbitrarily overlapped grids. For example, a grid can contain or be contained by another grid, or partially overlap another grid. All grids are treated equally unless the user demands otherwise (this is easily controlled through the CFD FASTRAN GUI).
- b. **User Input:** User input is obtained from the CFD-FASTRAN GUI. Since automation is the ultimate goal, minimum input from the user is required. The user need only define two sets of inputs for each grid:
  1. Non-Penetrable Surface (NPS), usually wall boundaries. These boundaries are automatically linked to the hole-cutting routines when a wall or blocked boundary is defined in the GUI.
  2. Interpolation Boundary Surfaces (IBS), usually the outer boundaries of a grid. These boundaries are also specified conveniently through the GUI.If the user so demands, he/she can also define a set of donor grids (for each IBS), in which the interpolation stencils for the IBS points will be located. Otherwise, the hole-cutter will find the stencil automatically based on some pre-defined criteria.
- c. **Hole Cutting:** The only situation in which a hole is necessary in a grid is the presence of a NPS (such as body surfaces) in the grid. Therefore for each grid, the NPS of this grid is used to cut holes in all other grids and to produce hole boundaries in all other grids. The first step is to identify the edges in other grids that intersect the NPS of a grid. Once these edges are identified, the nodes of the edges are differentiated based on whether they lie inside the NPS or outside of it. Once these nodes are identified, the cells that surround the nodes are blanked. The final step is to recursively blank out all the cells in the other grids that are interior to the NPS. This completes the hole-cutting procedure and grid cells that are immediately next to the hole are identified as Interpolated Boundary Cells. Of course, this type of hole-cutting process can be CPU intensive. This problem has been eliminated by employing state-of-the-art geometric intersection algorithms and data structures such as the Alternate Digital Tree (ADT).
- d. **Stencil Identifications:** The next step in the solution procedure is to find donor cells for the IBSs in each grid. For a chimera-boundary cell in a given grid, the respective donor is identified by searching the other grids for a cell that encloses the cell-centroid of the chimera-boundary cell. Once a donor is identified, the solution is injected from the donor into the chimera-boundary cell by means of an interpolation algorithm. In the present approach, the solution residing at the nodes of the donor is interpolated trilinearly to the chimera-cell center. In the

event wherein a chimera-boundary cell does not find an appropriate donor, it is marked as an orphan cell. The solution at the cell-center of the orphans is then treated as the average of the solution in its neighboring cells. Again, very efficient algorithms with the ADT data structure are used in the stencil searching process.

e. **Data Structures:** In the hole-cutting algorithm that was described above, the step that involves identifying the edges in other grids that intersect the faces on the NPSs of a grid, requires a laborious search. Similarly, in the interpolation algorithm, the step that involves identifying the donor that encloses the cell-center of a given IBS cell would result in an extensive search. The successful implementation of the chimera scheme hence depends on the use of efficient algorithms that expedites these search processes. For steady-state problems, the efficiency of these algorithms is not very critical. This is due to the fact that the hole-blanking needs to be done only once at the start of the solution process. Further, the interpolation stencil, constituted by nodes of the donor cell, for a given chimera boundary cell does not change in subsequent steps of the time-marching scheme. Hence, it needs to be identified only once. But, for unsteady simulations, both the hole-cutting and donor-search procedures have to be done repetitively, as the relative orientation of the overset grids change. Hence, care must be taken to devise data structures that will enable efficient implementation of the search algorithms.

The associated data structure used in the present approach is called the alternating digital tree (ADT). This offers the possibility of efficiently inserting points in a tree structure and optimally searching for points. This data structure is an extension of a binary tree which is used in one dimensional space. The ADT provides a very general method of building a tree for a given set of geometric objects in an  $N$  dimensional space by treating the objects as points in a  $2N$  dimensional space.

In the current approach, the hole-cutting process proceeds as follows, using the ADT data structure.

- An ADT is built with the faces that represent the solid wall boundary of the major grid. The faces are denoted as 6D points in the ADT, comprising the co-ordinates of the respective bounding boxes ( $x_{\min}, y_{\min}, z_{\min}, x_{\max}, y_{\max}, z_{\max}$ ). For every edge in the major grid, also represented by 6D co-ordinates of its bounding-box, the algorithm searches the ADT to identify the minor grid wall faces whose bounding-boxes overlap with that of the edge. This constitutes the list of faces that the edge could intersect.

The interpolation algorithm, using the ADT, proceeds as follows:

- An ADT is built for each grid with its cells, represented by the 6D co-ordinates of its bounding-box. For a given chimera-boundary cell in each grid, the algorithm searches the ADT of the other grids and finds a list of cells whose bounding-boxes overlap with that of the chimera-boundary cell. Using this short list of cells, the

algorithm then proceeds to find the donor that encloses the centroid of the chimera-boundary cell.

The automated hole cutting algorithm is demonstrated in Figure 7-12 and 7-13 for a NACES ejection seat grid overset onto a background grid. The background grid is shown with black grid lines and is flooded in gold. The NACES ejection seat grid is overset on the background grid and is shown with blue grid lines. In Figure 7-12, the symmetry plane view of the seat is presented. The hole cut in the background grid is easily visualized as the area surrounding the seat with the white background. The shape of this hole cut is essentially the shape of an inflated seat surface. In Figure 7-13, an axial view of the seat and background grid are presented. Once again, the hole cut in the background grid is seen to closely conform to the seat topology.

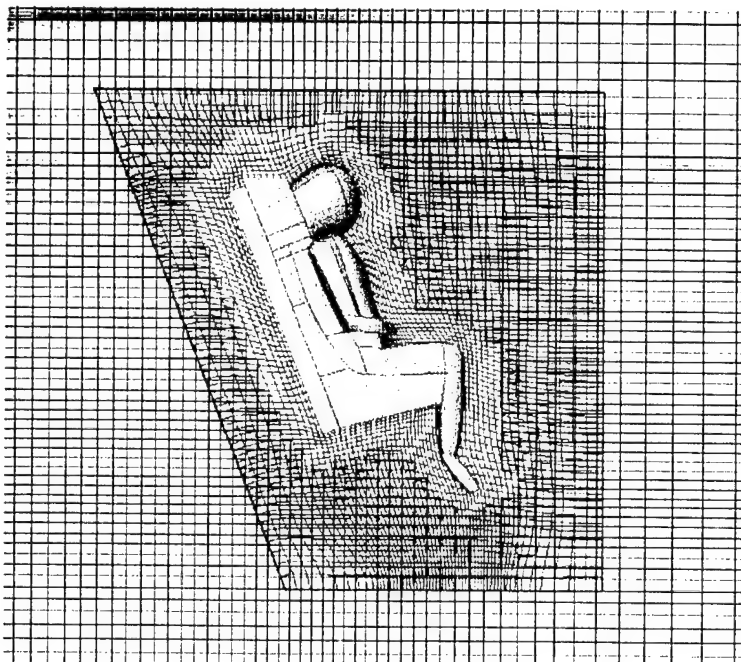


Figure 7-12. Symmetry Plane for Automated Hole Cutting for NACES Ejection Seat Grid on a Background Grid

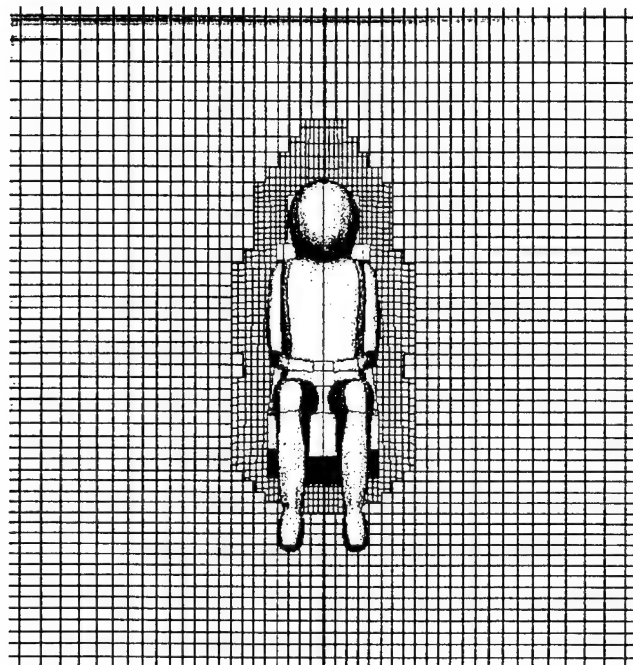


Figure 7-13. Axial Planes for Automated Hole Cutting NACES Ejection Seat Grid on a Background Grid

### 7.2.1 Chimera Adaptation for Moving Body Problems

For performing a transient moving-body problem with chimera, such as an ejection seat separating from an aircraft, there are three main solution steps:

- geometric modeling and grid generation,
- steady-state solution, and
- transient solution.

The first step in performing a transient moving-body problem is obtaining a fully converged steady-state solution. This steady-state solution serves as the starting point for the transient calculation. Generation of chimera grids and steady-state solutions have been discussed in detail previously. Due to the use of the chimera grid methodology, no additional geometric modeling or grid generation is required for simulating the transient problem. One important exception exists for steady-state solutions obtained using local or variable time-stepping options. If local time stepping is used, then the solution should be restarted and fully converged using a global time step. This process usually takes a few hundred iterations and ensures a consistent transition to time accurate solutions.

The transient solution process can be further broken down into five steps:

- time accurate flow solver step,
- calculation of body forces and moments,

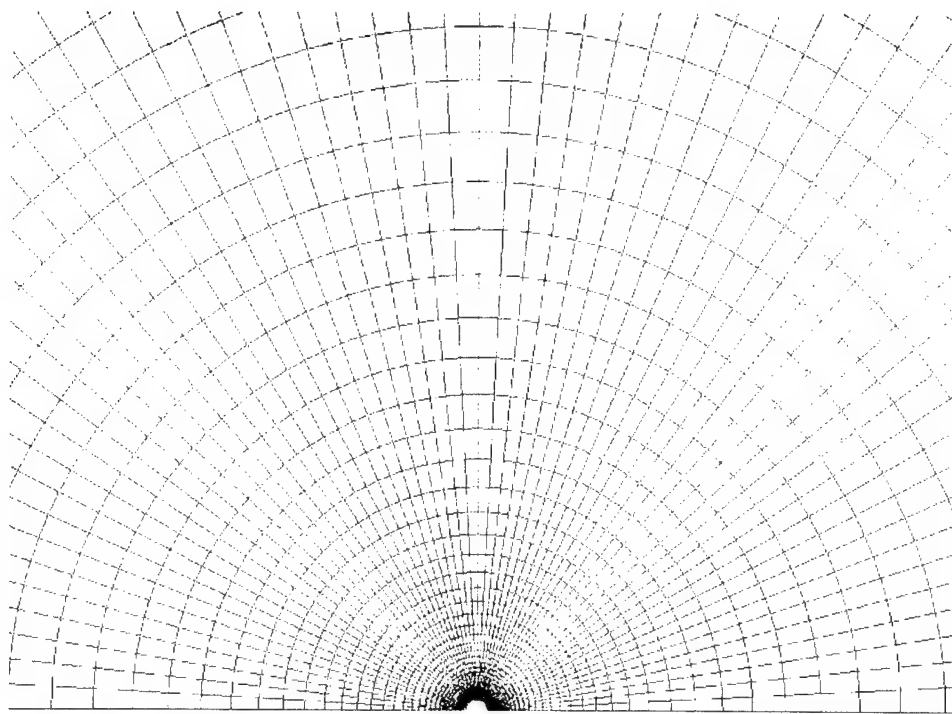
- calculation of body motion via 6DOF or prescribed motion,
- perform body motion and update chimera information, and
- repeat step 1

The simulation of moving body problems with CFD-FASTRAN is greatly simplified because all five of these steps are an integral part of the flow solver. No input/output or user interference is required. Flow solvers such as OVERFLOW that employ PEGSUS to perform chimera communication are much less efficient because step 2-4 are performed external to the flow solver. Also, to initiate moving body problems using PEGSUS requires complicated shell scripts and user interference. To initiate a moving body problem with CFD-FASTRAN, the user simply modifies the flow solver input to indicate the problem is unsteady and moving. The user specifies which grids are allowed to move and how their motion is to be determined. All of this input can be specified through the GUI or flow solver input file.

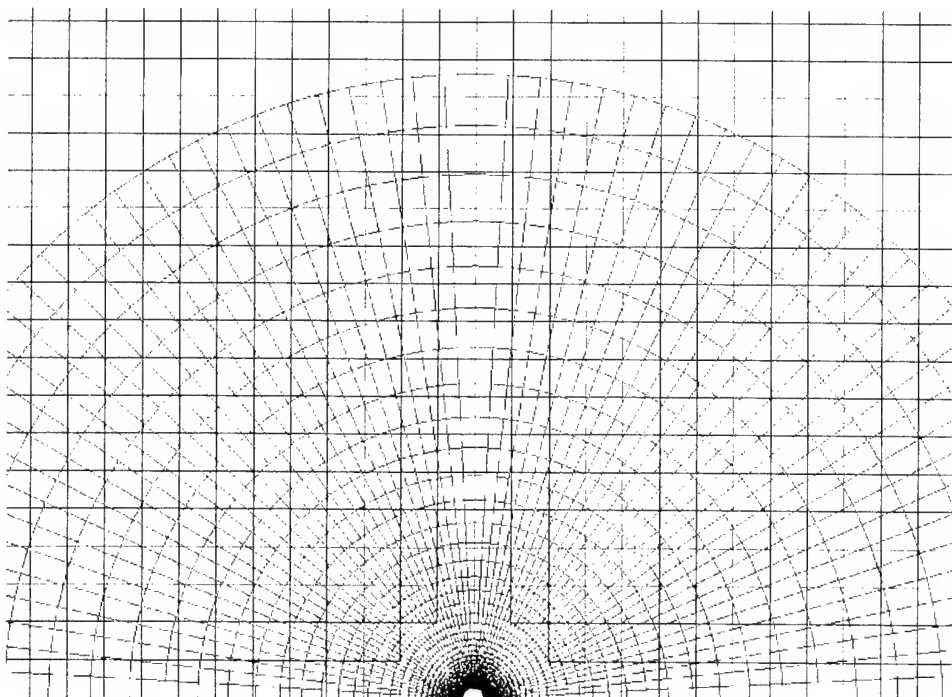
Chimera validations were conducted by comparing flow field solutions produced with the chimera methodology to those produced on single-domain grids. These comparisons not only ensure that the chimera algorithms have been incorporated correctly but also give a measure of the effects of chimera interpolations versus a fully conservative scheme. The results for two benchmark cases are presented: 1) flow over a circular cylinder, and 2) flow over an ejection seat in freestream.

**Case 1 Flow Over a 2D Cylinder** The flow over a two dimensional cylinder in freestream was simulated using both a single domain grid and a two domain chimera grid system. The free-stream conditions for the simulation were  $M_\infty=0.177$  and  $Re_\infty=8.27E06$ . The single domain and chimera grid systems are shown in Figures 7-14. The chimera grid system was constructed by extracting a subset of the single domain grid and oversetting it onto a background grid. This method produced a chimera grid system with an identical grid in the vicinity of the cylinder surface. Due to the importance of grid resolution, this constraint is necessary for making one-to-one comparisons between single grid systems and chimera grid systems.

Steady-state simulations were performed for both grid systems using Roe's flux-difference splitting in conjunction with first-order Godunov spatial reconstruction. Viscous effects were simulated by employing the high reynolds number k-e turbulence model with wall functions. Solution convergence was determined by monitoring the L2 norms of the conservative variables as well as the surface pressures. In Figure 7-15, the Mach Contours for the single domain and chimera grid systems are shown. The solutions are very similar. However, small differences in the Mach number contours can be seen, especially near the chimera boundaries. These mismatches in contours are the result of the changing grid resolution between the two solutions. These types of small mismatches are unavoidable due to the flow solution dependency on grid resolution. In Figure 7-16, the predicted pressure coefficients on the surface of the cylinder are compared for the single grid and chimera grid solutions. These solutions are nearly identical indicating the validity of the chimera solution.

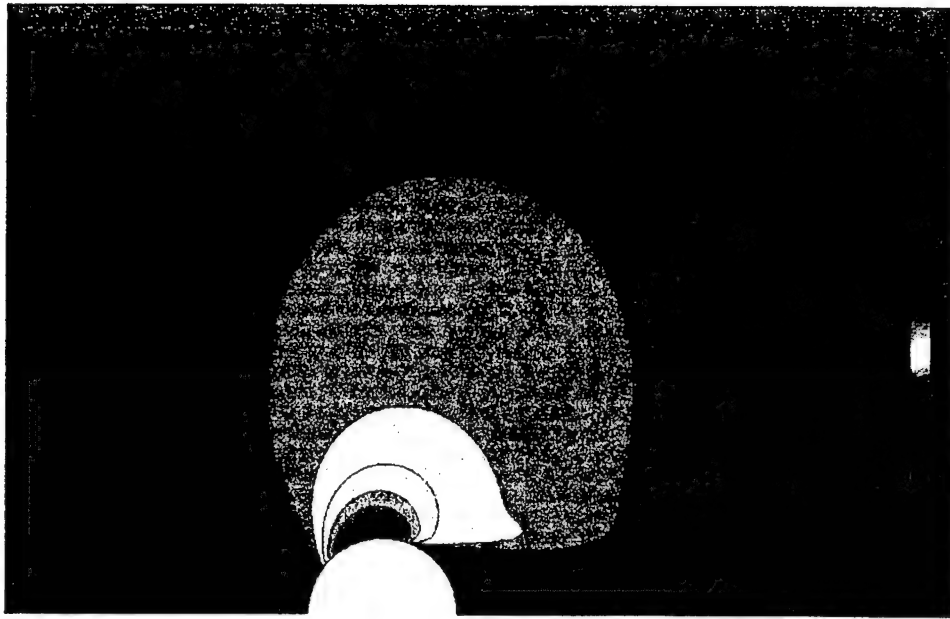


(a) Single Domain Grid System

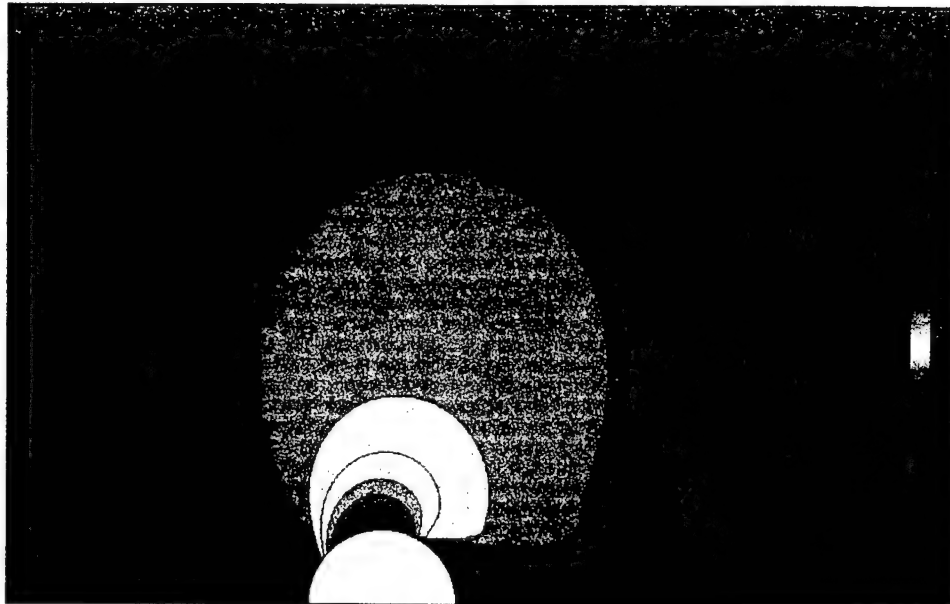


(b) Two Domain Chimera Grid System

Figure 7-14. Single Grid and Chimera Grid for Cylinder in Freestream



(a) Single Domain Grid System.



(b) Two Domain Chimera Grid System.

Figure 7-15. Cylinder Mach Number Contours for Single and Chimera Grid Systems

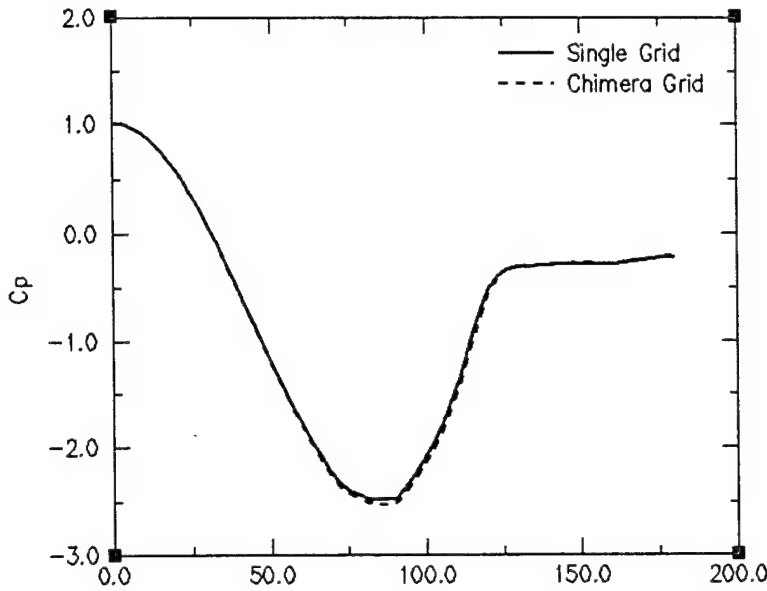


Figure 7-16. Cp Distributions on Cylinder Surface for Single Domain and Chimera Solutions.  $\beta=0$ . deg corresponds to leading edge, and  $\beta=180$ . deg corresponds to trailing edge. repeat step 1.

**Case 2 ACES-II Ejection Seat in Freestream** The flow over an ACES II ejection seat in freestream was simulated using both a single domain grid and a two domain chimera grid system. The free-stream conditions for the simulation were  $M_\infty=1.2$  and  $Re_\infty=1.0E6$  per foot. The seat was oriented at zero yaw and 30 degrees pitch (relative to seat back vertical). The single domain and chimera grid systems are shown in Figures 7-17. The single domain grid was an elliptically smoothed structured-blocked grid. The chimera grid system was constructed by extracting a subset of the single domain grid and oversetting it onto a background grid. This method produced a chimera grid system with an identical grid in the vicinity of the ejection seat surface. Due to the importance of grid resolution, this constraint is necessary for making one to-one comparisons between single grid systems and chimera grid systems.

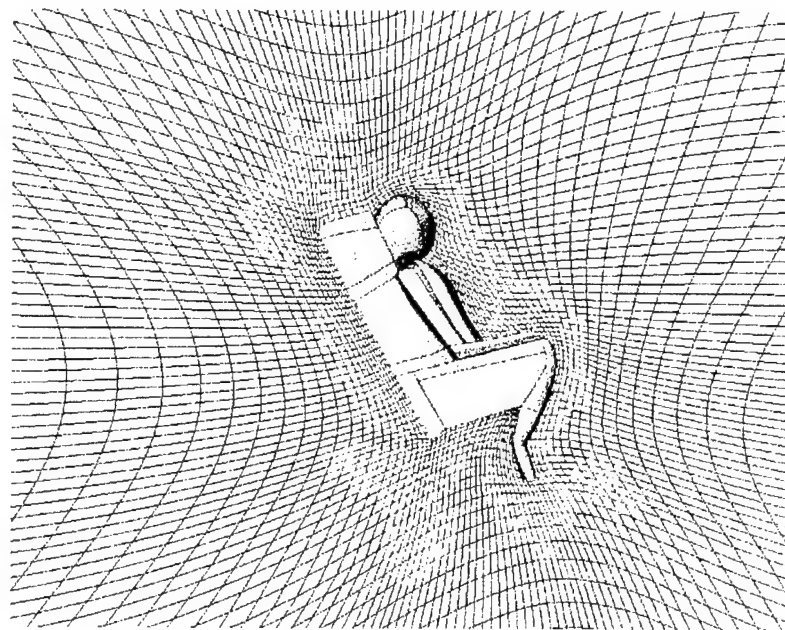
Steady-state simulations were performed for both grid systems using Roe's flux-difference splitting in conjunction with first-order Godunov spatial reconstruction. Viscous effects were simulated by employing the high reynolds number k-e turbulence model with wall functions. Solution convergence was determined by monitoring the L2 norms of the conservative variables as well as the changes in the aerodynamic coefficients. The aerodynamic coefficients approached asymptotic values after the L2 norms had reduced several orders of magnitude. Approximately 350 flow solver iterations (12 cpu hours) were required for solution convergence on a DEC Alpha Station 600 s/266 machine. The single domain solution operated at a speed of  $3.73E-04$  cpu-s per point per iteration, and the chimera domain solution operated at a speed of  $3.83E-04$  cpu-s per point per iteration. The overhead for this steady-state chimera case was only

2.7%. For the steady-state case the chimera hole cutting is only performed at the beginning of the solution. For this reason, the overhead is primarily associated with having multiple domains and performing interpolation updates. For moving body solutions the overhead will be higher because the chimera hole will have to be reformed at every time step.

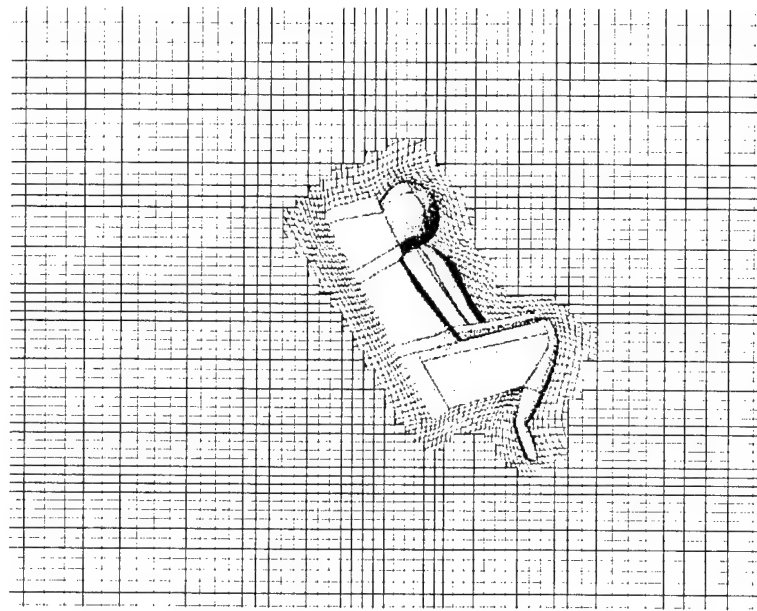
In Figure 7-18, the Mach Contours for single domain and chimera grid systems are shown. The solutions are very similar. However, small differences in the Mach number contours can be seen, especially near the chimera boundaries. These mismatches in contours are the result of the changing grid resolution between the two solutions. These types of small mismatches are unavoidable due to the flow solution dependency on grid resolution. In Table 7-1, the axial, normal, and pitching moment coefficients for the two solutions are compared. The axial force and pitching moment predicted from the chimera solution are nearly identical to the single grid values. The normal force coefficient is very small and the differences between the chimera and single grid solutions are on the order of the uncertainty in the predictions.

Table 7-1. Free-Stream Aerodynamic Coefficients for ACES-II Computed using Single Domain Grid and Chimera Grid System

	CX	CZ	CMM
Single Grid	-0.9935	0.0109	-0.1057
Chimera Grid	-0.9929	0.0000	-0.1098

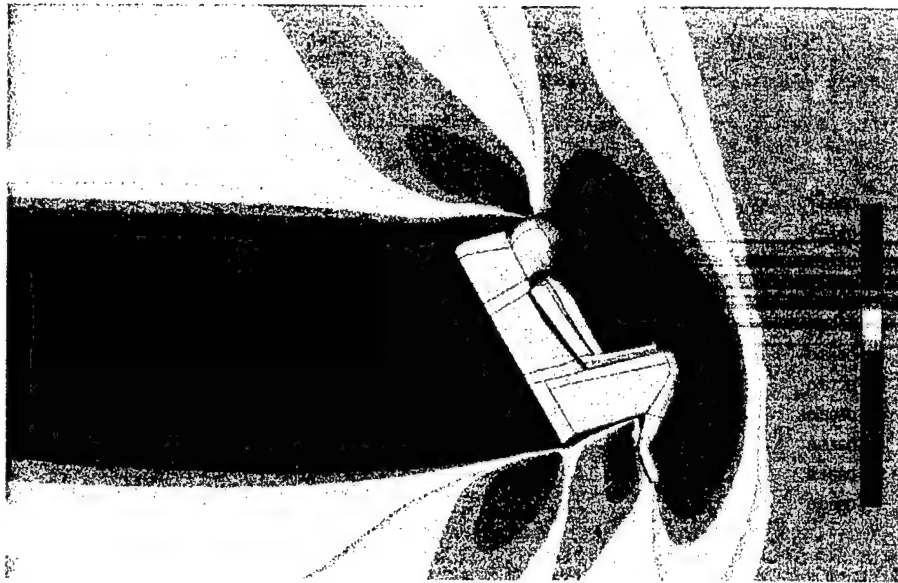


(a) Single Domain Grid System

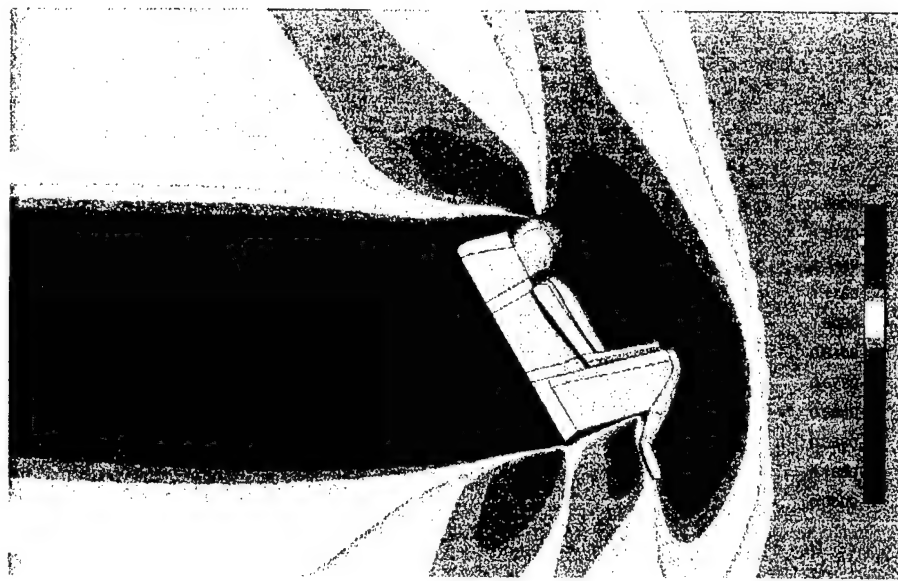


(b) Two Domain Chimera Grid System

Figure 7-17. Single Grid and Chimera Grid for ACES-II in Freestream



(a) Single Domain Grid System



(b) Two Domain Chimera Grid System

Figure 7-18. Mach Number Contours for Single and Chimera Grid Systems

## 8. CFD-FASTRAN DEMONSTRATION AND VALIDATION FOR SEAT/AIRCRAFT CALCULATIONS

### 8.1 Discussion of F-16 and ACES-II Wind Tunnel Test

The results of a half-scale wind tunnel test of an F-16 and Advanced Concept Ejection Seat (ACES-II) were used for validation of the steady state, seat and aircraft simulation capabilities. The test was sponsored by the Aerospace Medical Research Laboratory (AMRL) at Wright-Patterson Air Force Base and was conducted at the Arnold Engineering Development Center in the Propulsion Wind Tunnel (PWT), Transonic Wind Tunnel (16T). The results are presented in an AEDC test summary report [45] and data package [46].

The steady-state test was performed to evaluate the aerodynamic characteristics of the ACES-II ejection seat in and near the open cockpit of the F-16. The results comprise both six-component balance data and steady-state pressure data for the crewman/ejection seat combination. The test hardware consisted of a 0.5 scale ACES-II ejection seat/50th percentile crewman and a 0.5 scale F-16 aircraft forebody. The test installation is shown in Figure 8-1. Note that the configuration being tested has a forebody windscreens installed. Data were obtained for several forebody-ejection seat separation distances and aircraft angles of attack at Mach numbers from 0.4 - 1.2. Free-stream Reynolds number for the test runs were  $1.6 \times 10^6$  per foot for the subsonic Mach numbers and  $1.0 \times 10^6$  per foot for the 1.0 and 1.2 Mach numbers. A diagram of the ejection Seat Body Axis System (SBAS) is presented in Figure 8-2. All force and moment data are presented with respect to this coordinate system.

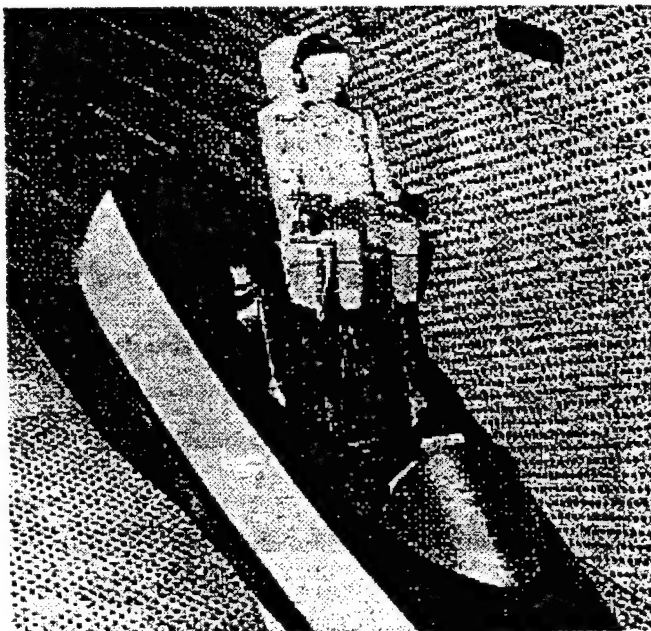


Figure 8-1. F-16/ACES-II Model Installation in PWT 16-T. [44]

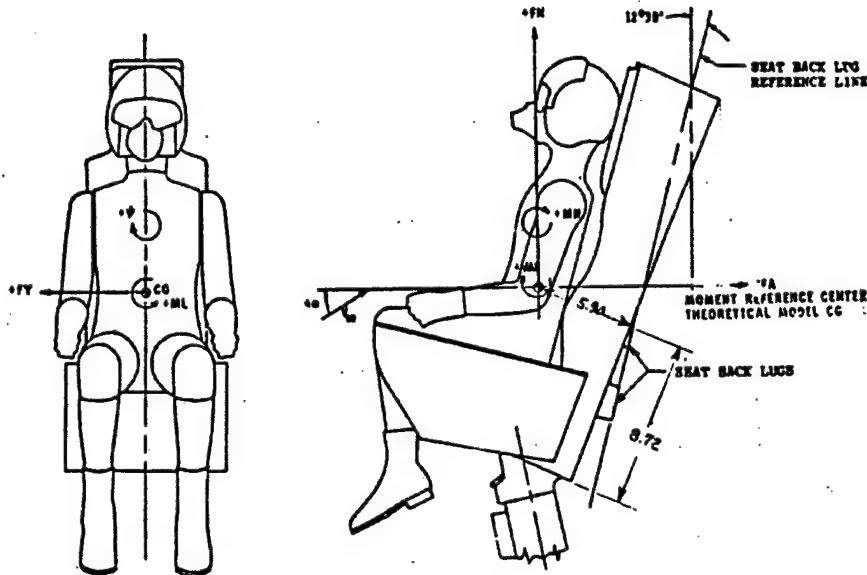


Figure 8-2. Seat Body Axis System [45]

Navy engineers requested that seat and aircraft validations and demonstrations be performed for the Mach 1.2 test conditions. At Mach 1.2, steady-state data were obtained for three seat and aircraft separation distances. The separation distance is measured relative to the installed seat/occupant position. These three configurations are referred to as Positions 1, 2, and 3. For Position 1, the seat is near the installation position. For Position 2, the seat is approximately half exposed from the cockpit, and for Position 3, the seat is almost completely exposed from the aircraft. The nominal test conditions for these three cases are presented in Table 8-1. In Table 8-2, the resultant force and moment coefficients for the three cases are presented. Table 8-3 contains static pressure measurements for the crewman head, crewman chest, crewman abdomen, crewman legs, and the ejection seat back. Table 8-4 presents the measurements uncertainties.

Table 8-1. Nominal Test Conditions for Selected Test Cases,  $M_\infty = 1.2$ ,  $Re_\infty = 1.0 \times 10^6$

Position	Eject Pos. (in)	$Q_\infty$ (lb/ft <sup>2</sup> )	$\alpha_{MAN}$ (deg)	$\alpha_{F-16}$ (deg)	$\beta$ (deg)
POS1	0.10	205	13.21	0	0
POS2	12.0	205.1	13.18	0	0
POS3	23.3	204.5	13.25	0	0

Table 8-2. Aerodynamic Coefficients for Selected Test Cases,  $M_{\infty} = 1.2$ ,  $Re_{\infty}=1.0 \times 10^6$

Position	CX	CZ	CY	CMM	CMN	CML
POS1	-0.0463	-0.0045	-0.0015	-0.0111	0.001	-0.0012
POS2	-0.4739	0.012	-0.0103	0.1268	0.0013	-0.0014
POS3	-1.0238	-0.0204	0.0034	0.062	0.001	-0.0026

Table 8-3. Static Pressure (psf) Measurements for Test Cases,  $M_{\infty} = 1.2$ ,  $Re_{\infty}=1.0 \times 10^6$

Position	PSH	PSC	PSA	PSL	PSSBR
POS1	315.4	182.4	183.1	185.8	226.9
POS2	426.8	468.6	244.7	194.4	148.1
POS3	421.1	434.2	397.2	487.9	97

Table 8-4. Measurement Uncertainties

Measurement	Uncertainty
$\alpha_{MAN}$	$\pm 0.10$ deg
$\alpha_{F-16}$	$\pm 0.10$ deg
$\beta$	$\pm 0.10$ deg
CX	$\pm 0.0126$
CZ	$\pm 0.0296$
CY	$\pm 0.0082$
CMM	$\pm 0.0075$
CMN	$\pm 0.0015$
CML	$\pm 0.0070$
PS	$\pm 1.9$ psf

## 8.2 OVERFLOW Demonstration Calculations

### 8.2.1 OVERFLOW Grids

A complicated geometry such as this is best handled in a multi-block manner. The OVERFLOW code supports multi-block capability using the grid oversetting approach. To model the desired geometry, three blocks of grid were used. They were generated separately and interfaced using the PEGSUS 4.0 overset grid code from AEDC.

The main grid was a single block, H-O topology mesh for the F-16 aircraft that surrounded the entire aircraft surface and was dimensioned to 87x41x55. This mesh ran along the entire canopy surface and would have been appropriate for an isolated aircraft simulation with a closed canopy. This topology allowed for excellent clustering of the mesh toward the aircraft surface to get many points within the boundary layer. A second grid was a single H-mesh rectangular block dimensioned to 46x64x21 with the ACESII pilot and ejection seat embedded in the interior of the block. The outer bounds of this mesh were arbitrary, and the grid was generated as if it were an isolated component. The third block was an H-mesh block dimensioned to 35x35x25 that was dedicated to the cockpit well. It was generated with clustering toward all the solid surfaces and with the top of the mesh extending out into the free stream past the canopy glass line. The extension of the cockpit grid into the free stream was to allow the overlapping volume to make the chimera approach work.

The basic grid hierarchy was that of the pilot mesh embedded within the cockpit mesh, which was then embedded (partially) within the aircraft mesh. To enable the inter-grid communication for the system, basically two information paths needed to be established. The first was between the exterior grid and the cockpit mesh, and the second was between the pilot grid and the cockpit mesh. The communication between the cockpit and exterior was established without resorting to any hole cutting within meshes, and was enabled by means of defining outer boundaries requiring interpolation on the upper surface of the cockpit mesh and the sides of the cockpit mesh that stuck up into the exterior mesh. The points from the exterior mesh that would have lain on the canopy surface were defined as points requiring interpolation and the information was sought from the cockpit grid.

The second communication path was by far the most difficult, primarily due to using a single H-mesh with dead zones for the pilot grid. As the two meshes were generated separately, it can be seen in Figure 8-3 that the pilot was in the proper place within the cockpit, but that the outer boundaries of the pilot mesh extended well outside the cockpit grid. It was necessary to trim the pilot mesh back so that those points outside the cockpit were blocked out and thrown away. This resulted in a rim of hole boundary points on the periphery of the pilot mesh and enabled communication to feed inward from the cockpit mesh. For the flow information to feed outward from the pilot mesh to the cockpit, it was necessary to cut holes in the interior of the cockpit mesh that corresponded to the position of the pilot. Since the pilot was defined by approximately 60+ patches of grid, an easier method of cutting the holes was sought. A PEGSUS technique known as using phantom meshes was employed to cut the desired holes. Two

additional blocks of mesh were created that were basically rectangular in shape and conformed fairly closely with the pilot. One block approximated his head and torso, and the second block approximated his legs and feet. These blocks were flagged as not being able to supply any information to interpolation points and thus were not linked to the three main grid blocks. Since they were of a simple shape, the volumes were defined by the six bounding faces and the holes in the cockpit mesh were cut as desired. The points on the edge of these holes obtained interpolation information from the pilot block, and thus the second direction of communication was established. The pilot and cockpit meshes with their respective holes are shown in Figure 8-4.

The pilot geometry used in past analysis was one where the pilot's foot was extended in almost the same direction as the back of the seat. With the pilot in the proper position within the cockpit, that is, having roughly the correct spacing between the pilot's head and the canopy, and between the back of the seat and the back of the cockpit, it was noted that the pilot's foot stuck out through the bottom of the cockpit. This is due to the fact that the two component's geometry definitions came from completely different sources coupled with the fact that the pilot's feet would not be in this position while inside the aircraft. The cockpit bottom hole cutting boundary simply chopped off the end of the foot. As this was in an area of the solution far from the main flow, it was felt that this approximation was perfectly reasonable. Chopping the end of the foot off resulted in some orphan points in that area but these points were successfully handled by the flow solver and were allowed to float without degrading the solution.

The configuration with the toes chopped off was run for several hundred steps using the OVERFLOW code at Mach 1.2 flight conditions. No problems with execution of the code were observed. While the simulation was running, some modifications to the pilot's foot were made for the CFD-FASTRAN grid. The end of the foot was essentially rotated upward 30 degrees about an axis extending horizontally through the pilot's ankle. This raised the bottom of the foot approximately 2.5 inches from its previous position and was enough to keep it completely within the cockpit domain. The foot modifications that are illustrated in Figure 8-5 were implemented with the OVERFLOW grid sets. These new grid blocks were generated and also run through PEGSUS, and the resulting overset grid for this configuration can be seen in Figure 8-6.

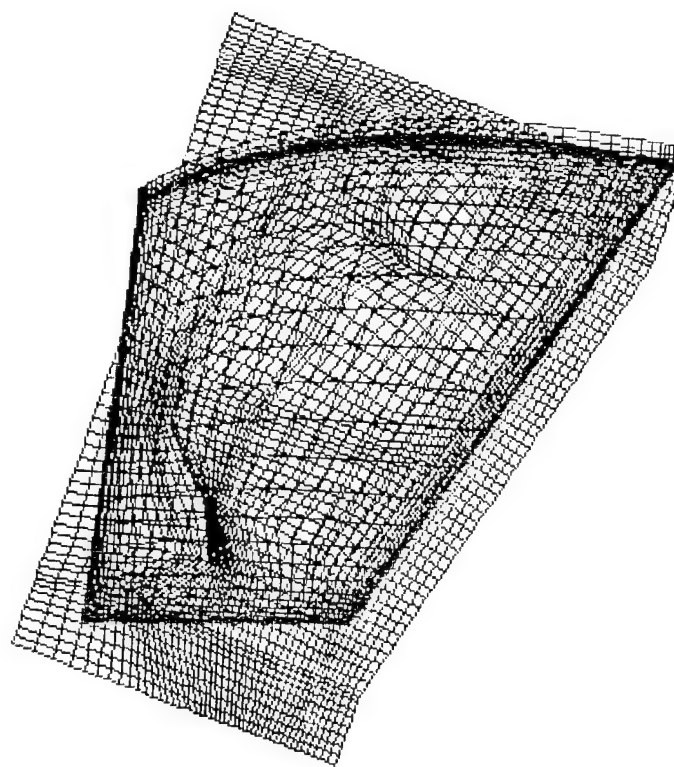


Figure 8-3. Superposition of Pilot and Cockpit Meshes before Oversetting

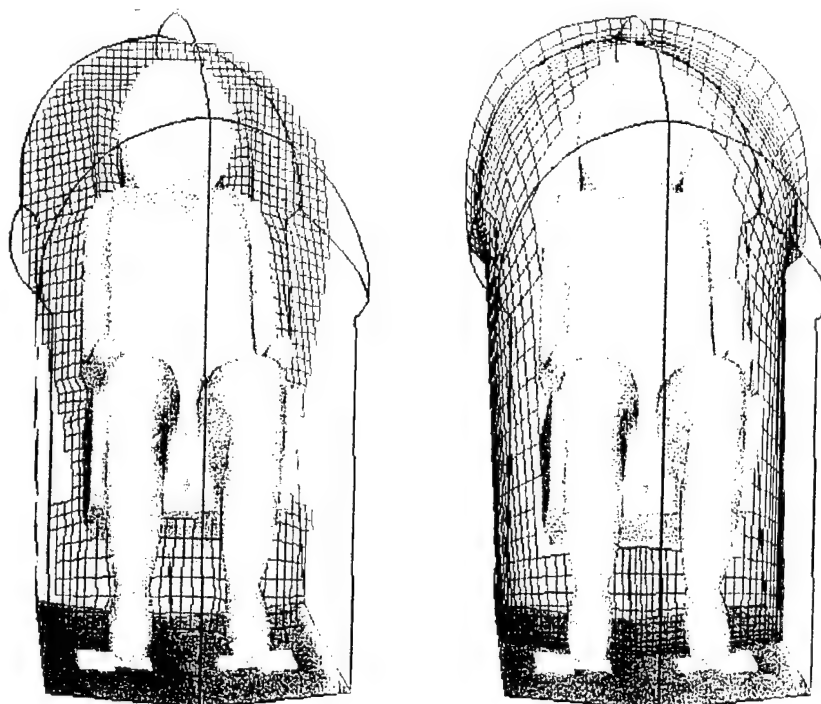


Figure 8-4. Pilot and Cockpit Meshes After Oversetting

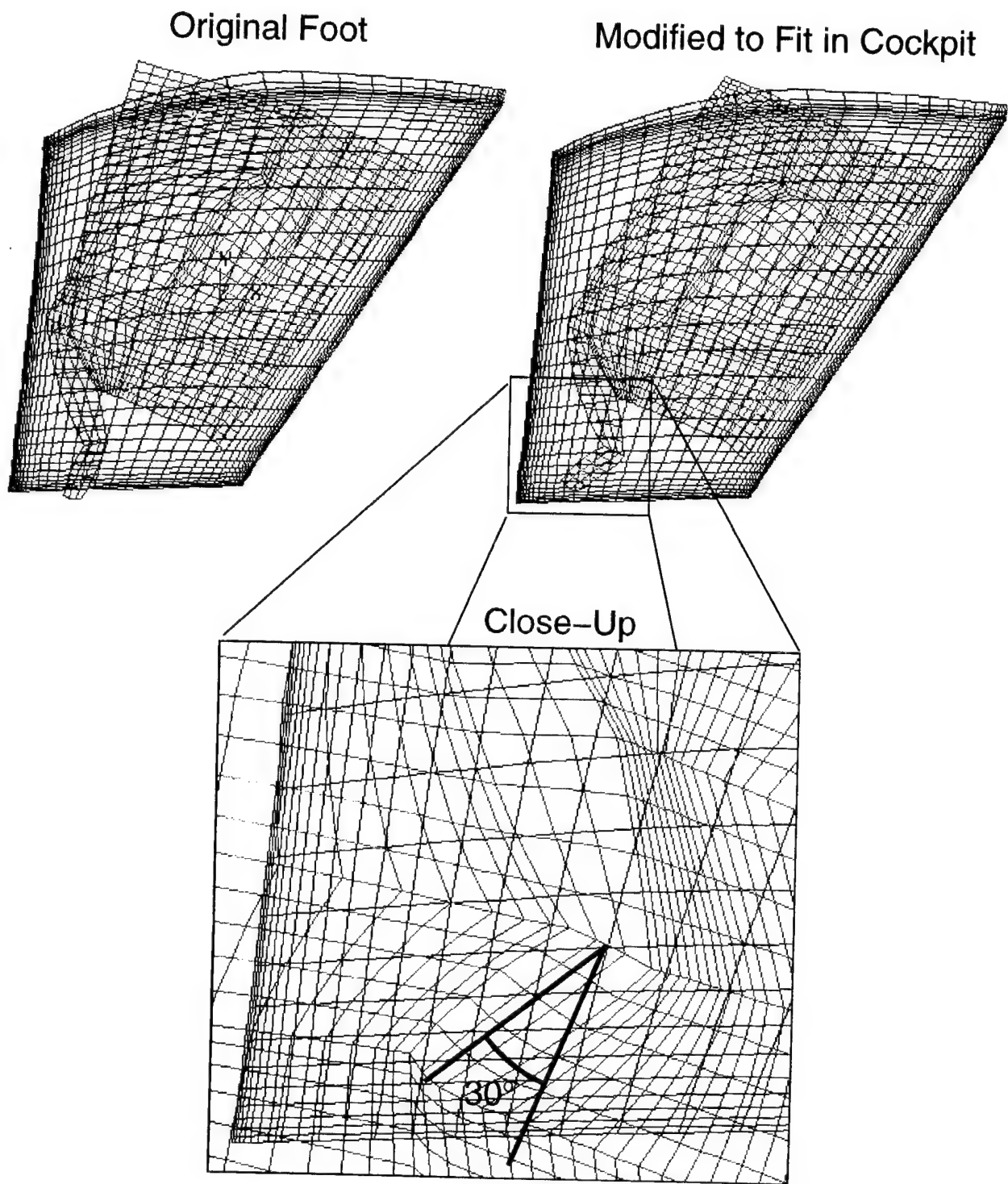


Figure 8-5. Modifications to Foot Geometry for OVERFLOW and CFD-FASTRAN Solutions

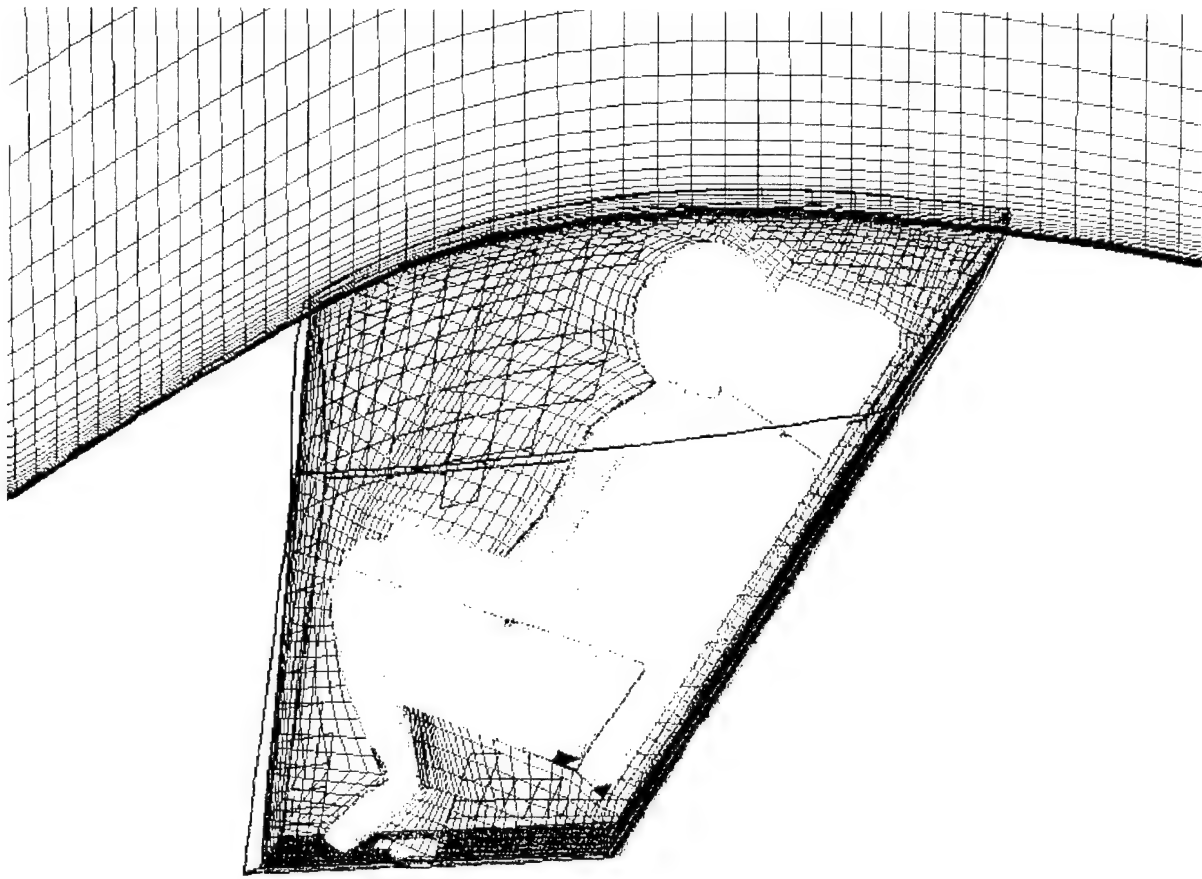


Figure 8-6. Overset Grids in Final Position

### 8.2.2 OVERFLOW Simulations

OVERFLOW simulations were performed on the F-16 aircraft and ACES-II pilot ejection seat at Position 1. The configuration was chosen to match the test data discussed in Section 8.1. The model was run for 2500 time steps and used approximately 116134 CPU seconds. The solutions were visually inspected every 500 time steps or so, and to outward appearances, were stabilized to the solution shown in Figure 8-8. The L2-norms of the three blocks decreased by approximately 1 - 1 1/2 orders.

The observed flow field in the OVERFLOW solution is consistent with CFD-FASTRAN results to be presented below. Figure 8-8 above shows a low Mach number region along the seat centerline right behind the pilot's head, with higher velocities above and below this point. By examining the particle traces shown in Figure 8-9, it can be seen that this is basically a stagnation point for the air feeding in sideways behind the pilot's seat. In this figure, a series of traces were released at various points along the forward rim of the canopy, and each family of traces was color-coded for better visualization. The magenta flow along the top is pushed outward at the back of the seat by the up-welling air from behind the seat. The red and orange families are largely un-deflected. The yellow and green families of traces seem to fall above and below the stagnation point, with some of

the yellow traces nearer the aircraft surface being pulled in and forming the vertical fountain along the back centerline. Some of the green traces get turned downward and circulate about the cockpit cavity before finally flowing out the back.

At this point, and after consultation with the Navy Technical Monitors, the decision was made to develop new multiple and moving grids technology for seat/aircraft analysis and implement into CFD-FASTRAN. Therefore the OVERFLOW calculations were abandoned and no more analysis was made.

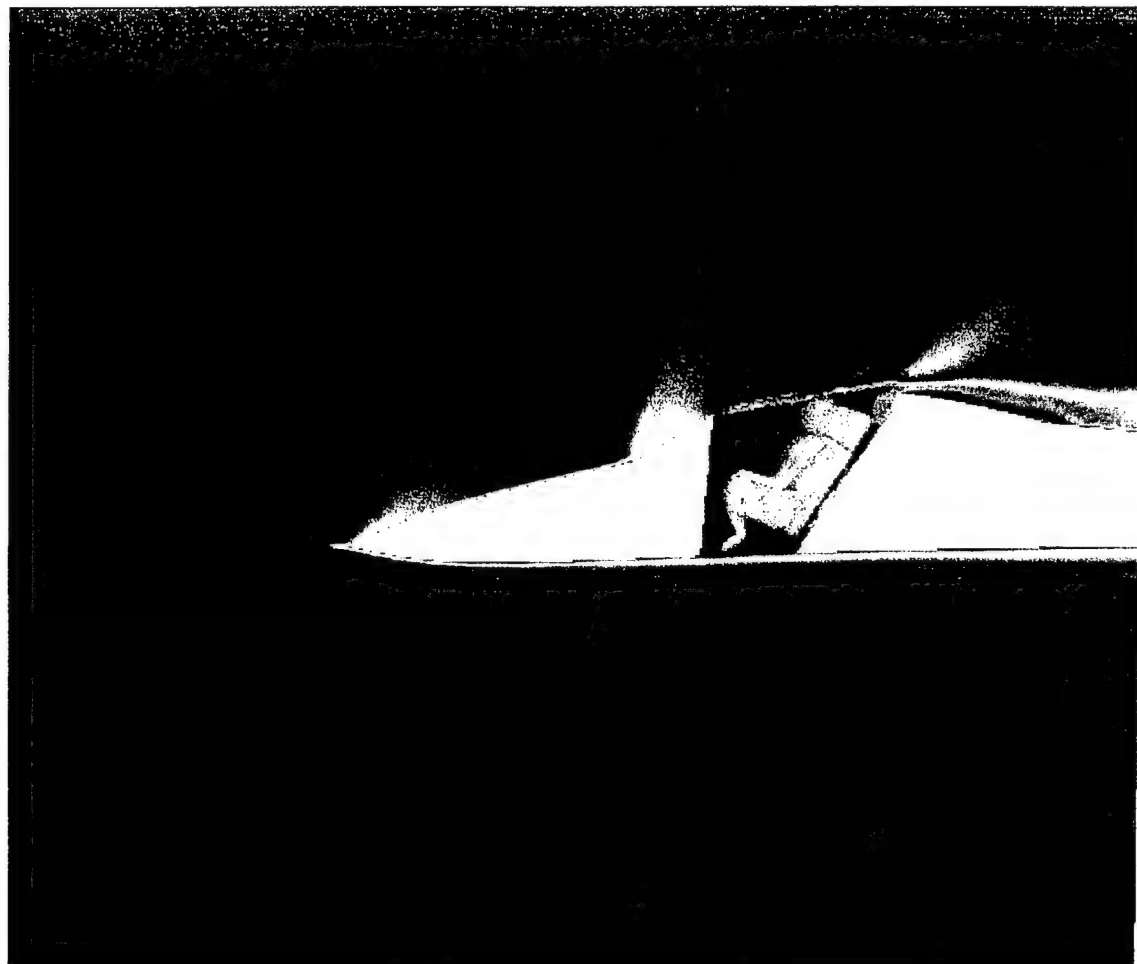


Figure 8-8. Mach Number Surfaces Along F-16 Aircraft Centerline

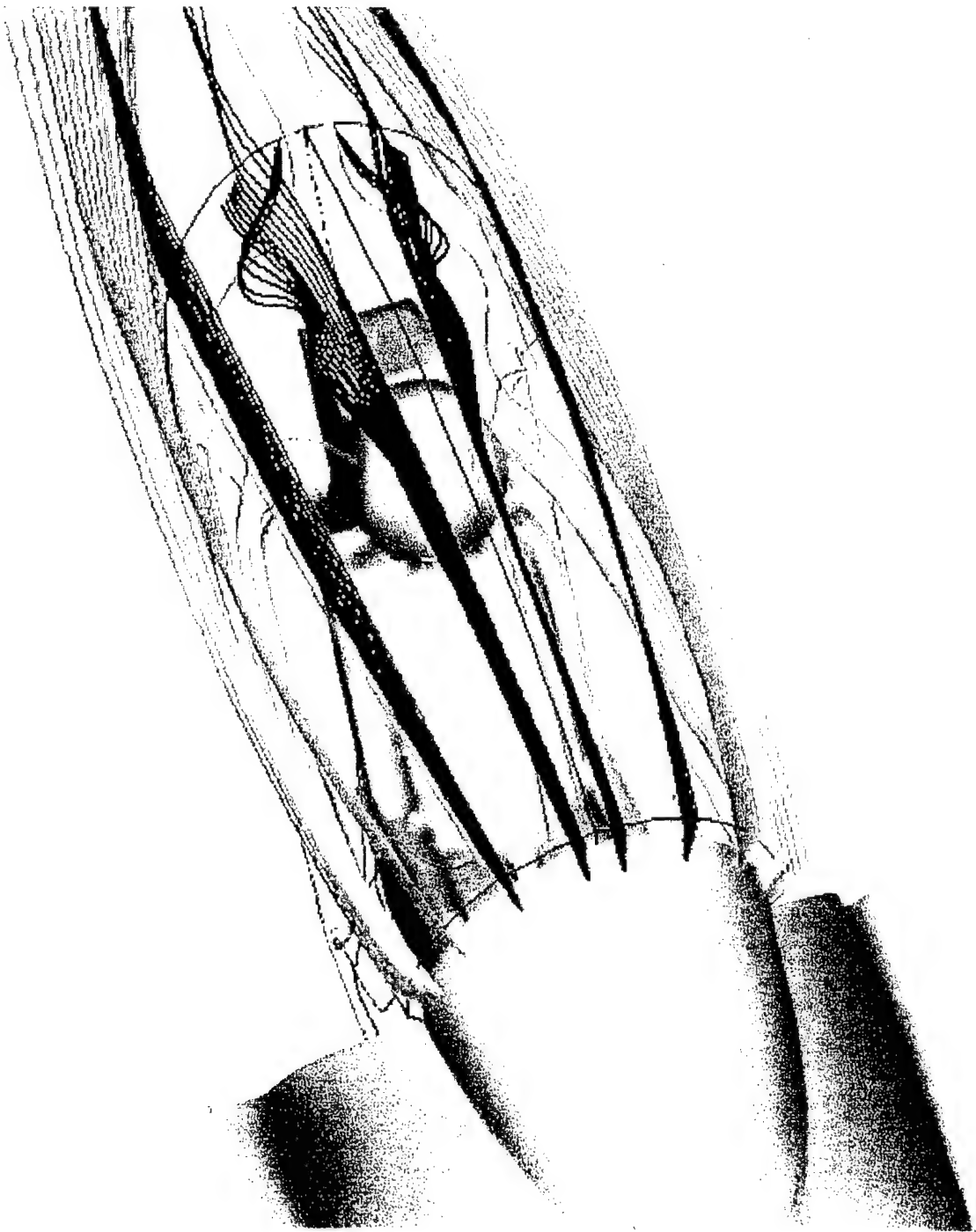


Figure 8-9. Particle Traces Highlighting Cockpit Flow Entrainment

## 8.3 Steady-State CFD-FASTRAN Analysis

### 8.3.1 Geometric Modeling and Grid Generation

In application of the chimera methodology, geometric modeling and grid generation for the seat and aircraft are treated separately as described in Section 7. The F-16 forebody and ACES-II ejection seat have completely separate grid topologies. The only constraint applied is that the grid resolution in the overlap regions be similar to ensure proper grid communication. As a result, grid generation for the seat and aircraft are discussed separately.

For the proposed test cases, both the aircraft and ejection seat are at zero sideslip angle. This configuration produces a flow field symmetry about the buttline of the aircraft. This symmetry allows for the computational problem to be reduced by only modeling half of the geometry. The first step in grid generation was obtaining surface definitions for the F-16 forebody. The Wright Laboratory CFD Research Branch provided an original surface definition for the F-16A forebody in PLOT3D format. Due to the nature of this study, the engine inlet on the underside of the forebody geometry was neglected. The original PLOT3D grid was used to create a CFD-GEOM geometry model. The cockpit and canopy lines were then delineated on the forebody geometry. The cockpit geometry was approximated as a simple rectangular well.

The forebody and cockpit geometries were originally modeled using two structured blocked grids. The main grid was a single block, H-O topology mesh for the F-16 aircraft that surrounded the entire aircraft surface as discussed previously for the OVERFLOW grids (Section 8.2.1). The second grid was an H-mesh topology block that formed the interior of cockpit and extended from the cockpit floor to the canopy surface. After preliminary simulations, the forebody grid was altered to include an H-mesh topology domain that extended from the canopy surface to the farfield. This additional domain formed a tunnel grid of improved resolution in the area of the seat/occupant. This topology allowed for the grid resolution in the vicinity of the cockpit to be increased without drastically increasing the number of grid points in the aircraft grid. This three grid topology resulted in improved grid resolution for chimera composition of the ejection seat grid. In Figure 8-10, a farfield view of the forebody grid system is shown with the domain boundaries outlined. In Figure 8-11, a close-up view of the symmetry plane and domain boundaries for the aircraft, cockpit, and tunnel grids is shown. The aircraft grid has dimensions 200x71x26 for 348,250 grid cells. The cockpit grid has dimensions 44x75x18 for 54094 cells, and the tunnel grid has dimensions 80x71x31 for 165,900 cells.

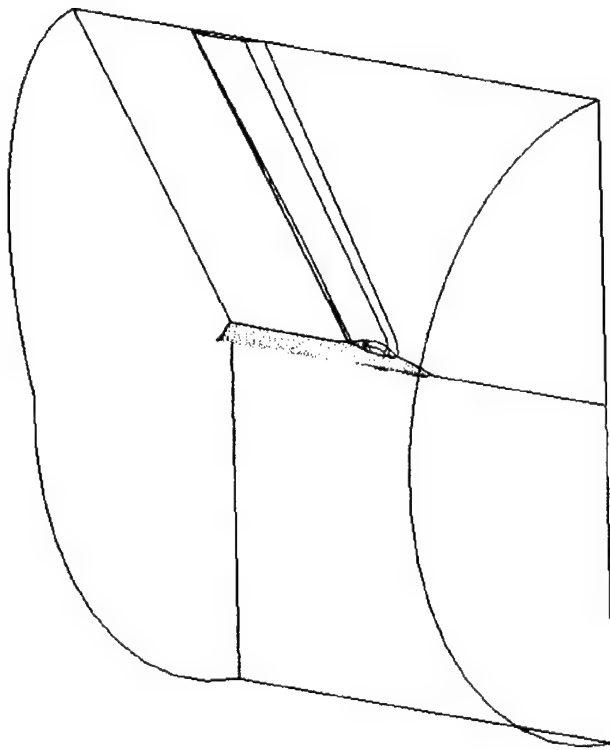


Figure 8-10. Outline of Grid Topology for F-16 Forebody Geometry

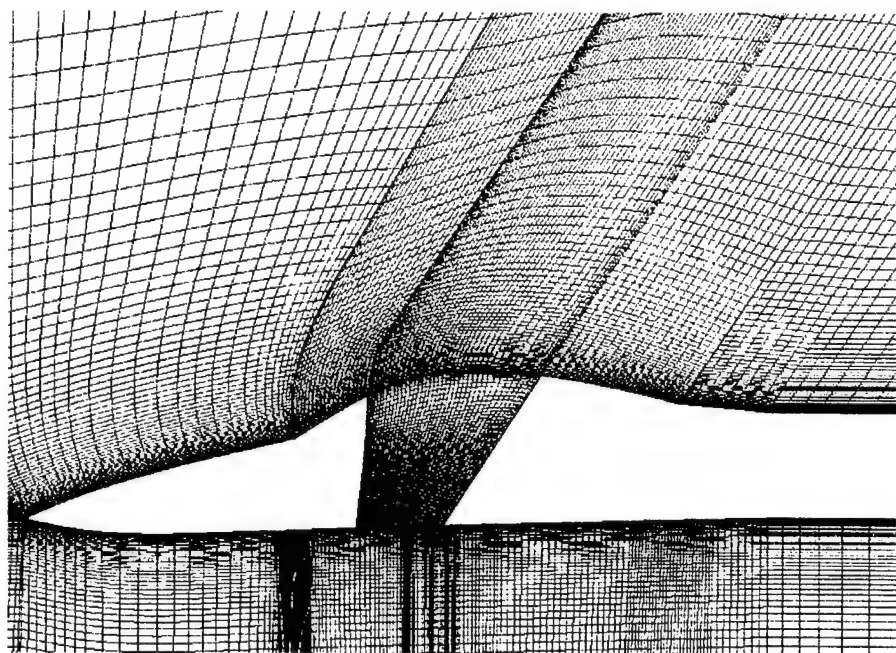


Figure 8-11. Symmetry Plane Grids for F-16 Forebody Geometry

The ACES-II geometry employed in the seat and aircraft calculations is the same as that developed for the seat alone computations. Details of the geometry development are discussed in Section 4 and will not be reproduced here. For application within the chimera methodology, a single H-mesh computational block was constructed that included the ACES-II geometry. The surface of the seat and occupant were constructed using internal blockages. An algebraic grid was constructed using CFD-GEOM with dimensions 46x62x19 for 49,410 cells. For application within chimera, the outer boundaries of the seat grid can be arbitrary. However for efficiency, the outer boundaries were confined to the cockpit and tunnel domains of the aircraft. This modification eliminated the primary aircraft grid (348,250 cells) from the chimera search and interpolation routines. This modification produces a significant increase in efficiency, especially for transient simulations. The surface geometry and boundary grids for the ACES-II seat are presented in Figure 8-12.

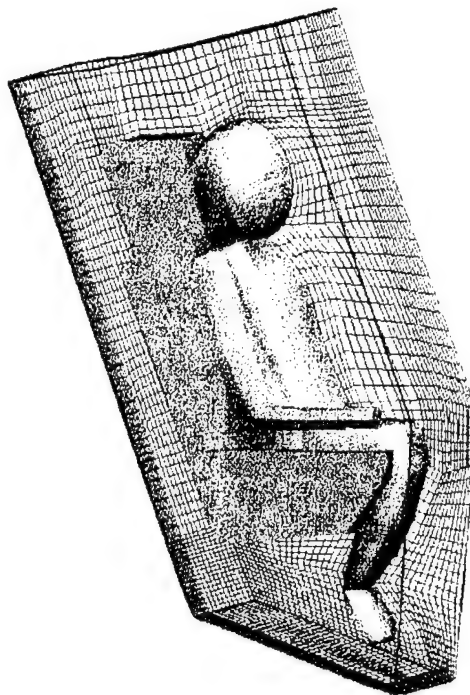


Figure 8-12. Surface Geometry and Domain Boundaries for ACES-II Chimera Grid

The F-16 forebody and ACES-II geometries were composited using CFD-GEOM. The combined geometries for ejection seat position one are shown in Figures 8-13 and 8-14. In Figure 8-14, a top view of the geometry is shown detailing the position of the seat/occupant within the cockpit well. In Figure 8-15, the overset symmetry plane grids of the seat and aircraft are presented. The forebody, cockpit, and tunnel grids are shown in blue. The seat/occupant grid is shown in red. The chimera hole in the cockpit and tunnel grids that accommodates the seat/occupant geometry can be seen in the overset region. The complete chimera grid system comprises 617,654 grid cells. The chimera grid systems for the other two ejection seat position are similar except the seat/occupant has been translated to the appropriate position.

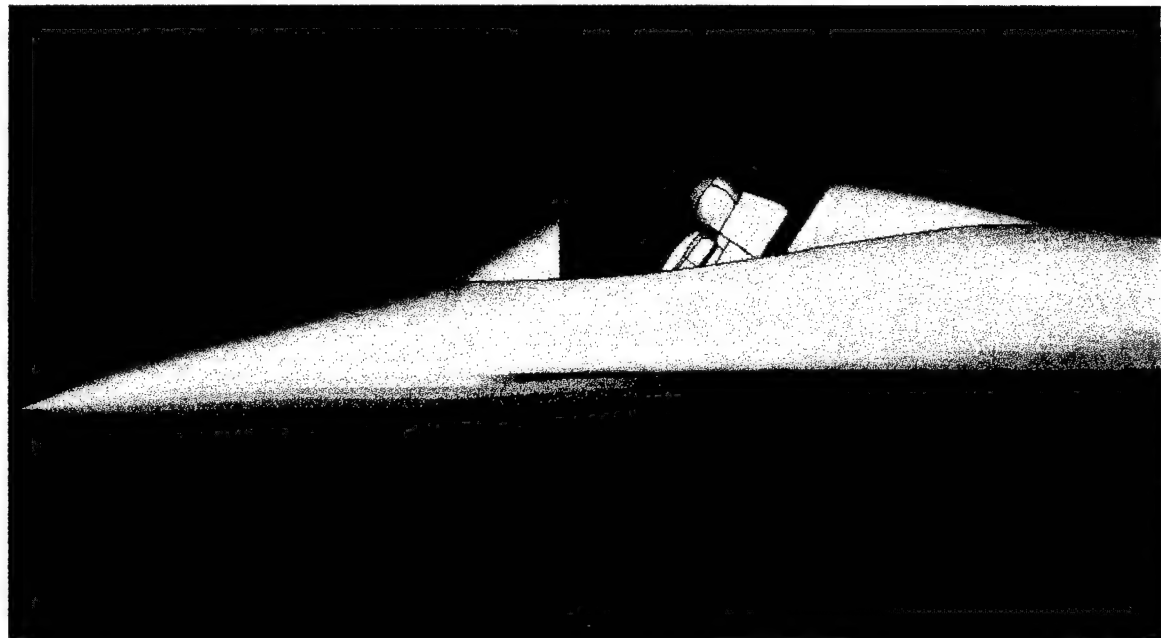


Figure 8-13. F-16 Forebody and ACES-II Surface Geometries, Side View

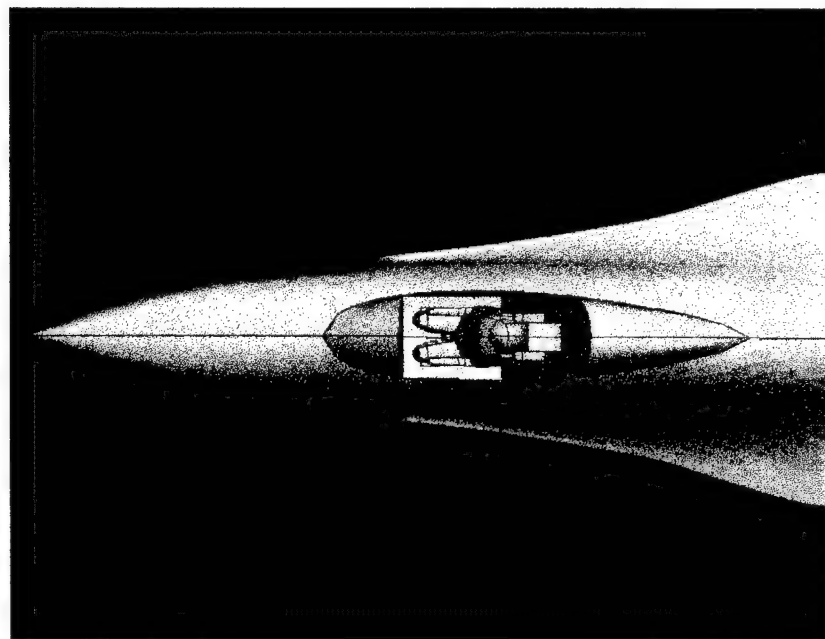


Figure 8-14. F-16 Forebody and ACES-II Surface Geometries, Top View

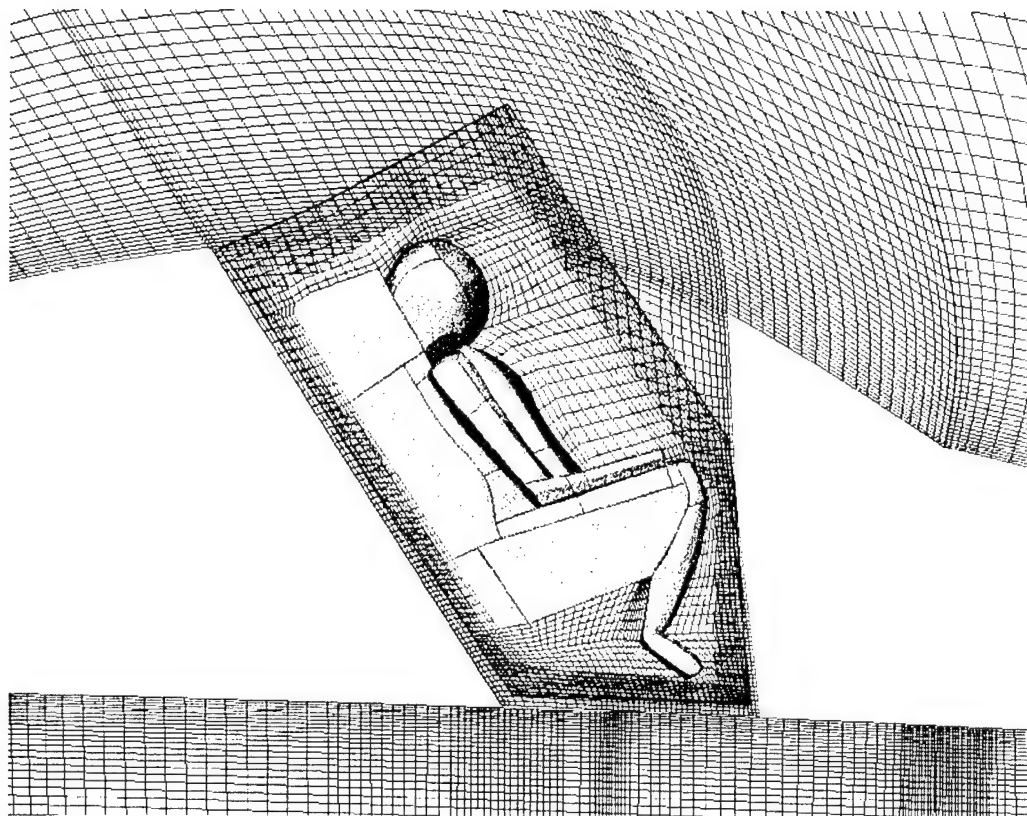


Figure 8-15. Chimera Symmetry Plane Grids for Seat and Aircraft, Position 1

### 8.3.2 Steady-State CFD-FASTRAN Simulations

Steady-state simulations were performed for the seat and aircraft configuration for the three ejection seat positions and free stream conditions specified in Tables 8-1-8-4. All simulations were performed using Roe's flux-difference splitting in conjunction with first-order Godunov spatial reconstruction. Viscous effects were simulated by employing the high-reynolds number  $k-\epsilon$  turbulence model with wall functions. Solution convergence was determined by monitoring the L2 norms of the conservative variables as well as the changes in the aerodynamic coefficients. Typically, the aerodynamic coefficients approached asymptotic values after the L2 norms had reduced several orders of magnitude. Approximately 30 CPU hours were required for solution convergence on a DEC Alpha Station 600 s/266 machine. Due to the shared workload on the machine wall clock times for convergence were typically two to three days.

In Figures 8-16 and 8-17, the Mach number contours in the symmetry plane and static surface pressures for ejection seat positions 1, 2, and 3 are presented. All of the expected flow features are clearly captured by the chimera scheme. Furthermore, the flow field solution across the structured and chimera interfaces are both smooth and continuous. This continuity demonstrates the applicability of the chimera method. A number of oblique shock waves can be seen emanating from the aircraft forebody and canopy windscreens. These oblique shocks reduce both the free-stream Mach number and dynamic pressure downstream of the forebody nose. As a result, these oblique shocks

also reduce the aerodynamic forces acting on the seat and occupant relative to free-stream aerodynamic forces.

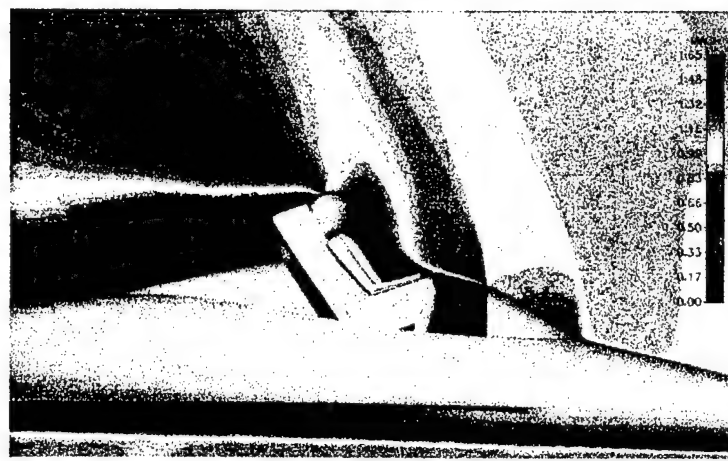
For position one, the pilot is located entirely inside the cockpit and is shielded by the canopy windscreens. The pilot's head is located in the shear layer produced by the windscreens and cockpit, see Figure 8-16a. This shear layer is the boundary between the slow moving air inside of the cockpit and the rapidly moving air outside of the cockpit. The flow field within the shear layer accelerates to supersonic speeds over the pilot's head and manifests itself in the form of a shockwave. For time accurate simulations, this shear layer was observed to oscillate slightly producing fluctuations in the flow field surrounding the seat and occupant. In Figure 8-17a, the pressures on the seat and occupant are seen to be relatively benign. However, an increase in the pressure on the front of the pilot's head can be detected, as well as, the pressure drop associated with the supersonic bubble attached to the top of the pilot's head.

At position two, the pilot is half exposed from the cockpit and experiences higher Mach numbers and dynamic pressures. The flow continues to accelerate around the seat and occupant producing several areas of locally supersonic flow, see Figure 8-17b. At this position, much of the shear layer flow is diverted under the pilot and accelerates up between the seat back and cockpit rear wall. As the flow accelerates out of the cockpit it lowers the static pressure between the seat back and rear cockpit wall. Conversely, the pressure on the head and chest of the pilot are dramatically increased as more of the seat is exposed from the cockpit, see Figure 8-17b.

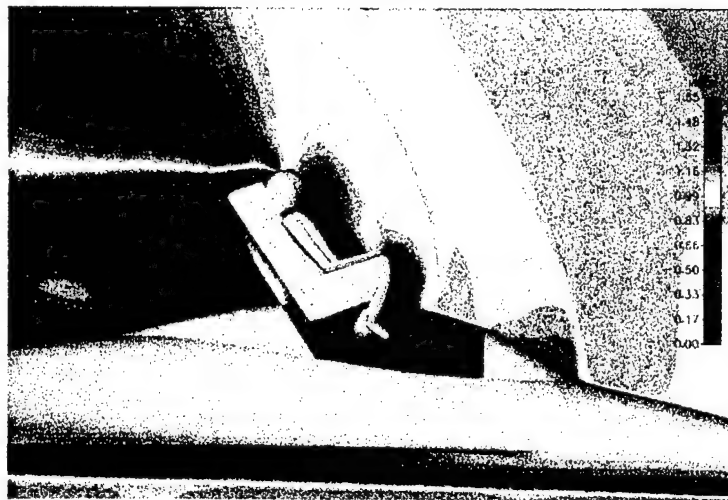
At position three, the pilot is almost completely exposed from the cockpit, see Figure 8-16c. The windscreens shear layer now impinges on the seat bucket and the pilot's legs greatly increasing the static surface pressures on the pilot, see Figure 8-17c. The peak pressures are now located at the pilot's head and legs. The pilot's chest is shielded from the highest pressures due to the attitude of the pilot's legs. This shielding is further evidenced by the angle and position of the bow shock that forms in front of the pilot.



a.) Eject Position One



b.) Eject Position Two



c.) Eject Position Three

Figure 8-16. Mach Number Contours for Symmetry Plane of Seat and Aircraft Solutions



a.) Eject Position One



b.) Eject Position Two



c.) Eject Position Three

Figure 8-17. Static Pressure Contours for Seat and Aircraft Solutions

### 8.3.3 Comparisons to Wind Tunnel Data

In Figure 8-17, the CFD and wind tunnel predictions for the aerodynamic coefficients are compared. The CFD results are also listed in Table 8-5 along with values for the seat in freestream. The overall comparison between the CFD and wind tunnel coefficients is quite good. The trends for axial, normal, and pitching moment coefficients are all accurately reproduced. However, the CFD solutions under predicted the axial force coefficient for the seat. At positions two and three, the difference is approximately 15%. In Figure 8-18, the calculated surface pressures on the seat and occupant are compared to the wind tunnel data. The CFD results are also listed in Table 8-6. Again, the overall comparison between CFD and wind tunnel predictions is quite good. All of the data trends are accurately reproduced. However, the CFD solutions predicted slightly lower surface pressures relative to the test data. The differences are small, approximately 5%. Due to the large surface areas of the chest and abdomen, these pressure differences are the primary cause for the differences in the predicted and measured axial force. These data comparisons are further discussed below as they relate to the flow field features analyzed in Section 8.3.2

At position one, all of the aerodynamic forces are small, and the CFD results compare excellently to the wind tunnel data. The small aerodynamic forces and moments are consistent with the observation that the pilot is located entirely inside of the cockpit and is shielded by the canopy windscreens. The influence of the windscreens shear layer can also be observed in the increased pressures on the pilot's head relative to the pilot's chest. As the pilot emerges from the cockpit to position two, the pressures on the pilot's head and chest rapidly increase while the pressures on his legs remain relatively constant. This results in the increased axial force and pitching moment observed in Figure 8-17. A decrease in the seat back pressure is also observed as the flow accelerates up between the seat back and cockpit rear wall. As the seat emerges further to position three, the pressures on the pilot's head and chest level off. However, the pressures on the abdomen and legs dramatically increase. This has the result of further increasing the axial force. At the same time though, the pitching moment is decreased due to the equalizing force applied to the legs. Throughout the seat translation the normal force remains small.

The primary differences between the CFD predictions and the wind tunnel data are the pressure loads on the chest and abdomen. The CFD predictions indicate that due to the seat attitude, the seat bucket and the pilot's legs shield the pilot's chest and abdomen from the highest pressure loads. The CFD solutions consistently predicted higher pressures on the pilot's head relative to the pilot's chest. Conversely, the wind tunnel tests predicted higher pressures on the pilot's chest relative to the pilot's head. This fundamental difference in the flow patterns is difficult to reconcile given the shielding effect observed in the CFD simulations. One possible explanation is the approximations in the CFD seat/occupant geometry.

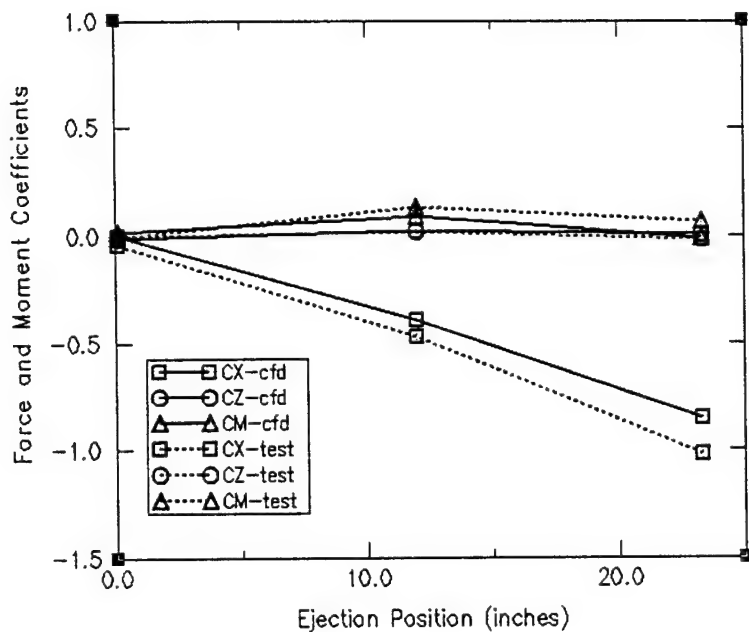
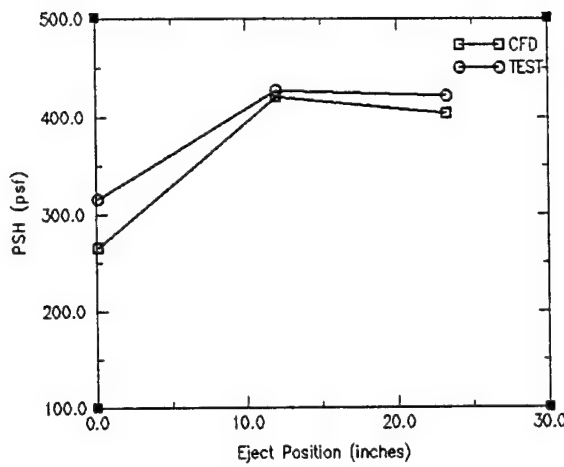


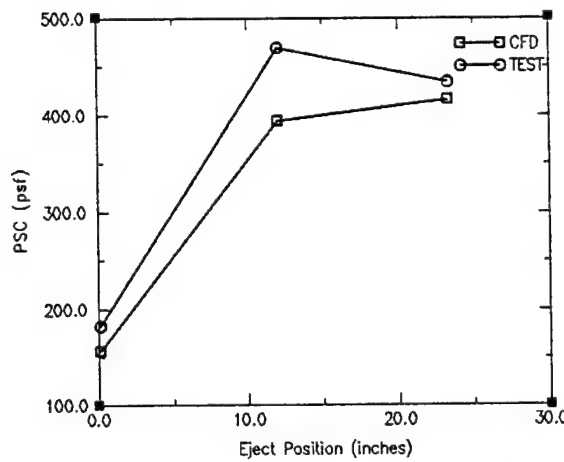
Figure 8-17. Comparison of CFD and Wind Tunnel Predictions of Aerodynamic Coefficients for Seat and Aircraft.

Table 8-5. Aerodynamic Coefficients for Seat and Aircraft Simulations

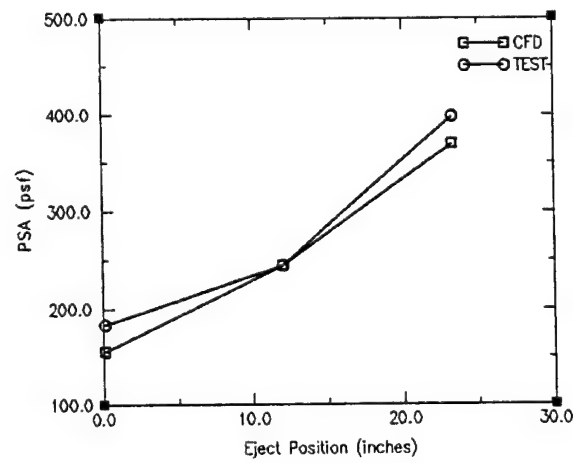
Position	CX	CZ	CY	CMM	CMN	CML
POS1	-0.0022	-0.0160	0	-0.0172	0	0
POS2	-0.3973	0.0185	0	0.0838	0	0
POS3	-0.8515	0.0029	0	-0.0169	0	0
Freestream	-0.9935	0.0109	0	-0.1057	0	0



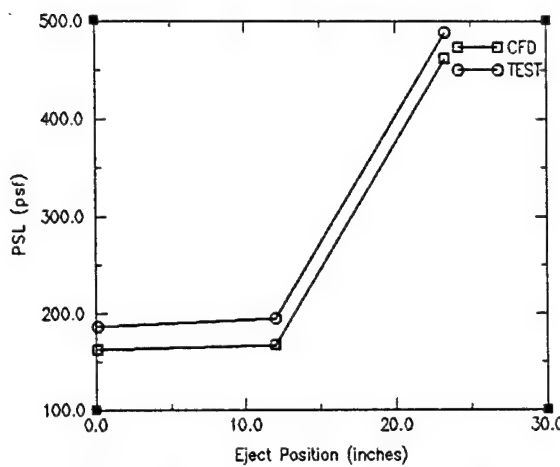
a.) Static Pressure for Occupant's Head



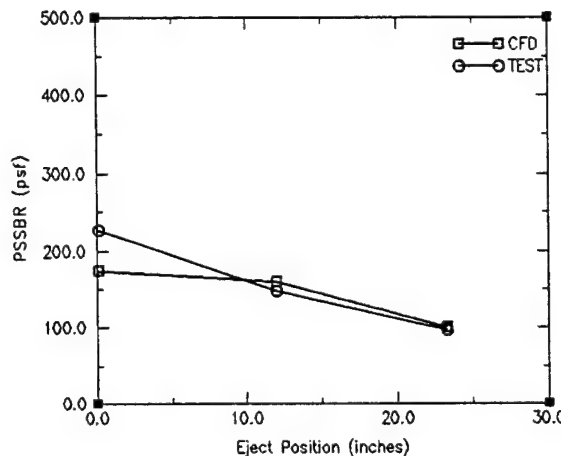
b.) Static Pressure for Occupant's Chest



c.) Static Pressure for Occupant's Abdomen



d.) Static Pressure for Occupant's Leg



e.) Static Pressure for Seat Back Reference

Figure 8-18. CFD and Wind Tunnel Predictions for Seat/Occupant Surface Pressures

Table 8-6. Static Pressure (psf) Predictions for Seat and Aircraft Simulations

Position	PSH	PSC	PSA	PSL	PSSBR
POS1	265.4	156.2	156.0	162.3	174.6
POS2	420.1	394.0	243.9	166.7	159.9
POS3	403.6	416.1	368.7	461.5	100.2
Freestream	440.4	425.6	322.5	451.6	173.9

## 8.4 Transient CFD-FASTRAN Analysis

### 8.4.1 Application of Chimera to Moving Bodies

For performing a transient moving-body problem with chimera, such as an ejection seat separating from an aircraft, there are three main solution steps:

- geometric modeling and grid generation,
- steady-state solution, and
- transient solution.

The first step in performing a transient moving-body problem is obtaining a fully converged steady-state solution. This steady-state solution serves as the starting point for the transient calculation. For the current transient ejection seat simulation, the steady-state solution from eject position one is used. For this reason, steps one and two have already been discussed in great detail. Due to the use of the chimera grid methodology, no additional geometric modeling or grid generation is required for simulating the transient problem. One important exception exists for steady-state solutions obtained using local or variable time-stepping options. If local time stepping is used, then the solution should be restarted and fully converged using a global time step. This process usually takes a few hundred iterations and ensures a consistent transition to time accurate solutions.

The transient solution process can be further broken down into five steps:

- time accurate flow solver step,
- calculation of body forces and moments,
- calculation of body motion via 6DOF or prescribed motion,
- perform body motion and update chimera information, and
- repeat step 1.

The simulation of moving body problems with CFD-FASTRAN is greatly simplified because all five of these steps are an integral part of the flow solver. No input/output or user interference is required. Flow solvers such as OVERFLOW that employ PEGSUS to perform chimera communication are much less efficient because step 2-4 are performed external to the flow solver. Also, to initiate moving body problems using PEGSUS requires complicated shell scripts and user interference. To initiate a moving body problem with CFD-FASTRAN, the user simply modifies the flow solver input to indicate the problem is unsteady and moving. The user specifies which grids are allowed to move and how their motion is to be determined. All of this input can be specified through the GUI or flow solver input file.

### 8.4.2 Seat and Aircraft Simulations

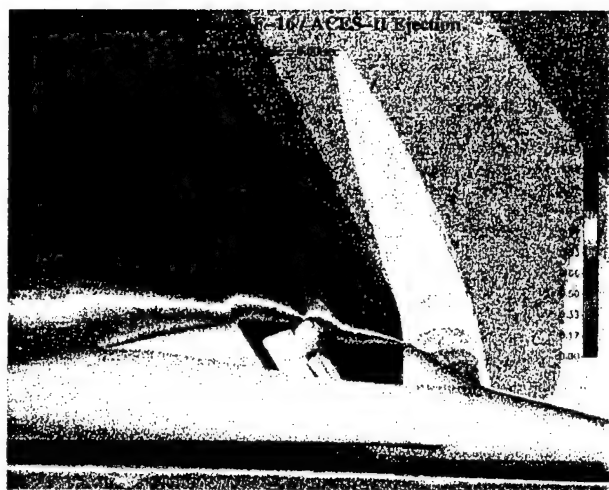
A single transient simulation was performed for the seat and aircraft configuration for the free-stream conditions specified in Tables 8-1 through 8-4. The seat was assumed to transition from position one to position three via a constant and prescribed velocity in 0.2 seconds. This time corresponds to 0.28 seconds full scale. The use of prescribed

motion is consistent with the ejection seat being attached to the catapult rail. Since an actual seat transient was not simulated in the wind tunnel, the transient CFD analysis serves only as a demonstration of the transient capabilities of the code and to make comparisons to the steady-state data and simulations. The transient calculation was performed for a seat angle of attack of  $17.25^\circ$  instead of  $13.25^\circ$ . As a result the transient calculation is not compared to the test data.

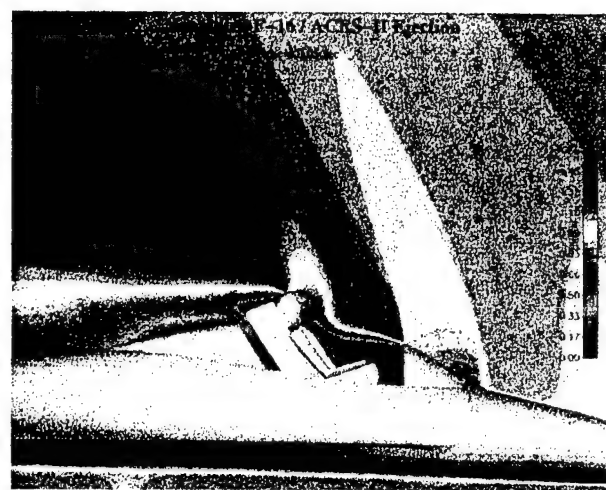
The steady-state solution at eject position one was used as the initial condition for the transient simulation. Two options existed for prescribing the time step in the time accurate solution. The first option employed a CFL condition and then calculated a minimum time step for the entire domain. The minimum time step would then be controlled by the smallest viscous cells in the flow field and would vary as the flow field developed. The second option simply required the specification of a constant time step. The latter was selected for several reasons. First, the use of a fixed time step allowed for flow field solutions to be saved at equal time intervals. Secondly, a much larger global time step could be specified relative to that indicated by the CFL condition and still maintain global stability. The time accurate time step for the transient simulation was determined by inspecting the maximum and minimum time steps from the steady-state solution,  $1E-06$  and  $7E-04$ , respectively. A median value of  $2.E-05$  was chosen. This value was selected to maximize the time step while preserving overall solution stability. Due to CPU constraints and the lack of data, the effect of a vary time step on solution accuracy was not investigated. However, the effects are expected to be small for time steps corresponding to CFL values in the stability range.

The transient simulation was performed using Roe's flux-difference splitting in conjunction with first-order Godunov spatial reconstruction. Viscous effects were simulated by employing the high-reynolds number  $k-\epsilon$  turbulence model with wall functions. The simulation required 10,000 flow solver iterations to reach the simulation time of 0.2 seconds. Approximately 322 CPU hours or  $1.76E-04$  cpu-secs per point per iteration were required to complete the solution on a DEC Alpha Station 600 s/266 machine. For a dedicated machine, the solution would have required two weeks. However, due to the shared workload on the machine the solution required approximately four weeks.

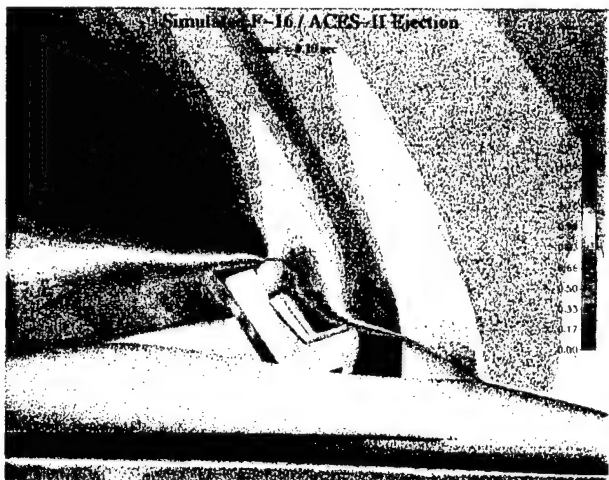
In Figures 8-19 and 8-20 Mach number contours in the symmetry plane and static surface pressures are presented for the transient solution at 0.05 second time intervals. The flow field features are very similar to those presented in Section 8.3 for the steady-state. In Figure 8-21, the aerodynamic coefficients for the transient simulation are presented along with the values from the steady-state calculations. A great deal of unsteady effects can be seen in the behavior of the transient coefficients. However, the time averaged values are in close agreement with the steady state values. This similarity indicates that for the conditions simulated the transient effects on the aerodynamic coefficients are small. Nonetheless, the proximity effects are still quite large.



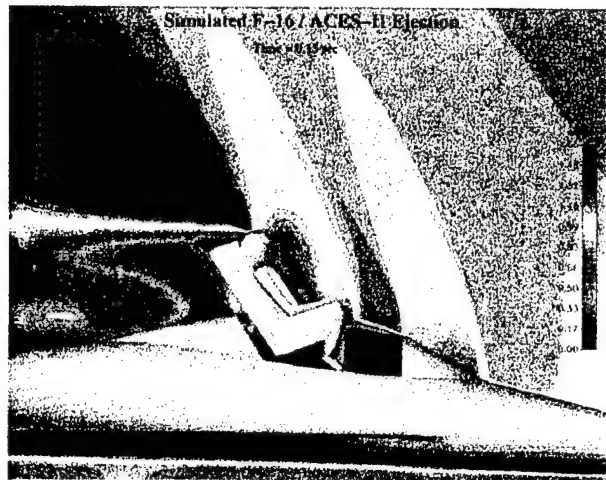
(a) Eject Time = 0.0 sec.



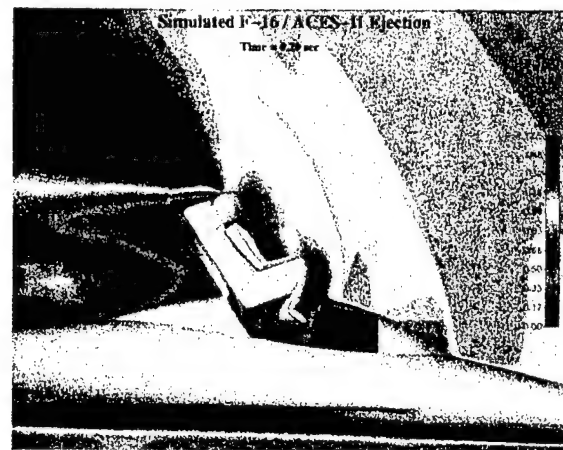
(b) Eject Time = 0.05 sec.



(c) Eject Time = 0.10 sec.

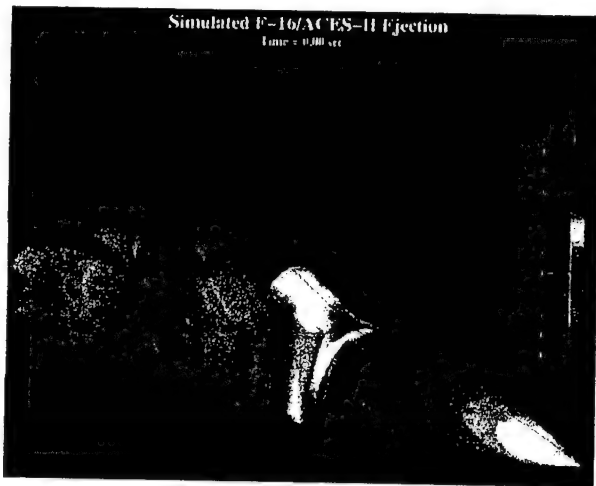


(d) Eject Time = 0.15 sec.



(e) Eject Time = 0.20 sec.

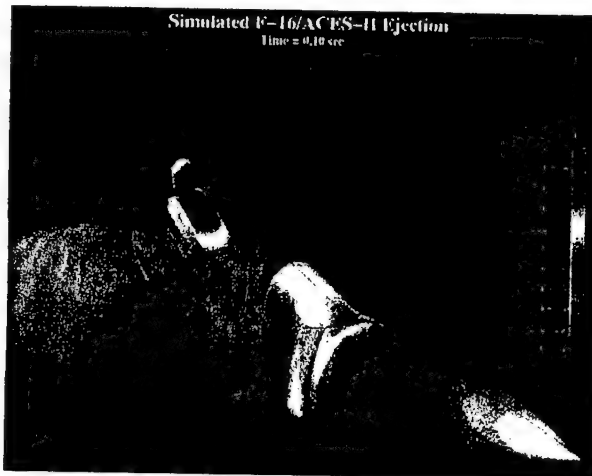
Figure 8-19. Mach Number Contours for Symmetry Plane of Seat and Aircraft Solutions



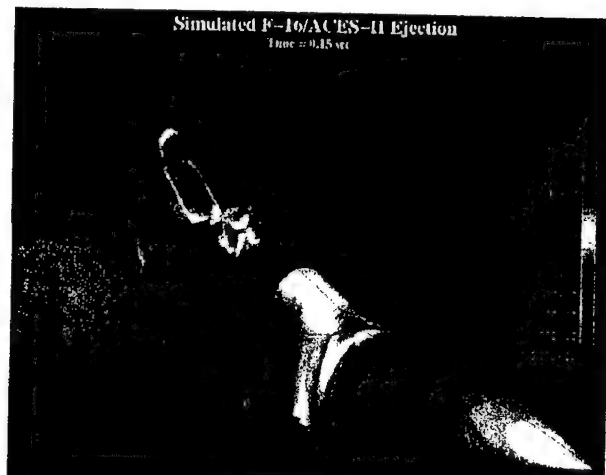
(a) Eject Time = 0.0 sec.



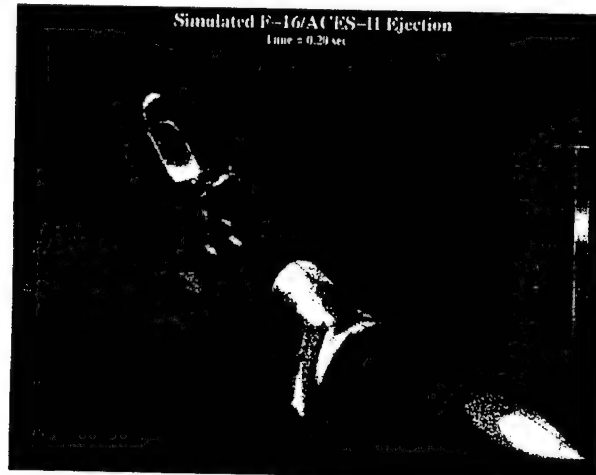
(b) Eject Time = 0.05 sec.



(c) Eject Time = 0.10 sec.



(d) Eject Time = 0.15 sec.



(e) Eject Time = 0.20 sec.

Figure 8-20. Static Surface Pressure Contours for Seat and Aircraft Solutions

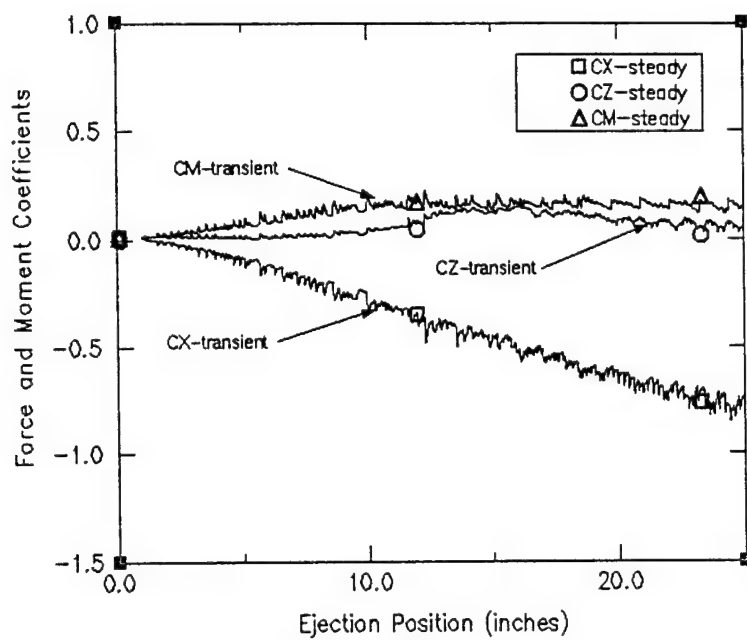


Figure 8-21. Comparison of Steady and Transient CFD Predictions of Aerodynamic Coefficients for Seat and Aircraft

## 9. CONCLUSIONS AND RECOMMENDATIONS

All of the objectives of this SBIR Phase I and II studies were successfully accomplished. The conclusions made from this SBIR effort along with the present status of commercialization and outlook for Phase III are described below.

### 9.1 Conclusions from Phase I and Phase II Studies

The Accomplishments of this SBIR effort may be summarized as follow:

- An integrated Computational Fluid Dynamics environment has been developed for escape system aerodynamics analysis. Geometry CAD modeling tools, elliptic grid generation package, two CFD flow solvers, and a flow visualization package have been adapted and partially developed under this project for escape system flow analysis. These tools have been integrated to create easy-to-use and efficient computational environment for escape system applications.
- A Partial Differential Equation program was developed for elliptic grid generation of seat and occupant grids. This program smooth seat/occupant grids with automatic clustering and orthogonality control on outside boundaries as well as seat/occupant surfaces. This program has been successfully used under this project and many other Phase III projects for grid generation of several escape system configurations.
- The geometry modeler and grid generator, CFD-GEOM, has been partially developed under this project and adapted for seat and aircraft application. Experience gained with this project has greatly impacted the development of CFD-GEOM, the only commercially available CFD grid generation software tightly integrating trimmed NURBS geometry definition with extensive grid creation capability supporting all cell types.
- The CFD-ACE code was adapted for seat and occupant aerodynamic analysis. Several numerical and physical modeling assessment and adaptations studies were performed. A set of guidelines were developed for escape system applications. CFD-ACE has been successfully used for the analysis of several escape system configuration under this project as well as several other Phase III projects.
- The CFD-FASTRAN code was adapted for seat and aircraft analysis for both steady-state and unsteady seat and aircraft separation. Two new multiple and moving bodies methodologies were developed and implemented into the code. The new moving bodies methodologies are being used in an ongoing commercialization effort for the CFD-FASTRAN code.
- Several geometry models and computational grids were developed for escape systems. These include NACES seat and occupant, ACES-II seat and occupant, F-

16 aircraft and cockpit, F-18 aircraft and cockpit and B-1A escape capsule. Several versions of these grids were created for single and multiple bodies analysis. All of these geometry and grid models were used in Phase III and other spin-off projects.

- CFD-ACE was extensively demonstrated and validated against several escape system configurations including the NACES seat and occupant, the ACES-II seat and occupant and the B-1A escape capsule. These calculations showed the correct and predictable flow trends and compared very well to wind tunnel test data where available.
- CFD-FASTRAN was demonstrated and validated for seat/occupant and seat/occupant and aircraft analysis. validations were performed using an ACES-II and F-16 wind tunnel configuration. Predictions compared favorably to wind tunnel test data. Also a demonstration calculation was performed with CFD-FASTRAN for the ACES-II separation from the F-16 aircraft using a prescribed trajectory. The demonstration calculations showed the correct flow trends and compared well to steady state predictions.

The above accomplishment clearly demonstrate the effectiveness of this SBIR program. The developed tools have been successfully used by the Navy for escape system flow analysis. The commercial potential of these tools have already been demonstrated as several CFD tools partially funded by this project have been commercialized and used by many private organizations.

## **9.2 Commercialization Status and Phase III Potential**

The CFD tools developed under this SBIR program have accelerated and greatly contributed to the commercialization efforts of several CFD tools, including CFD-ACE, CFD-FASTRAN, CFD-VIEW and CFD-GEOM. These codes are regularly advertised by CFDRC and are being used by more than 100 private organizations worldwide. New users from private as well government organizations are adopting these tools for their flow analysis tools.

The developed CFD tools have also resulted in several spin-off projects including applications for escape systems as well as for several automotive, aircraft and missile flow problems as outlined below:

- Several design support projects, sponsored by the Navy, to assess the NACES seat Pitot sensing system location and sensitivity to shock wave interference, and to analyze various stabilization device concepts.
- Several studies to assess the aerodynamic characteristics of escape capsules including rocket plume and aircraft proximity effects.
- Other Navy projects to develop CFD tools for the prediction of jettisoned aircraft canopies and rocket plume predictions and interference effects.
- Several studies related to the Fourth Generation Ejection seat design and

- qualifications including stagnation flow devices analysis.
- A study sponsored by Martin Baker for the analysis of Aerostabilizers (i.e. booms) on the NACES ejection seat.
- Automotive aerodynamic flow problems for modeling geometry of vehicles, for an auto manufacturer.
- Dynamic stall study for fighter aircraft lift surfaces performed the U.S. Air force.
- Dynamic flow analysis coupled with 6DOF for missile stage separation performed for U.S. Army Missile Command under the ARROW project.

This SBIR program and related spin-off projects have facilitated the evolution and development of several CFD methodologies for state-of-the art in CFD gridding and solution techniques. These include:

- Multi-domain structured grids with many-to-one interface meshing capability with pressure based flow solver for seat/occupant analysis in free stream.
- Hybrid structured/unstructured grids with a density based flow solver for seat/occupant with and without aircraft interference.
- Overset-hybrid gridding methodology for multiple complex bodies configurations for seat and aircraft steady state analysis.
- Traditional and conservative Chimera Overset gridding approach for multiple fixed and moving body problems to be applied for canopy trajectory simulation as well as seat and aircraft separation.

The Commercialization effort of the developed tools as well as the spin-off projects are expected to continue in the next few years for a very successful Phase III program.

## 10. REFERENCES

1. White, B.J., "Aeromechanical Properties of Ejection Seat Escape Systems," AFFDL-TR-74-57 (AD787194, April 1974).
2. Reichenau, D.E., "Aerodynamic Characteristics of a Full Scale ACES-II Ejection Seat with a Small Female or Large Male Manikin at Mach Numbers from 0.2 to 1.4," AEDC-TR-87-16, 1987.
3. Reichenau, D.E., "Aerodynamic Characteristics of a Half-Scale CREST Seat at Mach Numbers from 0.6 to 3.0," AEDC-TR-88-6, 1988.
4. Lundy, T.E., and Braddock, W.F., "Wind Tunnel Tests of the Flow Stagnation Protective Concept and Ejection Seat Stability Devices," AAMRL-TR-85-053, 1987.
5. Ayoub, P., and Yost, P., "Wind Tunnel Tests of a 0.65 Scale Ejection Seat with and without Yaw Stabilizers," NADC-84093-60, April 1984.
6. Hawkins, K.F., "Boeing Wind Tunnel Tests of the NACES Pitot-Static Sensors and Sequencers Unit," Contract No. N00019-85-C-0143, CDRL Item A003, Feb. 1987.
7. "CFD Analysis of Drag Reduction on an Ejection Seat During High Speed Ejection," Phase I Final Report, CFDRC Report No. 4125/1.
8. "CFD Analysis of Drag Reduction on an Ejection Seat During High Speed Ejection," all progress reports, CFDRC Project No. 4128.
9. Habchi, S.D., Ho, S.Y., Hufford, G.S., Marquette, T., and Ayoub, P., "Computational Aerodynamic Analysis of the Navy Aircrew Common Ejection Seat," AIAA-94-0395, AIAA 32nd Aerospace Sciences Meeting, Reno, NV, January 10-13, 1994.
10. Hufford, G.S. and Habchi, S.D., "Validation of CFD Methodology for Ejection Seat Applications," AIAA-94-0751, AIAA 32nd Aerospace Sciences Meeting and Exhibit, Reno, NV, January 10-13, 1994.
11. Habchi, S.D., Hufford, G.S., and Marquette, T., "Navier-Stokes Computational Analysis of the B-1A Escape Capsule," AIAA-95-0187, AIAA 33rd Aerospace Sciences Meeting and Exhibit, Reno, NV, January 9-12, 1995.
12. Habchi, S.D. and Hufford, G.S., "Transient Simulation of Turbulent Flow Over Blunt Bodies," AIAA-95-1837, 13th Applied Aerodynamics/Unsteady Aerodynamics, San Diego, CA, June 19-22, 1995.
13. CFD\_ACE Validation Cases Manual
14. "CFD Analysis of the NACES Ejection Seat," SBIR Phase I Final Report, CFDRC Report No. 4860/4.
15. Habchi, S.D. and Przekwas, A.J., "CFD Analysis of NACES Seat with Yaw Fins," Final Report for NADC, CFDRC Report 4127/1, December 1991.
16. Habchi, S.D., Hufford, G.S., and Przekwas, A.J., "CFD Analysis of NACES Seat with Yaw Fins Deployed at 60° Sweepback Angle," CFDRC Report 4129/1 for NAWC-A/D, August 1992.
17. Yang, H.Q., Habchi, S.D., and Przekwas, A.J., "A General Strong Conservation Formulation of Navier-Stokes Equations in Non-Orthogonal Curvilinear Coordinates," AIAA-92-0187, Jan. 1992.
18. Rubesin, M.W., "Turbulence Modeling for Aerodynamic Flow," AIAA-89-0606, Jan. 1989.
19. Launder, B.E., and Spalding, D.B., "The Numerical Computation of Turbulent

Flows," *Computer Methods in Applied Mechanics and Engineering*, vol. 3, 269-289, 1974.

20. Chien, K-Y, "Predictions of Channel and Boundary Layer Flows with a Low Reynolds Number Turbulence Model," *AIAA Journal*, vol. 20, 33-38.
21. Jones, G.W., Cincotta, J.J., and Walker, P.W., "Aerodynamic Forces on a Stationary and Oscillating Circular Cylinder at High Reynolds Numbers," *NASA-TR-R-300*, 1969.
22. Roshko, A., "Experiments on the Flow Past a Circular Cylinder," *JFM* 10, 345-356, 1961.
23. Jones, W.P. and Launder, B.E., "The Prediction of Laminarization with a 2-Equation Model of Turbulence," *Int. J. Heat and Mass Transfer*, vol. 15, pp. 301, 1972.
24. Jones, W.P. and Launder, B.E., "Predictions of Low Reynolds Number Phenomena with a 2-Equation Model of Turbulence," *Int. J. of Heat and Mass Transfer*, vol. 16, pp. 1119, 1973.
25. Chien, K-Y, "Predictions of Channel and Boundary Layer Flows with a Low Reynolds Number Turbulence Model," *AIAA Journal*, vol. 20, 33-38.
26. Achenbach, E., "Experiments on the Flow Past Spheres at Very High Reynolds Numbers," *JFM* 54, 565-575, 1972.
27. Bailey, A.B. and Hiatt, J., "Sphere Drag Coefficients for a Broad Range of Mach and Reynolds Numbers," *AIAA Journal*, vol. 10, 1436-1440, 1972.
28. Bailey, A.B. and Starr, R.F., "Sphere Drag at Transonic Speeds and High Reynolds Numbers," *AIAA Journal*, vol. 14, 1631, 1976.
29. Reichenau, D.A., "Aerodynamic Characteristics of a Full-Scale ACES-II Ejection Seat with a Small Female or Large Male Manikin at Mach Number from 0.2 to 1.4," *AEDCTR-87-16*, 1987.
30. Benson, J.M., "High Speed Wind Tunnel Tests of an 0.36 Scale Model of the B-1A Escape Module to Investigate General Stability and Control Characteristics," *Rockwell Report NA-71-116*, vol. 1-3, 1971.
31. Wurtzler, K., "Application of an Euler Code to the B-1A Escape Capsule," *AIAA-90-0431*, Jan. 1990.
32. Steger, J. L., Dougherty F. C., and Benek, J. A., "A Chimera Grid Scheme," *Advances in Grid Generation*, K. N. Ghia and H. Ghia, Eds., ASME FED Vol. 5, June 1983.
33. Benek, J. A., Steger, J. L., and Dougherty, F. C., "A Flexible Grid Embedding Technique with Application to the Euler Equations," *AIAA Paper 83-1944*, July 1983.
34. Suhs, N. E., and Tramel, R. W., "PEGSUS 4.0 Users Manual," *AEDC-TR-91-8*. Nov. 1991.
35. Benek, J. A., Donegan, T. L., and Suhs, N. E., "Extended Chimera Grid Imbedding Scheme with Application to Viscous Flows," *AIAA Paper 87-1126*, 1987.
36. Fox, J. H., Donegan, T. L., Jacocks J. L., and Nichols, R. H., "Computation of Euler Flow Field Produced about a Transonic Aircraft with Stores," *AIAA Paper 89-2219*, 1989.
37. Nichols, R. H., Jacocks J. L., and Rist, M. J. "Calculation of the Carriage Loads of Tandem Stores on a Fighter Aircraft," *AIAA Paper 92-0283*, Jan. 1992.

38. Jordan, J. K., "Computational Investigation of Mutual Interference Effects on the Influence Function Method of Store Load Prediction," Master's Thesis, University of Tennessee, December 1991.
39. Ahmad, J. U., Shanks, S. P., and Buning, P. G., "Aerodynamics of Powered Missile Separation from F/A-18 Aircraft," AIAA Paper 93-0766, Jan. 1993.
40. Meakin, R., "Transient Flow Field Responses about the Space Shuttle Vehicle During Ascent and SRB Separation," R. Aero. Soc., Store Carriage, Integration, and Release Conf., pp. 29.1 29.16, April 1990.
41. Lijewski, L. E., and Suhs, N. E., "Time Accurate Computational Fluid Dynamics Approach to Transonic Store Separation Trajectory Prediction," AIAA Journal of Aircraft, Vol. 31, No. 4, pp 886-891, July-August 1994.
42. Meakin R. and Suhs, N. E., "Unsteady Aerodynamic Simulation of Multiple Bodies in Relative Motion," AIAA Paper 89-1996, June 1989.
43. Thoms, R. D., and Jordan, J. K., "Investigation of Multiple-body Trajectory Prediction Using Time-Accurate Computational Fluid Dynamics," AIAA Paper 95-1870, 1995.
44. Hariharan, N. and Wang, Z.J., "Application of Conservative Chimera Methodology in Finite Difference Settings," AIAA-97-0627, 1997.
45. Reichenau, D.E.A., "Aerodynamic Characteristics of a 0.5-Scale Crewman/Ejection Seat Model During a Simulated Ejection from an F 16 Fighter at Free-Stream Mach Numbers from 0.4 to 1.2", AEDC-TSR 78-P42, October 1978.
46. Reichenau, D.E.A., "Data Package: AMRL Ejection Seat Test (MIST)", Project No: P41T-14, Test Unit: 16T, Arnold Engineering Development Center, September 1978.

## Appendix A.

## Project Related Technical Conference Publications

- AIAA-94-0395 Computational Aerodynamic Analysis of the Navy Aircrew Common Ejection Seat A-2
- AIAA-94-0751 Validation of CFD Methodology for Ejection Seat Applications A-17
- AIAA-95-0187 Navier-Stokes Computational Analysis of the B-1A Escape Capsule A-36
- AIAA-95-1837 Transient Simulation of Turbulent Flow Over Blunt Bodies A-54



**AIAA-94-0395**

**COMPUTATIONAL AERODYNAMIC  
ANALYSIS OF THE NAVY  
AIRCREW COMMON EJECTION SEAT**

**S.D. Habchi, S.Y. Ho, and G.S. Hufford  
CFD Research Corporation  
Huntsville, AL 35805**

**and**

**T. Marquette and P. Ayoub  
Naval Air Warfare Center - Aircraft Division  
Warminster, PA 18974**

**32nd Aerospace Sciences  
Meeting & Exhibit  
January 10-13, 1994 / Reno, NV**

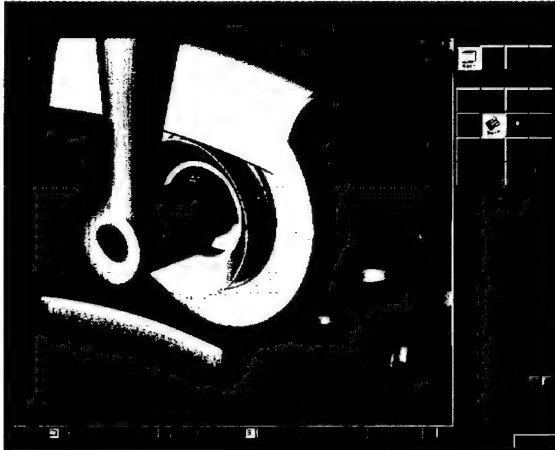
## **Appendix B.**

### **Selected Brochures of CFD Tools that were partially developed and commercialized under this contract**

- CFD-GEOM Brochure
- CFD-ACE Brochure
- CFD-FASTRAN Brochure
- CFD-VIEW Brochure



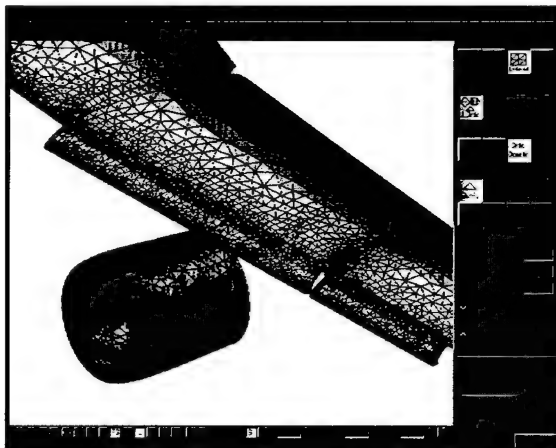
## Interactive 3D Geometry Modeling and Grid Generation Software



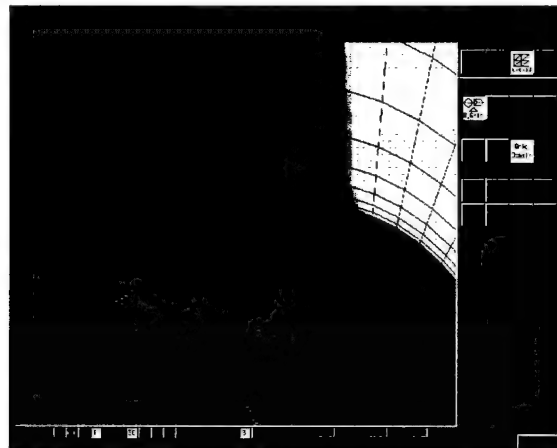
Trimmed NURBS



Structured Grid



Unstructured Grid



Hybrid Grid

## HIGHLIGHTS

- **Tight Integration** of trimmed NURBS geometry creation with extensive grid generation capabilities supporting all cell types
- **CAD Data Import** checking and repair for faster turn around
- **Automatic Database** updating of geometry/grid topology and boundary conditions
- **Easy-To-Learn & Use** with intuitive object oriented GUI
- **Available on** SGI, DEC, IBM, HP, SUN Workstations and Windows NT, Windows 95, LINUX PCs

Reduce lead time in model preparation. Enhance your CFD analyses. Try **CFD-GEOM!**

# What is CFD-GEOM?

CFD-GEOM is designed for fast and intuitive geometry/grid creation whether you are creating a model from scratch or importing data from another CAD program.

## *Extensive Geometry Construction*

### **Geometry Creation**

#### **Trimmed NURBS geometry library**

- Curve/curve intersection
- Surface/surface intersection
- Geometry projection to surface sets
- Trimming of curves and surfaces

#### **Curve creation**

- Interpolation through points
- From any U,V parametric line of a surface
- Tangent curves to lines
- Arcs and circles
- Lines and polylines
- Joining existing curves
- Splitting existing curves (parametric or at physical points)

#### **Surface creation**

- Extrusion of curves
- Revolution of curves
- Ruled surfaces
- Surfaces from 4 curve sets
- Interpolated surfaces through a set of grid points
- Splitting existing surfaces

### **Bi-Directional Relational Database**

**CAD import via IGES from CAD packages such as Pro-E, Unigraphics, AutoCAD, etc.**

**All geometry and grid modifications are followed by automatic database updating**

- Relational data structures provide very efficient model updating

#### **“Dirty Geometry” checking and repair**

- Automatic checks to determine trimmed surface set closure
- Automatic point and curve filtering to a given tolerance
- Automatic edge filtering
- Extensive user tools for other repair

**Automatic re-creation of solid model information from IGES input**

**Automatic water tight trimmed surface creation from external structured surface grids**

**Automatic recreation of topology information from external structured grid files such as Plot3D**

## *Flexible Capabilities to “Mix and Match” Geometry and/or Grids*

### **Hybrid Grid Systems**

#### **Prism grid creation from surface triangulation**

- Translation of triangulations
- Rotation of Triangulations
- Semi-structured boundary layer grids via the advancing normal technique

#### **Arbitrary mixing and matching of multi-block structured, unstructured and prism grids into a mixed element hybrid grid**

### **Parts Libraries**

**Capability to work on multiple models at one time using layers**

**Capability to mix and match geometries and grids on different layers with automatic duplicate entity filtering**

**Automatic connection of geometries and grids upon transfer between layers**

# *Versatile Grid Generation Capabilities*

## **Structured Grids**

### **Multi-block structured topology definition**

- User friendly topology creation
- Simplified creation of basic topologies (extruded and revolved topologies)
- Boundary conditions applied to topological entities
- Composite existing topological entities
- Full support for all types of 2D and 3D topologies
- Automatic topology detection from geometry

### **Multi-block structured grid definition and manipulation**

- Various TFI schemes for surface and volume grids including enforced boundary orthogonality and smoothing algorithms
- Project spatial TFI grids to surface sets
- Gridding on surfaces in parametric space
- Edge linking facility for each modification of grid points and distributions
- Edge substitution to easily transform one topology to a similar geometry
- Easy grid orientation updating
- Multi-to-one interface matching available via block skipping
- Grid quality assessment

## **Unstructured Grids**

### **Automatic and controllable surface triangulation**

- Direct triangulation of surface sets with automatic clustering to geometric features
- Extensive mechanisms to manipulate geometric features for clustering control
- Matching of unstructured surfaces for periodic boundaries

### **Capability to match triangulations at the boundaries of connected surface sets**

- Automatic subdivision of structured face entities for triangulation
- May mix and match trimmed surface entities with structured face entities

### **Automatic and controllable unstructured volume grids**

- Automatic tetrahedral sizing criteria from surface triangulation
- Specifying of minimum allowed solid angles for tetrahedral quality control
- Coarsening/refining control parameter for tetrahedral number from identical boundary surface triangulations

## *Extendable Output*

### **Geometry, Grid and BC Output**

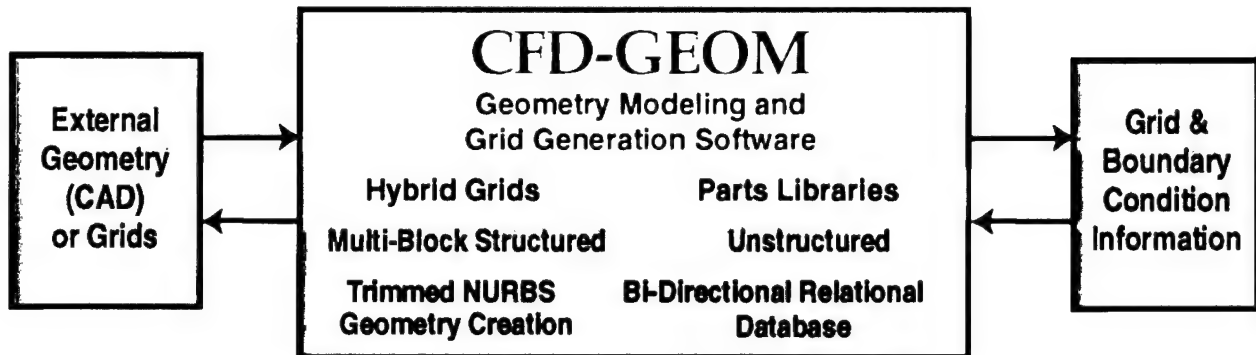
- Plot 3D Grid File
- IBC File: Interface Boundary Condition File for Multi-Block Structured Grids
- CFDRC Mixed Element Format
- CFDRC Data Transfer Facility
- Fast
- Patran
- Nastran
- IGES
- Easily customized for other formats

### **Boundary Condition Information**

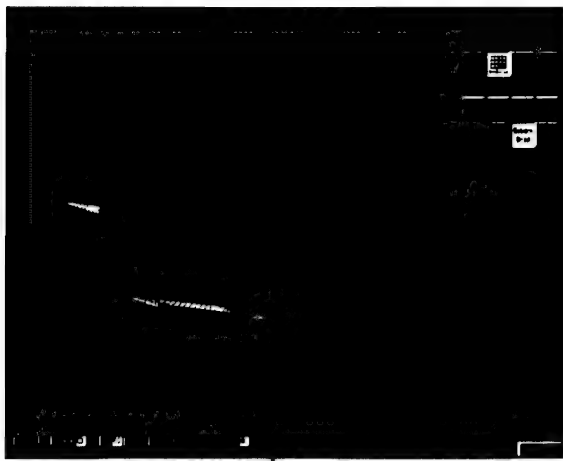
- User configurable boundary condition definition for any flow solver via a resource file
- User configurable boundary conditions propagate to grid and boundary condition files
- Boundary and volume condition setting on structured and unstructured entities
- Boundary condition output for all types of grid systems

**Try It!**

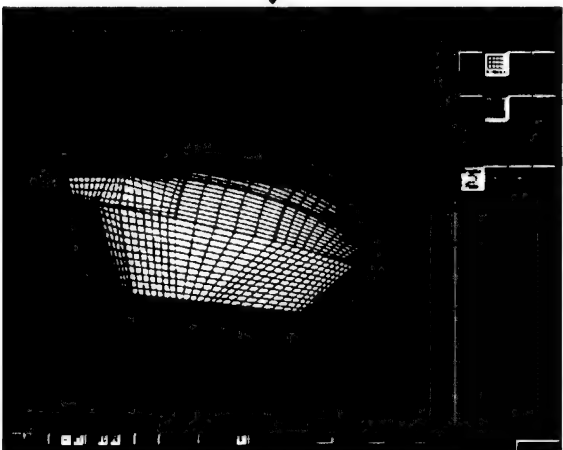
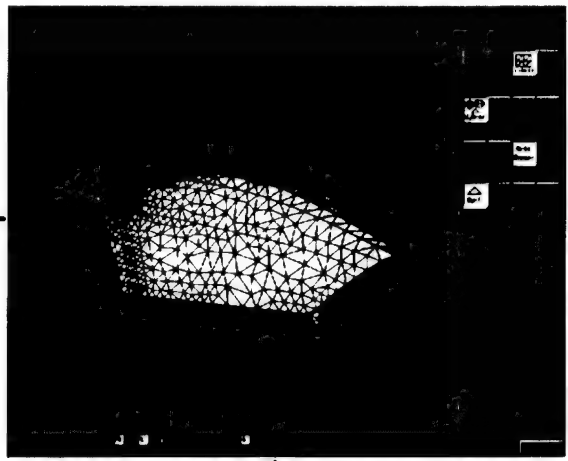
**CFD-GEOM is the most comprehensive grid generation system for CFD analysis. With a user manual, tutorial manual including over 30 step-by-step user tutorials and a dedicated support team, it is easy to begin using CFD-GEOM. Try it and see how you can significantly reduce your time to create useful CFD grids!**



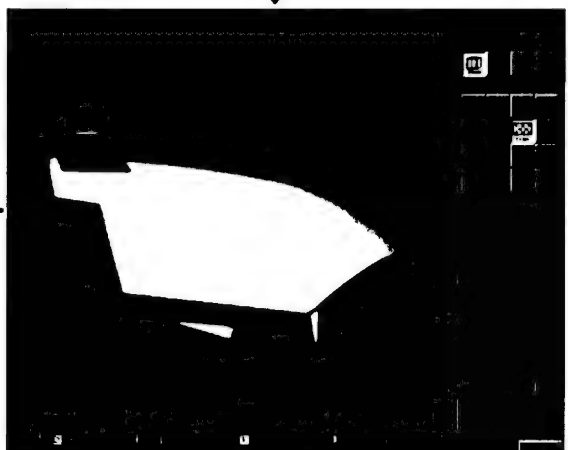
External Grid



Water Tight Trimmed NURBS, Unstructured Triangulation



Water Tight Trimmed NURBS, Topology, Structured Grid



IGES CAD

### Flexible Model Creation and Conversion

For further information, contact

**CFDRC**

"On the Leading Edge of CFD Technology"

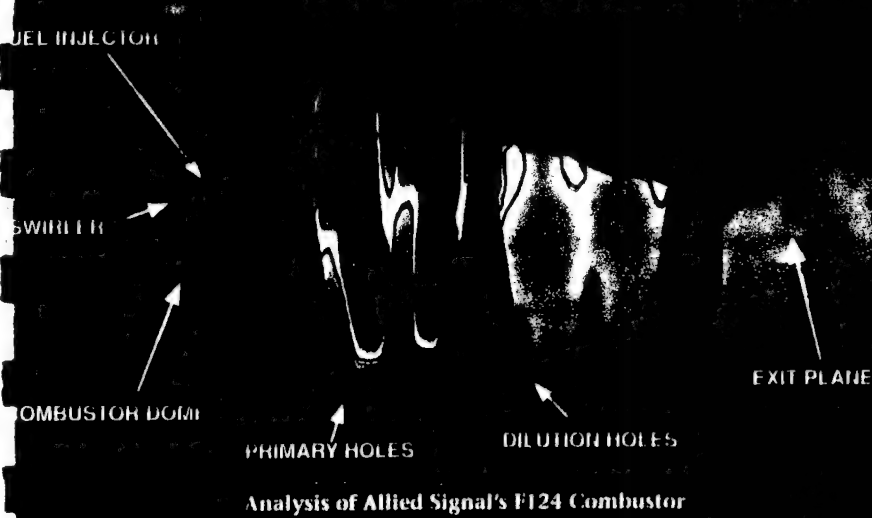
CFD Research Corporation  
3325 Triana Blvd., Huntsville, AL 35805  
Telephone: (205) 536-6576 Fax: (205) 536-6590  
email: [info@cfdrccom](mailto:info@cfdrccom) <http://www.cfdrccom>

**CFD-GEOM can output grid and boundary condition information for any CFDRC or non-CFDRC flow solver. Assistance is available to output your flow solver's format.**

# Advanced General Purpose CFD Code



Time Progression of Windshield Ice-melting Patterns  
**Climate Control and Window De-icing**



Analysis of Allied Signal's F124 Combustor



Multi-component CVD Reactor  
with a Rotating Susceptor

System Level Electronics Cooling



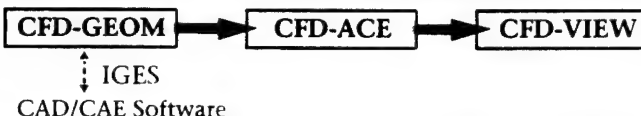
- Multi-Block, Structured Meshes with Many-to-one Cell Joins for Local Mesh Refinement, Implicitly Coupled for Efficient Analysis
- Highest Accuracy Finite Volume Methodology
- Extensive Combustion/Chemical Reaction Models using Multi-Step, Finite Rate Chemistry with Stiff Kinetics
- Surface Chemistry for CVD and PVT
- Multi-Component Diffusion
- Basic and Extended Mechanisms for NO<sub>x</sub> and CO
- Lagrangian Droplet/Particle Tracking with Collision, Coalescence and Evaporation
- Liquid Spray and Particulate Combustion
- Fan Model for Electronic, Automotive and Other Applications
- Incompressible and Compressible Transonic/Supersonic Flows
- Multi-Media, Multi-Block Conjugate Heat Transfer
- Rotating and Moving Meshes
- Concentrated and Distributed Flow Resistances (Non-Isotropic Porous Media, Perforated Plates)

**CFDRC**

**CFD RESEARCH CORPORATION**

# CFD-ACE Features

Fully Integrated Software for Virtual Prototyping and Parametric Design



## GEOMETRY AND MESH

CFD-ACE is fully integrated with CFD-GEOM for creation of geometry, mesh, and boundary conditions, and import from other CAD/CAE systems. The geometry capabilities include:

- Multi-Block, 2D/3D, Structured Meshes with Many-to-One Coupling Enabling Local Mesh Refinement
- Rotating Coordinates, Moving Meshes and Walls
- Internal Solid Objects, Concentrated and Distributed Resistances (Solid and Perforated Plates, Blockages, Porous Media)

## FLUID FLOW

A full range of flow conditions is handled by CFD-ACE, including:

- Incompressible/Compressible Flows, to Supersonic
- Steady/Transient
- Laminar Flow, with a Choice of Non-Newtonian Rheology
- Turbulent Flow, with a Variety of Models:
  - Eddy Viscosity
  - Baldwin-Lomax
  - $k-\epsilon$
  - Extended  $k-\epsilon$
  - Multi-Scale  $k-\epsilon$
  - $k-\omega$
  - RNG
  - Two Layer
- Profile and Time Varying Boundary Conditions

## HEAT AND MASS TRANSFER

Particular attention has been paid to the energy equation, ensuring fully conservative treatment under a wide range of conditions:

- Natural and Forced Convection
- Multi-Media, Multi-Block Conjugate Heat Transfer
- Radiation Heat Transfer (Discrete Ordinate Method)

- Variable Physical Properties, JANNAF Database, Kinetic Theory of Gases
- Mass Transfer with Multi-Component Diffusion
- Specified Temperature, Heat-Flux, Heat-Transfer Coefficient, and Adiabatic Thermal Boundary Conditions

## CHEMICAL REACTION AND COMBUSTION

CFDRC has extensive experience in combustion, providing a comprehensive capability in CFD-ACE:

- Combustion Models Include:
  - Instantaneous Reaction
  - Multi-Step, Finite Rate Chemistry
  - Equilibrium Chemistry
  - PDF Models
  - Heterogeneous Reactions
- Basic and Extended  $\text{NO}_x$  and CO Mechanisms
- Surface Chemistry for CVD and PVT Processes
- Two-Phase Spray and Particulate Combustion
  - Dispersed Phase
  - Collision, Coalescence and Evaporation
  - Drop Dispersion by Turbulence
  - Particle Melting/Solidification

## NUMERICS

CFD-ACE blends state-of-the-art numerical techniques to maximize solution robustness, accuracy, and efficiency:

- Finite Volume, Pressure Based, Strongly Conservative Formulation
- Fully Implicit Treatment of Multi-Block Interfaces
- Differencing Schemes (Upwind, Central, Osher-Chakravarthy, Second Order Upwind, Third Order Schemes)
- SIMPLEC/PISO Algorithms
- Solvers - Whole Field, CGS

## ADVANCED PHYSICAL MODELS

Available as Add-On Options:

- Atomization
- Cavitation
- Fluid-Structure Interaction
- Multi-Component Transport Based on Kinetic Gas Theory
- Monte-Carlo Based Microscopic Film Growth
- Joint Composition and Monte-Carlo PDF Models

## SUPPORT

CFDRC provides the highest level of technical support, drawing on hundreds of person-years experience in CFD development and industrial applications. Call on CFDRC's expertise to customize CFD-ACE for your specialized applications.

CFDRC develops and maintains all software in-house, ensuring reliable, one-stop service. Intuitive, object-oriented GUIs facilitate rapid learning and ease of use.

## FUTURE DIRECTIONS

CFDRC is continually bringing its R&D successes into the commercial software range. More efficient solvers, increased geometric flexibility via unstructured/hybrid, Chimera and Adaptive Cartesian Prism mesh technology are in progress, together with the growing choice for physical models.

For brochures on specific software packages, please contact:

**CFDRC**

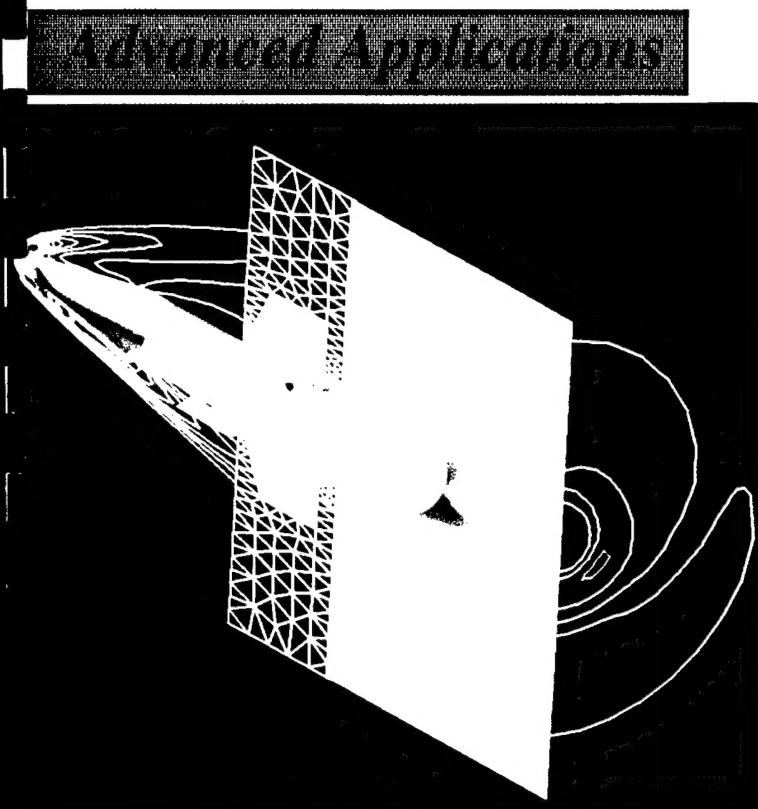
*"On the Leading Edge of CFD Technology"*

CFD Research Corporation

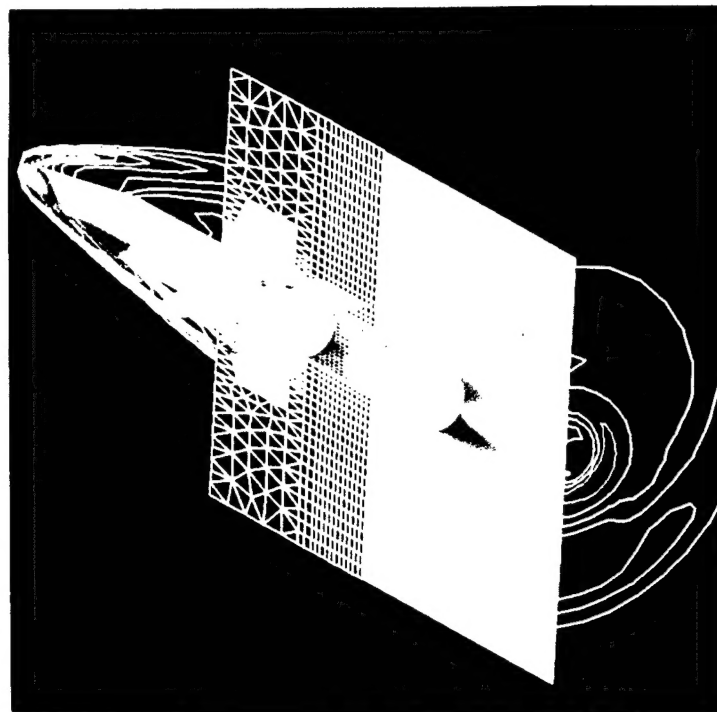
3325 Tiana Blvd., Huntsville, AL 35805

Telephone: (205) 536-6576 Fax: (205) 536-6590

email: [sales@cfdrccom](mailto:sales@cfdrccom)



### ▲ Missile separation dynamics



### CFD-FASTRAN

Multi-zone, using an efficient zone-by-zone solution procedure

Memory management, dynamically allocated high/low modes

Point, line, and full implicit time integration procedures

Implicit boundary conditions

Multi-grid convergence acceleration

High order reconstruction schemes including TVD, MUSCL, and k-exact

Time-accurate and steady state time integration with optional local time stepping

Dynamic mesh enrichment for multiple moving body flows and adaptive remeshing

Riemann Solvers: Roe's FDS and Van Leer's FVS

### Topology Options

▲ Structured/Unstructured/Hybrid

— Generalized discretizations including tetrahedra, hexahedra, triangles, quadrilaterals, and prisms

### Physics

▲ Euler, Navier Stokes Equations for 2-D, 3-D, and Axi-symmetric flows

▲ Baldwin Lomax turbulence model

### GUI and Visualization

▲ X-Windows/Motif Graphical User Interface for ease in generating flow solver input files

▲ Seamless Integration with CFD-VIEW, our powerful flow visualization package

### Further Information

For more information call

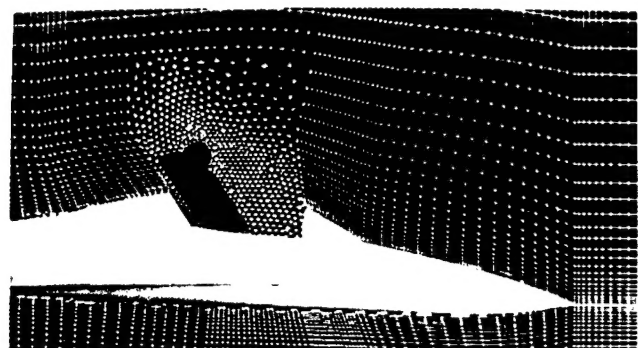
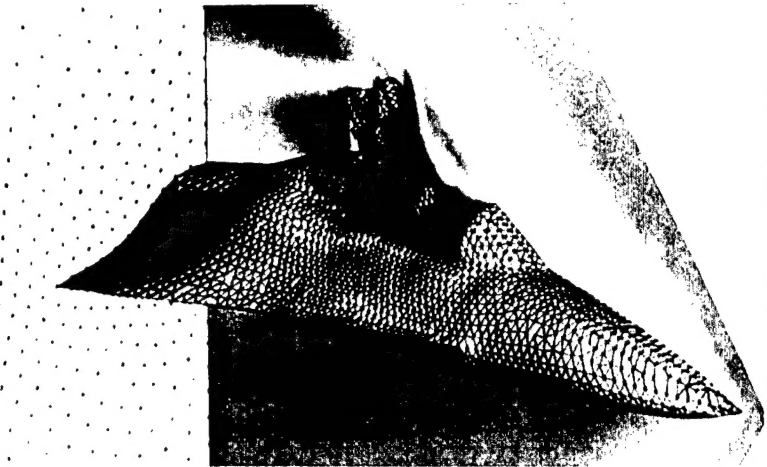
Mr. R. Sukumar or Dr. Ashok Singhal at  
(205) 536-6576.

# CFD-FASTRAN *Advanced Features*

***High Accuracy Computational Flow Solver for Unstructured, Structured and Hybrid Grids.***

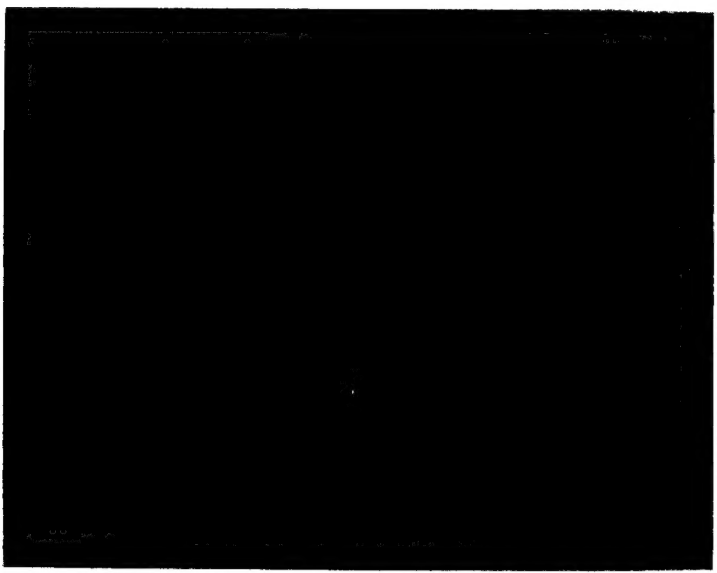
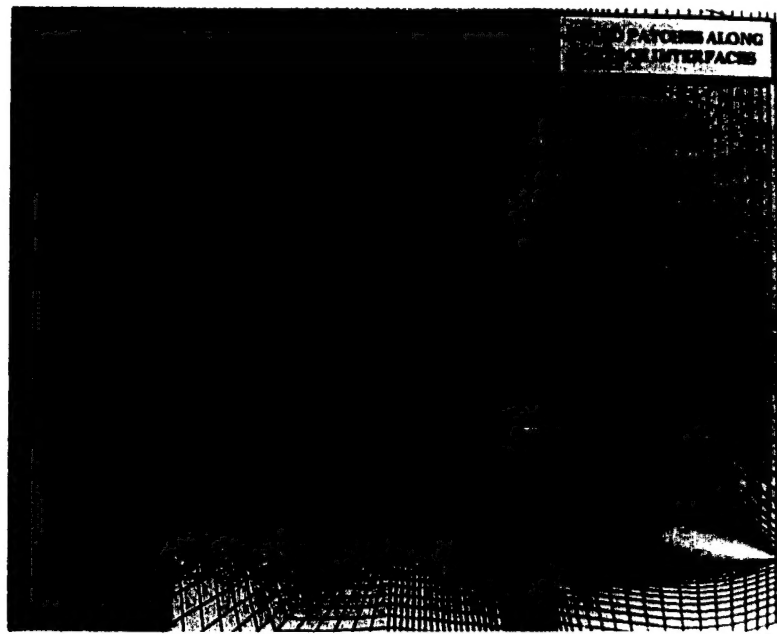
## *The Unstructured Arena*

- Multi-zone, three dimensional Navier Stokes solution procedures using high accurate reconstruction schemes.
- The use of fully implicit time integration methods overcome the poor convergence performance of typical explicit unstructured flow solvers.
- Advancing front grid generation using advancing layers concepts for viscous applications.



## *A Hybrid Approach*

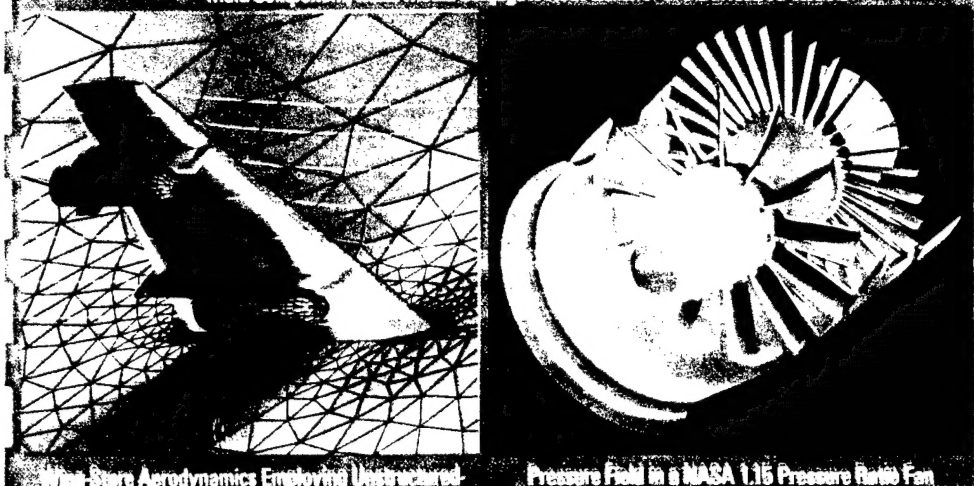
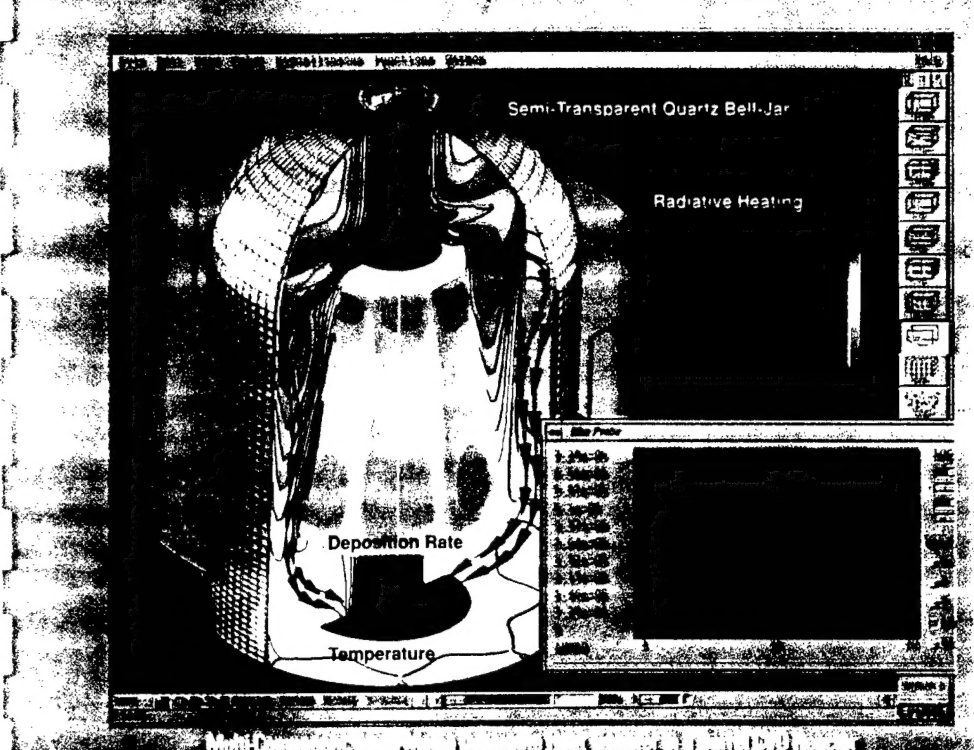
- From grid generation to flow solver to flow visualization, our hybrid methods seek to extract the benefits of combined structured/unstructured technologies.
- Frozen structured mesh interfaces serve as initial fronts for the grid generation process. This effective approach leads to conservative zonal interface treatment.



*Our unique attitude towards developing state of the art computational fluid dynamic software is to provide the user with the most technologically advanced methods in a computationally flexible environment that caters to the user's primary concerns of accuracy, efficiency, and reliability.*

# CFDRC

## Interactive 3D Graphics, Animation and Flow Visualization Software

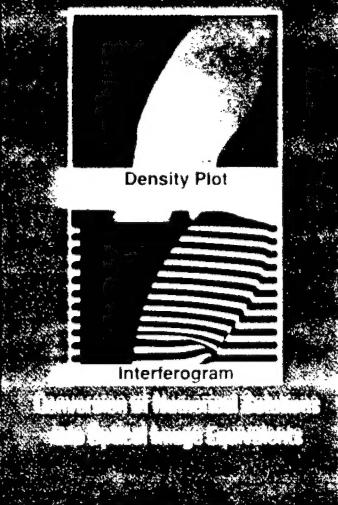


Flow-Field Aerodynamics Employing Unstructured Mesh Techniques

Pressure Field in a NASA 1.15 Pressure Ratio Fan



Direct Volume Rendering of Numerical Flow Simulation



Density Plot

Interferogram

### Highlights

- New Object-Oriented Interface, very easy and intuitive
- Fast Manipulation of Large Data Sets, taking advantage of 3D graphical hardware
- Structured/Unstructured/Hybrid Data Sets
- Optical Images – Interferogram, Schlieren, Shadowgraph, Planar Laser Induced Fluorescence (PLIF)
- CFD Function Calculator with extensive array of precalculated functions
- Math Calculator for evaluating new variables as a function of primitives
- Flow Ribbons and Particle Traces
- Interactive Point and Line Data Probes
- Transient Animation of Liquid Spray/Particle Data
- Interactive Animation
- Seamless Integration with CFDRC's Flow Solvers. Translators to other CFD codes can be made available

Enhancing Your Analysis  
Through High Quality  
Data Visualization

**Your View Matters To Us**

**CFDRC**

CFD RESEARCH CORPORATION

## ADVANCED DATA VISUALIZATION

- Object-oriented design of CFD-VIEW 3.0 is intuitive, easy-to-use, and fast. Directly click on any displayed entity to manipulate it; change any or all attributes, toggle on/off, or delete it.
- CFD-VIEW efficiently handles datasets with a hybrid combination of Structured as well as Unstructured data.
- Option to convert numerical solutions into optical images such as interferograms, planar laser induced fluorescence (PLIF), shadowgraphs, Schlieren images, vorticity, dilatation, etc. This enables direct comparison with experimental data from the laboratory.
- Fast, precise, interactive control of rotation, translation, and zooming, with 3D "virtual trackball."



Conversion of Numerical Solutions into Optical Image Equivalents

## CFD TAILORED OPTIONS

- The CFD function library offers twenty-four commonly used CFD variables, such as Mach number. Additionally, important CFD constants such as Universal Gas Constant R are stored for further calculations.
- 3D particle traces, defined individually or as rakes, and "oil streaks" confined to a particular surface.
- Flow ribbons to show 3D flow patterns in the flow field, optionally shaded with a secondary variable.

- Transient animation of liquid spray or dispersed particle data along with size/property variation. Valuable for applications such as fuel injection systems, spray analysis, and particulate flows.
- Topological Flow Visualization for automatic detection and display of critical points, saddle points, and lines. Valuable for external aerodynamics analysis.
- Selective grouping of walls, with capability to display different features for each wall group.

- Origin definition for convenience in image manipulation.
- Interactive color control of all display features.
- Applicable in visualizing numerical and experimental data from various disciplines, not just CFD.

## OPERATING ENVIRONMENT

- Available on Silicon Graphics, HP, IBM, Sun, and DEC workstations.
- Complete user customization of display features, colors, text, and language using standard X resource files.
- Postscript printer setup and output.
- "Turbo Mode" for speedy operation on lower-end machines.
- Model save/restore capability.
- Seamless integration with CFDRC's flow solvers CFD-ACE, CFD-FASTRAN, CFD-TWOPHASE and specific-purpose codes such as CFD-EHD, ATHOS3, etc.

## SUPPORT

CFD-VIEW is developed and supported in-house. CFDRC's engineers and scientists are available for assistance in adapting and customizing CFD-VIEW for your specialized visualization needs. Translators for any data format or code can be made available.

## FUTURE DIRECTIONS

- Concurrent visualization during analysis, as the solution develops.
- Concurrent visualization of solutions from multiple codes on clusters of workstations.

For brochures on specific software packages, please contact:

**CFDRC**

*"On the Leading Edge of CFD Technology"*

CFD Research Corporation

3325 Triana Blvd., Huntsville, AL 35805

Telephone: (205) 536-6576 Fax: (205) 536-6590

email: sales@cfdrccom